Dissociation dynamics of molecular ions in ultrafast, intense laser fields:

from diatomic to polyatomic molecules

by

Bethany Jochim

B. A., Augustana College, USA, 2011

AN ABSTRACT OF A DISSERTATION

submitted in partial fulfillment of the
requirements for the degree

Doctor of Philosophy

Department of Physics
College of Arts and Sciences

KANSAS STATE UNIVERSITY
Manhattan, Kansas

2019

Abstract

Out of the many tools for probing molecular dynamics, intense, ultrafast laser pulses are particularly well suited for this purpose. First, these pulses have temporal durations shorter than the typical rotational and vibrational periods of molecules and therefore allow the observation of molecular dynamics on their native timescales. Further, the broad bandwidth and high peak intensities of these laser pulses can result in the excitation of many transition pathways that may interfere and enable control of dynamics.

The primary focus of this work is the ultrafast laser-induced dissociation of molecular ions. We generate these ions as "fast" beam targets and study their fragmentation using a coincidence three-dimensional (3D) momentum imaging technique, which allows the measurement of all nuclear fragments, including neutrals. This approach is employed to study laser-induced processes in a variety of molecules. The goal of these efforts is not to study specific molecules but rather to use them as testing grounds to deepen our knowledge of laser-induced molecular dynamics in general.

For example, we find that permanent-dipole transitions, which are commonly overlooked in the interpretation of strong-field experiments, play a key role in laser-induced dissociation of metastable NO^{2+} ions. General consideration of these transitions in heteronuclear molecules is important in building our understanding towards more complex molecules. Speaking of more complex systems, we have also begun investigating the laser-induced dynamics of simple hydrocarbons. Our use of molecular ion beam targets gives us the unique ability to exercise control over the initial "configuration," i.e., geometry of these molecules. Utilizing $C_2H_2^q$ ion beam targets (where q is the molecular ion charge state) prepared in various initial configurations, including acetylene (HCCH), vinylidene (H_2CC), and *cis/trans*, we have determined that this property has an immense impact on the isomerization dynamics, a finding that we anticipate will lead to future work towards deeper understanding. More

broadly, this approach of probing molecules in different initial configurations offers a unique perspective that could be complementary to mainstream methods—not just in the case of C_2H_2 but other chemical systems as well.

We also describe some improvements to the 3D momentum imaging methods that facilitate the study of molecular dynamics. One of these developments is a method to distinguish and evaluate the momenta of neutral–neutral channels resulting from the fragmentation of negative ion beams. The second is a technique for imaging the breakup of long-lived metastable molecules decaying in flight to the detector and retrieving the lifetime(s) of the populated states.

Our collaborative efforts in adaptive closed-loop control are also discussed. Here, an evolutionary learning algorithm supplied with experimental feedback obtains optimally-shaped ultrashort laser pulses for driving targeted molecular dynamics. While the complexity of the shaped pulses can make interpretation challenging, the combination of these efforts with basic experiments like those we perform using ion beams can help.

In closing, the work presented in this thesis extends from diatomic to polyatomic molecules, following the natural progression of building from simpler to more complex systems. We believe that the results of these efforts aid in the advancement of understanding strong-field molecular dynamics and will stimulate future research endeavors along these directions.

Dissociation dynamics of molecular ions in ultrafast, intense laser fields:

from diatomic to polyatomic molecules

by

Bethany Jochim

B. A., Augustana College, USA, 2011

A DISSERTATION

submitted in partial fulfillment of the
requirements for the degree

Doctor of Philosophy

Department of Physics
College of Arts and Sciences

KANSAS STATE UNIVERSITY
Manhattan, Kansas

2019

Approved by:

Major Professor
Itzik Ben-Itzhak

Copyright

Bethany Jochim

2019

Abstract

Out of the many tools for probing molecular dynamics, intense, ultrafast laser pulses are particularly well suited for this purpose. First, these pulses have temporal durations shorter than the typical rotational and vibrational periods of molecules and therefore allow the observation of molecular dynamics on their native timescales. Further, the broad bandwidth and high peak intensities of these laser pulses can result in the excitation of many transition pathways that may interfere and enable control of dynamics.

The primary focus of this work is the ultrafast laser-induced dissociation of molecular ions. We generate these ions as "fast" beam targets and study their fragmentation using a coincidence three-dimensional (3D) momentum imaging technique, which allows the measurement of all nuclear fragments, including neutrals. This approach is employed to study laser-induced processes in a variety of molecules. The goal of these efforts is not to study specific molecules but rather to use them as testing grounds to deepen our knowledge of laser-induced molecular dynamics in general.

For example, we find that permanent-dipole transitions, which are commonly overlooked in the interpretation of strong-field experiments, play a key role in laser-induced dissociation of metastable NO^{2+} ions. General consideration of these transitions in heteronuclear molecules is important in building our understanding towards more complex molecules. Speaking of more complex systems, we have also begun investigating the laser-induced dynamics of simple hydrocarbons. Our use of molecular ion beam targets gives us the unique ability to exercise control over the initial "configuration," i.e., geometry of these molecules. Utilizing $C_2H_2^q$ ion beam targets (where q is the molecular ion charge state) prepared in various initial configurations, including acetylene (HCCH), vinylidene (H_2CC), and *cis/trans*, we have determined that this property has an immense impact on the isomerization dynamics, a finding that we anticipate will lead to future work towards deeper understanding. More

broadly, this approach of probing molecules in different initial configurations offers a unique perspective that could be complementary to mainstream methods—not just in the case of C_2H_2 but other chemical systems as well.

We also describe some improvements to the 3D momentum imaging methods that facilitate the study of molecular dynamics. One of these developments is a method to distinguish and evaluate the momenta of neutral–neutral channels resulting from the fragmentation of negative ion beams. The second is a technique for imaging the breakup of long-lived metastable molecules decaying in flight to the detector and retrieving the lifetime(s) of the populated states.

Our collaborative efforts in adaptive closed-loop control are also discussed. Here, an evolutionary learning algorithm supplied with experimental feedback obtains optimally-shaped ultrashort laser pulses for driving targeted molecular dynamics. While the complexity of the shaped pulses can make interpretation challenging, the combination of these efforts with basic experiments like those we perform using ion beams can help.

In closing, the work presented in this thesis extends from diatomic to polyatomic molecules, following the natural progression of building from simpler to more complex systems. We believe that the results of these efforts aid in the advancement of understanding strong-field molecular dynamics and will stimulate future research endeavors along these directions.

Table of Contents

List of Figures

Acknowledgments

I am forever indebted to many people for their help along this journey. They are too numerous to list, and no amount of words can truly convey how thankful I am.

First of all, I would like to thank my advisor, Itzik Ben-Itzhak. Itzik, you have taught me so much, not only how to think critically and approach scientific problems but also the importance of having an optimistic attitude, even when things get stressful or don't work out. Your enthusiasm and patient and clear guidance were helpful beyond measure as I progressed through my Ph.D. work. I also am incredibly grateful to Kevin Carnes. Kevin, your data acquisition and electronics expertise was truly vital to our experiments. Thank you for your patient help with SpecTcl, even at the end of the work day on a Friday during beamtime. Also, thank you for listening to all my practice talks and proofreading countless drafts over the years.

I would also like to thank the present and former graduate students and postdocs of Itzik's group. Mohammad Zohrabi, Ben Berry, Peyman Feizollah, Raju Pandiri, Travis Severt, Jyoti Rajput, Bishwanath Gaire, Nora Kling, Kelsie Betsch, Jarlath McKenna, and Utuq Ablikim, it was a true pleasure working with you. I learned a great deal from each of you and enjoyed our time in the lab together. I would also like to thank the bright and enthusiastic undergraduate students that I had the opportunity to work with: Reid Erdwien, Shitong Zhao, Drew Rotunno, and Eric Wells's summer students from Augustana University.

The J. R. Macdonald Laboratory (JRML) is a special place in that its groups frequently work together for the advancement of science. Brett Esry has taught me much about physics and what excellence in research and teaching looks like. Thank you, Brett, for always holding science to a high standard and asking critical questions that made me think deeply. Thank you also to the present and former members of Brett's group: Fatima Anis, Dustin Ursrey, Christian Madsen, Yujun Wang, Youliang Yu, Brandon Rigsbee, Shuo Zeng, Greg Armstrong, and Norio Takemoto. I would also like to thank Daniel Rolles's and Artem

Many other professors at Augustana outside of physics also helped mold the course of my education in significant ways. I will never forget that David O'Hara, my philosophy professor, taught me that the Greek $\sigma\chi o\lambda\acute{\eta}$, meaning "leisure," is the origin of the English word "school." In other words, we ought never lose sight of the undeniable joy in the quest for learning. I also thank my differential equations and linear algebra professor, Martha Gregg, for being a truly exceptional teacher and believing in me.

During my time at KSU, I have made many lasting friendships. Thank you to Sachiko Toda McBride, Sean McBride, Maia Magrakvelidze, Mo Zohrabi, Amy Rouinfar, Raju Pandiri, Manasa Thirugnanasambandam, Varun "Mac" Makhija, Xiaoming Ren, Ben Berry, Nora Kling, Kelsie Betsch, Travis Severt, Jyoti Rajput, Georgios Kolliopoulos, Leigh Graham, Bachana Lomsadze, Aram Vajdi, Adam Summers, Yubaraj Malakar, Stefan Zigo, Raiya Ebini, Jeff Powell, Jason Li, Farzaneh Ziaee, Kurtis Borne, Balram Kaderiya, Wes Erbsen, Omer Farooq, Dustin Ursrey, Dina Zohrabi, Sajed Hosseini, and many others. Thanks also to my longtime friend Carissa Nelson and husband Mark. You all helped make graduate school more bearable and fun.

Other people of note include my high school teachers, Mr. E. Jay Mickelson ("Mr. Mick") and Mrs. Elizabeth Vogt. Mr. Mick, my Latin *magister*, inspired me with his endless love and passion for learning. My English teacher Mrs. Vogt is one of the most important influences in my life, as she is the reason I know how to write, a skill that has served me well in my scientific career.

Lastly and most significantly, I would like to thank the dear ones in my life. A heartfelt thanks goes to my family: my mom, my dad, my brother, Joel, my four-legged family members, Chester (across the Rainbow Bridge), Linus, Rudy, Olive, and Wedge. I also thank the most important person in my life, Peyman. Without all your love and support, none of this would have been possible.

Dedication

Dedicated to my family.

Chapter 1

Introduction and motivation

1.1   Ultrafast laser–molecule interactions

The timescales for the rotational and vibrational motions of molecules are typically picoseconds (1 ps $= 10^{-12}$ s) and femtoseconds (1 fs $= 10^{-15}$ s), respectively. Therefore, these are the timescales that govern some key steps in chemical reactions, such as the breaking and forming of chemical bonds, the transformation of one molecular geometry to another, or the redistribution of energy in an excited molecule. The advent of ultrafast, intense laser pulses, which have temporal durations shorter than these rapid natural timescales of molecules, opened up a realm of inquiry into molecular dynamics, allowing the direct probing of these types of processes [1, 2].

In addition to their short temporal duration, other characteristics of intense, ultrashort laser pulses make studying molecular dynamics in their presence a rich and stimulating venture. In 1905, the "*Annus Mirabilis*," Albert Einstein explained, among other important phenomena, the photoelectric effect, wherein a single photon liberates a single electron in a material [3]. This is the "weak-field" limit of light-matter interaction, in which a single photon of a low intensity light source excites a molecule. In contrast, the aforementioned ultrafast intense pulses have high peak intensities, meaning that the photon flux interacting with molecules is extremely large. This "strong-field" regime thus opens up the possibility

of multiphoton processes. Furthermore, the electric fields of these pulses are of magnitudes comparable to the binding fields of molecules' valence electrons, allowing studies of strong-field ionization, which is fundamental to phenomena such as above threshold ionization (ATI) [4, 5] and high harmonic generation (HHG) [5–7].

Also, concomitant with the short temporal duration of these pulses is a broad bandwidth. That is, the pulses have a wide range of photon energies. Due to this property of ultrashort, intense laser pulses and the multiphoton nature of their interaction with molecules, they can stimulate many different transition pathways with the same final energy. These pathways can interfere constructively, leading to the enhancement of certain product channels, or destructively, leading to their suppression. This idea is the lifeblood of the field of coherent control, in which the driving laser field is tailored in order to exercise control over the laser-induced products via interference [8–10]. A classic analogy is drawn from Young's double-slit experiment in optics, in which light waves following different paths combine to produce spatial patterns of constructive and destructive interference. Photochemical control—essentially manipulating the quantum mechanical wave function itself—is one of the grand challenges of atomic, molecular, and optical physics [11].

Despite the many interesting applications of ultrashort laser pulses in studying molecules, interpretation of strong-field laser-molecule interactions remains challenging. This difficulty is mainly due to the large number of states populated via multiphoton transitions and the complexity of molecular structure. While a number of strong-field processes in benchmark molecules like H_2^+ have been reasonably well described [12–27], this research field has been trending towards larger and more complex molecules, which require ongoing experimental and theoretical developments in order to attain deeper understanding.

1.2 Avenues for studying molecular dynamics

How does one go about investigating light-driven molecular dynamics? The toolbox for these studies brims with myriad approaches involving measurement of different quantities from which to extract information. Some methods, such as transient absorption spectroscopy, in-

volve measurement of light. This technique enables tracking of evolving molecular dynamics through monitoring of the molecules' optical absorption as a function of time [28, 29].

Another route for studying photo-induced molecular dynamics is through the measurement of fragments. Electrons, for example, carry a wealth of information. One form of photoelectron spectroscopy, time-resolved photoelectron spectroscopy (TRPES) [30, 31], allows detailed study of short-lived (tens to hundreds of femtoseconds [32, 33]) transition states, i.e., intermediate states in chemical reactions. This task is made possible by measuring the time-dependent energies of electrons liberated from molecules using ultrashort pulse schemes [30, 31]. In laser-induced electron diffraction (LIED), quasi-free electrons return to the molecular core and scatter from it, creating interference patterns that carry information about changes in molecular structure [34, 35].

In addition to the electron spectra, examination of the more massive ionic fragments can also be illuminating. The past decades have seen immense progress in ion momentum imaging technology. Generally, the aim of ion momentum imaging methods, reviewed in Ref. [36], is to unravel the dynamics of photodissociation by means of the measured ionic fragment energy and angular distributions, as these yield information about the states and pathways involved in the process.

An abundance of other methods for learning about molecular dynamics exist, too many to enumerate in completeness here. Moreover, these methods are frequently blended to create even more powerful tools. One such "blended" method of particular pertinence to this dissertation work is coincidence momentum imaging of molecular fragmentation. A common implementation of this approach is the cold target recoil ion momentum spectroscopy (COLTRIMS) technique [37, 38]. In this case, the three-dimensional (3D) fragment momentum distributions of both ions and electrons are measured in coincidence. These distributions facilitate retrieval of the energetics and angular dependence of the breakup, which, as mentioned, provide clues about how the molecular dissociation proceeds.

1.3 Our focus

The main interest of our group is experimentally studying the interaction of intense, femtosecond laser pulses with molecular ions [17, 39, 40]. As our target is a keV beam of molecular ions, neutral fragments have sufficient energy to activate the detector, allowing kinematically-complete measurements of molecular dissociation. For measurements of dissociation, laser intensities lower than that required for ionization may be used, and since the fraction of the laser focal volume occupied by the low intensities is larger than that occupied by the high intensities, processes involving low total numbers of photons often dominate in such experiments (see manuscript in Section 4.6, for example). These aspects of our technique reduce the contributions of complicated multiphoton pathways, making it more likely that progress can be made through interplay with theory. Indeed, this approach has resulted in many fruitful studies of both diatomic (e.g., [21, 24, 41–43]) and triatomic (e.g., [44–47]) molecular ions. The work in this thesis has benefitted tremendously from an experiment–theory joint approach, as will be highlighted in our study of the NO^{2+} molecule, discussed in Chapter 4. Following the trends of this research area, we have begun to examine molecular dynamics in larger systems, such as $C_2H_2^q$, where q (–1, 0, 1, or 2) is the molecular ion charge state. Here, we are interested in exploring strong-field isomerization, specifically, the migration of hydrogen from one site in a molecule to another. Our progress on this front is presented in Chapter 3.

The fragmentation of these molecular ions is studied using the coincidence 3D momentum imaging technique developed by our group. As this technique has been described in detail previously [17, 39, 40, 48], it is only briefly outlined in Chapter 2. Advancements made in imaging methods that I have led are detailed in the same chapter. These advancements include developing an imaging technique for long-lived metastable molecules that decay in flight towards the detector and a method for distinguishing breakup channels consisting of neutral fragments only.

In addition to my ion beam and imaging work, I have also played a key role in a few adaptive closed-loop control experiments on neutral gas-phase targets, as highlighted in Chapter

5. In these experiments, performed in collaboration with Eric Wells from Augustana University, a genetic algorithm (GA), guided by feedback from time-of-flight mass spectrometry (TOFMS) [49] or velocity map imaging (VMI) [50], is used to search for optimal laser pulses to enhance or suppress a given fragmentation objective.

Importantly, in the work of our group, each specific molecule studied is chosen not because we are interested in learning about all its facets as a specific system. Rather, each molecule investigated serves as a convenient testbed for demonstrating a method and/or investigating a certain class of dynamics—dynamics that are likely important in other molecules as well.

1.4   Document structure

This dissertation presents the aforementioned studies as a series of published, submitted, and to-be-submitted manuscripts for which I was the first author or played a lead role. Manuscripts included in the same chapter are linked by a general overview, and each manuscript is preceded by a brief introduction. To conclude, Chapter 6 contains a summary and outlook regarding the studies presented in this thesis.

Chapter 2

Experimental methods

2.1 Scope

This work involved the use of laser systems, ion sources, experimental methods, and associated apparatuses detailed elsewhere. Thus, only the essential points are discussed. As we made developments in coincidence 3D momentum imaging of different scenarios, more details about these developments are discussed. These extensions include the imaging of channels consisting only of neutral fragments and of breakup in flight to the detector.

2.2 Ultrafast laser pulses

The laser pulses used in this work were provided by the Kansas Light Source (KLS) [51] or the PULSAR [52] Ti:Sapphire laser systems, which produce linearly-polarized pulses with a central wavelength of about 790 nm. The KLS laser system typically delivers Fourier Transform Limited (FTL) pulses with temporal duration 27–35 fs FWHM (full width at half maximum) in intensity. These pulses have energy of up to about 2 mJ and are produced at a repetition rate of 1–2 kHz. The PULSAR laser system typically delivers FTL pulses with temporal duration of 22–24 fs (FWHM in intensity). The repetition rate is 10 kHz, and the pulse energy, similar to KLS, is up to about 2 mJ.

2.3 Coincidence 3D momentum imaging of fragmentation of molecular ion beams

My main focus was employing a coincidence three-dimensional (3D) momentum imaging technique for laser-induced fragmentation of molecular ion beams, developed by our group [17, 39, 40, 53]. The studies presented in this thesis utilize ion beam targets produced in an electron-cyclotron resonance (ECR) ion source or in a duoplasmatron ion source, previously described in Refs. [39] and [54], respectively. Upon extraction from the ion source, molecular ions are accelerated to a specified energy, typically 5–25 keV. The choice of energy depends on the specifics of the fragmentation channel(s) of interest (e.g., the energy of breakup and the mass ratio of fragments) and other experimental considerations.
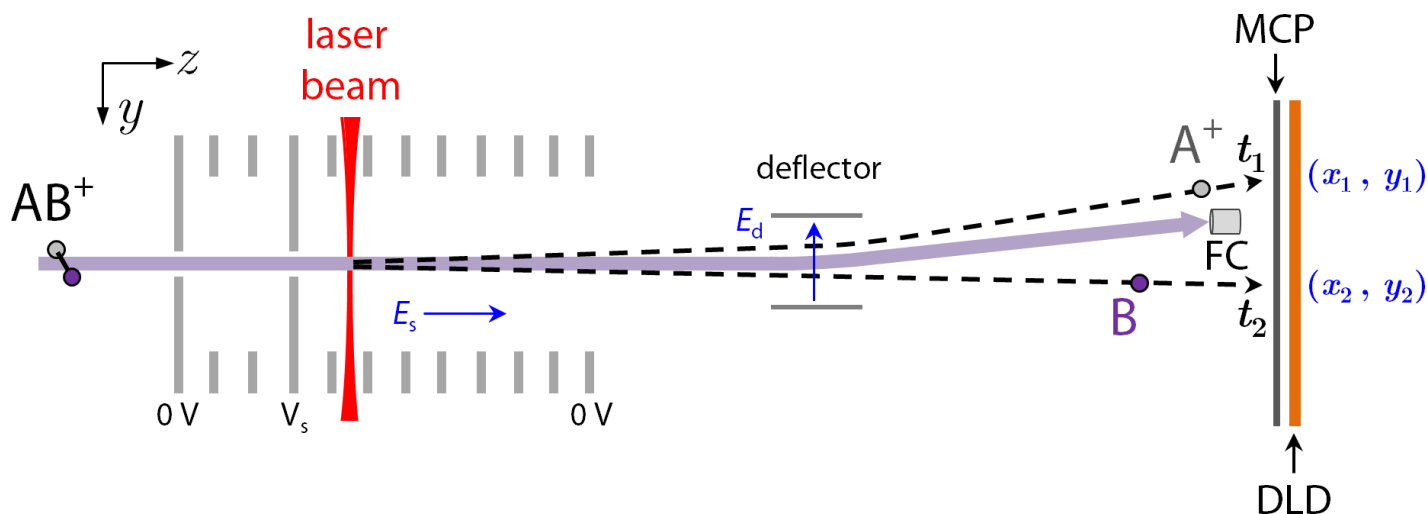
Figure 2.3.1: Schematic (not to scale) of our coincidence 3D momentum imaging setup. A molecular ion beam, AB^+, intersects a focused laser beam of intense, femtosecond pulses. A uniform static electric field E_s in the longitudinal (z) direction separates the laser-induced fragments temporally. A uniform static field E_d in the transverse (y) direction separates the fragments in position. The microchannel plate (MCP) and delay-line detector (DLD) assembly measures the position and time information for these fragments. A Faraday cup (FC) collects the unfragmented ion beam and allows measurement of its current.

A magnet is used to select the ion beam of interest based on its momentum-to-charge ratio, and a series of electrostatic ion optics, deflectors, lenses, and adjustable four-jaw slits are used to deliver a collimated ion beam to the interaction region, where it intersects the laser beam.

The experimental imaging setup is illustrated for two-body dissociation of an AB^+ ion beam in Fig. 2.3.1. Fragments from the laser–molecule interaction are separated in time by a static longitudinal electric field E_s. The uniform static electric field E_d of an imaging deflector separates the fragments in position on the detector. This microchannel plate (MCP) and delay line detector (DLD) assembly provides position and time information, (x, y, t), for each hit on an event-by-event basis. That is, this recorded information is associated with a particular laser shot. Fig. 2.3.2 shows sample position and time data for laser-induced dissociation of a $C_2H_2^+$ beam. From the position and time information, the 3D momenta of the fragments are determined, as described in the next section.
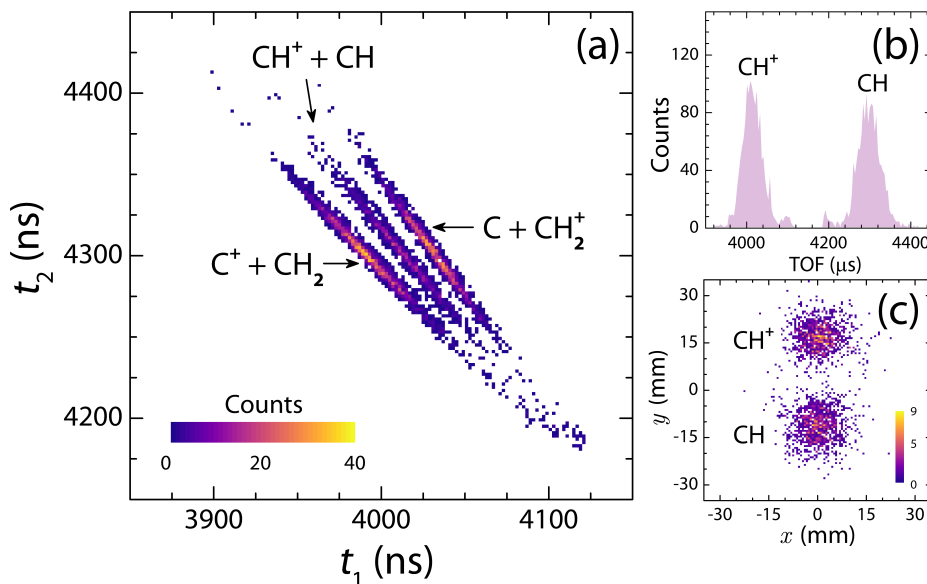
Figure 2.3.2: (a) Sample coincidence time-of-flight (CTOF) spectrum showing the laser-induced dissociation channels of a $C_2H_2^+$ beam after imposing momentum conservation. This plot shows the yield as a function of the time-of-flight of the first particle (t_1) and the second particle (t_2). The diagonal stripes occur as a result of momentum conservation. The (b) time-of-flight and (c) position spectra for the $CH^+ + CH$ channel.

2.4 Imaging principles

Imaging of molecular fragmentation is most easily introduced via the field-free case. In the coincidence 3D momentum imaging technique described above, the x direction is essentially field free. Let us consider the case of two-body fragmentation, for which the measured x position and time-of-flight values of the first fragment are x_1 and t_1, respectively, and those of the second fragment are x_2 and t_2, respectively. Suppose that the x-coordinate of laser-molecule interaction point is x_0 and the velocity of the center of mass (CM) of the molecule at this point is v_{0x}. For dissociation velocities of the first and second fragment v'_{1x} and v'_{2x} in the CM frame of the parent molecule, the equations of motion are

$$x_1 - x_0 = (v_{0x} + v'_{1x})t_1 \tag{2.4.1}$$

$$x_2 - x_0 = (v_{0x} + v'_{2x})t_2. \tag{2.4.2}$$

Also, momentum conservation in the CM frame gives

$$m_1 v'_{1x} + m_2 v'_{2x} = 0, \tag{2.4.3}$$

where the masses of the first and second fragments are m_1 and m_2, respectively. In Eqs. 2.4.1–2.4.3, the unknown quantities are in red. One can see that there are three equations and four unknowns. To eliminate the extra unknown, we utilize the fact that the laser beam is tightly focused (waist <100 μm) relative to the ion beam size (about 0.9×0.9 mm^2). To solve the equations, we hence replace x_0 by its average value, $\bar{x}_0$, which is obtained by exploiting known symmetries of the fragmentation. This analysis approach is discussed in more detail in Appendix A. Defining $\beta \equiv m_1/m_2$ and solving Eq. 2.4.3 for v'_{2x} leads to $v'_{2x} = -\beta v'_{1x}$. Substituting this expression for v'_{2x} into Eq. 2.4.2 and combining Eqs. 2.4.1 and 2.4.2 yields the velocity of the CM:

$$v_{0x} = \frac{\beta t_2 x_1 + t_1 x_2 - \bar{x}_0(t_1 + \beta t_2)}{(\beta + 1)t_1 t_2}. \tag{2.4.4}$$

And the CM-frame dissociation velocity is

$$v'_{1x} = \frac{x_1 - x_2}{t_1 + \beta t_2} - \frac{v_{0x}(t_1 - t_2)}{t_1 + \beta t_2}. \tag{2.4.5}$$

Next we proceed to the y-direction imaging. The main difference between the y direction and the x direction is that in the y direction there is an electric field E_d due to the imaging deflector. When the imaging deflector is used, the y-direction equation of motion for the first fragment, for example, changes as follows:

$$y_1 - y_0 = (v_{0y} + v'_{1y})t_1 + y_{D1}. \tag{2.4.6}$$

Here, y_1, y_0, and v_{0y} are the y-coordinate position, interaction point, and velocity of the CM, respectively. The y-component dissociation velocity in the CM frame is v'_{1y}. The last term y_{D1} is the y displacement caused by the imaging deflector field, explicitly given by

$$y_{D1} = \frac{q_1 V_d}{m_1 D}\left(\frac{1}{2}t_D^2 + t_D T\right). \tag{2.4.7}$$

Here, q_1 is the fragment's charge, and V_d and D are the voltage and plate separation of the imaging deflector, respectively. The time spent in the imaging deflector field is t_D, and T is the travel time from the exit of the imaging deflector to the detector. Retrieval of t_D and T are possible via simple kinematics using the measured time-of-flight and the known geometry of the setup, such as the deflector length and the deflector-to detector distance.

One further difference between the y and x directions is that the interaction region in the y direction extends as far as the width of the ion beam. As a result, the resolution of the y-direction imaging is typically not as good as that of the x direction. Note that if the ion beam is well collimated (i.e., the spread in v_{0y} is small), the resolution may be improved by replacing v_{0y} with $\overline{v}_{0y}$ and solving instead for the initial position y_0 for each event.

The z-direction equations include the acceleration due to E_s. Solutions for v_{0z} (the ion beam velocity at the interaction point) and v'_{1z} are hence more complicated than the x and y directions but rely upon the same principles of combining the equations of motion and momentum conservation. Also note that corrections for the fringe fields, detailed in Ref. [39],

are accounted for in data analysis. Upon calculation of the x, y, and z momenta, the angular dependence relative to the laser polarization and the kinetic energy release (KER) of the dissociation may also be readily evaluated.

2.5 Analysis of neutral–neutral channels

In our studies of negative ion beams, channels consisting only of neutral fragments can occur. As E_s and E_d have no effect on neutral particles, one may ask how these channels can be distinguished and analyzed given that the fragment time separation cannot be controlled.

One such set of channels from the laser-induced fragmentation of a $C_2H_2^-$ beam is illustrated in the CTOF spectrum in Fig. 2.5.1(a). The C + CH_2 channel is clearly visible, while the possible CH + CH channel, if it exists, is very weak.[1] First focusing on the C + CH_2 channel, we see that it has two "arms" of different slopes. The mass ratio of the first and second hits dictates these slopes, and this dependence can be determined from the time-of-flight equations, given below for the C and CH_2 fragments:

$$t_C = \frac{\ell}{v_{0z}(1 + u_{Cz})} \tag{2.5.1}$$

$$t_{CH_2} = \frac{\ell}{v_{0z}(1 - \beta u_{Cz})}, \tag{2.5.2}$$

where ℓ is the interaction–detector distance, $\beta = m_C/m_{CH_2}$, and $u_{Cz} \equiv v'_{Cz}/v_{0z}$, where v'_{Cz} is the C fragment z-direction dissociation velocity in the CM frame.

Expanding these equations to first order in u_{Cz} (as typically $u_{Cz} \ll 1$) results in

$$t_C = \frac{\ell}{v_{0z}}[1 - u_{Cz} + \mathcal{O}(u_{Cz}^2)] \simeq \frac{\ell}{v_{0z}}(1 - u_{Cz}) \tag{2.5.3}$$

$$t_{CH_2} = \frac{\ell}{v_{0z}}[1 + \beta u_{Cz} + \mathcal{O}(u_{Cz}^2)] \simeq \frac{\ell}{v_{0z}}(1 + \beta u_{Cz}). \tag{2.5.4}$$

---

[1] A scientific discussion of these channels follows in the paper in Chapter 3, Section 3.3.

Hence, when the C fragment arrives to the detector first, the CTOF slope will be

$$dt_{CH_2}/dt_C = (dt_{CH_2}/du_{Cz})/(dt_C/du_{Cz}) \simeq -\beta. \tag{2.5.5}$$

When the CH_2 fragment comes first, the slope will be approximately $-1/\beta$. As shown in Fig. 2.5.1(a), for the $C + CH_2$ channel, the left arm has a slope of about $-12/14 = -6/7$ and thus corresponds to C arriving first. The right arm has a slope of about $-14/12 = -7/6$ and thus corresponds to CH_2 arriving first. By similar logic, it is apparent that the $CH + CH$ channel would simply have a slope of -1, as the fragments in this channel are identical.
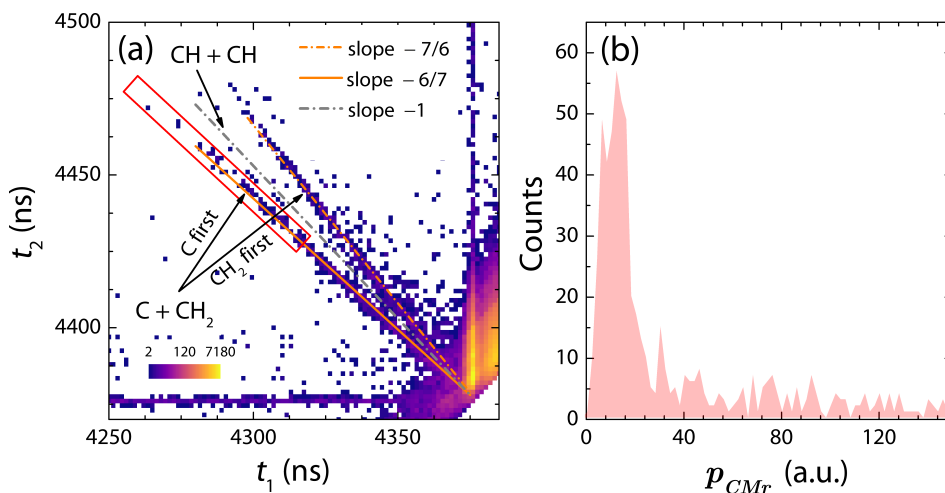
Figure 2.5.1: (a) The CTOF spectrum of laser-induced fragmentation of C_2H_2, produced from a $C_2H_2^-$ beam, zoomed in on the neutral–neutral channels. The lines show that the channels and the time order that the fragments hit the detector may be distinguished in part by the CTOF slopes. (b) The p_{CMr} distribution for data in the red box in (a).

The slopes of the CTOF arms are useful in distinguishing channels and determining the fragment order, i.e., the time order the fragments hit the detector, in a particular channel when the time-of-flight difference $t_{21} \equiv t_2 - t_1$ is sufficiently large. As t_{21} decreases, the task becomes more challenging, as the CTOF stripes merge together.
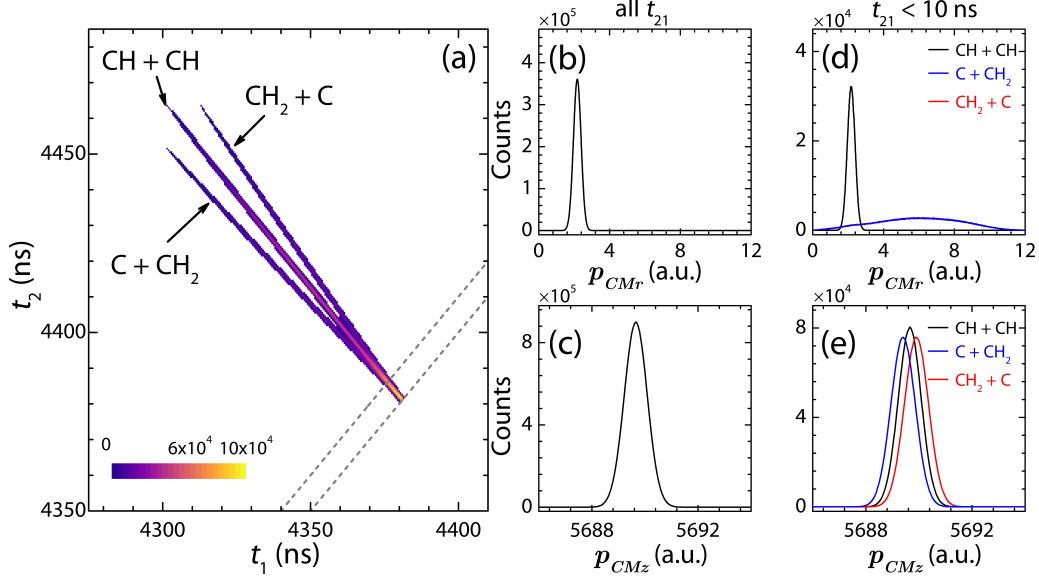
Figure 2.5.2: (a) Simulated CTOF spectra of the CH + CH and C + CH$_2$ channels. The CH + CH channel (b) p_{CMr} and (c) p_{CMz} distributions. The CH + CH channel (d) p_{CMr} and (e) p_{CMz} distributions for $t_{21} < 10$ ns [the region between the dashed gray lines in (a)]. The black lines show the distributions when the fragments are correctly identified as CH + CH, while the blue and red lines show these distributions when the fragments are misidentified as C + CH$_2$ (blue) and CH$_2$ + C (red). Note that "C + CH$_2$" means the first hit is identified as C, and "CH$_2$ + C" means the first hit is identified as CH$_2$. In (d), the red trace lies beneath the blue one.

To demonstrate channel separation for small t_{21}, we simulate data for the CH + CH and C + CH$_2$ channels, shown as a CTOF map in Fig. 2.5.2(a). The basis of this separation method is the fact that real, momentum-conserving events have well-defined CM momentum,

$$p_{CMx,y,z} = Mv_{0x,y,z}, \qquad (2.5.6)$$

where M is the mass of the parent molecule. Figs. 2.5.2(b) and (c) show the clearly-peaked p_{CM} distributions of the simulated CH + CH channel. As v_{0z} is retrieved from the measured t_1 and t_2 values, when t_{21} is small, the computed p_{CMz} is not a reliable means of channel identification, as illustrated in Fig. 2.5.2(e). In the limit of small t_{21}, however, the position separation of the first and second fragments is maximized. The momentum of the CM in the detector plane,

$$p_{CMr} \equiv \sqrt{p_{CMx}^2 + p_{CMy}^2}, \qquad (2.5.7)$$

13

allows channel identification. Panel (d) of Fig. 2.5.2 shows separation using p_{CMr}. As can be seen, when the fragments are misidentified, the resulting p_{CMr} distribution is not sharply peaked. It is important to note that the efficacy of the separation is dependent on a number of experimental factors. Examples include the degree of collimation of the ion beam, which influences the widths of the v_{0x} and v_{0y} distributions, the KER of the channels, and the position image size relative to the detector position resolution. Appendix B provides more detailed examples of the channel separation simulations and some efficiency estimates.

Based on the above logic, the algorithm for channel identification for small t_{21} is as follows (for the $C_2H_2^-$ example):

1. Pre-select data in a region where t_{21} is large and one can confidently assign the channel and fragment order, such as that marked by the red gate on the $C + CH_2$ channel in Fig. 2.5.1(a).

2. Compute p_{CMr} for the channel assignment and fragment order as determined by the slope, shown in Fig. 2.5.1(b).

3. Compute the average of the p_{CMr} distribution, $\bar{p}_{CMr} = \frac{1}{N} \sum_{i=1}^{N} p_{CMr_i}$, where N is the number of events and p_{CMr_i} is the detector-plane momentum of the CM for the ith event.

4. Select the data for small t_{21} and compute p_{CMr} three times for each event:

   (a) with C first and CH_2 second

   (b) with CH_2 first and C second

   (c) with CH first and CH second

5. Choose the channel/fragment order assignment corresponding to the minimum difference between p_{CMr} and $\bar{p}_{CMr}$.

6. Vary the pre-selection gate described in step 1 and repeat the rest of the steps. This allows one to gauge the sensitivity of the "gating" and to estimate errors, as the pre-selection gate is one of the dominant sources of error in the analysis.

2.6 COLTRIMS technique

I have also utilized the cold target recoil ion momentum spectroscopy (COLTRIMS) technique. The COLTRIMS setup is illustrated in Fig. 2.6.1. A focused laser beam of femtosecond pulses intersects a supersonic molecular beam. A uniform electric field accelerates the resulting ions toward an MCP and DLD detector assembly, which allows time and position information to be recorded in event mode for all charged fragments. Note that the COLTRIMS technique is also commonly used to measure electrons, but in the work highlighted in this thesis, only ions are measured. While the imaging equations are not exactly the same as those of the coincidence 3D momentum imaging technique for ion beams, the principles employed in COLTRIMS are exactly the same. More details about the COLTRIMS technique and the specific setup used can be found in Refs. [37, 38, 55].
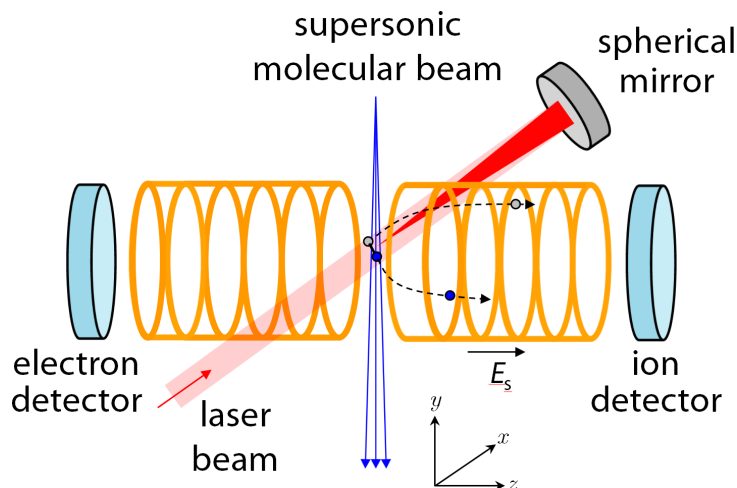
Figure 2.6.1: (a) Schematic of the COLTRIMS setup. A back-focused laser beam of intense, ultrashort pulses crosses a supersonic molecular beam. A uniform electric field accelerates ions from this interaction to a time- and position-sensitive detector. This figure is a modified version of a schematic that was provided by Artem Rudenko.

2.7 Imaging of dissociation in flight

The descriptions of imaging of molecular dissociation in the previous sections of this chapter focused on "prompt" breakup. That is, the target molecules fragment practically instantaneously upon interaction with the laser pulse. This section focuses on a technique we developed to image metastable molecules that travel for hundreds of ns to a few μs before fragmenting. In the following paper, published in *The New Journal of Physics* [56], we demonstrated this method using a COLTRIMS measurement of metastable doubly-charged ethylene molecules. Through this method, we retrieved the KER of the dissociation process and the lifetime(s) of the metastable states. With sufficient statistics, we anticipate that this technique could also be adapted to measurements made with our coincidence 3D momentum imaging setup for molecular ion beam targets. Simulations related to this technique are detailed in Appendix C.

The following paper is copyrighted by IOP Publishing & Deutsche Physikalische Gesellschaft. Reproduced with permission from B. Jochim *et al.* New. J. Phys. **19**, 103006 (2017). All rights reserved.

New Journal of Physics

The open access journal at the forefront of physics

PAPER

Three-dimensional momentum imaging of dissociation in flight of metastable molecules

Bethany Jochim[1] [ORCID] , Reid Erdwien, Y Malakar, T Severt, Ben Berry, Peyman Feizollah, Jyoti Rajput, B Kaderiya, W L Pearson, K D Carnes, A Rudenko and I Ben-Itzhak[1]

J. R. Macdonald Laboratory, Physics Department, Kansas State University, Manhattan, KS 66506, United States of America
[1] Authors to whom any correspondence should be addressed

E-mail: bjochim@phys.ksu.edu and ibi@phys.ksu.edu

Abstract

We investigate dissociation in flight of metastable molecular dications formed by ultrashort, intense laser pulses using the cold target recoil ion momentum spectroscopy technique. A method for retrieving the lifetime(s) of the transient metastable state(s) as well as the complete three-dimensional momenta of the dissociating fragments is presented. Specifically, we demonstrate and discuss this approach by focusing on dissociation in flight of the ethylene dication going to the deprotonation channel. Two lifetimes are found to be associated with this process, $C_2H_4^{2+} \rightarrow C_2H_3^+ + H^+$: $\tau_1 = 202 \pm 10$ ns and $\tau_2 = 916 \pm 40$ ns. For the corresponding channel in deuterated ethylene, lifetimes of $\tau_1 = 269 \pm 29$ ns and $\tau_2 = 956 \pm 83$ ns are obtained.

1. Introduction

Many processes in molecules happen on fast timescales. For example, rotations and vibrations typically occur on picosecond and femtosecond timescales, respectively. Molecular bond rearrangement and fragmentation often proceed on similarly short timescales, as shown in [1–5] and many others. Hence, femtosecond laser pulses, possessing temporal durations shorter than these timescales, can be used to influence and shed light on molecular dynamics [6–9].

Not all processes in molecules, however, proceed so swiftly. Multiply charged molecular ions can exist in metastable states that lead to fragmentation happening on long timescales that range from picoseconds to even seconds [10–12]. The lifetimes of these transient systems are governed by the relevant potential energy landscape and the mechanisms responsible for decay, which can include tunneling, predissociation, and radiative decay to repulsive states. Investigating the formation, properties, and decay of these metastable molecular ions experimentally and theoretically has been a prominent field of research (see review papers [10–12] and [13–24], for example).

We study the decay dynamics of metastable molecules by employing coincidence three-dimensional (3D) momentum imaging, which provides the complete 3D momenta of the fragments and therefore their kinetic energy release (KER) and angular distributions. This information can in turn facilitate understanding of the dissociation mechanism(s), demonstrated for example in [17, 25, 26]. Hence, the 3D momentum imaging technique has been a powerful tool in studies of molecular fragmentation following ionization by ultrashort intense laser pulses, x-ray (or extreme ultraviolet) photons, or fast ion impact [27, 28], as long as the breakup is prompt. Prompt breakup happens on a sub-picosecond timescale, much shorter than the flight times of the fragments to the detector. The ionization processes in such experiments can readily form multiply charged metastable molecular ions, seen for example in [17, 22, 23, 29–34].

Importantly, in coincidence measurements, a metastable molecular ion may survive beyond the interaction region, traveling through the spectrometer for a non-negligible time before undergoing dissociation in flight. In this unimolecular fragmentation process, which is a subset of delayed dissociation, the survival time of a fragmenting metastable molecule, t_d, is a significant fraction of the time of flight (TOF) of intact metastable ions,

t_m. In the present experiments, t_d is on the order of hundreds of nanoseconds to a few microseconds. In general, the observable range of t_d may differ depending on the specific metastable system, as well as the conditions of the experiment.

One of the striking signatures of dissociation in flight in the coincidence time-of-flight (CTOF) spectrum is a long, curved stripe that extends from the prompt breakup region and terminates at the intact metastable ion time of flight. This signature has been noted in CTOF spectra from a myriad of studies [35–48].

Field and Eland developed a method to extract the lifetimes of metastable states decaying in flight by fitting Monte-Carlo simulated time-of-flight-difference distributions $N(t_2 - t_1)$ to the corresponding measured time-difference spectrum. Here, t_1 and t_2 are the times of flight of the first and second fragments, respectively. They have demonstrated their technique for a vast array of molecules [36]. Subsequent studies have implemented this method of lifetime retrieval for other metastable molecules [39, 41–44]. Recently, making some simplifying assumptions, Larimian *et al* [47] calculated t_d kinematically and retrieved the lifetime for deprotonation of the metastable ethylene dication. They also retrieved the momentum distribution of the fragments using Abel inversion [49] of the position image and discussed possible decay routes.

Our aim in this work is to present a more direct approach for extracting information about dissociation in flight of metastable molecules from coincidence momentum imaging measurements, employing basic principles. This method takes advantage of the known symmetries regarding the fragmentation process and allows one to extract not only the lifetime(s) of the metastable molecule but also the momenta, KER, and angular distributions. This information can enable pinpointing of the likely metastable state(s) dissociating in flight, as well as their dissociation mechanisms. Furthermore, this technique is general and can be applied to many different systems that undergo dissociation in flight. While our method is versatile and can provide a wealth of information to deepen understanding of dissociation processes, the focus of this manuscript is the analysis method of retrieving this information from the measurement.

2. Experimental method

To demonstrate our approach, we examine the same dissociation-in-flight channel as Larimian *et al* [47]. Namely, we look at deprotonation of metastable ethylene dications, $C_2H_4^{2+} \rightarrow C_2H_3^+ + H^+$ (as well as the deuterated equivalent), using the cold target recoil ion momentum spectroscopy (COLTRIMS) technique [27, 28]. Laser pulses with central wavelength of 790 nm, 23 fs duration (full width at half maximum (FWHM) in intensity), and peak intensity of about $3 \times 10^{14}\,\mathrm{W\,cm^{-2}}$ are used to doubly ionize the ethylene molecules, introduced as a supersonic jet. The pulse duration was measured using second harmonic frequency-resolved optical gating (SHG FROG) [50], and the intensity was evaluated using the kink in the photoelectron spectrum of neon associated with $2U_p$ (where U_p is the average quiver energy of the free electron), which represents the transition from direct to rescattered electrons. To determine the $2U_p$ point, we measured the momenta of Ne^+ recoil ions at low extraction field, following the method detailed in [51, 52].

As shown in figure 1(a), we observe the well-known signature of dissociation in flight, a long stripe in the CTOF spectrum. In figure 1(b), we note another signature in a density plot of the ion yield as a function of the measured TOF and position, $N(\mathrm{TOF}, x)$, where two 'halos' extend from the light and heavy fragments to the small $C_2D_4^{2+}$ spot. Notably, in both the CTOF and $N(\mathrm{TOF}, x)$ spectra, the distributions of the two fragments converge to that of the intact metastable dication. Furthermore, as highlighted in figure 1(a), the predictions of Newton's equations of motion for dissociation in flight, which are marked by the open triangles, agree well with the measured data.

3. Analysis method and results

To accomplish our goal of directly extracting information about dissociation in flight of a metastable molecule from our measurements, we start from the kinematic equations. The coordinate system utilized is depicted in figure 2(a). We employ principles similar to those that have been applied for years to image collision- and laser-induced prompt molecular dissociation in CTOF measurements [27, 28]. The equations of motion become slightly different from those for prompt dissociation to account for the survival time of the dication, t_d. For two-body dissociation in flight of a generic metastable dication, $AB^{2+} \rightarrow A^+ + B^+$, we have the following equations in the x direction, which in our case is along the laser beam propagation and transverse to the spectrometer axis:

$$x_j - x_0 = v_{0x}t_j + v'_{jx}(t_j - t_d) \qquad [j = 1, 2]$$

Figure 1. Signatures of dissociation in flight in coincidence spectra for laser-induced deprotonation of deuterated ethylene. (a) Coincidence time-of-flight (CTOF) spectrum. The long stripe that is marked by an arrow and extends from the prompt $C_2D_3^+ + D^+$ breakup region to the time of flight (TOF) of the metastable dication, t_m, is a signature of dissociation in flight. The open triangles represent the predictions of Newton's equations of motion for dissociation in flight at different values of t_d, assuming $v'_{1z} = 0$, where v'_{1z} is the component of the dissociation velocity along the TOF axis. (b) Density plot of the ion yield as a function of TOF and x position, $N(\text{TOF}, x)$. Highlighted by the dashed blue lines are two 'halos' that are signatures of dissociation in flight. One 'halo' extends from the light fragment, D^+, and one extends from the heavy fragment, $C_2D_3^+$. Both shrink in size and converge to the small $C_2D_4^{2+}$ spot.

Figure 2. (a) A schematic view of the laser-molecule interaction region and coordinate system. (b) Diagram illustrating the measurement of dissociation in flight of doubly charged ethylene. This metastable dication dissociates at time t_d, and position and time information about the resulting H^+ (or D^+) and $C_2H_3^+$ (or $C_2D_3^+$) fragments is measured. (c) Cartoon demonstrating how $t_d^{(+)}$ and $t_d^{(-)}$ are related to the sign of v'_{1z}. (d) Computed time of flight as a function of t_d for $C_2D_4^{2+} \rightarrow C_2D_3^+ + D^+$ dissociation in flight, assuming $v'_{1z} = \pm 0.025$ mm ns^{-1} (associated with typical kinetic energy release of 4 eV, as discussed later). On this plot, an example set of $t_d^{(+)}$ and $t_d^{(-)}$ solutions is indicated by the blue and green vertical lines. Note that the difference between these delay times is small compared to t_m. Also, it is readily seen that both situations, $v'_{1z} < 0$ with $t_d^{(+)}$ and $v'_{1z} > 0$ with $t_d^{(-)}$, lead to the same pair of t_1 and t_2 values, indicated by the dotted horizontal lines.

$$\sum_{j=1}^{2} m_j v'_{jx} = 0. \tag{1}$$

Here, x_j is the measured position of fragment j, and x_0 is the initial position of the metastable dication. v_{0x} is the average initial x-component velocity of the dication in the laboratory frame ($v_{0x} \simeq 0$ for a cold jet), v'_{jx} is the x-component dissociation velocity in the AB^{2+} center-of-mass frame, t_j is fragment j's time of flight, and m_j is its mass. Clearly, t_d is needed to properly calculate the transverse momenta of the fragments. Note that the y-component equations (transverse to the spectrometer axis and along the jet flow) are similar to the x equations, except that v_{0y}, the supersonic jet velocity, is not negligible.

At this point, it is interesting to contrast momentum imaging of dissociation in flight to that of prompt breakup, for which $t_d \simeq 0$. In the case of prompt fragmentation, one can readily see that the transverse equations of motion are decoupled from motion along the z direction, which is parallel to the spectrometer axis. For the problem of dissociation in flight, however, this is not the case, as t_d leaves us with more unknowns than equations in the transverse directions. Thus, we need to determine t_d from the z-component kinematic equations first.

3.1. t_d and lifetime determination

How exactly can we retrieve t_d from the z-direction motion? First, we write the z-component equations of motion:

$$\ell - \frac{1}{2}a_m t_d^2 = (a_m t_d + v'_{jz})(t_j - t_d) + \frac{1}{2}a_j(t_j - t_d)^2 \qquad [j = 1, 2]. \tag{2}$$

Here, ℓ is the ion flight distance, a_m is the AB^{2+} acceleration, v'_{jz} is the z-component dissociation velocity of the jth fragment in the AB^{2+} center-of-mass frame, and a_j is its acceleration. We proceed to write the equations of motion in a more convenient dimensionless form. To that end, we multiply equation (2) by $2/a_m$:

$$\frac{2\ell}{a_m} - t_d^2 = 2\left(t_d + \frac{v'_{jz}}{a_m}\right)(t_j - t_d) + \frac{a_j}{a_m}(t_j - t_d)^2 \qquad [j = 1, 2]. \tag{3}$$

Noting that the AB^{2+} TOF is $t_m = \sqrt{2\ell/a_m}$, we replace the first term on the left-hand side of equation (3) with t_m^2. Further, dividing both sides by t_m^2 leads us to dimensionless z-component equations of motion. We also write the equation for momentum conservation in the AB^{2+} center-of-mass frame:

$$1 - t_{dm}^2 = 2\left(t_{dm} + \frac{v'_{jz}}{v_m}\right)(t_{jm} - t_{dm}) + \eta_j(t_{jm} - t_{dm})^2 \qquad [j = 1, 2]$$

$$\sum_{j=1}^{2} m_j v'_{jz} = 0. \tag{4}$$

Here, we have defined $t_{dm} \equiv t_d/t_m$, $t_{jm} \equiv t_j/t_m$, and $\eta_j \equiv a_j/a_m$. Also, we have substituted in $v_m = a_m t_m$, the velocity of the dication.

The equations above suggest that we can solve for t_{dm} (and hence t_d), as we have three equations and three unknowns, t_{dm}, v'_{1z}, and v'_{2z}. Combining the above equations of motion and the equation for momentum conservation, we eliminate v'_{jz} by substitution, resulting in an equation that can be solved for t_{dm}. Several subsequent algebraic steps lead us to the following quadratic equation:

$$at_{dm}^2 + bt_{dm} + c = 0$$
$$a = [2\beta(\eta_1 - 1) + (\eta_2 - 1)]t_{1m} + [\beta(\eta_1 - 1) + 2(\eta_2 - 1)]t_{2m}$$
$$b = 2[\beta(1 - \eta_1) + (1 - \eta_2)]t_{1m}t_{2m} + (1 + \beta) - (\beta\eta_1 t_{1m}^2 + \eta_2 t_{2m}^2)$$
$$c = (\beta\eta_1 t_{1m} + \eta_2 t_{2m})t_{1m}t_{2m} - (t_{1m} + \beta t_{2m}). \tag{5}$$

Here, $\beta = m_1/m_2$ is the ratio of the mass of the light fragment to that of the heavy fragment.

While the simplicity of our derivation and resulting equations makes the calculation of t_d and subsequent momentum imaging look quite straightforward, the problem is more convoluted than it initially seems. The quadratic equation for t_d has two solutions, which we denote as $t_d^{(+)}$ and $t_d^{(-)}$, where the superscripts correspond to the sign that is chosen in the quadratic formula.

For the vast majority of events, it is not clear which solution is correct, as both are physical based on obvious criteria: t_d must be real and $0 < t_d < t_m$. The root of this complication, illustrated in figures 2(c) and (d), is the link between the sign of v'_{1z} and the correct quadratic formula sign choice. Specifically, $t_d^{(+)}$ always corresponds to $v'_{1z} < 0$, meaning the H^+ (or D^+) is ejected away from the detector, and $t_d^{(-)}$ corresponds to $v'_{1z} > 0$. Of course, in setting out to solve for t_d, one does not know *a priori* the sign of v'_{1z}. Moreover, both situations—positive v'_{1z} with delay time $t_d^{(-)}$ and negative v'_{1z} with $t_d^{(+)}$—lead to the same measured set of time-of-flight values (t_1, t_2). This dilemma also thwarts retrieval of v'_{1z} and the z-component momenta, for which one needs to properly evaluate t_d.

As a noteworthy aside, this dual-solution t_d retrieval problem belongs to an extensive family of *inverse problems*, in which one is trying to retrieve initial conditions from observable parameters. This is an important problem faced in a wide array of fields in science and mathematics, such as medical imaging, x-ray crystallography, optics, geology, acoustics, and many others [53–55]. Frequently, the solution to an inverse problem is not unique, as is the case for dissociation in flight.

To address the inverse problem at hand, we utilize symmetry concepts. For any given t_d, reflection symmetry of v'_{1z} about 0 is expected, as the light fragment is equally likely to be ejected in either the forward or backward directions. Thus, one could select $t_d^{(+)}$ or $t_d^{(-)}$ randomly with equal probability and fit an exponential decay function to the resultant $N(t_d)$ distribution to get a lifetime τ.

In the case of dissociation in flight, however, the symmetry of the overall v'_{1z} distribution should be broken to some degree due to the lifetime of the metastable molecule. That is, if τ is the lifetime of the dication, the ratio of the number of molecules that survive for times $t_d^{(+)}$ and $t_d^{(-)}$, $N^{(+)}$ and $N^{(-)}$, respectively, is described by

Figure 3. $N(t_d)$ distributions obtained using the proposed self-consistent method for (a) $C_2H_4^{2+} \rightarrow C_2H_3^+ + H^+$ and (b) $C_2D_4^{2+} \rightarrow C_2D_3^+ + D^+$. These both represent typical trials from the last iteration. Note that in both plots, the statistical error bars are smaller than the symbols. Two-term exponential decay fits, plotted in blue, agree nicely with the data. The gray dashed line shown in (a), which doesn't agree with the data, is a single-term exponential decay fit.

$$N^{(+)}/N^{(-)} = e^{-[t_d^{(+)} - t_d^{(-)}]/\tau}. \tag{6}$$

Thus, one could correct for the symmetry breaking using this factor. The extent of this correction is determined by the magnitude of $|t_d^{(+)} - t_d^{(-)}|/\tau$. Since $t_d^{(+)}$ and $t_d^{(-)}$ are typically not dramatically different compared to the lifetime τ, this correction is small.

Thus, we use a self-consistent approach in which we start as suggested above, by choosing $t_d^{(+)}$ or $t_d^{(-)}$ randomly with equal likelihood for each event. Recall that this choice is exact in the limit $|t_d^{(+)} - t_d^{(-)}|/\tau \ll 1$. An exponential decay function $N(t_d) = N_0 e^{-t_d/\tau}$ is then fitted to the resulting $N(t_d)$ distribution to retrieve the lifetime. This lifetime allows computation of the aforementioned factor $N^{(+)}/N^{(-)}$, given in equation (6), which is then used to weight the choice of $t_d^{(+)}$ or $t_d^{(-)}$ in the next iteration. The obtained $N(t_d)$ distribution is again fit with an exponential decay function to retrieve a more accurate lifetime, again allowing calculation of a new weighting factor for the choice of $t_d^{(+)}$ or $t_d^{(-)}$. This process is repeated until the lifetime τ converges. Note that for a given iteration, the choice of $t_d^{(+)}$ or $t_d^{(-)}$ and the fitting procedure is repeated for multiple trials to account for the finite sample size of our data. Also, the lifetime τ used to compute the weighting factor for the subsequent iteration is the mean value of those obtained in the multiple trials. For more details about our iterative approach, visit appendix B.

When this self-consistent method is applied to our data, we find good convergence within just a few iterations. We performed the analysis on the C_2H_4 and C_2D_4 data to explore the possibility of isotopic effects. Typical trials from the final iteration are shown in figures 3(a) and (b). Two-term exponential decay fits agree well with both measurements, suggesting that at least two metastable states are contributing to the observed dissociation in flight of ethylene dications. The final converged lifetimes for $C_2H_4^{2+}$ are $\tau_1 = 202 \pm 10$ ns and $\tau_2 = 916 \pm 40$ ns. For $C_2D_4^{2+}$, we obtain $\tau_1 = 269 \pm 29$ ns and $\tau_2 = 956 \pm 83$ ns. The errors here represent the standard deviation of the trials in the last iteration.

Note that the weighting factor $N^{(+)}/N^{(-)}$ has been modified to account for the two lifetimes, τ_1 and τ_2, and thus becomes

$$N^{(+)}/N^{(-)} = \frac{N_0^{(1)} e^{-t_d^{(+)}/\tau_1} + N_0^{(2)} e^{-t_d^{(+)}/\tau_2}}{N_0^{(1)} e^{-t_d^{(-)}/\tau_1} + N_0^{(2)} e^{-t_d^{(-)}/\tau_2}}. \tag{7}$$

As mentioned, the two-term exponential fit indicates that at least two metastable states are responsible for the observed dissociation in flight. The single lifetime for $C_2H_4^{2+}$ reported by Larimian *et al*, 498 ± 12 ns [47], lies between the two lifetimes that we have measured. This discrepancy could be due to a number of reasons, such as differences in the laser pulse parameters, the method used to compute t_d, or the t_d range chosen for the exponential decay fit. Note that when we perform a single exponential decay fit, shown in figure 3(a), we obtain a lifetime of 491 ± 19 ns, consistent with the previous measurement.

We also note that our measurements suggest a possible small isotopic effect in the shorter lifetime, τ_1. The difference between the two shorter lifetimes is on the level of 2.2σ, while the longer lifetimes are the same within the measurement uncertainty. As dissociation in flight of ethylene dications is a low-rate channel, we expect that higher statistics data would make the presence or absence of an isotopic effect in the lifetimes more clear cut. Since we currently lack the good quality electronic structure information on these molecular ions needed to understand this isotopic effect and also to keep the focus on the method, we limit this discussion to highlighting the rich information afforded by our technique.

Figure 4. (a) Retrieved transverse momentum distribution of the D^+ fragments. In this measurement, the laser polarization is along the z (TOF) axis. As marked, φ is a rotation angle in the xy-plane that will be used to characterize the angular distribution (discussed further in the text). (b) Radial momentum distribution $N(p_{1r})$ of the D^+ fragments, where $p_{1r} = \sqrt{p_{1x}^2 + p_{1y}^2}$. The violet line indicates a fit to the data of the functional form for the projection of an isotropic distribution onto a plane, which is given explicitly on the figure. Here, A and B are fit parameters.

3.2. Momentum imaging

Having retrieved t_d and the lifetimes, we can proceed with performing momentum imaging, another aim of this work. While our solution of choosing $t_d^{(+)}$ or $t_d^{(-)}$ with some weighting works on a sample level and is thus a robust method for retrieving the lifetime(s), we note that for a large fraction of the individual events, $t_d^{(+)}$ or $t_d^{(-)}$ will be assigned incorrectly. Therefore, this method of computing t_d cannot be used for momentum imaging, as it is done on an event-by-event basis. As such, we need a single value of t_d for each event, even if it is approximate.

To approximate t_d, we neglect v'_{1z} in equations (4), as the term containing this quantity is typically on the order of a few percent compared to the other terms, as further detailed in appendix C. Moreover, as shown in the same appendix, the error that this approximation introduces in the retrieved t_d and the transverse momenta is also estimated to be at most a few percent. Having neglected v'_{1z}, the equation for t_d becomes linear and thus has a single solution for each event, given explicitly by

$$t_{dm} = \frac{(\eta_1 t_{1m}^2 - 1)(1 - \eta_2) - (\eta_2 t_{2m}^2 - 1)(1 - \eta_1)}{2(t_{2m} - t_{1m})(1 - \eta_1)(1 - \eta_2)}. \tag{8}$$

Employing this approximation of t_d, we have computed the transverse momentum of the D^+ fragments from $C_2D_4^{2+}$, shown in figure 4. The distribution of the radial momentum, $p_{1r} = \sqrt{p_{1x}^2 + p_{1y}^2}$, shown in figure 4(b), agrees well with the functional form for the projection of an isotropic distribution onto a plane [56]. To verify that the momentum distribution is isotropic, the complete 3D momentum distribution is needed. Therefore, the p_{1z} component should also be measured.

Is there any way to retrieve the z-direction momentum? Recall our initial fundamental problem in evaluating v'_{1z} that is associated with the $t_d^{(+)}$ and $t_d^{(-)}$ solutions. Now, we have gone even further and neglected v'_{1z} entirely, eliminating the possibility of recovering p_{1z} directly from the measurement. It is important to note that the polarization is typically aligned along the spectrometer axis (z direction) in COLTRIMS measurements in order to reduce losses of fast fragments, which are usually ejected along the laser field. This choice leads to equivalent x and y momentum components due to the axial symmetry about the laser field and prevents the direct determination of p_{1z}.

To retrieve the missing information, i.e., the p_{1z} momentum component along the laser field, we take advantage of this axial symmetry and align the laser polarization along the y axis. Under these conditions, the measured p_{1y} distribution is along the laser polarization, while p_{1x} is transverse. Moreover, the 'lost' p_{1z} distribution can be recovered from the measured p_{1x} distribution by taking advantage of the axial symmetry about the laser polarization. Under ideal conditions, this measurement is sufficient to retrieve the complete 3D momentum distributions of the fragments. In many cases, however, imperfections like spatial non-uniformities in the detector response may bias the results.

To circumvent this issue and verify that the momentum distribution is isotropic, we performed two measurements with the polarization along the z and y directions, as illustrated in figures 5(a) and (b), respectively. Note that while the angular distributions drawn in this figure do not resemble the isotropic distribution we measure in the present experiment, they help to better convey the difference between the two measurement schemes.

Figure 5. (a) and (b) Schematic angular distributions. Note that these do not reflect our measured angular distributions, but they help better illustrate the concept of our two-measurement scheme. (a) *First measurement*: the laser polarization is aligned along the z direction (spectrometer axis). As v'_{1z} is neglected, momentum information parallel to the polarization is not accessible in this configuration. (b) *Second measurement*: the laser polarization is parallel to the y axis (jet direction), and thus, the momentum distribution along the laser polarization can now be retrieved. Additionally, exploiting the azimuthal symmetry about the laser polarization allows for retrieval of the p_z distribution in this scheme, as $N(p_{1z}) = N(p_{1x})$. (c) Ratio of the $N(\varphi)$ distributions for the two measurement schemes. $N(\varphi_1)$ corresponds to the φ distribution measured with the laser polarization parallel to the time-of-flight axis, z, and $N(\varphi_2)$ is measured after rotating the polarization to be along the jet direction, y. The dotted red line corresponds to the average value of this ratio.

In the first measurement with the polarization along z, the momentum distribution along the polarization cannot be retrieved because v'_{1z} has been neglected. In the second measurement with the polarization along y, the momentum distribution parallel to the laser polarization can be retrieved directly, while the complete transverse momentum distribution can be recovered by using the axial symmetry about the laser field as discussed above.

Let us define φ as a rotation angle in the xy-plane in both measurements. This angle is sketched on figure 4(a). We denote $N(\varphi_1)$ as the distribution obtained in the first measurement (polarization along z) and $N(\varphi_2)$ as the distribution found in the second measurement (polarization along y). Computing the ratio of these distributions yields the result shown in figure 5(c). Note that the position-dependent detection efficiency cancels out in this ratio, thus eliminating the impact of detector imperfections.
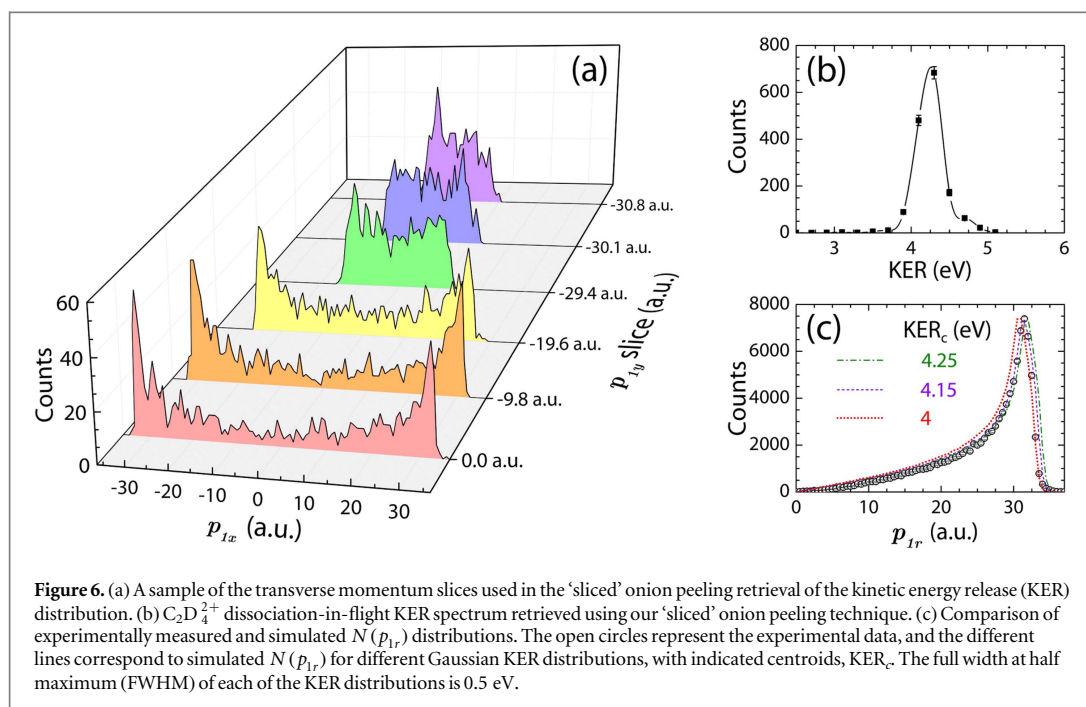
The ratio shown in figure 5(c) is rather flat, directly demonstrating that dissociation in flight yields an isotropic momentum distribution. This distribution is likely the result of t_d being much longer than the rotational timescale of the molecule. Thus, information about the initial alignment of the molecule with respect to the laser polarization is lost, and the resulting distribution is isotropic.

3.3. Kinetic energy release

Finally, just as accessing the z-component momenta is problematic, so too is retrieving the KER on an event-by-event basis. To obtain a KER distribution, we utilize a method based on the onion peeling technique, which has been widely used to analyze photofragment images [57–60]. The transverse momentum distribution, which was obtained using the method described in the previous section, serves as our projected 'onion,' which we slice along the p_x direction. Some sample slices for dissociation in flight of $C_2D_4^{2+}$ are shown in figure 6(a). As we carry out iterative onion peeling subtraction on the slices, the counts that are 'peeled' away are allocated into the appropriate KER bins to accumulate a distribution. For a given iteration being performed on a particular slice, the KER is found using the edges of the slice, as only events with the maximum KER reach this region. We employ this technique for measurements in which the laser polarization is along the y axis, even though the isotropic nature of the distribution would allow one to use data from either of the previously discussed measurement schemes. Further details about this KER retrieval method will be described in a forthcoming publication about the dissociation in flight of metastable carbon dioxide dications [61].

The KER distribution obtained using our 'sliced' onion peeling technique for dissociation in flight of $C_2D_4^{2+}$ is presented in figure 6(b). We estimate the uncertainty in the obtained KER to be about 0.3 eV[2]. The centroid of the KER, at about 4.2 eV, is in good agreement with that obtained by Larimian *et al* [47]. Finally, as an alternative method of retrieving the KER, we compare the measured $N(p_{1r})$ with several simulated $N(p_{1r})$ distributions corresponding to Gaussian KER distributions with different centroids and widths, as illustrated in figure 6(c). As

---

[2] This error estimate was obtained by propagating the error in the transverse momentum (taken to be the bin size) through to the KER.

Figure 6. (a) A sample of the transverse momentum slices used in the 'sliced' onion peeling retrieval of the kinetic energy release (KER) distribution. (b) $C_2D_4^{2+}$ dissociation-in-flight KER spectrum retrieved using our 'sliced' onion peeling technique. (c) Comparison of experimentally measured and simulated $N(p_{1r})$ distributions. The open circles represent the experimental data, and the different lines correspond to simulated $N(p_{1r})$ for different Gaussian KER distributions, with indicated centroids, KER_c. The full width at half maximum (FWHM) of each of the KER distributions is 0.5 eV.

can be seen, the simulated $N(p_{1r})$ distribution with a KER centroid of 4.15 eV and a FWHM of 0.5 eV agrees well with the measured $N(p_{1r})$. Furthermore, this result supports that obtained using the 'sliced' onion peeling approach. As mentioned, the KER can supply a great deal of insight into dissociation pathways, e.g., [17, 25, 26]. This pursuit, however, is beyond the scope of this paper, which focuses on the method.

4. Summary and outlook

In summary, we have developed a method to study dissociation in flight of metastable molecular ions using coincidence momentum imaging measurements. Our approach, which supplies valuable information about the relevant metastable states, including the lifetime(s) and momentum distributions of the dissociating fragments, has been realized through the application and symmetries of the relevant kinematic equations.
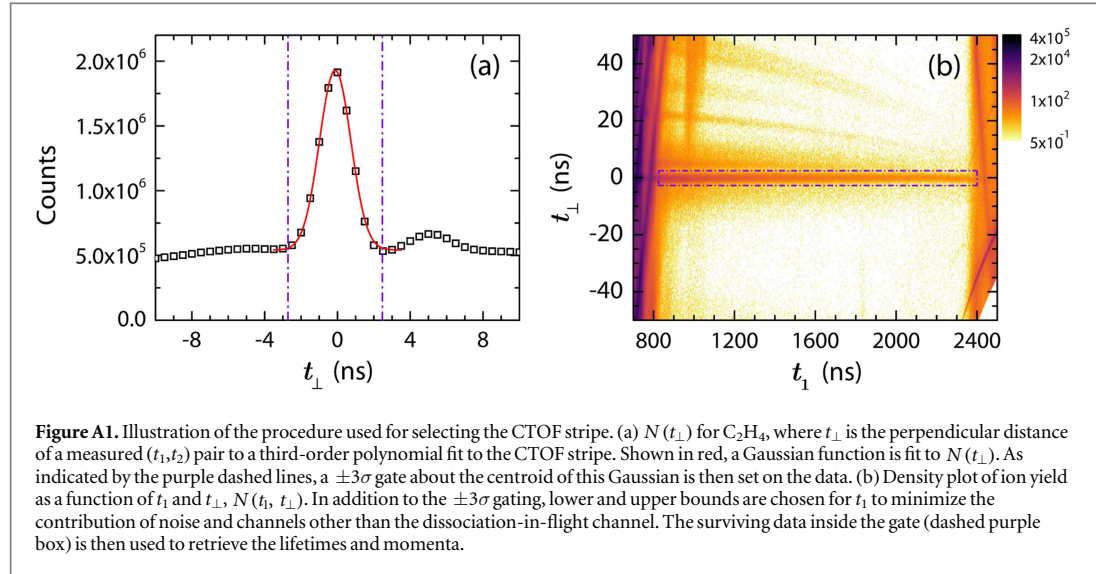
Encountered hurdles such as the inverse problem of choosing $t_d^{(+)}$ or $t_d^{(-)}$ and the related problem of retrieving v_{1z}' have been addressed by exploiting symmetries of the fragmentation. The readily expressed forward-backward symmetry breaking in the v_{1z}' distribution was used in a self-consistent manner to obtain the $N(t_d)$ distribution of the sample and hence the lifetimes of the metastable states dissociating in flight. This analysis allowed us to find two lifetimes in the deprotonation of metastable ethylene dications and a possible isotopic effect in the shorter lifetime.

The necessity of a single t_d value for each event to obtain the momenta was fulfilled by neglecting v_{1z}', an assumption which we have shown to be on solid ground, as it introduces minimal error in the calculation of t_d and the momenta. Furthermore, the azimuthal symmetry about the laser polarization was exploited to obtain all the components of the momentum rendered unretrievable by the t_d inverse problem.

Finally, while we have demonstrated this method for the specific case of deprotonation of metastable ethylene dications formed by intense femtosecond laser pulses, this technique is applicable to coincidence measurements on a variety of metastable molecular systems dissociating in flight, which could also be formed via other means, such as x-ray photoabsorption or fast charged particle impact.

Acknowledgments

Figure A1. Illustration of the procedure used for selecting the CTOF stripe. (a) $N(t_\perp)$ for C_2H_4, where $t_\perp$ is the perpendicular distance of a measured (t_1, t_2) pair to a third-order polynomial fit to the CTOF stripe. Shown in red, a Gaussian function is fit to $N(t_\perp)$. As indicated by the purple dashed lines, a $\pm 3\sigma$ gate about the centroid of this Gaussian is then set on the data. (b) Density plot of ion yield as a function of t_1 and $t_\perp$, $N(t_1, t_\perp)$. In addition to the $\pm 3\sigma$ gating, lower and upper bounds are chosen for t_1 to minimize the contribution of noise and channels other than the dissociation-in-flight channel. The surviving data inside the gate (dashed purple box) is then used to retrieve the lifetimes and momenta.

Appendix A. Gating on the dissociation-in-flight coincidence stripe

The long, curved dissociation-in-flight stripe in the CTOF spectrum fairly closely follows a third-order polynomial dependence as a function of t_1. To more effectively select true events while suppressing the contribution of random pairs (i.e., improve the signal to 'noise' ratio), we use the coefficients of a third-order polynomial fit to the curved coincidence stripe to straighten it and then apply a simple rectangular gate. More specifically, $t_\perp$, the perpendicular distance from each (t_1, t_2) data point to the polynomial fit is calculated. A Gaussian function is fit to the $N(t_\perp)$ distribution, and a $\pm 3\sigma$ gate is applied to the data, as shown in figure A1(a). Figure A1(b) shows the straightened stripe and gate around it. Note that for C_2H_4, the left and right gating bounds for t_1 were chosen to be 825 ns and 2400 ns, respectively, and for C_2D_4, they were 1200 ns and 2400 ns, respectively. These data selection schemes allow one to avoid the prompt breakup region, as well as the area of the CTOF spectrum near the end of the dissociation-in-flight stripe, where 'noise' and other channels dominate.

Appendix B. Dealing with limited statistics when determining lifetimes and convergence of the iterative method
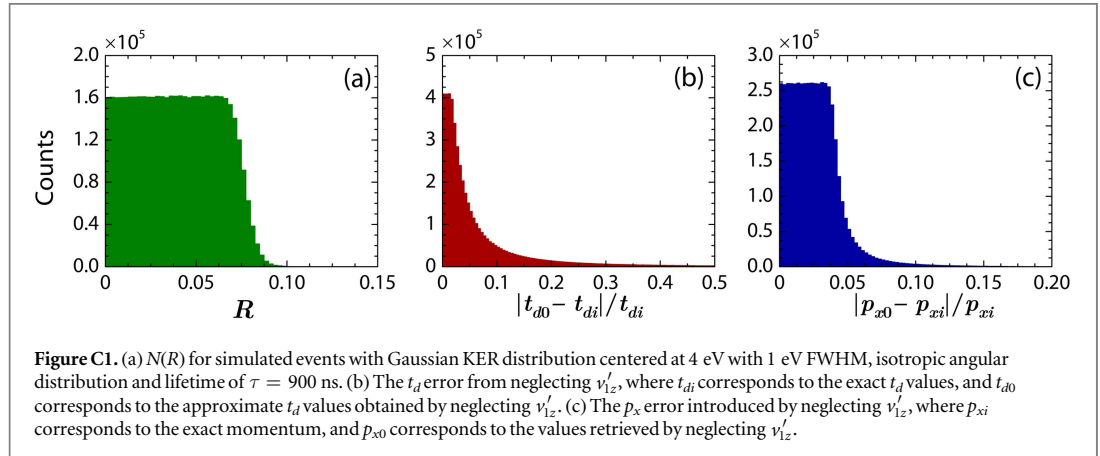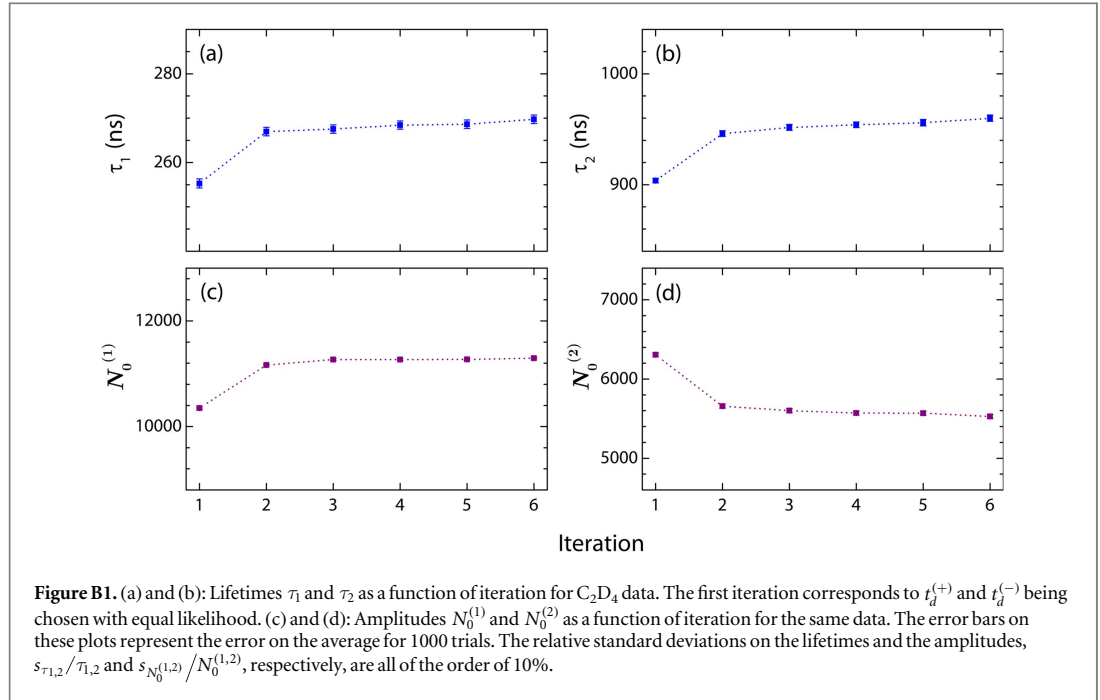
Recall that due to the inverse problem related to the sign of v'_{1z} (and associated sign choice in the t_d equation), we employ an iterative procedure that starts with a choice of $t_d^{(+)}$ or $t_d^{(-)}$ that is equally likely. Then, we use the values of τ in subsequent iterations to weight the choice of $t_d^{(+)}$ or $t_d^{(-)}$, using equation (7). As this method utilizes a random number generator to choose $t_d^{(+)}$ or $t_d^{(-)}$, it is imperative that the sample size be large enough to ensure true randomness.

As we are applying this analysis to experimental data of a relatively weak channel for which statistics are limited, one may worry about the robustness of the proposed method that relies on random number generation. To address this issue, as mentioned in section 3.1, each iteration of the lifetime determination procedure consists of multiple trials. That is, for each iteration, the analysis is simply repeated multiple times (each time with a randomly selected seed). Each trial uses the same solution choice weighting scheme. An exponential decay function is fit to the resulting $N(t_d)$ distributions to retrieve lifetimes for each trial. At the end of an iteration, the amplitudes $N_0^{(1)}$ and $N_0^{(2)}$ and lifetimes τ_1 and τ_2 used to calculate the weighting factor in equation (7) are the average values from all the trials in that iteration.

As mentioned, when applied to our ethylene data, the lifetimes and amplitudes converge within just a few iterations. Plots illustrating the convergence of these quantities are shown in figures B1(a)–(d). Note that in the first iteration, $t_d^{(+)}$ and $t_d^{(-)}$ are selected with equal probability, and each iteration consists of 1000 trials.

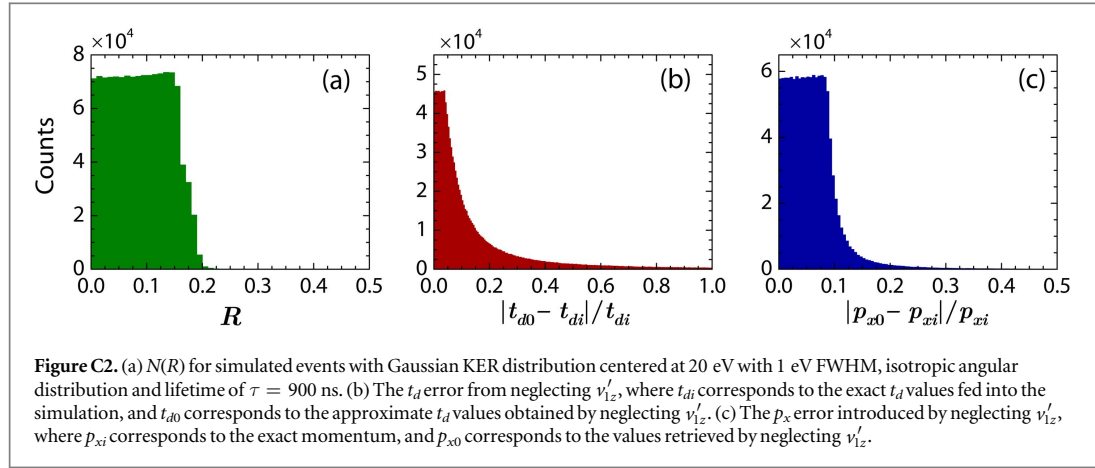## Appendix C. Approximation of t_d by neglecting v'_{1z}

To obtain a single value of t_d needed for evaluating the momentum of each event, an approximation is necessary. We start with the first expression in equations (4) and divide both sides by $t_{jm} - t_{dm}$ to obtain

Figure B1. (a) and (b): Lifetimes τ_1 and τ_2 as a function of iteration for C_2D_4 data. The first iteration corresponds to $t_d^{(+)}$ and $t_d^{(-)}$ being chosen with equal likelihood. (c) and (d): Amplitudes $N_0^{(1)}$ and $N_0^{(2)}$ as a function of iteration for the same data. The error bars on these plots represent the error on the average for 1000 trials. The relative standard deviations on the lifetimes and the amplitudes, $s_{\tau_{1,2}}/\tau_{1,2}$ and $s_{N_0^{(1,2)}}/N_0^{(1,2)}$, respectively, are all of the order of 10%.

Figure C1. (a) $N(R)$ for simulated events with Gaussian KER distribution centered at 4 eV with 1 eV FWHM, isotropic angular distribution and lifetime of $\tau = 900$ ns. (b) The t_d error from neglecting v'_{1z}, where t_{di} corresponds to the exact t_d values, and t_{d0} corresponds to the approximate t_d values obtained by neglecting v'_{1z}. (c) The p_x error introduced by neglecting v'_{1z}, where p_{xi} corresponds to the exact momentum, and p_{x0} corresponds to the values retrieved by neglecting v'_{1z}.

$$\frac{1 - t_{dm}^2}{t_{jm} - t_{dm}} = 2t_{dm} + 2\frac{v'_{jz}}{v_m} + \eta_j(t_{jm} - t_{dm}) \qquad [j = 1, 2]. \qquad (9)$$

This equation is solved for t_{dm} after neglecting the second term on the right-hand side that contains v'_{jz}. How valid is neglecting this term? To explore this question, we perform simulations using a few typical input random functional distributions, including a single-term exponential decay $N(t_d)$ distribution with $\tau = 900$ ns, a Gaussian KER distribution centered at 4 eV with a 1 eV FWHM, and an isotropic angular distribution. Let us denote the terms on the right-hand side of equation (9) as '1st term,' '2nd term,' and '3rd term,' in left-to-right order. We evaluate the quantity $R \equiv |2\text{nd term}|/(1\text{st term} + 3\text{rd term})$, shown in figure C1(a). For 99% of the events, $R < 10\%$. Furthermore, the error that neglecting the second term introduces into the recovered t_d and p_{1x}, shown in figures C1(b) and (c), is also reasonably small. For t_d, about 77% of the simulated events lie below the 5% error level, and for p_{1x}, about 98% of the events lie below the same error level.

Since the validity of neglecting v'_{1z} depends on the magnitude of v'_{1z}, and for our simulations we have assumed values of this quantity approximately matching the measured ones, it is reasonable to explore how large v'_{1z} can be before the approximation breaks down. Thus, we performed simulations with a few larger KER values (and hence larger maximum values of v'_{1z}). Even for a high KER of 20 eV (Gaussian distribution with 1 eV FWHM and the same lifetime and angular distribution as before), 99% of the simulated events have $R < 20\%$, as shown in figure C2(a). Moreover, as shown in figures C2(b) and (c), 75% of the events have <20% error in the

Figure C2. (a) $N(R)$ for simulated events with Gaussian KER distribution centered at 20 eV with 1 eV FWHM, isotropic angular distribution and lifetime of $\tau = 900$ ns. (b) The t_d error from neglecting v'_{1z}, where t_{di} corresponds to the exact t_d values fed into the simulation, and t_{d0} corresponds to the approximate t_d values obtained by neglecting v'_{1z}. (c) The p_x error introduced by neglecting v'_{1z}, where p_{xi} corresponds to the exact momentum, and p_{x0} corresponds to the values retrieved by neglecting v'_{1z}.

retrieved t_d, and about 98% of the events are below the same error level in p_{1x}. Given this extreme example, we are thus assured that neglecting v'_{1z} for momentum computation is a reasonable approximation for our case.

It is noteworthy that in general it is not merely the KER (and hence the maximum v'_{1z}) that is important for consideration but the ratio v'_{jz}/v_m, as can be readily seen in equation (9). Recall that v_m is the velocity of the dication. Therefore, in certain cases, it may also be desirable to increase the spectrometer voltage in the experiment to increase v_m and thereby improve the validity of this approximation.

Appendix D. Lifetime determination accuracy due to time-of-flight uncertainty

Due to the nature of our method for evaluating t_d, it is not straightforward to propagate errors in order to determine the uncertainty in the recovered lifetime(s). Here we demonstrate how simulations aid us in pinpointing important sources of error.
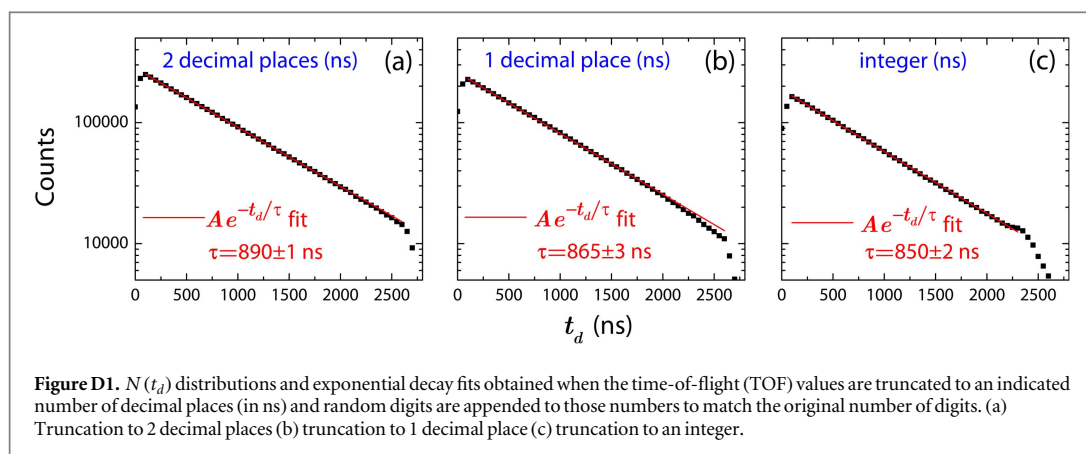
As measured TOF values are used to calculate t_d, a rather pertinent question is what effect the uncertainty in these quantities has on the retrieved lifetimes. Finite time resolution, number truncation by the time-to-digital converter (TDC) unit used (which has a 25 ps resolution), and uncertainty in the absolute time (i.e., the error associated with the exact time of the laser-molecule interaction) all influence the accuracy of the retrieved lifetime. While we have performed simulations to investigate each of these effects, for the sake of brevity, we use those exploring truncation to illustrate the impact that this type of uncertainty can have.

To examine the effects of truncation of the measured TOF values, we simulate events with the same parameters as in the previous appendix (4 eV KER centroid). Thus, each simulated event has an associated t_d and v'_{1z}. The $[j = 1, 2]$ equations in (4) are rearranged into quadratic expressions that can be solved for t_1 and t_2:

$$0 = \eta_1 t_1^2 + 2\left((1 - \eta_1)t_d + \frac{v'_{1z}t_m}{v_m}\right)t_1 + (\eta_1 - 1)t_d^2 - \frac{2v'_{1z}t_d t_m}{v_m} - t_m^2, \tag{10}$$

$$0 = \eta_2 t_2^2 + 2\left((1 - \eta_2)t_d - \frac{\beta v'_{1z}t_m}{v_m}\right)t_2 + (\eta_2 - 1)t_d^2 + \frac{2\beta v'_{1z}t_d t_m}{v_m} - t_m^2.$$

In solving for t_1 and t_2, we choose the positive root in the quadratic formula because choosing the negative root yields negative t_1 and t_2 values or $t_1 < t_d$, which is unacceptable, in contrast to the t_d equation for which both roots can make physical sense. The values of t_1 and t_2 are truncated to varying levels of precision in ns, simulating the possible digitizer accuracy. Then a random fraction is added to the truncated number, as is done for the measured (digitized) data, to match the original number of digits. For example, if t_i is a time-of-flight value truncated to n decimal place(s), the new TOF after adding the random fraction is $t_i' = t_i + r \times 10^{-n}$, where r is a random number between 0 and 1. The new values of t_1 and t_2 are then used to compute t_d and obtain a lifetime, which is then compared to the original input lifetime. A few examples of the effect of truncation on the recovered lifetime are shown in figures D1(a)–(c). As can be seen in the figure, as more of the true digits are initially truncated, the retrieved lifetime veers away from the original lifetime of 900 ns, and the range of $N(t_d)$ that can be used for fitting starts to deteriorate. As mentioned, similar tests were performed to examine the effects of finite resolution and absolute time uncertainty. These simulations yielded results comparable to the number truncation tests.

Figure D1. $N(t_d)$ distributions and exponential decay fits obtained when the time-of-flight (TOF) values are truncated to an indicated number of decimal places (in ns) and random digits are appended to those numbers to match the original number of digits. (a) Truncation to 2 decimal places (b) truncation to 1 decimal place (c) truncation to an integer.

While our simulations have proven instructive in identifying influential error sources such as those related to the measured time-of-flight values, note that the errors presented in the body of this manuscript reflect those evaluated by statistical means.

ORCID iDs

Bethany Jochim ⓘ https://orcid.org/0000-0003-2040-1453

References

[1] Osipov T, Cocke C L, Prior M H, Landers A, Weber T, Jagutzki O, Schmidt L, Schmidt-Böcking H and Dörner R 2003 *Phys. Rev. Lett.* **90** 233002

[2] Zyubina T S, Dyakov Y A, Lin S H, Bandrauk A D and Mebel A M 2005 *J. Chem. Phys.* **123** 134320

[3] Wells E *et al* 2013 *Nat. Commun.* **4** 2895

[4] Ergler T, Rudenko A, Feuerstein B, Zrost K, Schröter C D, Moshammer R and Ullrich J 2006 *Phys. Rev. Lett.* **97** 193001

[5] Chatterley A S, Lackner F, Neumark D M, Leone S R and Gessner O 2016 *Phys. Chem. Chem. Phys.* **18** 14644–53

[6] Zewail A H 1988 *Science* **242** 1645–53

[7] Zewail A 2000 *Pure Appl. Chem.* **72** 2219–31

[8] Assion A, Baumert T, Bergt M, Brixner T, Kiefer B, Seyfried V, Strehle M and Gerber G 1998 *Science* **282** 919–22

[9] Hertel I V and Radloff W 2006 *Rep. Prog. Phys.* **69** 1897

[10] Mathur D 1993 *Phys. Rep.* **225** 193–272 and references therein

[11] Mathur D 2004 *Phys. Rep.* **391** 1–118 and references therein

[12] Price S D 2007 *Int. J. Mass Spectrom. Ion Phys.* **260** 1–19 and references therein

[13] Andersen L H, Posthumus J H, Vahtras O, H Ågren, Elander N, Nunez A, Scrinzi A, Natiello M and Larsson M 1993 *Phys. Rev. Lett.* **71** 1812–5

[14] Mathur D, Andersen L H, Hvelplund P, Kella D and Safvan C P 1995 *J. Phys. B: At. Mol. Opt. Phys.* **28** 3415

[15] Bar-David A, Ben-Itzhak I, Bouhnik J, Gertner I, Levy Y and Rosner B 2000 *Nucl. Instrum. Methods Phys. Res.* B **160** 182–9

[16] Bouhnik J P, Gertner I, Rosner B, Amitay Z, Heber O, Zajfman D, Sidky E Y and Ben-Itzhak I 2001 *Phys. Rev.* A **63** 032509

[17] Beylerian C and Cornaggia C 2004 *J. Phys. B: At. Mol. Opt. Phys.* **37** L259

[18] Baková R, Fišer J, Šedivcová Uhlíková T and Špirko V 2008 *J. Chem. Phys.* **128** 144301

[19] Püttner R *et al* 2011 *Phys. Chem. Chem. Phys.* **13** 18436–46

[20] Brites V, Franzreb K, Harvey J N, Sayres S G, Ross M W, Blumling D E, Castleman A W and Hochlaf M 2011 *Phys. Chem. Chem. Phys.* **13** 15233–43

[21] Brites V, Franzreb K and Hochlaf M 2011 *Phys. Chem. Chem. Phys.* **13** 18315–21

[22] Buth C, Cryan J P, Glownia J M, Hoener M, Coffee R N and Berrah N 2012 *J. Chem. Phys.* **136** 214310

[23] Liu J C, Berrah N, Cederbaum L S, Cryan J P, Glownia J M, Schafer K J and Buth C 2016 *J. Phys. B: At. Mol. Opt. Phys.* **49** 075602

[24] Liu X J, Nicolas C, Patanen M and Miron C 2017 *Sci. Rep.* **7** 2898

[25] Hishikawa A, Liu S, Iwasaki A and Yamanouchi K 2001 *J. Chem. Phys.* **114** 9856–62

[26] Sayler A M, Wang P Q, Carnes K D, Esry B D and Ben-Itzhak I 2007 *Phys. Rev.* A **75** 063420

[27] Dörner R, Mergel V, Jagutzki O, Spielberger L, Ullrich J, Moshammer R and Schmidt-Böcking H 2000 *Phys. Rep.* **330** 95–192

[28] Ullrich J, Moshammer R, Dorn A, Dörner R, Schmidt L P H and Schmidt-Böcking H 2003 *Rep. Prog. Phys.* **66** 1463

[29] Price S D 1992 *J. Phys. B: At. Mol. Opt. Phys.* **25** 3631

[30] Hsieh S and Eland J H D 1997 *J. Phys. B: At. Mol. Opt. Phys.* **30** 4515

[31] Lundqvist M, Edvardsson D, Baltzer P, Larsson M and Wannberg B 1996 *J. Phys. B: At. Mol. Opt. Phys.* **29** 499

[32] Guo C and Wright K 2005 *Phys. Rev.* A **71** 021404

[33] Neumann N *et al* 2010 *Phys. Rev. Lett.* **104** 103201

[34] Ablikim U *et al* 2017 *Phys. Chem. Chem. Phys.* **19** 13419–31

[35] Besnard-Ramage M J, Morin P, Lebrun T, Nenner I, Hubin-Franskin M J, Delwiche J, Lablanquie P and Eland J H D 1989 *Rev. Sci. Instrum.* **60** 2182–5

[36] Field T A and Eland J H 1993 *Chem. Phys. Lett.* **211** 436–42

[37] Wang P and Vidal C 2002 *Chem. Phys.* **280** 309–29

[38] Wang P and Vidal C R 2003 *J. Chem. Phys.* **118** 5383–9

[39] Slattery A E, Field T A, Ahmad M, Hall R I, Lambourne J, Penent F, Lablanquie P and Eland J H D 2005 *J. Chem. Phys.* **122** 084317

[40] Sharma V, Bapat B, Mondal J, Hochlaf M, Giri K and Sathyamurthy N 2007 *J. Phys. Chem.* A **111** 10205–11

[41] Alagia M, Candori P, Falcinelli S, Lavollée M, Pirani F, Richter R, Stranges S and Vecchiocattivi F 2009 *J. Phys. Chem.* A **113** 14755–9

[42] Alagia M, Candori P, Falcinelli S, Mundim M S P, Pirani F, Richter R, Rosi M, Stranges S and Vecchiocattivi F 2011 *J. Chem. Phys.* **135** 144304

[43] Alagia M, Candori P, Falcinelli S, Mundim K, Mundim M, Pirani F, Richter R, Stranges S and Vecchiocattivi F 2012 Chemical physics of low-temperature plasmas (in honour of Prof Mario Capitelli) *Chem. Phys.* **398** 134–41

[44] Alagia M, Callegari C, Candori P, Falcinelli S, Pirani F, Richter R, Stranges S and Vecchiocattivi F 2012 *J. Chem. Phys.* **136** 204302

[45] Kübel M *et al* 2014 *New J. Phys.* **16** 065017

[46] Khan A and Misra D 2016 *J. Phys. B: At. Mol. Opt. Phys.* **49** 055201

[47] Larimian S *et al* 2016 *Phys. Rev.* A **93** 053405

[48] Wolter B *et al* 2016 *Science* **354** 308–12

[49] Dribinski V, Ossadtchi A, Mandelshtam V A and Reisler H 2002 *Rev. Sci. Instrum.* **73** 2634–42

[50] Trebino R, DeLong K W, Fittinghoff D N, Sweetser J N, Krumbügel M A, Richman B A and Kane D J 1997 *Rev. Sci. Instrum.* **68** 3277–95

[51] de Jesus V L B, Feuerstein B, Zrost K, Fischer D, Rudenko A, Afaneh F, Schröter C D, Moshammer R and Ullrich J 2004 *J. Phys. B: At. Mol. Opt. Phys.* **37** L161

[52] Rudenko A, Zrost K, Schröter C D, de Jesus V L B, Feuerstein B, Moshammer R and Ullrich J 2004 *J. Phys. B: At. Mol. Opt. Phys.* **37** L407

[53] Bertero M and Boccacci P 1998 *Introduction to Inverse Problems in Imaging* (Boca Raton, FL: CRC Press)

[54] Hussein E M A 2011 *Computed Radiation Imaging* (Amsterdam: Elsevier)

[55] Neto F D M and Neto A J d S 2013 *An Introduction to Inverse Problems with Applications* (Berlin: Springer)

[56] Zajfman D, Schwalm D and Wolf A 2003 *Multiparticle Imaging of Fast Molecular Ion Beams in Many-Particle Quantum Dynamics in Atomic and Molecular Fragmentation* 1st edn (Berlin: Springer)

[57] Bordas C, Paulig F, Helm H and Huestis D L 1996 *Rev. Sci. Instrum.* **67** 2257–68

[58] Winterhalter J, Maier D, Honerkamp J, Schyja V and Helm H 1999 *J. Chem. Phys.* **110** 11187–96

[59] Manzhos S and Loock H P 2003 *Comput. Phys. Commun.* **154** 76–87

[60] Whitaker B (ed) 2003 *Imaging in Molecular Dynamics* (Cambridge : Cambridge University Press)

[61] Erdwien R *et al* in preparation

2.8 VMI technique

We used the velocity map imaging (VMI) technique in collaboration with Augustana University to perform the experiment described in Chapter 5. In the VMI technique, which is illustrated in Fig. 2.8.1, a focused beam of femtosecond laser pulses irradiates molecules in an effusive jet. The VMI technique involves a non-uniform electric field created by a set of biased rings, which operates as an electrostatic lens. This scheme focuses fragments from different initial positions in the interaction volume to the same position on the detector if they have the same velocity. The detector consists of an MCP with a phosphor screen behind it. The fragments strike the MCP, and electrons emerging from the back of the MCP strike the phosphor screen to produce an image, recorded by a camera over several laser shots. In contrast to the ion beam imaging and COLTRIMS techniques described in the previous sections, the VMI technique does not typically operate in event mode. The application of Abel inversion methods, such as pBASEX [57], iterative [58], or onion peeling [59] allows the retrieval of slices in the 3D momentum distributions from the measured images. Further details about the VMI method can be found in Refs. [50, 60, 61].
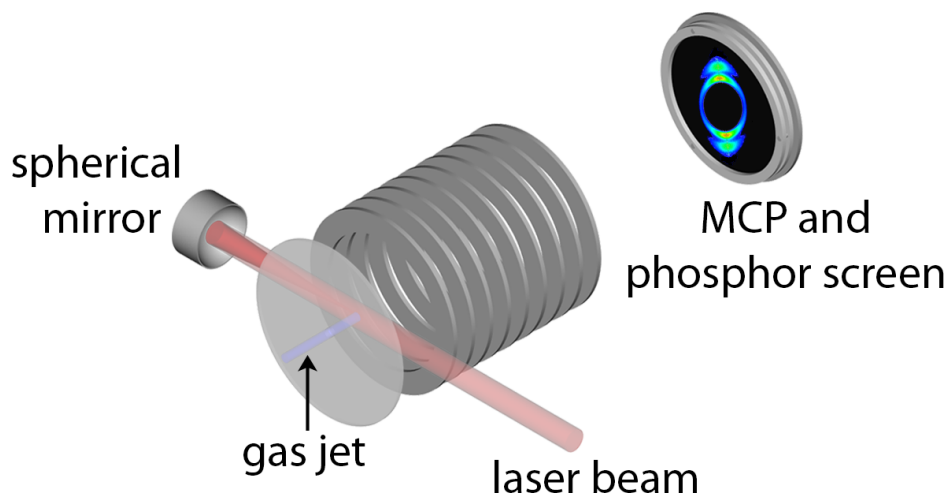
Figure 2.8.1: (a) Schematic of the velocity map imaging (VMI) setup. Charged fragments from the interaction of intense laser pulses with an effusive jet of molecules are focused such that those with the same velocity are projected onto the same position on the detector (see text).

Chapter 3

Strong-field hydrogen migration

3.1 Scope

This chapter focuses on a major theme of my work, examining the laser-induced dynamics of hydrocarbons, specifically isomerization. Section 3.2 gives a broad introduction to isomerization. Sections 3.3 and 3.4, respectively, contain a published paper and a submitted manuscript on this topic.

3.2 Isomerization

3.2.1 General overview

Isomerization is a process via which a molecule changes configuration while retaining its constituent atoms. The different configurations, called "isomers," typically have rather distinct chemical properties [62], and their rearrangements are prevalent in nature [63–65] and industry [66–68]. One curious example of an isomerization reaction in nature is used by the *Nicotiana attenuata* plant for defense [65]. This plant's leaves contain chemicals known as green leaf volatiles (GLVs). When the tobacco hornworm caterpillar feeds on this plant, its saliva elicits isomerization of the GLVs in the damaged leaves. One such GLV reaction is shown in Fig. 3.2.1. The newly-formed isomers attract insects that prey on the hornworm

hex-3-enal (*Z*)   hex-2-enal (*E*)
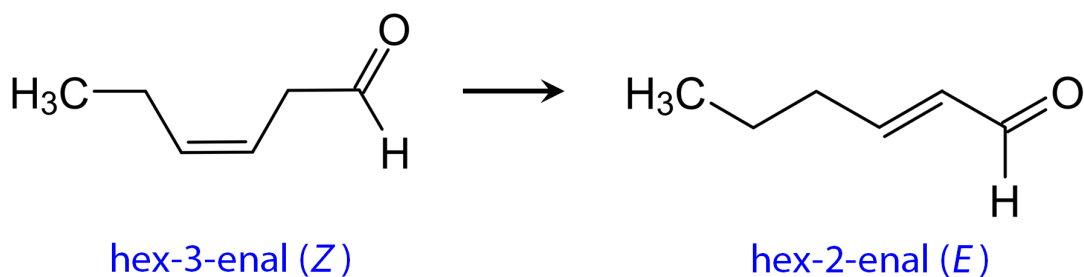
Figure 3.2.1: One of the isomerization processes that is found to occur when the hornworm caterpillar deposits its saliva on damaged leaves of the *Nicotiana attenuata* plant. The isomer on the right attracts the caterpillar's predators.

eggs and caterpillars.

Another instance of isomerization is the molecular switch [69], in which a controlled, reversible isomerization process produces changes in physical properties, such as the absorption spectrum, color, or pH level. The irradiation of light of different wavelengths is one way to activate this switch, stimulating the forward or reverse reactions between the two isomers [69].

3.2.2   Hydrogen migration in C_2H_2: a "simple" example

While there are several other examples of isomerization, it is best to begin with a simpler case to build our understanding. Hence, we focus on one of the simplest hydrocarbon molecules, C_2H_2. Fig. 3.2.2 illustrates the isomerization between the acetylene (HCCH) and vinylidene (H_2CC) configurations of neutral C_2H_2. This reaction is an example of hydrogen migration, a subset of isomerization in which hydrogen moves from one site to another in a molecule [70].
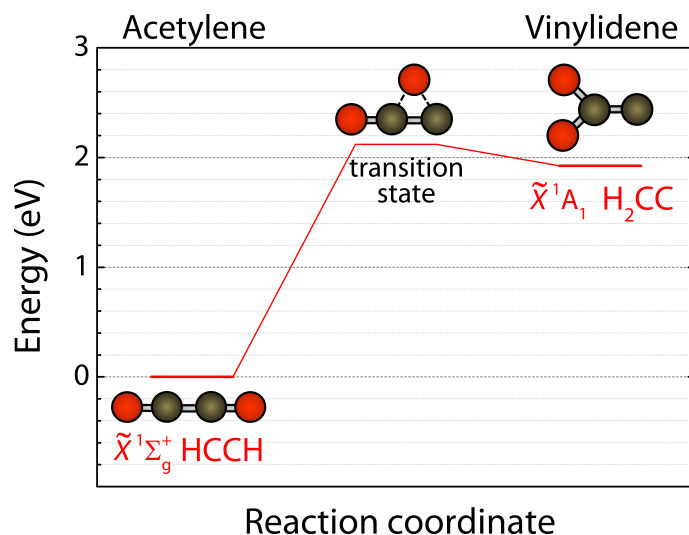
Figure 3.2.2: Schematic energy level diagram for isomerization of C_2H_2 from acetylene (HCCH), the configuration of the neutral ground state, to the higher-energy isomer, vinylidene (H_2CC). The energy levels are taken from Ref. [71].

Hydrogen migration in $C_2H_2^q$ has been the topic of many experimental and theoretical studies in chemistry and physics, from spectroscopy [71–79] to photofragmentation studies [80–102] . While spectroscopic studies of this system most often focus on dynamics in C_2H_2 molecules that remain intact, photofragmentation studies are fundamentally different in that they probe the dynamics on potential energy surfaces leading to dissociation. The signatures of hydrogen migration in spectroscopic studies involve measurables like photo-electron energies [72, 78, 79], fluorescence [73, 75–77], and stimulated emission [73, 74, 77]. In photofragmentation studies, common signatures for isomerization include the measurement of channels such as $C^{q_1} + CH_2^{q_2}$ (for an H_2CC final configuration) and $CH^{q_1} + CH^{q_2}$ (for an HCCH final configuration). Other photofragmentation studies focusing on three- or four-body breakup of C_2H_2 use the relative directions of the measured fragment momenta to identify isomerization [89, 92–94, 100].

33

3.3 Dependence on the initial configuration of strong field-driven isomerization of C_2H_2 cations and anions
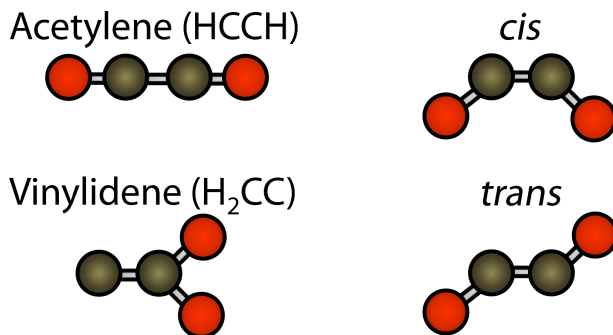

Figure 3.3.1: Various C_2H_2 configurations studied, including linear acetylene (HCCH), vinylidene (H_2CC), and *cis/trans*.

This section contains a paper published in *The Journal of Physical Chemistry Letters* [103] reporting the key role of the initial configuration in the ultrafast laser-induced isomerization of $C_2H_2^q$ ions ($q=-1,0,1$). Here, the "configuration" refers to the geometry of the target $C_2H_2^q$ molecule when it is probed by the laser. Using ion beam targets in various initial configurations, including HCCH, H_2CC, and *cis/trans*, illustrated schematically in Fig. 3.3.1, we demonstrate that the configuration greatly impacts the branching ratios of acetylene-like ($CH^{q_1} + CH^{q_1}$) and vinylidene-like ($C^{q'_1} + CH_2^{q'_2}$) fragmentation. A common expectation in strong-field-induced isomerization studies is that the hydrogen migration will proceed in a recurrent manner [92, 94, 96]. That is, a hydrogen shifts from one carbon site to the other and then returns to the original carbon site, motion that repeats itself with a period typically on the order of 60–100 fs [92, 94, 96]. One might then expect both $CH^{q_1} + CH^{q_1}$ and $C^{q'_1} + CH_2^{q'_2}$ breakup, dependent upon the stage of the oscillatory motion in which the C-C bond breaks. Therefore, our observation that the acetylene-like fragmentation yield may be almost entirely suppressed by changing the initial configuration is surprising.

The following article was reprinted with permission from B. Jochim *et al.* J. Phys. Chem. Lett. **10**, 2320 (2019). Copyright 2019 American Chemical Society.
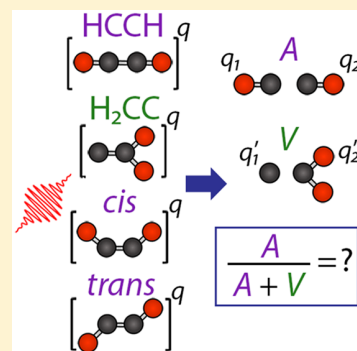
Dependence on the Initial Configuration of Strong Field-Driven Isomerization of C_2H_2 Cations and Anions

Bethany Jochim,*,[†] Ben Berry,[†] T. Severt,[†] Peyman Feizollah,[†] M. Zohrabi,[†] Kanaka Raju P.,[†] E. Wells,[‡] K. D. Carnes,[†] and I. Ben-Itzhak*,[†]

[†]J. R. Macdonald Laboratory, Department of Physics, Kansas State University, Manhattan, Kansas 66506, United States
[‡]Department of Physics, Augustana University, Sioux Falls, South Dakota 57197, United States

ABSTRACT: We have investigated the femtosecond laser-induced fragmentation of $C_2H_2^q$ ion beam targets in various initial configurations, including acetylene (linear HCCH), vinylidene (H_2CC), and *cis/trans*. The initial configuration is shown to have a tremendous impact on the branching ratio of acetylene-like ($CH^{q_1} + CH^{q_2}$) and vinylidene-like ($C^{q_1'} + CH_2^{q_2'}$) dissociation of a specific $C_2H_2^q$ molecular ion. In particular, whereas $C_2H_2^+$ generated from C_2H_2, a linear HCCH target, exhibits comparable levels of acetylene-like and vinylidene-like fragmentation, vinylidene or *cis/trans* configuration ion beams preferably undergo vinylidene-like fragmentation, with an acetylene branching ratio ranging from 13.9% to zero.

Photochemistry studies often involve probing molecular dynamics starting from stable configurations. The initial configuration, however, can have a great influence on the dynamics. Examining various geometries beyond those commonly studied can therefore offer a different perspective. One well-studied topic that may benefit from such an alternative approach is isomerization.

Widespread in nature[1−4] and key to many industrial applications,[5−7] isomerization reactions have been extensively studied in chemistry and physics, both experimentally and theoretically.[8,9] The C_2H_2 molecule in particular has proven to be a useful testing ground for examining isomerization. Conversion between its acetylene (HCCH) and vinylidene (H_2CC) isomers, an example of 1,2 hydrogen migration,[10] is one of the simplest bond rearrangement isomerization reactions.

A wide array of experimental techniques have been applied to examine isomerization of C_2H_2 molecules. Photodetachment spectroscopy measurements on $C_2H_2^-$ ions have collectively provided a fuller picture of the energetics and $H_2CC \rightarrow HCCH$ isomerization dynamics of the resulting transient neutral vinylidene.[11−16] With an alternative approach, stimulated emission spectroscopy (SEP)[17−19] and dispersed fluorescence (DF)[17,19−21] measurements have examined the reverse reaction, preparing acetylene (HCCH) in highly excited vibrational states close to the isomerization threshold and looking for signatures of HCCH → H_2CC transitions.

In addition to being heavily studied in traditional linear spectroscopy,[13−19,21] C_2H_2 isomerization has also garnered significant interest in the photofragmentation community. Here, a far less "gentle" approach is taken, breaking the molecule and extracting information from the measured

fragments. The signatures of isomerization are thus fundamentally different from those in the aforementioned types of spectroscopy. For example, common signatures in fragmentation studies are measurement of $C^{q_1} + CH_2^{q_2}$ final products for acetylene → vinylidene isomerization and $CH^{q_1'} + CH^{q_2'}$ for vinylidene → acetylene isomerization.

These photofragmentation studies have involved an assortment of excitation sources. Extreme ultraviolet (XUV) and X-ray sources have been fruitfully employed to study C_2H_2 isomerization through dissociative ionization.[22−34] Following early suggestions and demonstrations of the potential utility of intense, ultrafast laser pulses in probing C_2H_2 isomerization dynamics, particularly the relevant time scale(s), a plethora of studies have used these sources.[35−47]

Despite the abundance of studies of C_2H_2 isomerization, it is nevertheless an intriguing and important topic to explore further, as much remains unknown. For instance, in addition to the ongoing debate about topics like the lifetime of the neutral vinylidene,[12,13,48−51] open questions about the ions of C_2H_2 are even greater in number.[52]

In this Letter, we utilize our unique capability to prepare $C_2H_2^q$ ion beams in a variety of initial configurations to investigate the role these configurations play in ultrafast laser-induced isomerization and dissociation. To do so, we examine target configurations ranging from vinylidene to acetylene, including *cis/trans* configurations. These would not be easily accessible as neutral gas phase targets.

In our experiment, $C_2H_2{}^q$ ions are produced via fast electron impact in an ion source. Specifically, an electron cyclotron resonance (ECR) ion source is used to create the $C_2H_2{}^+$ beams, while the $C_2H_2{}^-$ beam is generated in a duoplasmatron source. The ions are accelerated to an energy of ~8 keV, and the ion beam of interest is selected with a magnet according to its momentum-to-charge ratio. At the laser interaction region, the ion beam has a cross section of ~0.9 mm × ~0.9 mm. The typical current varies widely depending on the specific ion beam over the range of 25 pA to 1 nA.

The Ti:sapphire laser used in this study[53] produces 790 nm central wavelength, 2 mJ, linearly polarized pulses with a duration of ~23 fs fwhm (full width at half-maximum in intensity) at a rate of 10 kHz. The pulse duration is measured with second-harmonic generation frequency-resolved optical gating (SHG FROG).[54] The laser beam is focused onto the ion beam target by an f = 203 mm, 90° off-axis parabolic mirror. Typical intensities utilized in our experiment fall in the range of 10^{13}–10^{15} W/cm^2. The peak intensity is determined from the measured power, pulse duration, and focal profile image.[55] The intensity is controlled by translating the position of the laser focus relative to the ion beam center as well as by attenuating the laser power.[55,56]

Our setup is schematically illustrated in Figure 1. Signals from a microchannel plate delay-line detector provide arrival
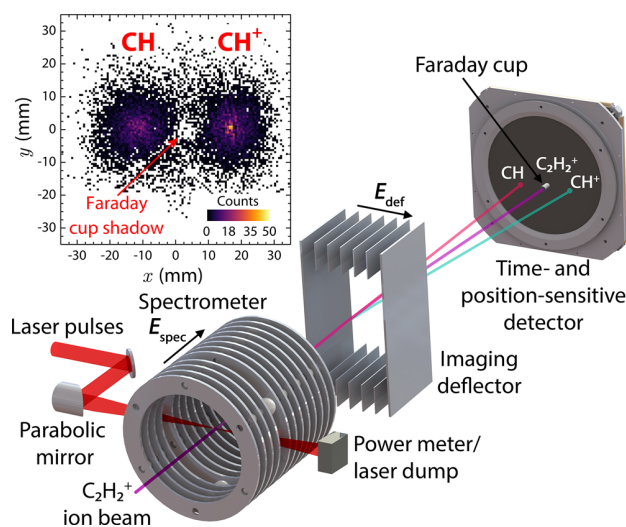

Figure 1. Schematic of our coincidence three-dimensional momentum imaging setup showing the $C_2H_2{}^+ \rightarrow CH^+ + CH$ breakup channel. Intense, femtosecond laser pulses interact with the ion beam inside a spectrometer that provides a longitudinal field, E_{spec}, to separate fragments in time. An imaging deflector supplies a transverse field, E_{def}, which separates the fragments in position. The inset shows a sample position spectrum.

time and position information and hence enable calculation of the velocity for each fragment on an event-by-event basis. Each fragmentation channel appears as a diagonal stripe in the coincidence time-of-flight (CTOF) spectrum due to momentum conservation, like those shown in Figure 2a. The typical event rate depends strongly upon the particular ion beam, with event rates for our measurements being at most on the order of 0.1 Hz (for $C_2H_2{}^+$ from C_2H_2) to 0.001 Hz (for $C_2H_2{}^+$ from $C_2H_2F_2$). Further details regarding our experimental technique can be found in our previous publications.[57,58]

Momentum conservation allows the discernment of true events from background signals and random coincidences. Random coincidences originate from the interaction of a single laser pulse with multiple molecules, whereby a fragment from one molecule is accidentally paired with another from a different molecule.[57,59−62] To eliminate these events, we pair fragments from different laser shots to generate a spectrum mimicking the random coincidences, scale this generated spectrum to a purely random feature like those marked in Figure 2a, and then subtract it from the measured data.

Recall that in fragmentation studies, a commonly used signature of molecules being in the acetylene configuration is measurement of the $CH^{q_1} + CH^{q_2}$ channel, which we denote as A. Similarly, a signature of molecules in the vinylidene configuration is measurement of the $C^{q_1{}'} + CH_2{}^{q_2{}'}$ channel, which we denote as V. We adopt this notation from this point forward.

For the case of $C_2H_2{}^+$ ions being produced from C_2H_2, these ions predominantly exist in the same configuration as the parent C_2H_2, HCCH. This assertion is based on electron impact ionization studies.[63−66] The results for this target are similar to those of the aforementioned photofragmentation studies starting from a neutral C_2H_2 target.[22−47] Like those studies, we observe both acetylene-like and vinylidene-like two-body breakup channels, visible in the CTOF spectrum in Figure 2a.

Given our ability to measure neutral fragments directly, we focus on the two-body dissociation channels, $CH^+ + CH$ (A), $C^+ + CH_2$ (V_1), and $C + CH_2{}^+$ (V_2), i.e., those with no ionization of the target, and compute their branching ratios after imposing momentum conservation. Note that the presence of two V channels is merely a consequence of the fact that either the C or the CH_2 fragment is positively charged. The CTOF spectrum for these channels after analysis is shown in Figure 2c. The branching ratios are summarized in Table 1, where the sum of the vinylidene-like channel yields, $V_1 + V_2$, is denoted as V. These results suggest a substantial amount of isomerization of the initially acetylene (linear HCCH configuration) target, as the $V/(A + V)$ branching ratio is ~60%.

While the $C_2H_2{}^+$ target produced from C_2H_2 likely has a linear HCCH geometry, the $C_2H_2{}^-$ target possesses the other isomeric configuration of C_2H_2, vinylidene. This beam is produced by electron attachment in a duoplasmatron ion source loaded with a mixture of 10% ethylene and 90% argon. $C_2H_2{}^-$ is known to be long-lived in its electronic ground state, $\tilde{X}$ $^2B_2$. It remains in the vinylidene configuration for >100 s,[12,67,68] decaying by adiabatic electron loss and subsequent isomerization of the resulting neutral vinylidene to acetylene.[69] The linear HCCH$^-$ isomer, on the other hand, has a large negative electron affinity (EA) of −2.6 eV, and it autodetaches within a few femtoseconds.[69−71] Because the ion beam travel time from the ion source to the laser interaction region in our setup is approximately 20 μs, the $C_2H_2{}^-$ target survives purely in the vinylidene configuration.

In stark contrast to the $C_2H_2{}^+$ results, we find that the laser-induced fragmentation of $C_2H_2{}^-$ is conspicuously reminiscent of the initial target configuration. Predominantly vinylidene-like breakup is observed for all $C_2H_2{}^{q+}$ daughter ions, as evident from the CTOF spectrum in Figure 2b. Figure 2d contains the CTOF spectrum of events fulfilling momentum conservation for two-body dissociation of the $C_2H_2{}^+$ daughter
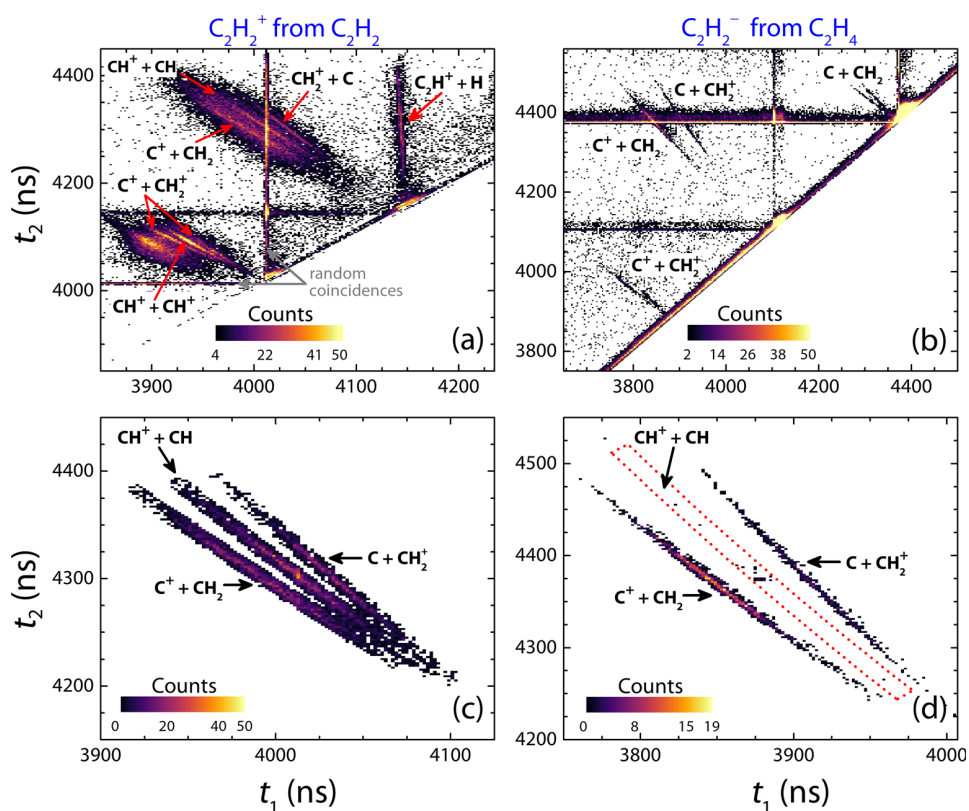
Figure 2. Coincidence time-of-flight (CTOF) spectra for fragmentation of $C_2H_2^+$ generated from C_2H_2 (left) and $C_2H_2^-$ (right). (a and b) Raw data. (c and d) Fragmentation channels of $C_2H_2^+$ after momentum conservation. The dashed red box in panel d indicates the expected position of the CH$^+$ + CH channel, i.e., the channel associated with the HCCH final configuration. Gray arrows in panel a mark examples of random coincidence features (see the text). Note that there are other channels not discussed here that will be covered in a future publication(s). For instance, the rate of CH$^+$ + CH$^+$ in panel a is ~0.2 Hz.

Table 1. Branching Ratios for Different Initial $C_2H_2^q$ Configurations ($q = -1$, 0, or 1) Exposed to Laser Pulses with an Intensity of ~3 × 10^{15} W/cm^2 [a]

target	source gas	current (nA)	initial configuration	A	A/(A + V) (%)
$C_2H_2^+$	C_2H_2	1.0	HCCH	CH$^+$ + CH	37.6 ± 3.8
$C_2H_2^+$	$C_2H_2F_2$	0.025	H$_2$CC	CH$^+$ + CH	13.9 ± 2.4
$C_2H_2^+$	$C_2H_2Br_2$	0.1	*cis/trans*	CH$^+$ + CH	1.7 ± 0.3
$C_2H_2^-$	C_2H_4	0.2	H$_2$CC	CH$^+$ + CH	0.1 ± 0.5
$C_2H_2^-$	C_2H_4	0.2	H$_2$CC	CH + CH	3.9 ± 2.5
$C_2H_2^{-}$[b]	C_2H_4	0.2	H$_2$CC	CH$^+$ + CH	0.1 ± 0.1
$C_2H_2^{-}$[b]	C_2H_4	0.2	H$_2$CC	CH + CH	3.6 ± 1.2

[a]The labels A and V refer to the CH^{q_1} + CH^{q_2} and C$^{q_1'}$ + CH$_2^{q_2'}$ channels, respectively (note $q_1 + q_2 = q_1' + q_2'$ for each case). Also, in some cases, V includes two channels, as either the C or the CH$_2$ fragment can be positively charged. [b]The neutral target is produced from the $C_2H_2^-$ beam by a pump pulse 300 fs before interaction with the probe pulse (see the text).

of $C_2H_2^-$, specifically the CH$^+$ + CH (A), C$^+$ + CH$_2$ (V_1), and C + CH$_2^+$ (V_2) channels. The acetylene branching ratio for this process, displayed in Table 1, is consistent with zero. Moreover, this trend of negligible acetylene-like breakup persists for the range of peak laser intensities studied (5 × 10^{14} to 3 × 10^{15} W/cm^2).

The contrast between the $C_2H_2^+$ and $C_2H_2^-$ outcomes discussed so far is surprising. These observations suggest that while $C_2H_2^+$ generated from C_2H_2, an HCCH target, isomerizes efficiently, the reverse process does not occur for $C_2H_2^-$, a target of the H$_2$CC initial configuration. More precisely, isomerization of the vinylidene target leading to dissociation is not observed. One should note that this does not preclude the possibility of isomerization of molecules that

remain bound. Also, while it is likely that the contrasting $C_2H_2^+$ and $C_2H_2^-$ results are due to very different excitation pathways, it is not easy to resolve the participating electronic states in the present strong field study, as many electronic states could be populated. For isolating dissociation pathways, further work employing single-photon excitation of these systems[32,72,73] could be informative.

Some theoretical studies have suggested that neutral vinylidene that results from $C_2H_2^- \rightarrow C_2H_2 + e^-$ photo-detachment not only isomerizes to acetylene but then undergoes multiple acetylene ↔ vinylidene recrossings.[50,74] This process happens due to the fact that acetylene is highly excited after crossing the vinylidene → acetylene barrier. The period of these recrossings is calculated to be on the order of
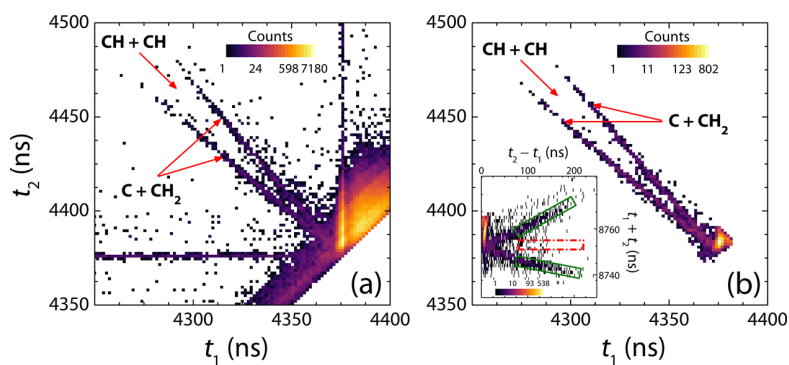
Figure 3. CTOF spectra for fragmentation of $C_2H_2^-$ by a two-pulse scheme zoomed in on the neutral−neutral fragmentation channels. (a) Raw data. (b) After imposing momentum conservation. The inset shows a rotated spectrum. The dashed red and solid green boxes indicate where yields of CH + CH and C + CH_2 were evaluated, respectively.
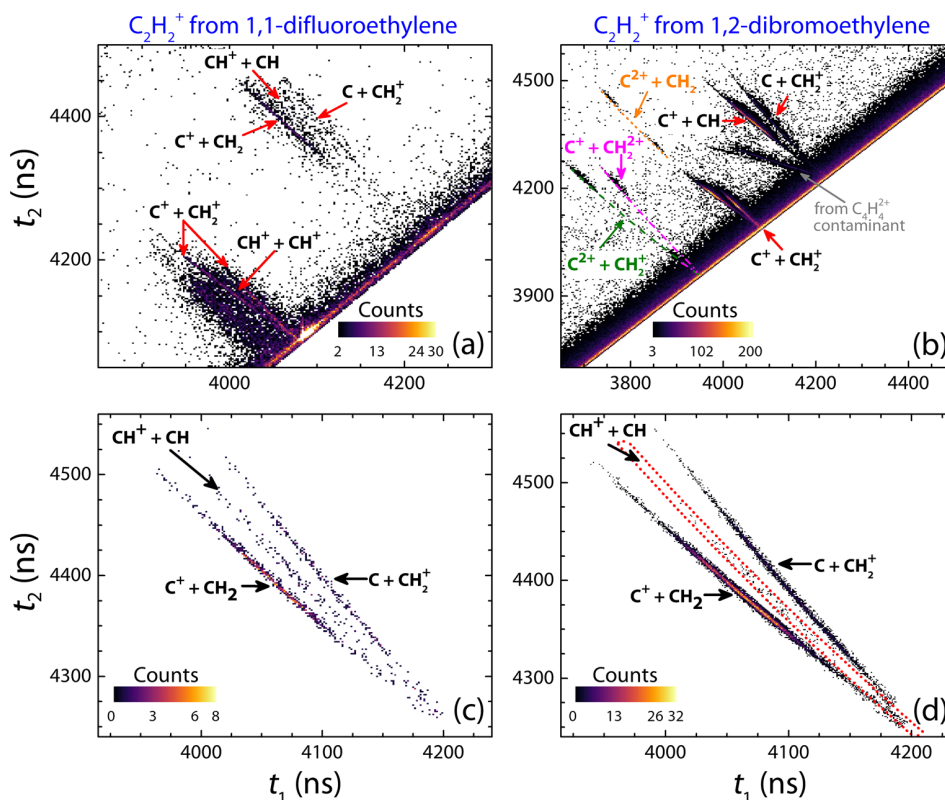

Figure 4. CTOF spectra for laser-induced fragmentation of $C_2H_2^+$ generated from 1,1-difluoroethylene (left) and 1,2-dibromoethylene (right). (a and b) Raw data. (c and d) The three fragmentation channels of $C_2H_2^+$ after momentum conservation. The dashed red box in panel d highlights the expected position of the CH^+ + CH channel.

100 fs, but the exact period depends heavily upon the initial conditions.[50]

In light of this idea, we performed a two-pulse measurement, where the first pulse causes photodetachment and possibly initiates isomerization and the second pulse probes any ensuing recrossing dynamics. The pump pulse that removes the weakly bound electron of $C_2H_2^-$ (EA = 0.49 eV[12]) has a peak intensity of 2×10^{14} W/cm^2 and efficiently neutralizes the $C_2H_2^-$ molecules within the laser focus, according to our estimates. To arrive at this conclusion, we use our estimated ion beam density, $\sim 6 \times 10^3$ molecules/cm^3 (i.e., ~ 0.03 molecule/pulse), and the measured rate of neutral C_2H_2 molecules (~ 285 Hz) for a single 5×10^{14} W/cm^2 pulse,

which results in negligible fragmentation. The probe pulse is delayed by 300 fs with respect to the pump pulse, close to the typical recrossing period, and has a much higher peak intensity of 2×10^{15} W/cm^2.

Here too, the vinylidene-like breakup channel, C + CH_2, heavily dominates, as clearly shown in Figure 3. In contrast, the acetylene-like fragmentation channel, CH + CH, is hardly visible. Careful analysis including momentum conservation and random coincidence subtraction sets an upper bound for the acetylene branching ratio at 3.6 ± 1.2%. This result is consistent with that of a single pulse similar to the probe pulse, for which the acetylene branching ratio is 3.9 ± 2.5%. Moreover, in the pump−probe measurement, the branching

ratio of the acetylene-like fragmentation channel for which two electrons are removed, $CH^+ + CH$, is $0.1 \pm 0.1\%$ (see Table 1), also in accord with the single-pulse results. Theory more closely replicating the initial conditions would aid in guiding future two-pulse experiments sampling recrossing dynamics.

To further explore this strong dependence of isomerization on the initial configuration, we look at another vinylidene-like target, $C_2H_2^+$ generated from 1,1-difluoroethylene. Charge inversion mass spectrometry measurements indicate that a beam of $C_2H_2^+$ produced from 1,1-dichloroethylene is long-lived in the vinylidene configuration, with a lifetime of >8.5 μs.[75,76] Given the chemical similarity between 1,1-dichloroethylene and 1,1-difluoroethylene, it is most likely that a $C_2H_2^+$ beam generated from the latter is also of the vinylidene configuration. Panels a and c of Figure 4 contain the measured CTOF spectra for this target. One can see that both vinylidene-like and acetylene-like breakup occurs, with a vast majority of vinylidene-like breakup.

While a beam of $C_2H_2^+$ generated from 1,1-difluoroethylene has the vinylidene configuration like $C_2H_2^-$, there also are compelling reasons to examine the former target. Here, we observe dissociation and thus can avoid any complication ionization might add. In contrast, in the $C_2H_2^-$ case, it is possible that fragmentation of $C_2H_2^+$ daughter ions involves sequential ionization. For example, the weakly bound electron could be removed early in the laser pulse, followed by propagation on the C_2H_2 surface(s) and eventual removal of the second electron. This process is clearly different from dissociation of a $C_2H_2^+$ target initially in the vinylidene configuration, such as that produced from 1,1-difluoroethylene.

As a final example, we generate a *cis/trans* $C_2H_2^+$ beam from 1,2-dibromoethylene. The dibromoethylene sample is composed of a mixture of the *cis* and *trans* isomers with a *cis:trans* ratio of approximately 1:3. This sample and information regarding its *trans:cis* isomer ratio were obtained from Sigma-Aldrich. Intuitively, removal of the bromine atoms will result in $C_2H_2^+$ far from equilibrium, with excitation likely in the symmetric (*trans*) and antisymmetric (*cis*) C−C−H bending vibrational modes.[77] What impact will this excitation have on the branching ratio between acetylene-like and vinylidene-like channels?

The CTOF spectra in panels b and d of Figure 4 and the branching ratio in Table 1 show that, similar to the $C_2H_2^-$ results, the predominant breakup is vinylidene-like. This behavior continues over the range of intensities explored (5 $\times$ 10^{13} to 3 $\times$ 10^{15} W/cm^2). For this *cis/trans* target, it should be noted that it is unclear if the initial bending excitation of the ion beam facilitates unimolecular HCCH → H$_2$CC isomerization in flight to the laser interaction or if the isomerization is laser-induced. While in assessing the geometry of this target we have assumed a logic similar to that applied for the H_2CC^+ beam produced from 1,1-difluoroethylene,[75,76] a future study of the lifetimes of *cis/trans* beams would shed further light on this issue. The key point, however, is that isomerization to vinylidene is much more likely in the *cis/trans* case than in the case of $C_2H_2^+$ produced from C_2H_2. Furthermore, the branching ratios measured with the *cis/trans* target are significantly different from those measured with the other targets.

The *cis/trans* $C_2H_2^+$ measurement suggests that the initial bending excitation of the ions enhances isomerization toward the vinylidene configuration. This observation is in agreement with previous work highlighting the influence of bending motion on the isomerization process, both for acetylene becoming vinylidene and vice versa. The previously mentioned DF and SEP spectroscopy measurements[17−21] exploit a high degree of vibrational excitation to examine the coupling of acetylene and vinylidene states resulting in isomerization of HCCH. In these spectroscopic measurements, the minimum energy path for hydrogen migration falls along the C−C−H bending coordinate. Several theoretical studies have also emphasized that bending excitation in acetylene molecules has a decisive impact on the isomerization dynamics.[50,78−81] Moreover, photoelectron spectroscopy experiments on the vinylidene anion $C_2H_2^-$ by the Neumark group and collaborators have shown that excitation of the in-plane rocking mode of vinylidene readily leads to isomerization, as this state connects to the C−C−H bending vibrational states of acetylene.[16]

In summary, our measurements of the laser-induced fragmentation of $C_2H_2^q$ ion beams with assorted unique configurations demonstrate the strong effect of the initial configuration on the isomerization dynamics. While $C_2H_2^+$ generated from C_2H_2, a linear HCCH molecule, exhibits acetylene-like and vinylidene-like fragmentation at similar levels, the vinylidene and *cis/trans* configuration $C_2H_2^+$ molecules that we examined mainly fragment in a vinylidene-like manner, a markedly different and surprising outcome. These intriguing results, which raise the question of the reversibility of the isomerization process, call for future theoretical endeavors to explain them. Measurements of *cis/trans* targets appear to be congruent with experimental and theoretical work pinpointing the pivotal influence of bending excitation in isomerization, but similarly, further work is needed for a detailed understanding and to disentangle the possible unimolecular and laser-driven dynamics.

Finally, we anticipate that our approach for studying $C_2H_2^q$ ($q = -1$, 0, or 1) isomerization is not limited to this particular problem. Rather, ion beam targets offer an avenue for examining photoinduced dynamics in a variety of chemical systems in initial configurations that are not easily accessible, a unique vantage point that is complementary to mainstream approaches for studying molecular dynamics.

■ AUTHOR INFORMATION

Corresponding Authors
*E-mail: bjochim@phys.ksu.edu.
*E-mail: ibi@phys.ksu.edu.

ORCID ⊙
Bethany Jochim: 0000-0003-2040-1453
E. Wells: 0000-0002-1044-4479

Notes
The authors declare no competing financial interest.

■ REFERENCES

(1) Wald, G. Molecular Basis of Visual Excitation. *Science* **1968**, *162*, 230−239.

(2) Gai, F.; Hasson, K. C.; McDonald, J. C.; Anfinrud, P. A. Chemical Dynamics in Proteins: The Photoisomerization of Retinal in Bacteriorhodopsin. *Science* **1998**, *279*, 1886−1891.

(3) Polli, D.; Altoè, P.; Weingart, O.; Spillane, K. M.; Manzoni, C.; Brida, D.; Tomasello, G.; Orlandi, G.; Kukura, P.; Mathies, R. A.; et al. Conical intersection dynamics of the primary photoisomerization event in vision. *Nature* **2010**, *467*, 440.

(4) Allmann, S.; Baldwin, I. T. Insects Betray Themselves in Nature to Predators by Rapid Isomerization of Green Leaf Volatiles. *Science* **2010**, *329*, 1075−1078.

(5) Perry, S. F. Isomerization. *Ind. Eng. Chem.* **1952**, *44*, 2037−2039.

(6) Durán, R. P.; Amorebieta, V. T.; Colussi, A. J. Pyrolysis of acetylene: a thermal source of vinylidene. *J. Am. Chem. Soc.* **1987**, *109*, 3154−3155.

(7) Valavarasu, G.; Sairam, B. Light Naphtha Isomerization Process: A Review. *Pet. Sci. Technol.* **2013**, *31*, 580−595.

(8) Dugave, C.; Demange, L. Cis-trans isomerization of organic molecules and biomolecules: implications and applications. *Chem. Rev.* **2003**, *103*, 2475−2532.

(9) Levine, B. G.; Martínez, T. J. Isomerization through conical intersections. *Annu. Rev. Phys. Chem.* **2007**, *58*, 613−634.

(10) Schaefer, H. F. The 1,2 hydrogen shift: a common vehicle for the disappearance of evanescent molecular species. *Acc. Chem. Res.* **1979**, *12*, 288−296.

(11) Burnett, S. M.; Stevens, A. E.; Feigerle, C. S.; Lineberger, W. C. Observation of X $^1A_1$ vinylidene by photoelectron spectroscopy of the $C_2H_2^-$ ion. *Chem. Phys. Lett.* **1983**, *100*, 124−128.

(12) Ervin, K. M.; Ho, J.; Lineberger, W. C. A study of the singlet and triplet states of vinylidene by photoelectron spectroscopy of $H_2C = C^-$, $D_2C = C^-$, and $HDC = C^-$. vinylidene−acetylene isomerization. *J. Chem. Phys.* **1989**, *91*, 5974−5992.

(13) Levin, J.; Feldman, H.; Baer, A.; Ben-Hamu, D.; Heber, O.; Zajfman, D.; Vager, Z. Study of unimolecular reactions by Coulomb explosion imaging: the nondecaying vinylidene. *Phys. Rev. Lett.* **1998**, *81*, 3347−3350.

(14) Gerardi, H. K.; Breen, K. J.; Guasco, T. L.; Weddle, G. H.; Gardenier, G. H.; Laaser, J. E.; Johnson, M. A. Survey of Ar-tagged predissociation and vibrationally mediated photodetachment spectroscopies of the vinylidene anion, $C_2H_2^-$. *J. Phys. Chem. A* **2010**, *114*, 1592−1601.

(15) DeVine, J. A.; Weichman, M. L.; Zhou, X.; Ma, J.; Jiang, B.; Guo, H.; Neumark, D. M. Non-adiabatic effects on excited states of vinylidene observed with slow photoelectron velocity-map imaging. *J. Am. Chem. Soc.* **2016**, *138*, 16417−16425.

(16) DeVine, J. A.; Weichman, M. L.; Laws, B.; Chang, J.; Babin, M. C.; Balerdi, G.; Xie, C.; Malbon, C. L.; Lineberger, W. C.; Yarkony, D. R.; et al. Encoding of vinylidene isomerization in its anion photoelectron spectrum. *Science* **2017**, *358*, 336−339.

(17) Abramson, E.; Field, R. W.; Imre, D.; Innes, K. K.; Kinsey, J. L. Fluorescence and stimulated emission $S_1 \rightarrow S_0$ spectra of acetylene: regular and ergodic regions. *J. Chem. Phys.* **1985**, *83*, 453−465.

(18) Chen, Y.; Jonas, D. M.; Kinsey, J. L.; Field, R. W. High resolution spectroscopic detection of acetylene−vinylidene isomerization by spectral cross correlation. *J. Chem. Phys.* **1989**, *91*, 3976−3987.

(19) Yamanouchi, K.; Ikeda, N.; Tsuchiya, S.; Jonas, D. M.; Lundberg, J. K.; Adamson, G. W.; Field, R. W. Vibrationally highly excited acetylene as studied by dispersed fluorescence and stimulated emission pumping spectroscopy: vibrational assignment of the feature states. *J. Chem. Phys.* **1991**, *95*, 6330−6342.

(20) Jacobson, M. P.; Silbey, R. J.; Field, R. W. Local mode behavior in the acetylene bending system. *J. Chem. Phys.* **1999**, *110*, 845−859.

(21) Jacobson, M. P.; Field, R. W. Acetylene at the threshold of isomerization. *J. Phys. Chem. A* **2000**, *104*, 3073−3086.

(22) Eland, J. H. D.; Wort, F. S.; Lablanquie, P.; Nenner, I. Mass spectrometric and coincidence studies of double photoionization of small molecules. *Z. Phys. D: At., Mol. Clusters* **1986**, *4*, 31−42.

(23) Eland, J. H. D.; Price, S. D.; Cheney, J. C.; Lablanquie, P.; Nenner, I.; Fournier, P. G. Towards a spectroscopy of doubly charged ions. *Philos. Trans. R. Soc., A* **1988**, *324*, 247−255.

(24) Cooper, G.; Ibuki, T.; Iida, Y.; Brion, C. Absolute dipole oscillator strengths for photoabsorption and the molecular and dissociative photoionization of acetylene. *Chem. Phys.* **1988**, *125*, 307−320.

(25) Thissen, R.; Delwiche, J.; Robbe, J. M.; Duflot, D.; Flament, J. P.; Eland, J. H. D. Dissociations of the ethyne dication $C_2H_2^{2+}$. *J. Chem. Phys.* **1993**, *99*, 6590−6599.

(26) Osipov, T.; Cocke, C. L.; Prior, M. H.; Landers, A.; Weber, T.; Jagutzki, O.; Schmidt, L.; Schmidt-Böcking, H.; Dörner, R. Photoelectron-photoion momentum spectroscopy as a clock for chemical rearrangements: isomerization of the di-cation of acetylene to the vinylidene configuration. *Phys. Rev. Lett.* **2003**, *90*, 233002.

(27) Flammini, R.; Fainelli, E.; Maracci, F.; Avaldi, L. Vinylidene dissociation following the Auger-electron decay of inner-shell ionized acetylene. *Phys. Rev. A: At., Mol., Opt. Phys.* **2008**, *77*, 044701.

(28) Osipov, T.; Rescigno, T. N.; Weber, T.; Miyabe, S.; Jahnke, T.; Alnaser, A. S.; Hertlein, M. P.; Jagutzki, O.; Schmidt, L. P. H.; Schöffler, M.; et al. Fragmentation pathways for selected electronic states of the acetylene dication. *J. Phys. B: At., Mol. Opt. Phys.* **2008**, *41*, 091001.

(29) Jiang, Y. H.; Rudenko, A.; Herrwerth, O.; Foucar, L.; Kurka, M.; Kühnel, K. U.; Lezius, M.; Kling, M. F.; van Tilborg, J.; Belkacem, A.; et al. Ultrafast extreme ultraviolet induced isomerization of acetylene cations. *Phys. Rev. Lett.* **2010**, *105*, 263002.

(30) Alagia, M.; Callegari, C.; Candori, P.; Falcinelli, S.; Pirani, F.; Richter, R.; Stranges, S.; Vecchiocattivi, F. Angular and energy distribution of fragment ions in dissociative double photoionization of acetylene molecules at 39 eV. *J. Chem. Phys.* **2012**, *136*, 204302.

(31) Jiang, Y. H.; Senftleben, A.; Kurka, M.; Rudenko, A.; Foucar, L.; Herrwerth, O.; Kling, M. F.; Lezius, M.; Tilborg, J. V.; Belkacem, A.; et al. Ultrafast dynamics in acetylene clocked in a femtosecond XUV stopwatch. *J. Phys. B: At., Mol. Opt. Phys.* **2013**, *46*, 164027.

(32) Gaire, B.; Lee, S. Y.; Haxton, D. J.; Pelz, P. M.; Bocharova, I.; Sturm, F. P.; Gehrken, N.; Honig, M.; Pitzer, M.; Metz, D.; et al. Photo-double-ionization of ethylene and acetylene near threshold. *Phys. Rev. A: At., Mol., Opt. Phys.* **2014**, *89*, 013403.

(33) Liekhus-Schmaltz, C. E.; Tenney, I.; Osipov, T.; Sanchez-Gonzalez, A.; Berrah, N.; Boll, R.; Bomme, C.; Bostedt, C.; Bozek, J. D.; Carron, S.; et al. Ultrafast isomerization initiated by X-ray core ionization. *Nat. Commun.* **2015**, *6*, 8199.

(34) Li, Z.; Inhester, L.; Liekhus-Schmaltz, C.; Curchod, B. F. E.; Snyder, J. W.; Medvedev, N.; Cryan, J.; Osipov, T.; Pabst, S.; Vendrell, O.; Bucksbaum, P.; Martinez, T. J. Ultrafast isomerization in acetylene dication after carbon K-shell ionization. *Nat. Commun.* **2017**, *8*, 453.

(35) Hishikawa, A.; Matsuda, A.; Fushitani, M.; Takahashi, E. J. Visualizing recurrently migrating hydrogen in acetylene dication by intense ultrashort laser pulses. *Phys. Rev. Lett.* **2007**, *99*, 258302.

(36) Hishikawa, A.; Matsuda, A.; Takahashi, E. J.; Fushitani, M. Acetylene-vinylidene isomerization in ultrashort intense laser fields studied by triple ion-coincidence momentum imaging. *J. Chem. Phys.* **2008**, *128*, 084302.

(37) Matsuda, A.; Fushitani, M.; Takahashi, E. J.; Hishikawa, A. Visualizing hydrogen atoms migrating in acetylene dication by time-resolved three-body and four-body Coulomb explosion imaging. *Phys. Chem. Chem. Phys.* **2011**, *13*, 8697−8704.

(38) Xie, X.; Doblhoff-Dier, K.; Roither, S.; Schöffler, M. S.; Kartashov, D.; Xu, H.; Rathje, T.; Paulus, G. G.; Baltuška, A.; Gräfe, S.; et al. Attosecond-recollision-controlled selective fragmentation of polyatomic molecules. *Phys. Rev. Lett.* **2012**, *109*, 243001.

(39) Wells, E.; Rallis, C.; Zohrabi, M.; Siemering, R.; Jochim, B.; Andrews, P.; Ablikim, U.; Gaire, B.; De, S.; Carnes, K.; et al. Adaptive strong-field control of chemical dynamics guided by three-dimensional momentum imaging. *Nat. Commun.* **2013**, *4*, 2895.

(40) Ibrahim, H.; Wales, B.; Beaulieu, S.; Schmidt, B. E.; Thiré, N.; Fowe, E. P.; Bisson, E.; Hebeisen, C. T.; Wanie, V.; Giguére, M.; et al. Tabletop imaging of structural evolutions in chemical reactions demonstrated for the acetylene cation. *Nat. Commun.* **2014**, *5*, 4422.

(41) Gong, X.; Song, Q.; Ji, Q.; Pan, H.; Ding, J.; Wu, J.; Zeng, H. Strong-field dissociative double ionization of acetylene. *Phys. Rev. Lett.* **2014**, *112*, 243001.

(42) Xie, X.; Doblhoff-Dier, K.; Xu, H.; Roither, S.; Schöffler, M. S.; Kartashov, D.; Erattupuzha, S.; Rathje, T.; Paulus, G. G.; Yamanouchi, K.; et al. Selective control over fragmentation reactions in polyatomic molecules using impulsive laser alignment. *Phys. Rev. Lett.* **2014**, *112*, 163003.

(43) Gong, X.; Song, Q.; Ji, Q.; Lin, K.; Pan, H.; Ding, J.; Zeng, H.; Wu, J. Channel-Resolved Above-Threshold Double Ionization of Acetylene. *Phys. Rev. Lett.* **2015**, *114*, 163001.

(44) Kübel, M.; Siemering, R.; Burger, C.; Kling, N. G.; Li, H.; Alnaser, A. S.; Bergues, B.; Zherebtsov, S.; Azzeer, A. M.; Ben-Itzhak, I.; et al. Steering Proton Migration in Hydrocarbons Using Intense Few-Cycle Laser Fields. *Phys. Rev. Lett.* **2016**, *116*, 193001.

(45) Burger, C.; Kling, N. G.; Siemering, R.; Alnaser, A. S.; Bergues, B.; Azzeer, A. M.; Moshammer, R.; de Vivie-Riedle, R.; Kübel, M.; Kling, M. F. Visualization of bond rearrangements in acetylene using near single-cycle laser pulses. *Faraday Discuss.* **2016**, *194*, 495–508.

(46) Kübel, M.; Burger, C.; Siemering, R.; Kling, N. G.; Bergues, B.; Alnaser, A. S.; Ben-Itzhak, I.; Moshammer, R.; de Vivie-Riedle, R.; Kling, M. F. Phase- and intensity-dependence of ultrafast dynamics in hydrocarbon molecules in few-cycle laser fields. *Mol. Phys.* **2017**, *115*, 1835–1845.

(47) Burger, C.; Atia-Tul-Noor, A.; Schnappinger, T.; Xu, H.; Rosenberger, P.; Haram, N.; Beaulieu, S.; Légaré, F.; Alnaser, A. S.; Moshammer, R.; et al. Time-resolved nuclear dynamics in bound and dissociating acetylene. *Struct. Dyn.* **2018**, *5*, 044302.

(48) Carrington, T.; Hubbard, L. M.; Schaefer, H. F.; Miller, W. H. Vinylidene: Potential energy surface and unimolecular reaction dynamics. *J. Chem. Phys.* **1984**, *80*, 4347–4354.

(49) Germann, T. C.; Miller, W. H. Quantum mechanical calculation of resonance tunneling in acetylene isomerization via the vinylidene intermediate. *J. Chem. Phys.* **1998**, *109*, 94–101.

(50) Hayes, R. L.; Fattal, E.; Govind, N.; Carter, E. A. Long live vinylidene! a new view of the $H_2=CC: \rightarrow HC\!:\!CH$ rearrangement from ab initio molecular dynamics. *J. Am. Chem. Soc.* **2001**, *123*, 641–657.

(51) Guo, L.; Han, H.; Ma, J.; Guo, H. Quantum dynamics of vinylidene photodetachment on an accurate global acetylene-vinylidene potential energy surface. *J. Phys. Chem. A* **2015**, *119*, 8488–8496.

(52) Boyé-Péronne, S.; Gauyacq, D.; Liévin, J. Vinylidene-acetylene cation isomerization investigated by large scale ab initio calculations. *J. Chem. Phys.* **2006**, *124*, 214305.

(53) Ren, X.; Summers, A. M.; P., Kanaka Raju; Vajdi, A.; Makhija, V.; Fehrenbach, C. W.; Kling, N. G.; Betsch, K. J.; Wang, Z.; Kling, M. F.; Carnes, K. D.; Ben-Itzhak, I.; Trallero-Herrero, C.; Kumarappan, V. Single-shot carrier-envelope-phase tagging using an *f*–2*f* interferometer and a phase meter: a comparison. *J. Opt.* **2017**, *19*, 124017.

(54) Trebino, R.; DeLong, K. W.; Fittinghoff, D. N.; Sweetser, J. N.; Krumbügel, M. A.; Richman, B. A.; Kane, D. J. Measuring ultrashort laser pulses in the time-frequency domain using frequency-resolved optical gating. *Rev. Sci. Instrum.* **1997**, *68*, 3277–3295.

(55) Sayler, A. M.; Wang, P. Q.; Carnes, K. D.; Ben-Itzhak, I. Determining intensity dependence of ultrashort laser processes through focus *z*-scanning intensity-difference spectra: application to laser-induced dissociation of H_2^+. *J. Phys. B: At., Mol. Opt. Phys.* **2007**, *40*, 4367.

(56) Wang, P.; Sayler, A. M.; Carnes, K. D.; Esry, B. D.; Ben-Itzhak, I. Disentangling the volume effect through intensity-difference

spectra: application to laser-induced dissociation of H_2^+. *Opt. Lett.* **2005**, *30*, 664–666.

(57) Ben-Itzhak, I.; Sayler, A. M.; Leonard, M.; Maseberg, J.; Hathiramani, D.; Wells, E.; Smith, M.; Xia, J.; Wang, P.; Carnes, K.; et al. Bond rearrangement caused by sudden single and multiple ionization of water molecules. *Nucl. Instrum. Methods Phys. Res., Sect. B* **2005**, *233*, 284–292.

(58) Wang, P. Q.; Sayler, A. M.; Carnes, K. D.; Xia, J. F.; Smith, M. A.; Esry, B. D.; Ben-Itzhak, I. Dissociation of H_2^+ in intense femtosecond laser fields studied by coincidence three-dimensional momentum imaging. *Phys. Rev. A: At., Mol., Opt. Phys.* **2006**, *74*, 043411.

(59) Bay, Z.; Slawsky, M. M. General Relation between Genuine and Chance Coincidences and Its Application to Measurement of High Activity Sources. *Phys. Rev.* **1950**, *77*, 414–415.

(60) Eland, J. H. D. Photoelectron-photoion coincidence spectroscopy: I. Basic principles and theory. *Int. J. Mass Spectrom. Ion Phys.* **1972**, *8*, 143–151.

(61) Knoll, G. F. *Radiation Detection and Measurement*, 3rd ed.; John Wiley & Sons, 2000.

(62) Henrichs, K.; Waitz, M.; Trinter, F.; Kim, H.; Menssen, A.; Gassert, H.; Sann, H.; Jahnke, T.; Wu, J.; Pitzer, M.; et al. Observation of electron energy discretization in strong field double ionization. *Phys. Rev. Lett.* **2013**, *111*, 113003.

(63) Zheng, S.-H.; Srivastava, S. K. Electron-impact ionization and dissociative ionization of acetylene. *J. Phys. B: At., Mol. Opt. Phys.* **1996**, *29*, 3235.

(64) Josifov, G.; Lukic, D.; Djuric, N.; Kurepa, M. Total, direct and dissociative electron impact ionization cross sections of the acetylene molecule. *J. Serb. Chem. Soc.* **2000**, *65*, 517–527.

(65) Feil, S.; Głuch, K.; Bacher, A.; Matt-Leubner, S.; Böhme, D. K.; Scheier, P.; Märk, T. D. Cross sections and ion kinetic energy analysis for the electron impact ionization of acetylene. *J. Chem. Phys.* **2006**, *124*, 214307.

(66) Feil, S.; Sulzer, P.; Mauracher, A.; Beikircher, M.; Wendt, N.; Aleem, A.; Denifl, S.; Zappa, F.; Matt-Leubner, S.; Bacher, A.; et al. Electron Impact Ionization/Dissociation of Molecules: Production of Energetic Radical Ions and Anions. *Journal of Physics: Conference Series* **2007**, *86*, 012003.

(67) Jensen, M. J.; Pedersen, U. V.; Andersen, L. H. Stability of the ground state vinylidene anion H_2CC^-. *Phys. Rev. Lett.* **2000**, *84*, 1128–1131.

(68) Goode, G. C.; Jennings, K. R. Reactions of O^- Ions with Some Unsaturated Hydrocarbons. *Adv. Mass Spectrom.* **1974**, *6*, n/a.

(69) Chandrasekhar, J.; Kahn, R. A.; von Ragué Schleyer, P. The preferred structure of $C_2H_2^-$. *Chem. Phys. Lett.* **1982**, *85*, 493–495.

(70) Frenking, G. The neutral and ionic vinylidene–acetylene rearrangement. *Chem. Phys. Lett.* **1983**, *100*, 484–487.

(71) Falcetta, M. F.; DiFalco, L. A.; Ackerman, D. S.; Barlow, J. C.; Jordan, K. D. Assessment of various electronic structure methods for characterizing temporary anion states: application to the ground state anions of N_2, C_2H_2, C_2H_4, and C_6H_6. *J. Phys. Chem. A* **2014**, *118*, 7489–7497.

(72) Cosby, P. C.; Möller, R.; Helm, H. Photofragment spectroscopy of N_2^{2+}. *Phys. Rev. A: At., Mol., Opt. Phys.* **1983**, *28*, 766–772.

(73) Pedersen, H. B.; Altevogt, S.; Jordon-Thaden, B.; Heber, O.; Rappaport, M. L.; Schwalm, D.; Ullrich, J.; Zajfman, D.; Treusch, R.; Guerassimova, N.; et al. Crossed Beam Photodissociation Imaging of HeH^+ with Vacuum Ultraviolet Free-Electron Laser Pulses. *Phys. Rev. Lett.* **2007**, *98*, 223202.

(74) Schork, R.; Köppel, H. Barrier recrossing in the vinylidene–acetylene isomerization reaction: A five-dimensional ab initio quantum dynamical investigation. *J. Chem. Phys.* **2001**, *115*, 7907–7923.

(75) Hayakawa, S.; Takahashi, M.; Arakawa, K.; Morishita, N. Definitive evidence for the existence of a long-lived vinylidene radical cation, $H_2C = C^+$. *J. Chem. Phys.* **1999**, *110*, 2745–2748.

(76) Hayakawa, S. Charge inversion mass spectrometry: dissociation of resonantly neutralized molecules. *J. Mass Spectrom.* **2004**, *39*, 111−135.

(77) Steinfeld, J. I. *Molecules and Radiation: An Introduction to Modern Molecular Spectroscopy*; Dover Publications, 2005.

(78) McCoy, A. B.; Sibert, E. L. The bending dynamics of acetylene. *J. Chem. Phys.* **1996**, *105*, 459−468.

(79) Sibert, E. L.; McCoy, A. B. Quantum, semiclassical and classical dynamics of the bending modes of acetylene. *J. Chem. Phys.* **1996**, *105*, 469−478.

(80) Ma, J.; Xu, D.; Guo, H.; Tyng, V.; Kellman, M. E. Isotope effect in normal-to-local transition of acetylene bending modes. *J. Chem. Phys.* **2012**, *136*, 014304.

(81) Han, H.; Li, A.; Guo, H. Toward spectroscopically accurate global ab initio potential energy surface for the acetylene-vinylidene isomerization. *J. Chem. Phys.* **2014**, *141*, 244312.

3.4 Experimental study of laser-induced isomerization dynamics of specific $C_2H_2^q$ ions

Studies of intense laser-induced isomerization of C_2H_2 often employ gas-phase targets and therefore concentrate on dissociative ionization. The following manuscript, which has been submitted to *Physical Review A*, highlights the advantages of studying isomerization of $C_2H_2^q$ ion beam targets using coincidence 3D momentum imaging. As a major strength of this approach is measurement of dissociation, we are able to study isomerization dynamics occurring within a single charge state. Moreover, studying ion beam targets allows us to operate at laser intensities far below that required for ionization, opening the possibility of examining one- or few-photon processes. Given these simplifications, more direct theory–experiment comparisons may be made, offering an alternative approach for understanding of strong-field isomerization processes.

Experimental study of laser-induced isomerization dynamics of specific $C_2H_2^q$ ions

Bethany Jochim,[1] M. Zohrabi,[1] T. Severt,[1] Ben Berry,[1] K. J. Betsch,[1]
Peyman Feizollah,[1] J. Rajput,[1] E. Wells,[2] K. D. Carnes,[1] and I. Ben-Itzhak[1]

[1]*J. R. Macdonald Laboratory, Department of Physics,*
Kansas State University, Manhattan, Kansas 66506 USA
[2]*Department of Physics, Augustana University, Sioux Falls, South Dakota 57197 USA*
(Dated: October 31, 2019)

We investigate intense, ultrafast laser-induced isomerization and two-body fragmentation of acetylene monocations and dications using coincidence three-dimensional momentum imaging. Whereas the vast majority of previous work on strong-field isomerization and fragmentation of acetylene has necessarily involved ionization, by focusing solely on dissociation of ion-beam targets, we ensure that the dynamics ensue within a single molecular ion species, potentially simplifying interpretation. We demonstrate the rich information that can be extracted from such a measurement and discuss advantages and disadvantages of this approach.

I. INTRODUCTION

Measuring the photo-induced breakup of hydrocarbons has been demonstrated as a valuable means of examining isomerization reactions, specifically hydrogen migration. Numerous light sources have been used for these studies [1], which are most commonly performed by irradiating neutral target molecules to initiate dynamics.

One specific molecule that has attracted a great deal of interest as a prototype for studying isomerization is acetylene, which has the linear HCCH configuration in its ground state. Isomerization of this molecule entails migration of a hydrogen from one carbon site to the other to form the vinylidene isomer, H_2CC. Key investigations into the photofragmentation of C_2H_2 [2–17] have taken advantage of powerful coincidence three-dimensional (3D) momentum imaging techniques, such as cold target recoil ion momentum spectroscopy (COLTRIMS) [18, 19]. In these studies, one commonly-used signature of C_2H_2 isomerization has been measurement of the $C^+ + CH_2^+$ channel for rearrangement into the vinylidene configuration. Measurement of $CH^+ + CH^+$, in contrast, has been taken as a signature for remaining in the acetylene configuration.

Other means of identifying C_2H_2 isomerization include monitoring the molecule's structural changes through the relative angles of the fragment momenta in three- and four-body Coulomb explosion imaging (CEI) measurements [4, 5, 7, 11, 14], which involve triple or quadruple ionization, respectively. While CEI has its own limitations [16, 20, 21], the fact that ionization is involved by necessity in the observation of all these signatures and that the final charge state is not necessarily the same as that undergoing isomerization may also obscure interpretation. Based on these types of signatures, some studies have concluded that C_2H_2 isomerization occurs in the monocation [12, 22–24], while others have pointed to the dication states [2–4, 6, 8–17, 25]. It is important to note that these different interpretations are not necessarily conflicting, as the particular pathways could depend sensitively upon the experimental parameters. However,

they may also indicate some ambiguity in the interpretation.

The rich information provided by the aforementioned coincidence momentum imaging techniques, such as the kinetic energy release (KER) and angular distributions, can be illuminating in determining which potential energy surfaces may be involved in the isomerization and pathways toward the final products [6, 8]. The dynamics, however, can be quite complex. For molecules exposed to intense laser fields, it is probable that many multiphoton pathways contribute to the measured data, making interpretation challenging. As a specific example, for dissociative double ionization of C_2H_2 by an intense 800-nm femtosecond laser pulse, the common interpretation that hydrogen migration occurs exclusively in the dication [4, 13–15, 17, 24, 26] awaits more direct substantiation. Here, the signature dissociative ionization channels likely involve the exchange of many photons with the laser field. Thus, despite the detailed information provided by the measurements, one cannot readily exclude the case in which hydrogen migration is initiated or completed in the neutral or monocation intermediate states before the final ionization step(s). Hence, as pointed out by Gong *et al.* [12], experimental determination of the charge state in which isomerization occurs is a highly-coveted goal.

While Gong and co-workers [12] used above-threshold double ionization of acetylene to distinguish hydrogen migration on the monocation and dication surfaces of C_2H_2, in this article we propose a complementary approach that restricts isomerization to a specific $C_2H_2^q$ molecular ion. In this approach, we perform kinematically-complete measurements of laser-induced dissociation of molecular ions, introduced as a beam target, sidestepping altogether the ambiguity introduced by ionization. Here, the laser field excites the molecule to a dissociative state of the same molecular ion and may also initiate isomerization. Thus, laser intensities lower than that required for ionization may be used, limiting the contributions of complex multiphoton pathways and reducing the number of potential surfaces involved. While the dilute nature of

an ion-beam target leads to lower counting rates than can be achieved with gas-phase targets, none of the detailed information provided by other coincidence 3D momentum imaging techniques is sacrificed. Note that the focus of this manuscript is mainly to present this approach, which can be quite powerful in making future advances in studying isomerization of $C_2H_2^q$ and other molecular ions. At present, however, further work is needed to attain deeper understanding of the dynamics.

II. EXPERIMENTAL METHOD

We demonstrate this method for studying $C_2H_2^q$ isomerization limited to a particular charge state using $C_2D_2^{2+}$ and $C_2H_2^+$ as specific examples. Our experiment is illustrated in Fig. 1. Molecular ions are produced via fast electron impact in an electron-cyclotron resonance (ECR) ion source. The $C_2H_2^+$ and $C_2D_2^{2+}$ beams are generated by loading this ion source with C_2H_2 and CD_4 gas, respectively. The ions are accelerated upon extraction from the ECR source to energies of 42 keV and 8 keV for the $C_2D_2^{2+}$ and $C_2H_2^+$ beams, respectively. The ion beam is selected by a magnet and then electrostatically steered and focused to produce a collimated target that has a ~0.9×0.9 mm^2 cross section at its intersection with the laser beam. The flight time of the target molecular ions from the ion source to the intersection with the laser is ~10 μs for $C_2D_2^{2+}$ and ~20 μs for $C_2H_2^+$.

Based on electron impact ionization studies, the $C_2H_2^+$ target is known to be predominantly in the acetylene (linear HCCH) configuration [27–30]. While the production mechanism for the dication beam from methane gas is admittedly less straightforward than that of the $C_2H_2^+$ beam, the $C_2D_2^{2+}$ beam is also most likely in the acetylene configuration [31].

The initial state of molecular ions at the moment they are probed by a laser pulse is a consequence of their production via fast electron impact in the ion source and the ensuing decay processes occurring during their flight to the laser interaction region. While fast electron impact preferentially populates lower electronic states, highly-excited states may also be populated. Moreover, this ionization is a vertical transition involving minimal angular momentum transfer. Therefore, the rotational population is similar to that of neutral molecules at room temperature [32, 33], and the Franck-Condon principle provides a good estimate of the vibrational population [32–34]. The long flight time to the interaction region (tens of microseconds) allows decay of the excited electronic states, as in most cases radiative decay proceeds much faster than the flight times. The exception to this trend is the case of metastable electronic states, e.g., those requiring a spin flip for decay to the electronic ground state [35, 36]. For the $C_2H_2^+$ beam, a metastable state may be initially populated [37], as discussed in Sec. III B, but more complete structure and lifetime information is essential to say with certainty that this is the case. We note
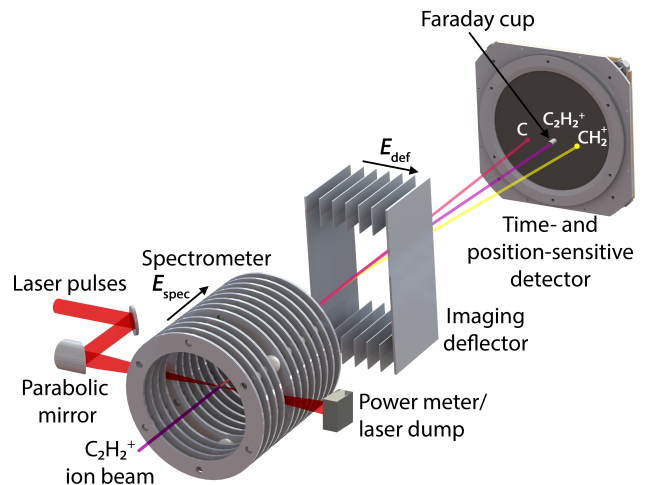

FIG. 1. Schematic of the coincidence 3D momentum imaging setup, illustrated with the $C_2H_2^+ \rightarrow C + CH_2^+$ breakup channel. A laser beam of femtosecond pulses intersects the ion beam inside the spectrometer. The laser-induced fragments are separated in time by a longitudinal field E_{spec}, created by the spectrometer. The fragments are also separated in position by E_{def}, a transverse field created by an imaging deflector.

that the present $C_2D_2^{2+}$ target is likely vibrationally and rotationally hot due to its formation from methane via "source chemistry," but this molecule is still most likely in the electronic ground state when probed by the laser.

The Ti:Sapphire laser system used in this study creates Fourier-transform-limited (FTL) pulses of 790-nm central wavelength, ~60-nm bandwidth [full width at half maximum (FWHM)], 2-mJ energy, and ~23-fs duration (FWHM in intensity) [38]. The pulse duration is measured using second harmonic generation frequency-resolved optical gating (SHG-FROG) [39]. An $f = 203$-mm focal length $90°$ off-axis parabolic mirror focuses the laser beam onto the ion-beam target. Translation of the laser focus away from the ion-beam center and/or insertion of power-attenuating optics enable control of the peak intensity of the laser [35, 40]. We also utilize second harmonic pulses, which are produced by sum frequency generation in a β-barium borate (BBO) crystal [41]. The measured spectrum centroid for these pulses is ~395 nm with a bandwidth of ~10 nm (FWHM). Their temporal duration, measured by self diffraction frequency resolved optical gating (SD-FROG) [42], is ~50 fs (positively chirped).

The laser-induced fragments are measured in coincidence using a position- and time-sensitive detector downstream, allowing evaluation of their complete 3D momenta. From the momenta, the KER and angular distributions are retrieved. Importantly, the keV energy of the ion beam allows us to also measure the neutral fragments. Therefore, we can perform kinematically-complete measurements of the dissociation channels of keV beams, such as $C_2H_2^+ + n\omega \rightarrow C^+ + CH_2$. Additional details about this experimental method can be

found in Refs. [43–47].

Similar to several of the studies mentioned in the introduction, we use $C_2H_2^q \rightarrow C^{q_1} + CH_2^{q_2}$ ($q = q_1 + q_2$) measurement as a signature of isomerization from the acetylene configuration to the vinylidene configuration. We note here that this does not preclude the possibility of isomerization of C_2H_2 ions that remain bound. While we can detect these molecular ions through use of an imaging deflector, we cannot determine their internal configuration.

III. RESULTS AND DISCUSSION

A. $C_2D_2^{2+}$

In the $C_2D_2^{2+}$ case, as expected, acetylene-like breakup, $CD^+ + CD^+$ (A), and vinylidene-like breakup, $C^+ + CD_2$ (V), are observed, as shown by the coincidence time-of-flight (CTOF) spectrum in Fig. 2. Imposing momentum conservation on these identified channels, we obtain their branching ratios. At 798-nm central wavelength and peak intensity 5×10^{15} W/cm^2, the acetylene branching ratio is A/(A + V) $\sim 51.5 \pm 3.5\%$. In contrast, the acetylene branching ratio measured with 392-nm pulses at peak intensity 6×10^{14} W/cm^2 is $\sim 82.9 \pm 2.1\%$, a significant difference. This observation points to the possibility of controlling $C_2D_2^{2+}$ isomerization with laser parameters like wavelength, pulse duration, and intensity. While control of isomerization [13, 26, 48–50] and fragmentation [10, 49, 51–55] have been topics of significant exploration, their study utilizing a molecular-ion-beam approach would enable focusing on dissociation, in contrast to the previous studies that examined dissociative ionization.

The KER spectra for the A channel measured with
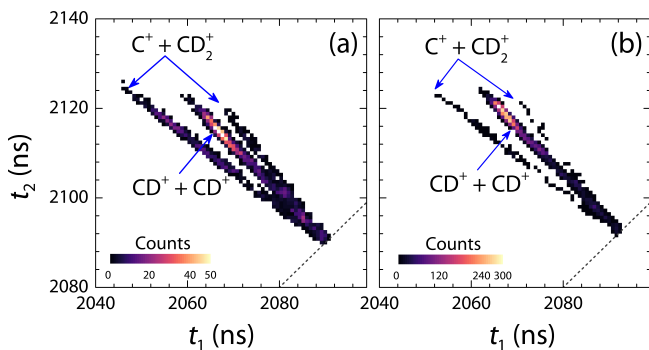
FIG. 2. The coincidence time-of-flight (CTOF) spectra of the dissociation channels $CD^+ + CD^+$ (A) and $C^+ + CD_2^+$ (V) for (a) 798-nm pulses and (b) 392-nm pulses after imposing momentum conservation. The gray dashed line indicates where $t_1 = t_2$. Under the present experimental conditions, in the V channel, CD_2^+ fragments may sometimes reach the detector before C^+ fragments. This is manifested by the righthand branch of the V channel.
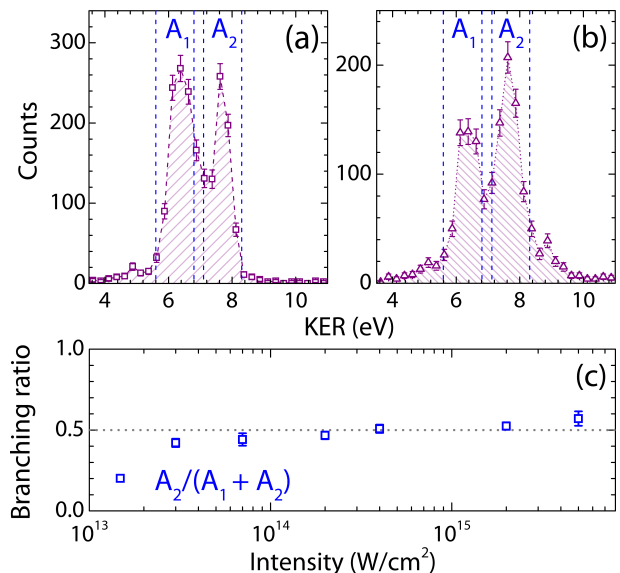
FIG. 3. Kinetic energy release (KER) spectra for the $CD^+ + CD^+$ channel measured at 798-nm wavelength and peak intensity (a) 5×10^{13} W/cm^2 and (b) 5×10^{15} W/cm^2. (c) Branching ratio of KER peaks A_1 and A_2 as a function of peak intensity. The regions marked by the blue dashed lines in panels (a) and (b) indicate where the yields of these peaks were evaluated.

798-nm photons are shown in Fig. 3(a) and (b). This channel exhibits two peaks centered at ~ 6.3 eV (A_1) and ~ 7.6 eV (A_2). The fact that A_1 and A_2 are separated by close to the energy of one photon could indicate that they are due to pathways involving the absorption of n and $n + 1$ photons, respectively, and have the same dissociation limit. The contribution of the higher-KER peak, A_2, grows with respect to A_1 as the laser intensity increases, shown by the branching ratio in Fig. 3(c). This enhancement of peak A_2 is consistent with the suggestion that its underlying process is an $n + 1$–photon process (i.e., above-threshold dissociation), in contrast to an n–photon process associated with A_1. However, future work is needed for deeper understanding of the underlying pathways, as well as the observed competition between the two KER peaks.

Curiously, the KER peaks A_1 and A_2 are markedly different from the ~ 5-eV KER measured for the $CH^+ + CH^+$ (A) channel in studies of neutral C_2H_2 targets. These neutral-target studies involved probing C_2H_2 with laser pulses similar to ours [3] or removing a carbon k-shell electron, leading to double ionization [6].

To shed light on this dissimilarity, we explore possible dissociation pathways leading to the measured $CD^+ + CD^+$ ($CH^+ + CH^+$) products using potential energy curves corresponding to the C–C stretch of the linear acetylene dication, reported by Thissen et al. [56]. These potentials are shown in Fig. 4. In the neutral-target studies mentioned above [3, 6], the suggested dissociation pathway associated with 5-eV KER involves the $^1\Sigma_g^+$
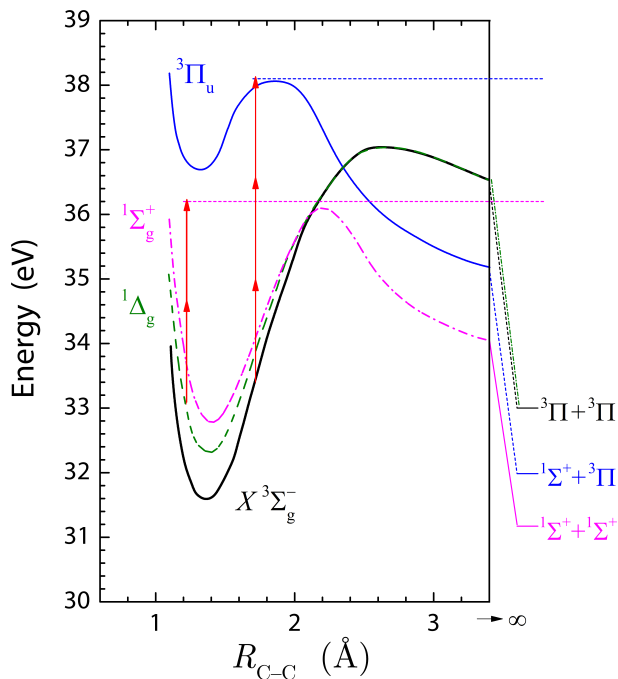
FIG. 4. A few of the lowest potential energy curves for the C–C stretch of the linear HCCH dication (with the C–H bond fixed at its equilibrium distance). Adapted from Ref. [56].
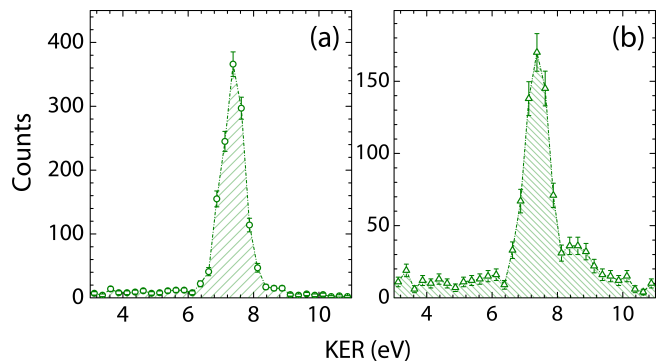

FIG. 5. Kinetic energy release (KER) spectra for the $C^+ + CD_2^+$ channel measured at 798-nm wavelength and peak intensity (a) 5×10^{13} W/cm^2 and (b) 5×10^{15} W/cm^2.

threshold dissociation. One may also speculate that this higher-KER peak may be due to dissociation to the lowest dissociation limit ($^1\Sigma^+$ + $^1\Sigma^+$) due to spin-orbit coupling of the triplet and singlet states. A more complete theoretical treatment of the molecular structure and dissociation dynamics, however, is needed to explore this possibility. It is also important to recall that the $C_2D_2^{2+}$ ions in this study are vibrationally and rotationally hot, and therefore, the measured angular distributions do not give clear-cut guidance in determination of the dissociation pathways. Under these conditions, which may involve bending and asymmetric stretching, selection rules are not strictly valid.

The KER spectrum of the V channel, $C^+ + CD_2^+$, on the other hand, exhibits a single peak at $\sim$7.4 eV, as shown in Fig. 5. Determining the dissociation pathways is more complex than the A-channel case and requires the complete potential energy surfaces on which the isomerization occurs. In this case, our measured KER is also significantly higher than the $\sim$5-eV KER measured for this channel when probing a neutral C_2H_2 target with similar laser pulses [3]. Here again, the underlying reason for this difference is likely related to the different dynamics occurring in the triplet states, but detailed verification requires more complete structure calculations and better understanding of the strong-field isomerization process.

B. $C_2H_2^+$

For the $C_2H_2^+$ target, as previously reported [57], we observe both acetylene-like and vinylidene-like dissociation through the measurement of the CH$^+$ + CH (A), $C^+ + CH_2$ (V$_1$), and C + CH$_2^+$ (V$_2$) channels, as highlighted in the CTOF spectrum in Fig. 6(a). Note that the presence of two vinylidene channels is due to the fact that either the C or CH$_2$ fragment can be positively charged. While this spectrum is zoomed in to focus on the dissociation channels of $C_2H_2^+$, we also measure the dissociative ionization channels CH$^+$ + CH$^+$ and $C^+ + CH_2^+$. For reference, at 6×10^{14} W/cm^2, the rate of the CH$^+$ + CH$^+$

state, as it has a barrier along the C–C stretch coordinate leading to the lowest CH$^+$ + CH$^+$ limit ($^1\Sigma^+$ + $^1\Sigma^+$, labeled in Fig. 4). The barrier lies about 5 eV above this dissociation limit. In the strong-field case [3], the $^1\Sigma_g^+$ state is reached by multiphoton ionization. Alternatively, multiphoton ionization can lead to population of the lowest singlet electronic state of the dication, $^1\Delta_g$. Following that, two-photon excitation to the $^1\Sigma_g^+$ state, indicated by the arrows in Fig. 4, may lead to dissociation. The triplet electronic states of the linear acetylene dication, on the other hand, lead to KER that is lower (barrier of $X\,^3\Sigma_g^-$ is $\sim$4 eV above $^3\Pi$ + $^3\Pi$) or higher (barrier of $^3\Pi_u$ is $\sim$6 eV above $^1\Sigma^+$ + $^3\Pi$) than that of the pathways involving the singlets and therefore are not the main contributors in the case of photofragmentation starting from neutral C_2H_2 targets.

In contrast, the triplet states play a dominant role in the present case, as $C_2D_2^{2+}$ ions arrive to the interaction region in the $X\,^3\Sigma_g^-$ electronic ground state, as explained in Sec. II. Because the laser field does not couple states of different spin multiplets, the dissociation pathways dominating the previous neutral C_2H_2 studies [3, 6] are closed, assuming that there are no metastable states initially populated. Instead, the dication may dissociate by three-photon absorption to the $^3\Pi_u$ state, as shown in Fig. 4. The $^3\Pi_u$ state barrier along the C–C stretch coordinate lies about 6 eV above its associated dissociation limit, $^1\Sigma^+$ + $^3\Pi$. This KER is consistent with the $\sim$6.4-eV KER of peak A$_1$.

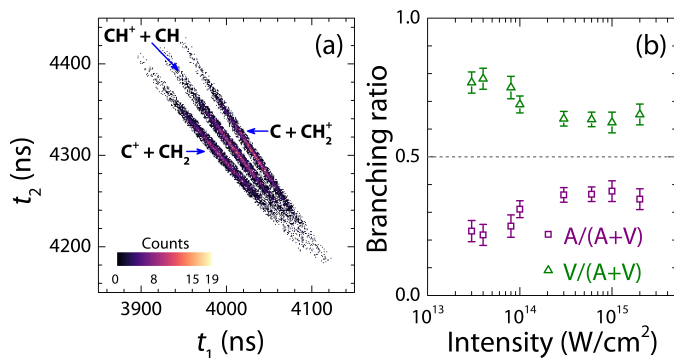As discussed earlier, peak A$_2$ may be due to above-

FIG. 6. (a) The CTOF spectrum of acetylene-like and vinylidene-like dissociation channels of a $C_2H_2^+$ target, measured with 790-nm pulses at a peak intensity of 6×10^{14} W/cm^2. (b) Laser intensity-dependent branching ratios of these dissociation channels. Note that $V = V_1 + V_2$.

channel is about 0.2 Hz, while that of $CH^+ + CH$ is about 0.4 Hz. It is worth noting that the measured rate of the dissociative ionization channel $CH^+ + CH^+$ decreases relative to that of the dissociation channel $CH^+ + CH$ with decreasing intensity.

The intensity-dependent branching ratios for the dissociation channels are shown in Fig. 6(b), where the vinylidene channels are grouped ($V = V_1 + V_2$). The $\gtrsim 60\%$ vinylidene breakup branching ratio over all intensities suggests a significant amount of isomerization of the initial acetylene configuration $C_2H_2^+$ target. Also, the modulation of the branching ratio with laser intensity suggests some control over the isomerization process. Focal-volume averaging, which is important when ionization is not needed, likely reduces the observed intensity dependence.

The KER of the A and V dissociation channels, shown in Fig. 7(a)–(c), peak near 0 and die off approximately exponentially, extending up to ~3 eV. Exponential decay fits to these distributions are shown on the figures. Fast-decaying KER distributions peaking at low energies could indicate transitions to the vibrational continuum leading to dissociation upon a flat portion of a potential energy surface where little to no kinetic energy is gained [58]. The transition probability for such processes typically peaks near threshold and drops quickly with increasing energy above threshold [59]. The measured low KER of the A channel is consistent with the predicted flat surface towards dissociation for the ground state of the cation [60, 61]. This KER distribution of the A channel is also similar to results attributed to the breakup of $C_2H_2^+$ initiated by collisions of C_2H_2 with MeV projectiles [62].

Following assumptions similar to those in our discussion of $C_2D_2^{2+}$ dissociation pathways in Sec. III A, we first consider the case of $C_2H_2^+$ in its $X\,^2\Pi_u$ electronic ground state when probed by the laser. A few dissociation pathways starting from the $X\,^2\Pi_u$ state will yield the low KER that is measured for the $CH^+ + CH$ (A) channel. To discuss these possibilities, we turn to the

potential energy curves of the linear acetylene monocation along the C–C stretch coordinate, reported by Perić and Engels (Fig. 7 in Ref. [61]). One candidate is a five-photon excitation from a low-lying vibrational level of the $X\,^2\Pi_u$ state to the $1\,^2\Pi_g$ state, followed by a C–C stretch and dissociation to the lowest $CH^+ + CH$ limit (x $^1\Sigma^+$ + x $^2\Pi$). Another possibility is a six-photon transition from a low-lying vibrational level of the $X\,^2\Pi_u$ state to the $1\,^2\Sigma_u^+$ state, leading to the first-excited $CH^+ + CH$ dissociation limit ($a\,^3\Pi$ + x $^2\Pi$). Note that stimulated emission after some C–C stretch may lead to dissociation to the lowest $CH^+ + CH$ limit of the $X\,^2\Pi_u$ electronic ground state. Likewise, a seven-photon transition from the $X\,^2\Pi_u$ state to the $1\,^2\Sigma_g^+$ state (denoted as $A\,^2\Sigma_g^+$ in Refs. [12, 22, 24, 37]), followed by C–C stretching and stimulated emission to the electronic ground state will yield the measured KER. The latter pathway involves the $A\,^2\Sigma_g^+$ state invoked previously [12, 22, 24] to explain isomerization in the acetylene monocation.

The pathways described above include both parallel ($\Pi \leftrightarrow \Pi$) and perpendicular ($\Pi \leftrightarrow \Sigma$) transitions. The measured angular distributions should therefore include contributions peaking at both $\cos\theta = 0$ and ± 1 [59, 63, 64], as that in Fig. 7(d) does. This measured angular distribution, however, points to a lower photon number than the pathways mentioned above, which could mean that much higher lying vibrational levels of the $X\,^2\Pi_u$ state are involved instead.

The inquiry into plausible dissociation pathways becomes even richer upon consideration of the prediction
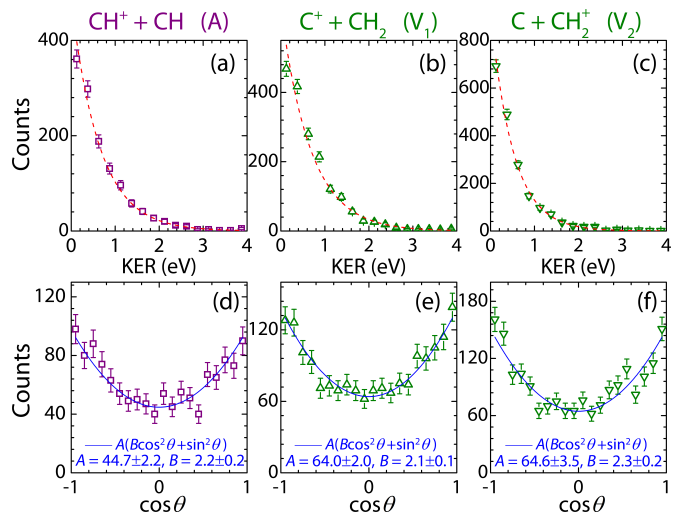

FIG. 7. The KER (top row) and angular (bottom row) distributions for the dissociation channels of $C_2H_2^+$ for laser pulses centered at 790 nm with peak intensity of 8×10^{13} W/cm^2. (a) and (d): $CH^+ + CH$. (b) and (e): $C^+ + CH_2$. (c) and (f): $C + CH_2^+$. The red dashed lines in (a)–(c) are exponential decay fits ($N_0\exp^{-KER/a}$) to the data. Note that θ is defined as the angle between the laser polarization and the momentum vector of the ionic fragment.

by Hochlaf *et al.* [37] that the lowest quartet states of the acetylene cation, specifically the first-excited state, $1\,^4\Sigma_u^+$, and the lowest state, $1\,^4\Pi_g$, are long lived. The computed radiative lifetime of the $1\,^4\Sigma_u^+$ state [37] is much shorter than the flight time of the $C_2H_2^+$ molecules from the ion source to the interaction region (recall, $\sim$20 μs). Thus, $C_2H_2^+$ molecules in this state will decay to the lowest quartet state before reaching the interaction region. The lifetime of the $1\,^4\Pi_g$ state has not been reported, so it remains unclear if molecules in this state survive to be probed by the laser in our experiment.

For the sake of discussion, let us assume that the $1\,^4\Pi_g$ state does survive. The C–C stretch quartet potential energy curves calculated by Hochlaf *et al.* (Fig. 1(b) in Ref. [37]) suggest that highly-excited vibrational levels of the $1\,^4\Pi_g$ state would be populated, as this electronic state's minimum lies at a much larger C–C separation than that of neutral ground state C_2H_2. Thus, one-photon excitation from the $1\,^4\Pi_g$ state to the $1\,^4\Sigma_u^-$ or $1\,^4\Pi_u$ states can lead to $CH^+ + CH$ dissociation. These perpendicular and parallel transitions would also lead to angular distributions with contributions peaking at both $\cos\theta = 0$ and ± 1 but involving lower photon numbers than the proposed pathways involving doublet states. In this regard, the quartet pathways appear more consistent with the data presented in Fig. 7, hinting that the metastable state $1\,^4\Pi_g$ plays a key role. This possibility, however, awaits more careful investigation because it depends on the unknown lifetime of this quartet state.

Figures 7(e) and (f) show the angular distributions of the vinylidene channels, which are quite similar to the acetylene channel angular distribution. This similarity may indicate that the first excitation step is the same for all three channels, followed by propagation of the nuclear wave packet to different dissociation limits. Again, this speculation requires theoretical verification.

Identification of the pathways for vinylidene-like breakup requires information beyond what is readily available and thus calls for further work, which we hope our findings will encourage.

IV. SUMMARY AND OUTLOOK

In summary, we demonstrate a method to limit the isomerization dynamics of $C_2H_2^q$, a topic that has gen-

erated great interest, to a single charge state, avoiding the uncertainty caused by ionization. Even though the low density of an ion-beam target results in lower counting rates than those of gas-phase targets, as we have shown, we are still afforded the detailed array of information provided by coincidence 3D momentum imaging, including branching ratios, KER, and angular distributions. We have demonstrated use of this information to determine plausible dissociation pathways for acetylene-like breakup of the monocation and dication.

For excitation to a repulsive state, laser pulses of intensities lower than that needed for ionization may in principle be used, allowing one to reduce the contributions of complex multiphoton pathways. The lack of ionization will also likely allow more direct comparisons with and guidance by theory. Thus, we anticipate that such an approach can facilitate a more thorough understanding of isomerization and fragmentation dynamics. While this manuscript leaves the door open in terms of reaching this deeper insight, we hope to have demonstrated our method to be one that has some advantages in molecular dynamics studies. We have also pointed out that many interesting avenues of study exist, such as control of the acetylene and vinylidene fragmentation branching ratios with different laser parameters.

Finally, on a more general note, one may readily recognize that this type of approach is not limited to exploring $C_2H_2^q$ isomerization. We anticipate that the use of molecular ion beams could be beneficial in examining bond rearrangement and other interesting strong-field dynamics in many different systems.

V. ACKNOWLEDGMENT

[1] T. Yatsuhashi and N. Nakashima, J. Photochem. Photobiol., C **34**, 52 (2018).

[2] T. Osipov, C. L. Cocke, M. H. Prior, A. Landers, T. Weber, O. Jagutzki, L. Schmidt, H. Schmidt-Böcking, and R. Dörner, Phys. Rev. Lett. **90**, 233002 (2003).

[3] A. S. Alnaser, I. Litvinyuk, T. Osipov, B. Ulrich, A. Landers, E. Wells, C. M. Maharjan, P. Ranitovic, I. Bochareva, D. Ray, and C. L. Cocke, J. Phys. B **39**, S485 (2006).

[4] A. Hishikawa, A. Matsuda, M. Fushitani, and E. J. Takahashi, Phys. Rev. Lett. **99**, 258302 (2007).

[5] A. Hishikawa, A. Matsuda, E. J. Takahashi, and M. Fushitani, J. Chem. Phys. **128**, 084302 (2008).

[6] T. Osipov, T. N. Rescigno, T. Weber, S. Miyabe, T. Jahnke, A. S. Alnaser, M. P. Hertlein, O. Jagutzki, L. P. H. Schmidt, M. Schöffler, L. Foucar, S. Schössler, T. Havermeier, M. Odenweller, S. Voss, B. Feinberg, A. L. Landers, M. H. Prior, R. Dörner, C. L. Cocke,

and A. Belkacem, J. Phys. B **41**, 091001 (2008).

[7] A. Matsuda, M. Fushitani, E. J. Takahashi, and A. Hishikawa, Phys. Chem. Chem. Phys. **13**, 8697 (2011).

[8] B. Gaire, S. Y. Lee, D. J. Haxton, P. M. Pelz, I. Bocharova, F. P. Sturm, N. Gehrken, M. Honig, M. Pitzer, D. Metz, H.-K. Kim, M. Schöffler, R. Dörner, H. Gassert, S. Zeller, J. Voigtsberger, W. Cao, M. Zohrabi, J. Williams, A. Gatton, D. Reedy, C. Nook, T. Müller, A. L. Landers, C. L. Cocke, I. Ben-Itzhak, T. Jahnke, A. Belkacem, and T. Weber, Phys. Rev. A **89**, 013403 (2014).

[9] X. Gong, Q. Song, Q. Ji, H. Pan, J. Ding, J. Wu, and H. Zeng, Phys. Rev. Lett. **112**, 243001 (2014).

[10] X. Xie, K. Doblhoff-Dier, H. Xu, S. Roither, M. S. Schöffler, D. Kartashov, S. Erattupuzha, T. Rathje, G. G. Paulus, K. Yamanouchi, A. Baltuška, S. Gräfe, and M. Kitzler, Phys. Rev. Lett. **112**, 163003 (2014).

[11] C. E. Liekhus-Schmaltz, I. Tenney, T. Osipov, A. Sanchez-Gonzalez, N. Berrah, R. Boll, C. Bomme, C. Bostedt, J. D. Bozek, S. Carron, R. Coffee, J. Devin, B. Erk, K. R. Ferguson, R. W. Field, L. Foucar, L. J. Frasinski, J. M. Glownia, M. Gühr, A. Kamalov, J. Krzywinski, H. Li, J. P. Marangos, T. J. Martinez, B. K. McFarland, S. Miyabe, B. Murphy, A. Natan, D. Rolles, A. Rudenko, M. Siano, E. R. Simpson, L. Spector, M. Swiggers, D. Walke, S. Wang, T. Weber, P. H. Bucksbaum, and V. S. Petrovic, Nat. Commun. **6**, 8199 (2015).

[12] X. Gong, Q. Song, Q. Ji, K. Lin, H. Pan, J. Ding, H. Zeng, and J. Wu, Phys. Rev. Lett. **114**, 163001 (2015).

[13] M. Kübel, R. Siemering, C. Burger, N. G. Kling, H. Li, A. S. Alnaser, B. Bergues, S. Zherebtsov, A. M. Azzeer, I. Ben-Itzhak, R. Moshammer, R. de Vivie-Riedle, and M. F. Kling, Phys. Rev. Lett. **116**, 193001 (2016).

[14] C. Burger, N. G. Kling, R. Siemering, A. S. Alnaser, B. Bergues, A. M. Azzeer, R. Moshammer, R. de Vivie-Riedle, M. Kübel, and M. F. Kling, Faraday Discuss. **194**, 495 (2016).

[15] M. Kübel, C. Burger, R. Siemering, N. G. Kling, B. Bergues, A. S. Alnaser, I. Ben-Itzhak, R. Moshammer, R. de Vivie-Riedle, and M. F. Kling, Mol. Phys. **115**, 1835 (2017).

[16] Z. Li, L. Inhester, C. Liekhus-Schmaltz, B. F. E. Curchod, J. W. Snyder, N. Medvedev, J. Cryan, T. Osipov, S. Pabst, O. Vendrell, P. Bucksbaum, and T. J. Martinez, Nat. Commun. **8**, 453 (2017).

[17] C. Burger, A. Atia-Tul-Noor, T. Schnappinger, H. Xu, P. Rosenberger, N. Haram, S. Beaulieu, F. Légaré, A. S. Alnaser, R. Moshammer, R. T. Sang, B. Bergues, M. S. Schuurman, R. de Vivie-Riedle, I. V. Litvinyuk, and M. F. Kling, Struct. Dyn. **5**, 044302 (2018).

[18] R. Dörner, V. Mergel, O. Jagutzki, L. Spielberger, J. Ullrich, R. Moshammer, and H. Schmidt-Böcking, Phys. Rep. **330**, 95 (2000).

[19] J. Ullrich, R. Moshammer, A. Dorn, R. Dörner, L. P. H. Schmidt, and H. Schmidt-Böcking, Rep. Prog. Phys. **66**, 1463 (2003).

[20] A. M. Sayler, E. Eckner, J. McKenna, B. D. Esry, K. D. Carnes, I. Ben-Itzhak, and G. G. Paulus, Phys. Rev. A **97**, 033412 (2018).

[21] I. Luzon, E. Livshits, K. Gope, R. Baer, and D. Strasser, J. Phys. Chem. Lett. **10**, 1361 (2019).

[22] Y. H. Jiang, A. Rudenko, O. Herrwerth, L. Foucar, M. Kurka, K. U. Kühnel, M. Lezius, M. F. Kling, J. van Tilborg, A. Belkacem, K. Ueda, S. Düsterer, R. Treusch, C. D. Schröter, R. Moshammer, and J. Ullrich, Phys. Rev. Lett. **105**, 263002 (2010).

[23] Y. H. Jiang, A. Senftleben, M. Kurka, A. Rudenko, L. Foucar, O. Herrwerth, M. F. Kling, M. Lezius, J. V. Tilborg, A. Belkacem, K. Ueda, D. Rolles, R. Treusch, Y. Z. Zhang, Y. F. Liu, C. D. Schrter, J. Ullrich, and R. Moshammer, J. Phys. B **46**, 164027 (2013).

[24] H. Ibrahim, B. Wales, S. Beaulieu, B. E. Schmidt, N. Thiré, E. P. Fowe, E. Bisson, C. T. Hebeisen, V. Wanie, M. Giguére, J.-C. Kieffer, M. Spanner, A. D. Bandrauk, J. Sanderson, M. S. Schuurman, and F. Légaré, Nat. Commun. **5**, 4422 (2014).

[25] J. H. D. Eland, F. S. Wort, P. Lablanquie, and I. Nenner, Z. Phys. D: At., Mol. Clusters **4**, 31 (1986).

[26] E. Wells, C. Rallis, M. Zohrabi, R. Siemering, B. Jochim, P. Andrews, U. Ablikim, B. Gaire, S. De, K. Carnes, B. Bergues, R. de Vivie-Riedle, M. Kling, and I. Ben-Itzhak, Nat. Commun. **4**, 2895 (2013).

[27] S.-H. Zheng and S. K. Srivastava, J. Phys. B **29**, 3235 (1996).

[28] G. Josifov, D. Lukic, N. Uric, and M. Kurepa, J. Serb. Chem. Soc. **65**, 517 (2000).

[29] S. Feil, K. Głuch, A. Bacher, S. Matt-Leubner, D. K. Böhme, P. Scheier, and T. D. Märk, J. Chem. Phys. **124**, 214307 (2006).

[30] S. Feil, P. Sulzer, A. Mauracher, M. Beikircher, N. Wendt, A. Aleem, S. Denifl, F. Zappa, S. Matt-Leubner, A. Bacher, S. Matejcik, M. Probst, P. Scheier, and T. D. Märk, J. Phys.: Conf. Ser. **86**, 012003 (2007).

[31] Acetylene is a common product of methane in plasma environments through the recombination of CH_x radicals [65–69].

[32] H. Helm and P. C. Cosby, J. Chem. Phys. **86**, 6813 (1987).

[33] Z. Amitay, A. Baer, M. Dahan, J. Levin, Z. Vager, D. Zajfman, L. Knoll, M. Lange, D. Schwalm, R. Wester, A. Wolf, I. F. Schneider, and A. Suzor-Weiner, Phys. Rev. A **60**, 3769 (1999).

[34] F. von Busch and G. H. Dunn, Phys. Rev. A **5**, 1726 (1972).

[35] A. M. Sayler, P. Q. Wang, K. D. Carnes, and I. Ben-Itzhak, J. Phys. B **40**, 4367 (2007).

[36] M. Zohrabi, J. McKenna, B. Gaire, N. G. Johnson, K. D. Carnes, S. De, I. A. Bocharova, M. Magrakvelidze, D. Ray, I. V. Litvinyuk, C. L. Cocke, and I. Ben-Itzhak, Phys. Rev. A **83**, 053405 (2011).

[37] M. Hochlaf, S. Taylor, and J. H. D. Eland, J. Chem. Phys. **125**, 214301 (2006).

[38] X. Ren, A. M. Summers, Kanaka Raju P., A. Vajdi, V. Makhija, C. W. Fehrenbach, N. G. Kling, K. J. Betsch, Z. Wang, M. F. Kling, K. D. Carnes, I. Ben-Itzhak, C. Trallero-Herrero, and V. Kumarappan, J. Opt. **19**, 124017 (2017).

[39] R. Trebino, K. W. DeLong, D. N. Fittinghoff, J. N. Sweetser, M. A. Krumbgel, B. A. Richman, and D. J. Kane, Rev. Sci. Instrum. **68**, 3277 (1997).

[40] P. Wang, A. M. Sayler, K. D. Carnes, B. D. Esry, and I. Ben-Itzhak, Opt. Lett. **30**, 664 (2005).

[41] R. W. Boyd, *Nonlinear Optics, Third Edition*, 3rd ed. (Academic Press, Inc., Orlando, FL, USA, 2008).

[42] D. J. Kane and R. Trebino, IEEE J. Quantum Electron. **29**, 571 (1993).

[43] I. Ben-Itzhak, P. Q. Wang, J. F. Xia, A. M. Sayler, M. A. Smith, K. D. Carnes, and B. D. Esry, Phys. Rev. Lett. **95**, 073002 (2005).

[44] P. Q. Wang, A. M. Sayler, K. D. Carnes, J. F. Xia, M. A. Smith, B. D. Esry, and I. Ben-Itzhak, Phys. Rev. A **74**, 043411 (2006).

[45] A. M. Sayler, *Measurements of Ultrashort Intense Laser-Induced Fragmentation of Simple Molecular Ions*, Ph.D. thesis, Kansas State University (2008).

[46] B. Gaire, *Imaging of slow dissociation of the laser induced fragmentation of molecular Ions*, Ph.D. thesis (2011).

[47] B. Gaire, J. McKenna, M. Zohrabi, K. D. Carnes, B. D. Esry, and I. Ben-Itzhak, Phys. Rev. A **85**, 023419 (2012).

[48] S. Kaziannis, N. Kotsina, and C. Kosmidis, J. Chem. Phys. **141**, 104319 (2014).

[49] H. Li, N. G. Kling, B. Frg, J. Stierle, A. Kessel, S. A. Trushin, M. F. Kling, and S. Kaziannis, Struct. Dyn. **3**, 043206 (2016).

[50] Atia-tul-noor, N. Haram, H. Xu, U. S. Sainadh, R. T. Sang, and I. V. Litvinyuk, Phys. Rev. A **97**, 033402 (2018).

[51] X. Xie, K. Doblhoff-Dier, S. Roither, M. S. Schöffler, D. Kartashov, H. Xu, T. Rathje, G. G. Paulus, A. Baltuška, S. Gräfe, and M. Kitzler, Phys. Rev. Lett. **109**, 243001 (2012).

[52] X. Xie, S. Roither, M. Schöffler, E. Lötstedt, D. Kartashov, L. Zhang, G. G. Paulus, A. Iwasaki, A. Baltuška, K. Yamanouchi, and M. Kitzler, Phys. Rev. X **4**, 021005 (2014).

[53] X. Xie, E. Lötstedt, S. Roither, M. Schöffler, D. Kartashov, K. Midorikawa, A. Baltuška, K. Yamanouchi, and M. Kitzler, Sci. Rep. **5**, 12877 (2015).

[54] Q. Song, X. Gong, Q. Ji, K. Lin, H. Pan, J. Ding, H. Zeng, and J. Wu, J. Phys. B **48**, 094007 (2015).

[55] H. Li, N. G. Kling, T. Gaumnitz, C. Burger, R. Siemering, J. Schötz, Q. Liu, L. Ban, Y. Pertot, J. Wu, A. M. Azzeer, R. de Vivie-Riedle, H. J. Wörner, and M. F. Kling, Opt. Express **25**, 14192 (2017).

[56] R. Thissen, J. Delwiche, J. M. Robbe, D. Duflot, J. P. Flament, and J. H. D. Eland, J. Chem. Phys. **99**, 6590 (1993).

[57] B. Jochim, B. Berry, T. Severt, P. Feizollah, M. Zohrabi, Kanaka Raju P., E. Wells, K. D. Carnes, and I. Ben-Itzhak, J. Phys. Chem. Lett. **10**, 2320 (2019).

[58] W. Demtröder, *Atoms, Molecules and Photons: an introduction to Atomic-, Molecular- and Quantum physics* (Springer, 2018).

[59] A. M. Sayler, P. Q. Wang, K. D. Carnes, B. D. Esry, and I. Ben-Itzhak, Phys. Rev. A **75**, 063420 (2007).

[60] M. Davister and R. Locht, Chem. Phys. **191**, 333 (1995).

[61] M. Perić and B. Engels, Chem. Phys. **238**, 47 (1998).

[62] S. Yoshida, T. Majima, T. Asai, M. Matsubara, H. Tsuchida, M. Saito, and A. Itoh, Nucl. Instrum. Methods Phys. Res., Sect. B **408**, 203 (2017), proceedings of the 18th International Conference on the Physics of Highly Charged Ions (HCI-2016), Kielce, Poland, 11-16 September 2016.

[63] R. N. Zare, Mol. Photochem. **4**, 1 (1972).

[64] A. Hishikawa, S. Liu, A. Iwasaki, and K. Yamanouchi, J. Chem. Phys. **114**, 9856 (2001).

[65] M. Ioffe, S. Pollington, and J. Wan, J. Catal. **151**, 349 (1995).

[66] A. V. Kirikov, V. V. Ryzhov, and A. I. Suslov, Tech. Phys. Lett. **25**, 794 (1999).

[67] M. Heintze, M. Magureanu, and M. Kettlitz, J. Appl. Phys. **92**, 7022 (2002).

[68] G.-B. Zhao, S. John, J.-J. Zhang, L. Wang, S. Muknahallipatna, J. C. Hamann, J. F. Ackerman, M. D. Argyle, and O. A. Plumb, Chem. Eng. J. **125**, 67 (2006).

[69] C. Shen, Y. Sun, D. Sun, and H. Yang, Sci. China: Chem. **53**, 231 (2010).

Chapter 4

Dissociation of metastable dications

4.1 Scope

This chapter focuses on our strong-field molecular dynamics studies that take advantage of the properties of the metastable dication NO^{2+}. Sections 4.2 and 4.3 open with a general introduction to the unique properties of molecular dications and why we are interested in them, respectively. Section 4.4 provides some background on the transitions pertinent to the manuscripts that follow in Sections 4.5 and 4.6. These manuscripts highlight our investigations into processes occurring in NO^{2+} exposed to intense laser fields, specifically permanent-dipole transitions and few-photon electronic transitions.

4.2 The study of molecular dications

Some of the earliest hints of the existence of molecular dications arose in J. J. Thomson's experiments on streams of positively-charged particles in Crookes tubes [104]. On the theoretical side, Linus Pauling conducted seminal investigations into the properties of dications, specifically the doubly-charged helium dimer, He_2^{2+} [105]. More detailed experimental observations of and theoretical calculations for species such as CO^{2+}, NO^{2+}, N_2^{2+}, and many others have followed in the decades afterward [106–109].

Many diatomic dications exist in metastable states. These states have local minima in their potentials, as illustrated by the schematic example AB^{2+} potential energy curves in Fig. 4.2.1. Also illustrated in this figure, these metastable states are chemically unstable because these local minima lie above the dissociation limit and therefore have a finite lifetime. The magnitudes of these lifetimes and specific mechanisms for decay depend on the potential energy landscape of the populated state(s) and the coupling of the states to each other. For example, in Fig. 4.2.1, population in the X state may either decay by tunneling through its barrier or by coupling with the A state.
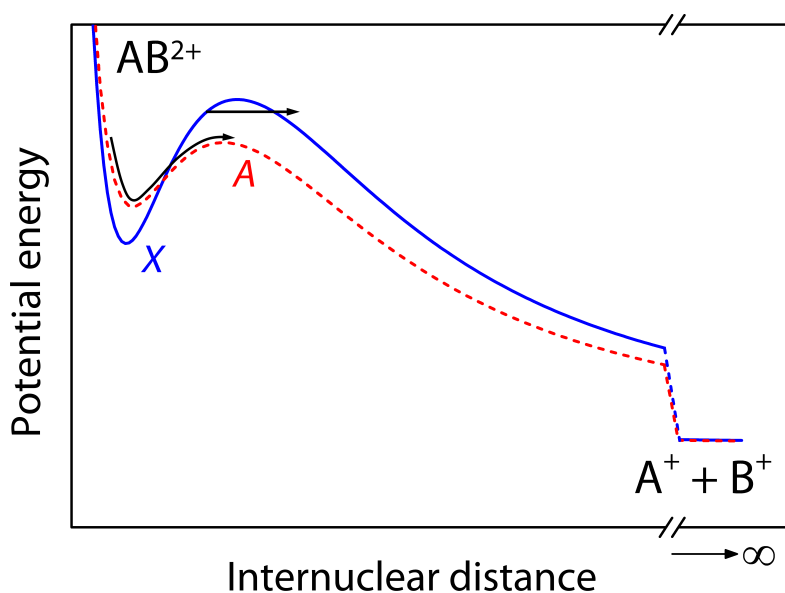
Figure 4.2.1: Schematic potential energy curves of a metastable dication. The arrows illustrate some possible $AB^{2+} \rightarrow A^+ + B^+$ decay mechanisms of the X state: tunneling and predissociation via X–A state coupling.

4.3   Our interest in molecular dications

One reason metastable molecular dications have been of interest to our group is that their decay allows us to probe targets with a limited initial population. More specifically, the molecular ions decay in flight from the ion source to their interaction point with the laser beam. This decay often means that the molecules interacting with the laser are in a reduced

range of vibrational states in a single electronic state. As fewer states are populated at the moment the molecular ion is probed by a laser pulse, understanding of the laser-induced dynamics becomes more feasible. Moreover, as emphasized in Chapter 1, Section 1.3, each molecular dication studied serves as a test case for examining different interesting laser-induced processes.

4.4 Electronic transitions and permanent-dipole transitions

The probability for a transition between two states Ψ_1 and Ψ_2 driven by an external electric field is proportional to the dipole matrix element,

$$\mathbf{D}_{21} = \langle \Psi_2 | \mathbf{D} | \Psi_1 \rangle. \tag{4.4.1}$$

In this expression, $\mathbf{D}$ is the dipole operator. In a diatomic molecule's center-of-mass (CM) frame, this operator is given by

$$\mathbf{D} = e \Big(\sum_{i=1}^{2} Z_i \mathbf{R}_i - \sum_{j=1}^{n} \mathbf{r}_j \Big). \tag{4.4.2}$$

In Eq. 4.4.2, eZ_i and $\mathbf{R}_i$ are the charges and positions of the two nuclei, respectively, and $\mathbf{r}_j$ are the positions of the n electrons. The coordinates are illustrated in Fig. 4.4.1.
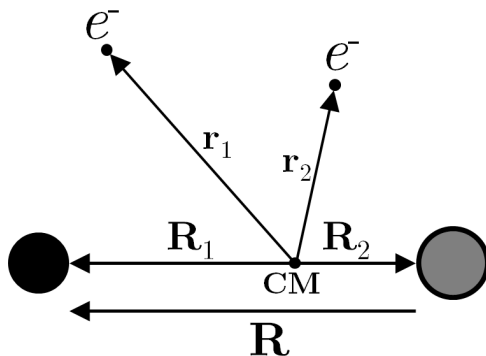
Figure 4.4.1: Coordinate system for a two-electron diatomic molecule. The position vectors of the nuclei with respect to the center of mass (**CM**) are $\mathbf{R_1}$ and $\mathbf{R_2}$ ($\mathbf{R} = \mathbf{R_1} - \mathbf{R_2}$). The electron position vectors with respect to **CM** are $\mathbf{r_1}$ and $\mathbf{r_2}$.

In the Born-Oppenheimer (BO) approximation, the wave functions can be written as the product of the electronic and nuclear wave functions,

$$\Psi = \Phi(\mathbf{R}; \mathbf{r}_1, ... \mathbf{r}_n) F_v(\mathbf{R}), \tag{4.4.3}$$

where the electronic wave functions Φ depend parametrically on the internuclear separation, $\mathbf{R}$. Insertion of Eq. 4.4.2 and the BO wave functions, Ψ_1 and Ψ_2, into Eq. 4.4.1 yields

$$\mathbf{D}_{21} = \langle F_{v'}(\mathbf{R}) | \mathbf{D}_{\mathbf{elec}}(R) | F_v(\mathbf{R}) \rangle, \tag{4.4.4}$$

where the prime refers to Ψ_2. $\mathbf{D}_{\mathbf{elec}}(R)$ is the electronic dipole matrix element, given by

$$\mathbf{D}_{\mathbf{elec}}(R) = e \Big\langle \Phi_{s'} \Big| \sum_{i=1}^{2} Z_i \mathbf{R}_i - \sum_{j=1}^{n} \mathbf{r}_j \Big| \Phi_s \Big\rangle \tag{4.4.5}$$

$$= e \left[\Big\langle \Phi_{s'} \Big| \sum_{i=1}^{2} Z_i \mathbf{R}_i \Big| \Phi_s \Big\rangle - \Big\langle \Phi_{s'} \Big| \sum_{j=1}^{n} \mathbf{r}_j \Big| \Phi_s \Big\rangle \right]. \tag{4.4.6}$$

Transitions for which $s' \neq s$ are called electronic transitions. For the case of transitions within the same electronic state, i.e., $s' = s$, Eq. 4.4.6 represents the permanent electric dipole moment. In this case, the second term in Eq. 4.4.6 goes to zero, as the integrand is an odd function of the electron coordinates. For homonuclear molecules, $\mathbf{R}_1 = -\mathbf{R}_2$, so the first term in Eq. 4.4.6 goes to zero, and hence the permanent dipole moment is zero. For heteronuclear molecules, in contrast, $\mathbf{R}_1 \neq -\mathbf{R}_2$. Thus, the permanent dipole moment is non-zero. Therefore, while dipole transitions within the same electronic state are not allowed in homonuclear molecules, they are allowed in heteronuclear molecules.

4.5 Direct evidence of the dominant role of multiphoton permanent-dipole transitions in strong-field dissociation of NO^{2+}

The manuscript in this section, submitted to *Physical Review Letters*, focuses on our work showing direct experimental evidence for the significance of multiphoton transitions driven

by the permanent dipole moment in NO^{2+} molecules. While permanent-dipole-driven transitions are commonly observed in high precision ro-vibrational spectroscopy of molecules [110, 111], in strong-field molecular physics, previous experimental evidence for these transitions has been indirect [112] or controversial [113, 114]. Our measured KER and angular distributions point to transitions involving only the electronic ground state of NO^{2+} and leading to its vibrational continuum. The experimental evidence is further confirmed by our time-dependent Schrödinger equation (TDSE) calculations.

Direct evidence of the dominant role of multiphoton permanent-dipole transitions in strong-field dissociation of NO^{2+}

Bethany Jochim,[1] M. Zohrabi,[1] B. Gaire,[1] F. Anis,[1] Tereza
Uhlíková,[2] K. D. Carnes,[1] E. Wells,[3] B. D. Esry,[1] and I. Ben-Itzhak[1]

[1]*J. R. Macdonald Laboratory, Department of Physics,*
Kansas State University, Manhattan, Kansas 66506 USA
[2]*Department of Analytical Chemistry, Institute of Chemical Technology, Prague Technická, Prague 6, Czech Republic*
[3]*Department of Physics, Augustana University, Sioux Falls, South Dakota 57197 USA*
(Dated: February 12, 2019)

We study laser-induced dissociation of a metastable NO^{2+} ion beam into N$^+$ + O$^+$, focusing on the prominent contribution by molecules breaking parallel to the polarization at high peak laser intensity ($\sim 10^{15}$ W/cm^2). Our experimental results and time-dependent Schrödinger equation calculations show that, contrary to commonly-held intuition that electronic transitions always prevail, the dominant process underlying this highly-aligned dissociation is a multiphoton permanent-dipole transition involving only the electronic ground state and leading to its vibrational continuum. Strong-field permanent-dipole transitions should thus be considered generally, as they may play a significant role in other heteronuclear molecules. Moreover, their role should only grow in importance for longer wavelengths, a trending direction in ultrafast laser studies.

Photochemical control is one goal at the heart of atomic, molecular, and optical physics [1–5]. Intense, femtosecond laser pulses possess fields comparable to the binding fields of molecules' valence electrons and temporal durations shorter than typical molecular vibration and rotational periods. As such, a multitude of studies over the past decades have established these pulses as promising tools for manipulating strong-field molecular processes and gradually edifying our understanding of them, see, e.g., reviews [2, 4–9] and references [10–17].

A framework for understanding the interactions of laser pulses with small molecules has been realized in studies of the simplest diatomic molecule, H$_2$$^+$ [7, 18]. All the main dissociative mechanisms in this benchmark system, bond softening [19], above-threshold dissociation (ATD) [20], etc., rely solely on the laser-induced coupling of different electronic states. Following the natural progression from simple to more complex, we build upon this framework to explore strong-field dynamics of multielectron molecules, applying the fundamental concepts developed in H$_2$$^+$ studies. Among multielectron systems, heteronuclear molecules present intriguing complexities. For instance, their nonzero permanent dipole moments, created by the offset between their centers of mass and charge, allow transitions within the same electronic state to occur, opening up more pathways for dissociation and control.

Several theoretical studies have noted that permanent-dipole transitions can play an important role in strong-field dynamics [21–37]. While the wealth of theoretical results is compelling, there has been little experimental consideration of strong-field-driven permanent-dipole transitions. Few experimental studies have highlighted strong-field permanent-dipole transitions, and the existing work has been controversial or did not present any direct evidence. For instance, Kiess *et al.* reported the

first experimental evidence of permanent-dipole transitions in the benchmark heteronuclear diatomic molecule HD$^+$ [38], but this measurement lacked the ability to distinguish H and D fragments. Utilizing a coincidence technique, McKenna *et al.* later attributed the same kinetic energy release (KER) peak to a one-photon bond softening mechanism, which does not involve the permanent dipole moment [39]. Recently, Wustelt *et al.* [40] attributed an intensity-dependent KER shift in HeH$^+$ to stretching prior to ionization, which involves vibrational excitation of the electronic ground state. However, they were unable to measure dissociation, leaving open the question of whether the stretching occurred on the ground state or excited states.

In many molecules, the permanent dipole moment is generally quite weak compared to the transition dipole moment [41]. In HD$^+$, discussed above, for example, the magnitude of the $1s\sigma$–$2p\sigma$ transition dipole moment at the one-photon crossing in the light-dressed diabatic Floquet picture [42, 43] is more than 3.5 times larger than the $1s\sigma$–$1s\sigma$ permanent dipole moment at the internuclear distance relevant to the two-photon process proposed by Kiess *et al.* [44]. Hence, one might expect that permanent-dipole transitions have much smaller probabilities in comparison to electronic transitions. Indeed, in interpretation, it has generally become a common tendency to ignore permanent-dipole transitions in molecules in favor of electronic transitions, e.g., references [45–58].

The lack of attention given to permanent-dipole transitions is perhaps due to the widespread use of Ti:Sapphire (800 nm) laser light in experimental studies. With their 1.5-eV energy on the order of the electronic state spacing in typical diatomic molecules, 800-nm photons are typically inefficient at inciting and probing permanent dipole-driven dynamics. However, with the trend towards use

of mid-infrared sources to enhance insight into tunneling ionization and high-harmonic generation [59], it is likely that permanent dipole-driven dynamics are increasingly relevant to strong-field molecular processes.

In this Letter, we show clear experimental and theoretical evidence that the permanent dipole moment plays a key role in the main strong-field dissociation peaks of NO^{2+}. Specifically, we observe dominant permanent dipole-driven, three-photon transitions on the $X\,^2\Sigma^+$ ground state, leading to dissociation into $N^+ + O^+$. The permanent dipole moments of dications tend to be larger than those of their neutral counterparts. In the present case, the ground state permanent dipole moment of NO^{2+} at the equilibrium internuclear distance is 0.75 a.u., whereas the corresponding quantity for NO is only 0.06 a.u. [60]. The larger permanent dipole moment of the dication makes it a good candidate for studying the impact of this property on strong-field dynamics.

In addition to its relatively strong permanent dipole moment, the electronic structure properties of NO^{2+} make it an attractive candidate for study. As NO^{2+} is metastable like many other dications [61–63], only certain states survive from creation to interaction with the laser (~20-μs travel time in our setup). The three lowest states of NO^{2+}, $X\,^2\Sigma^+$, $A\,^2\Pi$ and $B\,^2\Sigma^+$, shown in Fig. 1, as well as two higher-lying states, $C\,^2\Sigma^+$ and $c\,^4\Pi$, are the only calculated states with bound potentials in the Franck-Condon region. The $C\,^2\Sigma^+$ and $c\,^4\Pi$ states fragment rapidly via tunneling or predissociation [64]. The $A\,^2\Pi$ and $B\,^2\Sigma^+$ states have predissociative, tunneling, and radiative lifetimes ranging from fractions of a microsecond to a few microseconds [65], leaving only the electronic ground state populated when probed by the laser.

Akin to CO^{2+}, which we have studied previously [57], the electronic ground state of NO^{2+} "cools" vibrationally via predissociation, specifically spin-orbit coupling with $A\,^2\Pi$ [65]. Given the ion travel time mentioned above, this further limits the initial population to v=0–12 of the $X\,^2\Sigma^+$ state.

The laser field does not couple electronic states of differing spin, and the next-highest doublet state after $B\,^2\Sigma^+$, $2\,^2\Pi$ (not shown in Fig. 1), lies an additional 5 eV above the minimum of the $B\,^2\Sigma^+$ state. Therefore, our NO^{2+} ion beam allows probing of the laser-induced response of a three-channel system. Moreover, the $X\,^2\Sigma^+$ and $A\,^2\Pi$ states are strongly coupled by one-photon transitions in a typical intense femtosecond laser pulse and are energetically well isolated from the $B\,^2\Sigma^+$ state. Hence, $X\,^2\Sigma^+\rightarrow A\,^2\Pi$ transitions are expected to dominate the dissociation.

To calculate the initial vibrational population of the NO^{2+} beam, shown in Fig. 1(b), we assume that the ions are produced via vertical transitions from the ground state of the neutral molecule to that of the dication [66]. The normalized vibrational state wavefunctions nec-
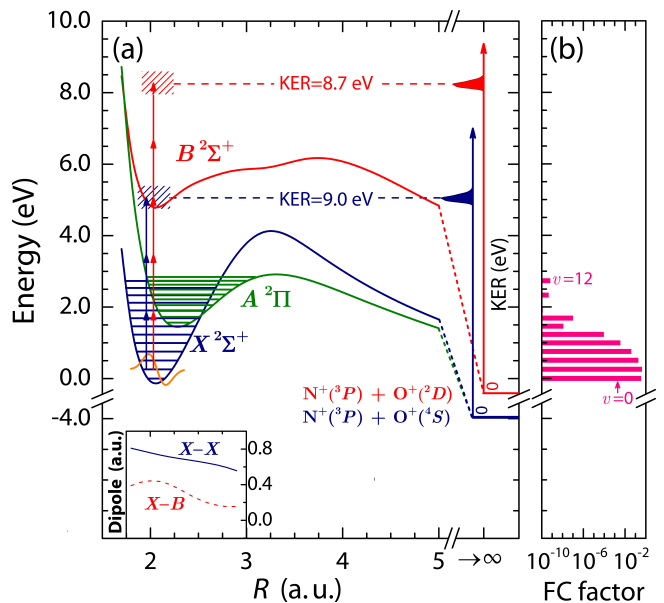

FIG. 1. (a) Lowest-lying doublet potential energy curves of NO^{2+}. The $B\,^2\Sigma^+$ state dissociation limit is –0.42 eV, and that of the $X\,^2\Sigma^+$ and $A\,^2\Pi$ states is –3.96 eV, where zero is defined as v=0 of $X\,^2\Sigma^+$. The arrows represent $X\,^2\Sigma^+\rightarrow X\,^2\Sigma^+$ (navy) and $X\,^2\Sigma^+\rightarrow B\,^2\Sigma^+$ (red) multiphoton transitions, both starting from v=1, whose schematic vibrational wave function is shown in orange. The navy and red hatched areas represent the vibrational continua of the $X\,^2\Sigma^+$ and $B\,^2\Sigma^+$ states, respectively. The schematic peaks with the corresponding colors on the right-hand side represent KER distributions for these bound–free pathways. The $X\,^2\Sigma^+$ permanent dipole moment and $X\,^2\Sigma^+$–$B\,^2\Sigma^+$ transition dipole moment are shown in the inset. (b) Franck-Condon (FC) population for the $X\,^2\Sigma^+$ state of NO^{2+} resulting from NO $\rightarrow NO^{2+}$ vertical electron impact ionization in the ion source followed by predissociation in flight to the interaction region.

essary for this analysis were calculated using a phase-amplitude method [67], yielding vibrational energies that are consistent with those of Baková et al. [65].

In our experiment, a beam of NO^{2+} ions is produced by fast electron impact on vibrationally-cold NO gas in an electron-cyclotron resonance (ECR) source and is accelerated to 9.2 keV, momentum analyzed, and focused by an electrostatic lens system. The resultant collimated 0.9×0.9-mm^2 ion beam travels to the laser interaction region. A multipass Ti:Sapphire laser is used to produce 774-nm, 2-mJ, 27-fs pulses (full-width at half-maximum [FWHM] in intensity measured with second harmonic generation frequency-resolved optical gating [SHG FROG]) at 2 kHz. These pulses are focused onto the target ion beam by a 90-degree off-axis, f=203-mm parabolic mirror to a peak intensity of up to ~5×10^{15} W/cm^2. The laser intensity is evaluated by imaging the focus and is controlled in the experiment by changing the position of the focus relative to the center of the target ion beam. The laser-induced dissociation fragments carry
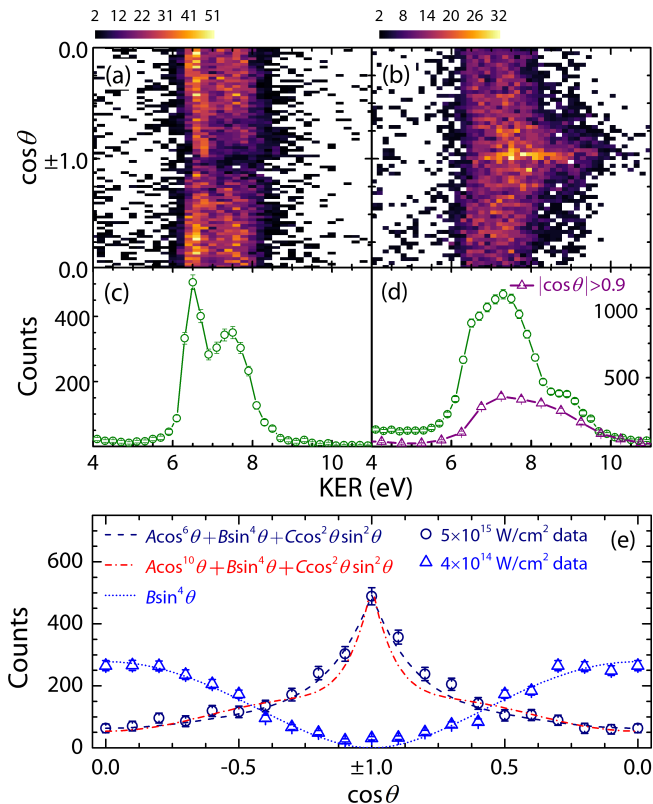
FIG. 2. (a) and (b) Density plots of $NO^{2+} \rightarrow N^+ + O^+$ dissociation as a function of KER and $\cos\theta$ for laser intensities 4×10^{14} W/cm^2 and 5×10^{15} W/cm^2, respectively. θ is the angle between the laser polarization and the N^+ velocity vector. (c) and (d) One-dimensional KER plots of dissociation at laser intensities 4×10^{14} W/cm^2 and 5×10^{15} W/cm^2, respectively. (e) Number of dissociation events as a function of $\cos\theta$. The 5×10^{15} W/cm^2 data, shown in navy, is for an 8.0–10.0 eV KER slice, and the 4×10^{14} W/cm^2 data, shown in blue, is for a 7.0–9.0 eV KER slice. The lines show functions fitted to the data.

a few keV of energy in the lab frame and are measured using a coincidence three-dimensional (3D) momentum imaging technique that has been described in detail in previous publications [68–70].

Lower intensity pulses ($\leq 10^{15}$ W/cm^2) produce KER spectra with a two-peak structure, shown in Figs. 2(a) and 2(c), primarily resulting from dissociation perpendicular to the laser polarization, as expected for a $\Delta\Lambda=1$ transition [71]. The origins of these two peaks will be discussed in a forthcoming publication.

In contrast, higher intensity pulses ($\sim 5\times10^{15}$ W/cm^2) yield a prominent highly-aligned feature at $|\cos\theta|=1$, shown in Figs. 2(b) and 2(e). Note that θ is defined as the angle between the laser polarization and the N^+ velocity vector. This highly-aligned feature cannot come from $X\,^2\Sigma^+ \rightarrow A\,^2\Pi$ transitions because a $\Delta\Lambda=1$ transition should exhibit an angular distribution peaked at $|\cos\theta|=0$. Moreover, from Fig. 2(e), it is readily seen that there are two angular features in the different in-

tensity regimes: (1) a sharp, aligned feature, and (2) a distribution peaking at $|\cos\theta|=0$. The aligned feature also extends to higher KER (8–11 eV), highlighted by the $|\cos\theta|>0.9$ slice in Fig. 2(d). This parallel, higher-KER part of the high-intensity data is our focus.

What are the underlying dynamics of this aligned feature? Following the dominant line of thought in the field, a purely electronic $X\,^2\Sigma^+ \rightarrow B\,^2\Sigma^+$ transition would be a natural choice. Such a transition starting from the peak of the vibrational population ($v=1$) would produce 8.7-eV KER, as illustrated in Fig. 1(a), consistent with the data. Similar $X\,^2\Sigma^+ \rightarrow B\,^2\Sigma^+$ transitions starting from neighboring vibrational levels can produce the remainder of the high-KER, highly-aligned feature. As mentioned above, however, permanent-dipole transitions can also play an important role. An intriguing possibility is a three-photon vibrational excitation driven by the permanent dipole moment and involving solely the $X\,^2\Sigma^+$ state. Starting from the peak of the Franck-Condon population, such a transition would produce 9.0-eV KER, shown schematically in Fig. 1(a), also consistent with our measurements.

The angular fits for the high intensity data in Fig. 2 (e) shed some light on what dynamics are occurring. These support $X\,^2\Sigma^+ \rightarrow X\,^2\Sigma^+$ transitions over $X\,^2\Sigma^+ \rightarrow B\,^2\Sigma^+$ transitions. The fit function containing the $\cos^6\theta$ term, which corresponds to a three-photon parallel transition, fits the data quite nicely, whereas the fit function containing the $\cos^{10}\theta$ term, which corresponds to a five-photon parallel transition, is clearly too narrow and does not fit the data as well. As a side note, the $\cos^2\theta\sin^2\theta$ term corresponds to a $X\,^2\Sigma^+ \rightarrow X\,^2\Sigma^+ \rightarrow A\,^2\Pi$ pathway, i.e., a parallel one-photon permanent-dipole transition on the ground state followed by a perpendicular one-photon electronic transition to the first excited state.

While our experimental results strongly support the important role of permanent-dipole transitions, to further strengthen our claims, we solved the time-dependent Schrödinger equation (TDSE) in the Born-Oppenheimer representation [72]. The necessary potential energy curves, transition dipole moments, and permanent dipole moments were obtained by extending previous *ab initio* calculations [65]. These were computed using the complete active space self-consistent field (CASSCF) and internally-contracted multireference configuration interaction (icMRCI) methods as implemented in the MOL-PRO suite of programs [73]. The full active space consisted of $1\sigma - 6\sigma$, 1π and 2π orbitals with all electrons correlated, and the Dunning correlation consistent basis set cc-pV6Z was used [74]. Relativistic corrections were carried out using the Douglas-Kroll-Hess Hamiltonian as implemented in MOLPRO [75–77]. The relativistic curves, which we included in our TDSE calculations, differ by no more than 0.1 eV from the uncorrected ones at any internuclear distance.

In the TDSE calculations, the three relevant electronic

states ($X\,^2\Sigma^+$, $A\,^2\Pi$, and $B\,^2\Sigma^+$) were considered, with initial population in v=0–12 (J=0) of the $X\,^2\Sigma^+$ state only. We performed our calculations at 800-nm wavelength and 35-fs pulse duration and repeated them at three intensities from 5.0×10^{13} to 2.0×10^{14} W/cm^2. Vibration and nuclear rotation were included, but ionization was neglected [72]. Our calculations converged to about 1%.

The KER spectra obtained from our TDSE calculations are shown in Fig. 3. As can be seen in panel (a), theory predicts that $X\,^2\Sigma^+\rightarrow X\,^2\Sigma^+$ transitions are more likely than $X\,^2\Sigma^+\rightarrow B\,^2\Sigma^+$ transitions by about five orders of magnitude. Moreover, when the permanent dipole moment is not included in the calculation, the $X\,^2\Sigma^+\rightarrow X\,^2\Sigma^+$ peak vanishes, demonstrating that transitions driven by the permanent dipole moment lead to this aligned, high-KER feature. Figure 3(a) also shows that the permanent dipole moment plays a key role in $X\,^2\Sigma^+\rightarrow B\,^2\Sigma^+$ transitions, as without the permanent dipole moment in the calculation, the $X\,^2\Sigma^+\rightarrow B\,^2\Sigma^+$ feature is also absent.

This dominance of $X\,^2\Sigma^+\rightarrow X\,^2\Sigma^+$ transitions over $X\,^2\Sigma^+\rightarrow B\,^2\Sigma^+$ transitions by several orders of magnitude persists even after Franck-Condon averaging over the initial vibrational population, as shown in Fig. 3(b). The vibrational structure seen in this calculated spectrum is not observed experimentally, as the resolution degrades with increasing KER. Specifically, at 9.0-eV KER, a conservative estimate of the resolution is 0.1 eV (1σ) [69, 78] for the present experimental conditions, which in conjunction with the laser bandwidth washes out the measured vibrational peaks.

One may wonder about the difference between the experimental and theoretical intensities. First, focal-volume averaging tends to lower the effective intensity of the experiment [43, 79]. Second, since including ionization in the theory is currently beyond reach, the calculations must be limited to intensities where ionization is acceptably small. We experimentally determined that this is true at 1×10^{14} W/cm^2 ($<$1% of dissociation), but it fails at 1×10^{15} W/cm^2 ($\sim$25% of dissociation). Therefore, using intensities up to 2×10^{14} W/cm^2 in the theory is reasonable.

The prevalence of $X\,^2\Sigma^+\rightarrow X\,^2\Sigma^+$ transitions over $X\,^2\Sigma^+\rightarrow B\,^2\Sigma^+$ transitions is due in large part to the lower number of photons required and the relative magnitudes of the dipole couplings. The dipole moments are shown in the inset in Fig. 1(a). At the internuclear distances near the $X\,^2\Sigma^+$ minimum, the ratio of the $X\,^2\Sigma^+$ permanent dipole moment to the $X\,^2\Sigma^+$–$B\,^2\Sigma^+$ transition dipole moment is around 1.8 and relatively constant. Moreover, it is possible that the dominance of the permanent-dipole driven pathways is further enhanced by intermediate resonant transitions to highly-excited vibrational levels of $X\,^2\Sigma^+$. For example, the NO^{2+} molecule can undergo resonant v=1 $\rightarrow$ v=8 and v=8 $\rightarrow$ v=16 pho-
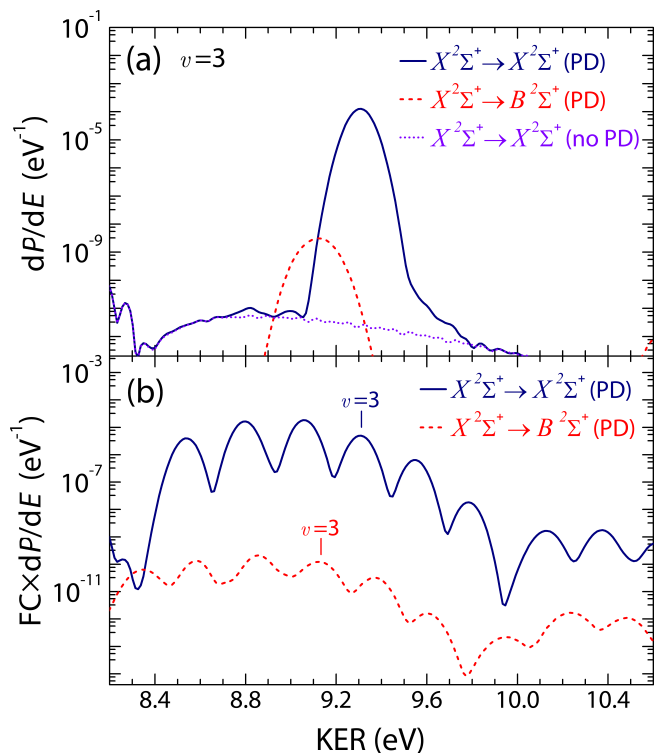

FIG. 3. Calculated KER spectra corresponding to (a) transitions starting at v=3 of the $X\,^2\Sigma^+$ state and (b) transitions starting from v=0–12 weighted by their Franck-Condon factors. "PD" indicates that the permanent dipole moment is included, and "no PD" indicates that it is not included. Note that the $X\,^2\Sigma^+\rightarrow B\,^2\Sigma^+$ KER spectrum (no PD) is too small in amplitude to be seen on the graph ($dP/dE\sim10^{-14}$ eV^{-1}). These calculations were performed at a laser intensity of 10^{14} W/cm^2.

toexcitations before subsequently absorbing a final photon to arrive at the $X\,^2\Sigma^+$ continuum.

Lastly, it is worth pointing out that our measurement technique and ion beam target choice draw a noteworthy distinction between our study and the sizeable body of existing work on NO^{2+} [80–82]. The majority of the previous studies are non-coincidence and utilize a neutral NO initial target. An overarching conclusion of this previous work is that N$^+$ and O$^+$ fragments are mainly produced via indirect mechanisms that involve a series of dissociation and ionization steps. Starting with an NO^{2+} ion beam target likely reduces the number of intermediate states participating in the strong-field dynamics, and thus interpretation in our case is simpler and can potentially even involve fundamentally different physics.

In summary, elucidation of the plausible dissociation pathways underlying the high intensity data from our experiment has proven to be an intriguing problem. Through the choice of a molecule that happens to have a strong permanent dipole moment, use of a powerful experimental method which affords us the ability to isolate this pathway experimentally via the KER and angular

distributions, and theoretical support, we have demonstrated that the commonly-overlooked permanent dipole moment can in some cases have a non-negligible and in fact dominating influence on the laser-induced dynamics, driving pathways involving a multiphoton vibrational excitation. With the field trending towards longer wavelengths and theory indicating that permanent-dipole transitions are important, this work will likely be a significant factor for strong-field physics researchers to consider in the future.

[1] P. Brumer and M. Shapiro, Annu. Rev. Phys. Chem. 43, 257 (1992).

[2] A. Zewail, Pure and Applied Chemistry 72, 2219 (2000).

[3] M. Shapiro and P. Brumer, Rep. Prog. Phys. 66, 859 (2003).

[4] P. Nuernberger, G. Vogt, T. Brixner, and G. Gerber, Phys. Chem. Chem. Phys. 9, 2470 (2007).

[5] D. Keefer and R. de Vivie-Riedle, Acc. Chem. Res. 51, 2279 (2018).

[6] T. Brixner and G. Gerber, ChemPhysChem 4, 418 (2003).

[7] J. H. Posthumus, Rep. Prog. Phys. 67, 623 (2004).

[8] M. Dantus and V. V. Lozovoy, Chem. Rev. 104, 1813 (2004).

[9] I. V. Hertel and W. Radloff, Rep. Prog. Phys. 69, 1897 (2006).

[10] R. S. Judson and H. Rabitz, Phys. Rev. Lett. 68, 1500 (1992).

[11] A. Assion, T. Baumert, M. Bergt, T. Brixner, B. Kiefer, V. Seyfried, M. Strehle, and G. Gerber, Science 282, 919 (1998).

[12] R. J. Levis, G. M. Menkir, and H. Rabitz, Science 292, 709 (2001).

[13] T. Ergler, A. Rudenko, B. Feuerstein, K. Zrost, C. D. Schröter, R. Moshammer, and J. Ullrich, Phys. Rev. Lett. 97, 193001 (2006).

[14] A. Hishikawa, A. Matsuda, M. Fushitani, and E. J. Takahashi, Phys. Rev. Lett. 99, 258302 (2007).

[15] D. Geißler, P. Marquetand, J. González-Vázquez, L. González, T. Rozgonyi, and T. Weinacht, J. Phys. Chem. A 116, 11434 (2012).

[16] U. Lev, L. Graham, C. B. Madsen, I. Ben-Itzhak, B. D. Bruner, B. D. Esry, H. Frostig, O. Heber, A. Natan, V. S. Prabhudesai, D. Schwalm, Y. Silberberg, D. Strasser, I. D. Williams, and D. Zajfman, J. Phys. B 48, 201001 (2015).

[17] M. Nairat, V. V. Lozovoy, and M. Dantus, J. Phys. Chem. A 120, 8529 (2016).

[18] H. Ibrahim, C. Lefebvre, A. D. Bandrauk, A. Staudte, and F. Légaré, J. Phys. B 51, 042002 (2018).

[19] P. H. Bucksbaum, A. Zavriyev, H. G. Muller, and D. W. Schumacher, Phys. Rev. Lett. 64, 1883 (1990).

[20] A. Giusti-Suzor, X. He, O. Atabek, and F. H. Mies, Phys. Rev. Lett. 64, 515 (1990).

[21] A. Kondo, W. J. Meath, S. H. Nilar, and A. J. Thakkar, Chem. Phys. 186, 375 (1994).

[22] A. Datta, S. Saha, and S. S. Bhattacharyya, J. Phys. B 30, 5737 (1997).

[23] A. Conjusteau, A. D. Bandrauk, and P. B. Corkum, J. Chem Phys. 106, 9095 (1997).

[24] C. M. Dion, A. Keller, O. Atabek, and A. D. Bandrauk, Phys. Rev. A 59, 1382 (1999).

[25] A. Kondorskiy and H. Nakamura, Phys. Rev. A 66, 053412 (2002).

[26] J. T. Paci, D. M. Wardlaw, and A. D. Bandrauk, J. Phys. B 36, 3999 (2003).

[27] G. L. Kamta and A. D. Bandrauk, Phys. Rev. Lett. 94, 203003 (2005).

[28] W. J. Meath, J. Opt. Soc. Am. B 25, 865 (2008).

[29] N. Elghobashi-Meinhardt, L. Gonzlez, I. Barth, and T. Seideman, J. Chem. Phys. 130, 024310 (2009).

[30] D. Ursrey, F. Anis, and B. D. Esry, Phys. Rev. A 85, 023429 (2012).

[31] Q. Su, Y. Han, and S.-L. Cong, J. Chem. Phys. 138, 024304 (2013).

[32] E. Dehghanian, A. D. Bandrauk, and G. Lagmago Kamta, J. Chem. Phys. 139, 084315 (2013).

[33] E. de Lima, E. Rosado, L. Castelano, and R. E. de Carvalho, Phys. Lett. A 378, 2657 (2014).

[34] A. Nikodem, R. D. Levine, and F. Remacle, J. Phys. Chem. A 120, 3343 (2016).

[35] V.-H. Hoang, S.-F. Zhao, V.-H. Le, and A.-T. Le, Phys. Rev. A 95, 023407 (2017).

[36] D. Ursrey and B. D. Esry, Phys. Rev. A 96, 063409 (2017).

[37] L. Yue, P. Wustelt, A. M. Sayler, F. Oppermann, M. Lein, G. G. Paulus, and S. Gräfe, Phys. Rev. A 98, 043418 (2018).

[38] A. Kiess, D. Pavičić, T. W. Hänsch, and H. Figger, Phys. Rev. A 77, 053401 (2008).

[39] J. McKenna, A. M. Sayler, B. Gaire, N. G. Johnson, M. Zohrabi, K. D. Carnes, B. D. Esry, and I. Ben-Itzhak, J. Phys. B 42, 121003 (2009).

[40] P. Wustelt, F. Oppermann, L. Yue, M. Möller, T. Stöhlker, M. Lein, S. Gräfe, G. G. Paulus, and A. M. Sayler, Phys. Rev. Lett. 121, 073203 (2018).

[41] B. Lasorne and G. Worth, eds., Coherent Control of Molecules (Collaborative Computational Project on Molecular Quantum Dynamics (CCP6), 2006).

[42] A. Giusti-Suzor, F. H. Mies, L. F. DiMauro, E. Charron, and B. Yang, J. Phys. B 28, 309 (1995).

[43] J. Posthumus, ed., Molecules and Clusters in Intense Laser Fields (Cambridge University Press, 2001).

[44] B. D. Esry and H. R. Sadeghpour, Phys. Rev. A **60**, 3604 (1999).

[45] J. Lavancier, D. Normand, C. Cornaggia, J. Morellec, and H. X. Liu, Phys. Rev. A **43**, 1461 (1991).

[46] C. Cornaggia, J. Lavancier, D. Normand, J. Morellec, P. Agostini, J. P. Chambaret, and A. Antonetti, Phys. Rev. A **44**, 4499 (1991).

[47] P. Dietrich and P. B. Corkum, J. Chem. Phys. **97**, 3187 (1992).

[48] K. Codling and L. J. Frasinski, J. Phys. B **26**, 783 (1993).

[49] M. Stankiewicz, L. J. Frasinski, G. M. Cross, P. A. Hatherly, K. Codling, A. J. Langley, and W. Shaikh, J. Phys. B **26**, 2619 (1993).

[50] S. M. Hankin, D. M. Villeneuve, P. B. Corkum, and D. M. Rayner, Phys. Rev. Lett. **84**, 5082 (2000).

[51] S. A. Hosseini and D. Goswami, Phys. Rev. A **64**, 033410 (2001).

[52] S. M. Hankin, D. M. Villeneuve, P. B. Corkum, and D. M. Rayner, Phys. Rev. A **64**, 013405 (2001).

[53] E. Wells, M. J. DeWitt, and R. R. Jones, Phys. Rev. A **66**, 013409 (2002).

[54] J. Wu, H. Zeng, and C. Guo, J. Phys. B **39**, 3849 (2006).

[55] J. Wu, H. Zeng, and C. Guo, J. Phys. B **40**, 1095 (2007).

[56] P. A. Orr, I. D. Williams, J. B. Greenwood, I. C. E. Turcu, W. A. Bryan, J. Pedregosa-Gutierrez, and C. W. Walter, Phys. Rev. Lett. **98**, 163001 (2007).

[57] J. McKenna, A. M. Sayler, F. Anis, N. G. Johnson, B. Gaire, U. Lev, M. A. Zohrabi, K. D. Carnes, B. D. Esry, and I. Ben-Itzhak, Phys. Rev. A **81**, 061401 (2010).

[58] M. Kotur, T. C. Weinacht, C. Zhou, and S. Matsika, Phys. Rev. X **1**, 021010 (2011).

[59] C. Vozzi, M. Negro, and S. Stagira, J. Mod. Opt. **59**, 1283 (2012).

[60] R. D. Nelson, Jr., D. R. Lide, Jr., and A. A. Maryott, *Selected Values of Electric Dipole Moments for Molecules in the Gas Phase* (U.S. National Bureau of Standards, U.S. Govt. Print. Off., 1967).

[61] D. Mathur, Phys. Rep. **225**, 193 (1993), and references therein.

[62] D. Mathur, Phys. Rep. **391**, 1 (2004).

[63] S. D. Price, Int. J. Mass Spectrom. **260**, 1 (2007), and references therein.

[64] D. Edvardsson, M. Lundqvist, P. Baltzer, B. Wannberg, and S. Lunell, Chem. Phys. Lett. **256**, 341 (1996).

[65] R. Baková, J. Fišer, T. Šedivcová Uhlíková, and V. Špirko, J. Chem. Phys. **128**, 144301 (2008).

[66] Z. Amitay, A. Baer, M. Dahan, J. Levin, Z. Vager, D. Zajfman, L. Knoll, M. Lange, D. Schwalm, R. Wester, A. Wolf, I. F. Schneider, and A. Suzor-Weiner, Phys. Rev. A **60**, 3769 (1999).

[67] E. Y. Sidky and I. Ben-Itzhak, Phys. Rev. A **60**, 3586 (1999).

[68] I. Ben-Itzhak, P. Q. Wang, J. F. Xia, A. M. Sayler, M. A. Smith, K. D. Carnes, and B. D. Esry, Phys. Rev. Lett. **95**, 073002 (2005).

[69] P. Q. Wang, A. M. Sayler, K. D. Carnes, J. F. Xia, M. A. Smith, B. D. Esry, and I. Ben-Itzhak, Phys. Rev. A **74**, 043411 (2006).

[70] A. M. Sayler, *Measurements of Ultrashort Intense Laser-Induced Fragmentation of Simple Molecular Ions*, Ph.D. thesis, Kansas State University (2008).

[71] A. M. Sayler, P. Q. Wang, K. D. Carnes, B. D. Esry, and I. Ben-Itzhak, Phys. Rev. A **75**, 063420 (2007).

[72] F. Anis and B. D. Esry, Phys. Rev. A **77**, 033416 (2008).

[73] H.-J. Werner, P. J. Knowles, G. Knizia, F. R. Manby, M. Schütz, *et al.*, "Molpro, version 2012.1, a package of ab initio programs," (2012), see http://www.molpro.net.

[74] T. H. Dunning, J. Chem. Phys. **90**, 1007 (1989).

[75] M. Douglas and N. M. Kroll, Ann. Phys. **82**, 89 (1974).

[76] B. A. Hess, Phys. Rev. A **32**, 756 (1985).

[77] B. A. Hess, Phys. Rev. A **33**, 3742 (1986).

[78] B. Gaire, *Imaging of Slow Dissociation of the Laser Induced Fragmentation of Molecular Ions*, Ph.D. thesis, Kansas State University (2011).

[79] J. J. Hua and B. D. Esry, Phys. Rev. A **78**, 055403 (2008).

[80] A. Talebpour, S. Larochelle, and S. L. Chin, J. Phys. B **30**, 1927 (1997).

[81] C. Guo and K. Wright, Phys. Rev. A **71**, 021404 (2005).

[82] C. Guo, J. Phys. B **38**, L323 (2005).

4.6 Importance of one- and two-photon transitions in strong-field dissociation of NO^{2+}

The manuscript in this section is a draft that we plan to submit to *Physical Review A*. In this work, despite being in the strong-field regime with peak intensity on the order of 10^{14} W/cm^2, the dominant processes are found to be transitions between the lowest two electronic states involving a low total photon number, namely one or two photons. These transitions, which are identified using the KER and angular distributions along with first-order perturbation theory, occur in the low-intensity regions that occupy the majority of the laser focal volume.

Importance of one- and two-photon transitions in the strong-field dissociation of NO^{2+}

Bethany Jochim,[1] M. Zohrabi,[1] B. Gaire,[1] Tereza Uhlíková,[2] K. D. Carnes,[1] E. Wells,[3] B. D. Esry,[1] and I. Ben-Itzhak[1]

[1] *J. R. Macdonald Laboratory, Department of Physics,*
Kansas State University, Manhattan, Kansas 66506 USA
[2] *Department of Analytical Chemistry, Institute of Chemical Technology, Prague Technická, Prague 6, Czech Republic*
[3] *Department of Physics, Augustana University, Sioux Falls, South Dakota 57197 USA*
(Dated: October 31, 2019)

Employing a coincidence three-dimensional momentum imaging technique, we investigate the ultrafast, intense laser-induced dissociation of a metastable NO^{2+} ion beam into N$^+$+ O$^+$. Based on the kinetic energy release and angular distributions, measured using both 774-nm and second-harmonic 387-nm pulses, we show that the main processes driving dissociation in pulses of about 10^{14} W/cm^2 peak intensity are one- and two-photon transitions from the $X\,^2\Sigma^+$ ground state to the $A\,^2\Pi$ first-excited state.

I. INTRODUCTION

Studying dynamics of molecules exposed to ultrashort laser pulses has been an ever-expanding area of research for many years now. Ultrafast photochemistry studies have made great strides in capturing detailed "snap-shots" of chemical reactions [1–6]. One possible application of improved understanding of these dynamics is quantum control of molecular dynamics using ultrafast lasers [7–12]. In this application, insight into the dynamics can allow one to pinpoint the most important laser-pulse characteristics for stimulating certain molecular processes, which could in turn guide a more refined approach to control [13, 14].

While ultrafast lasers are powerful tools, interpreting strong-field-driven molecular dynamics can be challenging. The multiphoton nature of the interaction along with the broad bandwidth of short pulses and the complicated electronic structure of molecules often means that several states could participate in the dynamics. Three-dimensional (3D) momentum imaging technology, however, has proven invaluable in navigating this complexity. The rich information provided by these techniques [15–22] has been fruitfully employed to determine pathways important for dynamics. For example, Gong *et al.* [23] reported the use of ion-electron coincidence momentum imaging of H$_2$ dissociative ionization to obtain pathway-resolved photoelectron angular distributions. In another example utilizing ion-electron coincidences, Kunitski *et al.* [24] reported pathway-resolved two-center interference effects in the photoelectron momentum spectra from dissociative ionization of neon dimers.

In addition to neutral-target studies, 3D momentum imaging has also been applied to understand strong-field dynamics of molecular-ion beams [25–33], targets that have unique and potentially advantageous features. For example, ion beams allow the study of states unavailable through use of conventional gas-phase targets. Our group has previously studied the laser-induced dissociation of CO^{2+} molecules [34]. In that work, rapid decay of the metastable CO^{2+} molecules in flight from the ion source to the laser interaction region facilitated probing of vibrationally-cold (i.e., only $v=0$) molecules in the electronic ground state. This simplification led to dynamics more tractable than the case of electronically- and vibrationally-hot CO^{2+} produced by the interaction of intense pulses with a neutral CO target. In the present work, we will take advantage of similar simplifying traits, an approach that aids in our progress towards better understanding of the strong-field dynamics of increasingly complex molecules.

Another compelling aspect of studying molecular ion beams in intense laser fields is that in contrast to the case of neutral targets, the necessity of ionization is removed. Thus, important dynamics may be driven by the lower intensity "wings" of the laser pulse profile. That is, even for high peak intensities, transitions involving low total photon numbers may play a key role.

Specifically, in this article, we report on femtosecond laser-induced dissociation pathways of metastable NO^{2+} ions induced by a strong ($\sim$10^{14} W/cm^2) laser pulse. We find that in this intensity regime, one- and two-photon transitions dominate. In particular, as expected, the coupling between the two lowest-lying electronic states, the $X\,^2\Sigma^+$ ground state and the $A\,^2\Pi$ first-excited state, primarily dictates the dynamics.

II. EXPERIMENTAL TECHNIQUE

We produce an NO^{2+} ion beam by fast electron impact ionization of nitric oxide gas inside an electron-cyclotron resonance (ECR) ion source. The ions are accelerated to 9.2 keV, momentum analyzed using a magnet, then steered and focused by electrostatic deflectors and lenses, respectively. The cross section of the resulting collimated ion beam is about 0.9×0.9 mm^2 in the interaction region, where it intersects a laser beam of femtosecond pulses. The coincidence 3D momentum imaging method used to perform kinematically-complete measurements of the ensuing dissociation has been described in earlier studies [27, 35, 36].

A Ti:Sapphire laser system generates the linearly-polarized laser pulses at a rate of 2 kHz with 774-nm central wavelength, 2-mJ energy, and temporal duration

of 27-fs FWHM (full-width at half-maximum in intensity). The pulse duration is measured using the second harmonic generation frequency-resolved optical gating (SHG FROG) technique [37]. A 90-degree off-axis, f=203-mm parabolic mirror focuses the laser beam onto the ion-beam target. The peak intensity [38] is controlled in the experiment by shifting the position of the focus relative to the ion-beam center [39]. We decrease the laser intensity in this manner instead of using attenuation optics, as it preserves the temporal pulse shape and increases the interaction volume, thereby improving the counting rate. We also utilize 387-nm pulses in this work, produced by sum-frequency generation in a β-barium borate (BBO) crystal [40].

III. PROPERTIES OF THE NO^{2+} BEAM

In our experiment, the NO^{2+} ions have a flight time of about 20 μs from their creation to the crossing with the laser beam. This long flight time from the source, along with the inherent properties of NO^{2+}, simplify our study significantly. Specifically, except for the $X\,^2\Sigma^+$ ground state, all of the calculated electronic states of NO^{2+} (including all possible spin multiplets) with bound potentials in the Franck-Condon (FC) region of NO have lifetimes of a few microseconds or less [41, 42]. Therefore, only the $X\,^2\Sigma^+$ ground state is non-negligibly populated by the time the NO^{2+} molecules interact with the laser pulse. Also, the laser field couples only states with the same spin multiplicity. Thus, the number of electronic states to consider is reduced to those shown in Fig. 1(a). Furthermore, the $v'>12$ states of the $X\,^2\Sigma^+$ state predissociate into N$^+$+O$^+$ by spin-orbit coupling with the first-excited state, $A\,^2\Pi$, within fractions of a microsecond [42]. This means that we only probe the $X\,^2\Sigma^+$ state in vibrational levels $v'=0-12$ in our experiment, all with lifetimes greater than 10 μs [42].

We estimate the initial population of the surviving $v'=0-12$ vibrational states of the $X\,^2\Sigma^+$ state by calculating FC factors between these states and the NO vibrational ground state. This is a reasonable approximation, as suggested by production of H$_2^+$ and its isotopologues by fast electron impact in similar ion sources [43–45]. Moreover, the rotational distribution of ions generated by electron impact is similar to that of the neutral molecules at room temperature [44, 45]. While the populated vibrational levels of the $X\,^2\Sigma^+$ state are, rigorously speaking, resonances rather than bound states, their long lifetimes translate to resonance widths of about 10^{-11} eV [42]. We thus treat them as bound states in estimating the vibrational population:

$$\mathcal{F}_{v'} = |\langle \psi_{v'} | \psi_{v=0}\rangle|^2. \tag{1}$$

Here, $\psi_{v=0}$ is the vibrational ground state wave function of NO, and $\psi_{v'}$ is the wave function of vibrational state v' in the $X\,^2\Sigma^+$ ground state of NO^{2+}. The vibrational wave functions were calculated using a phase-amplitude
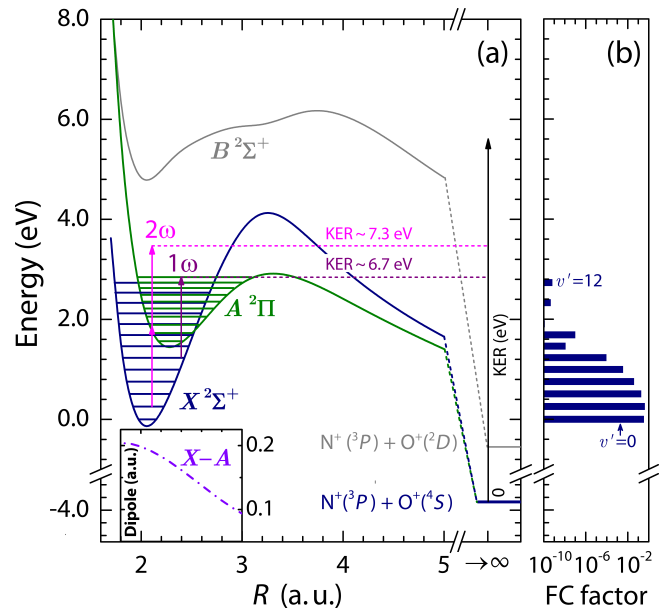

FIG. 1. (a) Lowest-lying doublet potential energy curves of NO^{2+}. Zero energy is defined as $v'=0$ of $X\,^2\Sigma^+$. The $B\,^2\Sigma^+$ state dissociation limit is –0.55 eV, and that of the $X\,^2\Sigma^+$ and $A\,^2\Pi$ states is –3.87 eV. The inset shows the $X\,^2\Sigma^+$–$A\,^2\Pi$ transition dipole moment [42]. (b) Franck-Condon (FC) population for the $X\,^2\Sigma^+$ state of NO^{2+} resulting from NO → NO^{2+} vertical ionization by fast electron impact in the ion source followed by predissociation in flight to the interaction region (see text).

method [46]. The resulting FC factors are shown in Fig. 1(b). Note that most of the initial population is in the $v'=0-5$ states.

IV. RESULTS AND DISCUSSION

Given the energy separation of the $X\,^2\Sigma^+$ and $A\,^2\Pi$ states relative to the photon energy, illustrated in Fig. 1(a), it is evident that these states would be easily coupled by the absorption of one or two 774-nm photons. The next-highest doublet state, $B\,^2\Sigma^+$, is well separated from these lowest two states. Thus, at laser intensities at which four-photon transitions (such as would be required for N$^+$ + O$^+$ dissociation on the $B\,^2\Sigma^+$ state) are negligible, one would expect transitions between the $X\,^2\Sigma^+$ and $A\,^2\Pi$ states to be the most important.

We focus on dissociation of NO^{2+} into N$^+$+O$^+$, measured in coincidence. From these measurements, we extract the kinetic energy release (KER) and angular distributions for the laser-induced dissociation. Density plots of the measured N$^+$ + O$^+$ yield as a function of KER and $\cos\theta$ as well as KER projections are shown in Fig. 2 for 1×10^{14} and 4×10^{14} W/cm^2 peak laser intensities. Note that θ is defined as the angle between the velocity of the N$^+$ fragment and the laser polarization. In this intensity regime, N$^+$+O$^+$ breakup occurs predominantly perpen-

dicular to the laser polarization direction. Moreover, the KER spectrum has two peaks centered at about 6.5 and 7.5 eV, as clearly seen in Figs. 2(c) and (d). As will be detailed in the following discussion, these peaks are due to one- and two-photon $X\,^2\Sigma^+ \to A\,^2\Pi$ transitions, respectively.

A.   One-photon transitions

Let us first consider the lower-energy peak centered at around 6.5 eV in Fig. 2(c). Here, we first take the "standard" approach to determining strong-field dissociation pathways by examining the KER and angular distributions [47]. The purple comb above the KER distribution indicates the expected KER values for one-photon $X\,^2\Sigma^+ \to A\,^2\Pi$ transitions from the indicated initial vibrational levels of the $X\,^2\Sigma^+$ state and leading to $N^+ + O^+$ dissociation. One can see that such transitions starting from $v' = 4$ and 5 match the measured KER for the 6.5-eV peak reasonably well. These transitions are near-resonant transitions to $v'' = 7$ and 9 of the $A\,^2\Pi$ state, respectively.

Next, we shift our attention to the angular distribution of this peak. Assuming the validity of the axial recoil approximation and that the initial angular distribution of the NO^{2+} molecules is isotropic, the change of the angular momentum quantum number, $\Delta\Lambda$, for the transition imprints itself on the angular distribution. Specifically, for an n-photon transition from a Σ state corresponding

FIG. 3.   Measured angular distributions of narrow KER ranges (indicated on each panel) for (a) 774 nm, 1×10^{14} W/cm^2 (b) 774 nm, 4×10^{14} W/cm^2 and (c) 387 nm, 1×10^{14} W/cm^2. The data in each panel is fitted with the indicated angular distribution (see text).

to $\Delta\Lambda = 0$ (parallel transition), the expected angular distribution follows $\cos^{2n}\theta$. For an n-photon transition leading to $\Delta\Lambda = \pm1$ (perpendicular transition), on the other hand, the expected distribution is $\sin^{2n}\theta$ [34, 47, 48]. The angular distribution for the 6.5-eV feature, shown in Fig. 3(a), fits a $\sin^2\theta$ distribution reasonably well, further supporting the idea that a one-photon $X\,^2\Sigma^+ \to A\,^2\Pi$ transition is responsible for the observed dissociation. Note that this $\sin^2\theta$ function does not match the data near $\cos\theta = \pm1$, as shown in Fig. 3(a), suggesting a minor contribution of another process involving parallel transitions.

As the KER and angular distributions suggest the dominant contributions of one-photon processes, we apply first-order perturbation theory to further examine the dissociation pathways leading to the lower-KER peak. The KER spectrum, $N(\mathrm{KER})$, is the sum of the dissociation probabilities multiplied by the FC factor:

$$\frac{dP}{dE''} = \sum_{v'} \mathcal{F}_{v'} \frac{dP_{v'}}{dE''}. \tag{2}$$

In Eq. 2, v' denotes the initial vibrational level in the $X\,^2\Sigma^+$ state, and E'' is the final total energy. Thus, $\mathrm{KER} = E'' - E_\infty$, where E_∞ is the dissociation limit.

FIG. 2.   (a) and (b) The yield of $N^+ + O^+$ as a function of KER and $\cos\theta$ for 774-nm pulses with peak intensity 4×10^{14} W/cm^2 and 1×10^{14} W/cm^2, respectively. (c) and (d) 1D KER projections of panels (a) and (b), respectively. In (c), the purple and magenta combs indicate expected KER values for one-photon and two-photon $X\,^2\Sigma^+ \to A\,^2\Pi$ transitions, respectively. The numbers above the combs indicate the initial vibrational level of the $X\,^2\Sigma^+$ state for these transitions.
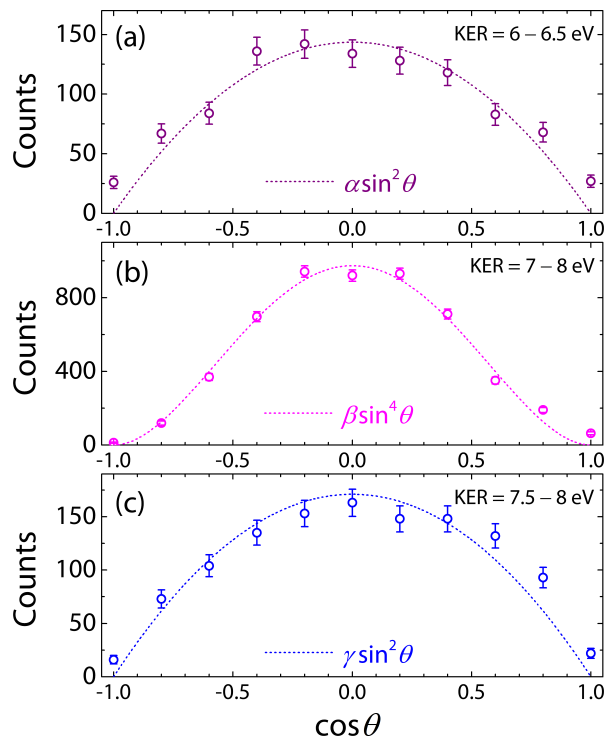
The dissociation probabilities given by first-order perturbation theory in the rotating-wave approximation [49] are

$$\frac{dP_{v'}}{dE''} = I_0 \frac{\pi}{4\sigma_E^2} |D_{v'}(E'')|^2 \exp\left[-\left(\frac{E''_{fi} - E_0}{\sqrt{2}\,\sigma_E}\right)^2\right]. \quad (3)$$

Here, I_0 is the laser peak intensity, σ_E is the laser energy bandwidth, and E_0 is the central photon energy. The quantity E''_{fi} is given by $E''-E_{v'}$, where $E_{v'}$ is the energy of the initial vibrational level in $X\,^2\Sigma^+$. $D_{v'}(E'')$ is the dipole matrix element:

$$D_{v'}(E'') = \langle\psi_{E''}|D|\psi_{v'}\rangle. \quad (4)$$

Here, $\psi_{E''}(R)$ is an energy-normalized vibrational resonance wave function or continuum wave function of the $A\,^2\Pi$ state. The $X\,^2\Sigma^+$–$A\,^2\Pi$ transition dipole moment, shown in Fig. 1(a), is denoted as D. The dipole matrix elements in Eq. 4 were computed at the central photon energy, i.e., $E'' = E_{v'} + E_0$. This is a reasonable approximation, as the continuum wave function does not change significantly within the bandwidth of the laser, and the transition dipole moment does not change substantially over the relevant range of internuclear distance, as shown in the inset in Fig. 1(a).

Note that Eq. 3 assumes that all the molecules undergoing transitions dissociate. While this is true for transitions to the vibrational continuum of the $A\,^2\Pi$ state, for transitions populating the $A\,^2\Pi$ state vibrational resonances, Eq. 3 must be multiplied by $1-\exp(-t/\tau_{v''})$ to account for the tunneling lifetimes of the resonances. Here, t is the NO^{2+} flight time in the spectrometer field that still allows identification of the $N^+ + O^+$ coincidence events [50]. This t is on the order of a few nanoseconds. The values of the tunneling lifetimes, $\tau_{v''}$, are taken from Baková et al. [42].

The computed dissociation probabilities for each initial state v' are shown in Fig. 4(a). The sharp line for the $v'=5$ transition arises due to the narrow width of the $v''=9$ resonance, which is on the order of 10^{-5} eV [42]. As shown, dissociation via $X\,^2\Sigma^+\,(v'=5) \rightarrow A\,^2\Pi\,(v''=9)$ is predicted to dominate. The tunneling lifetime of $v''=9$ is about 14 ps, allowing $N^+ + O^+$ to be detected. Dissociation from $X\,^2\Sigma^+(v' \leq 4)$, on the other hand, is unlikely due to the $>600\,\mu s$ tunneling lifetimes of the populated vibrational resonances in $A\,^2\Pi\,(v'' \leq 7)$ [42]. Moreover, the radiative decay rates of $v'' \leq 7$ in $A\,^2\Pi$ are dominant over those of tunneling by greater than three orders of magnitude [42]. The likelihood of dissociation by transitions with $v' \geq 6$ is also low relative to $v'=5$ dissociation, as the former are bound–free transitions, and the vibrational population decreases with increasing v', as shown in Fig. 1(b).

The dissociation probabilities are convoluted with the estimated KER resolution, treated as a gaussian distribution with width of 0.49 eV (FWHM) at 6.5-eV KER (see also Ref. [51]). The convoluted probability distributions were added together and scaled to the experimental data
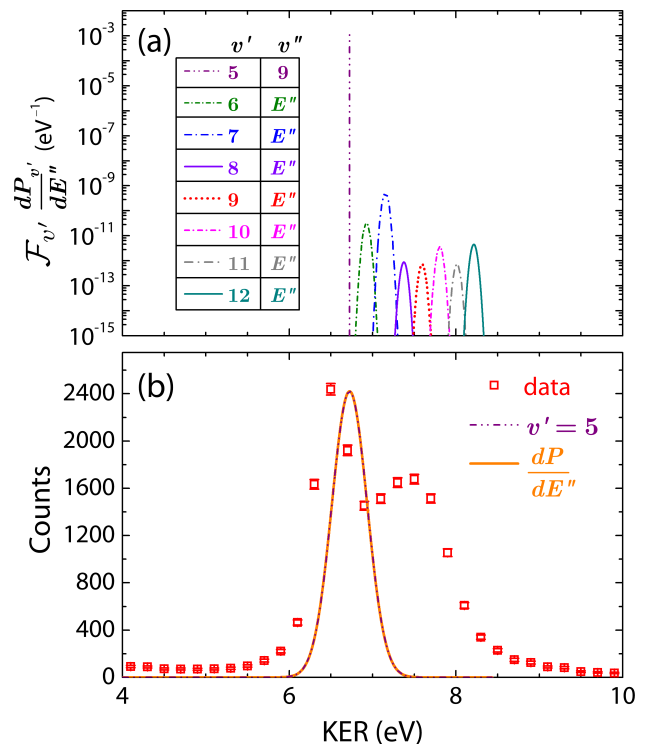

FIG. 4. (a) Dissociation probabilities. Here, E'' denotes the vibrational continuum of the $A\,^2\Pi$ state. (b) Comparison of the first-order perturbation theory and experimental KER spectra for 774-nm and peak intensity of 4×10^{14} W/cm^2. The purple dash-dotted curve shows the calculated dissociation probability for $v'=5$, and the solid orange curve shows $\frac{dP}{dE''}$ (Eq. 2). Due to the dominance of $v'=5$, these curves very nearly overlap. The calculations are convoluted with the instrumental resolution (see text) and scaled to the data.

at the lower-KER peak. The result, shown in Fig. 4(b) by the solid orange curve, agrees with the data to a reasonable extent but with a small shift to higher KER. This observed energy shift could be due to an energy scaling uncertainty of about 3% in our imaging setup [49]. Other possible causes of this discrepancy include small inaccuracies in the calculated potential energy curves.

Finally, it is important to note that while the lower-KER peak is reasonably well-reproduced by our perturbation theory calculations, the higher-KER peak is not. Thus, one-photon dissociation is not likely to be the dominant contribution to this higher-energy peak.

B. Two-photon transitions

Shown by the purple comb in Fig. 2(c), one-photon transitions from higher vibrational states of the $X\,^2\Sigma^+$ ground state, for example $v'=7-9$, would lead to KER matching that of the 7.5-eV peak. As mentioned above, however, these vibrational states have low initial population, and first-order perturbation theory from them does not reproduce this KER feature. On the other hand,
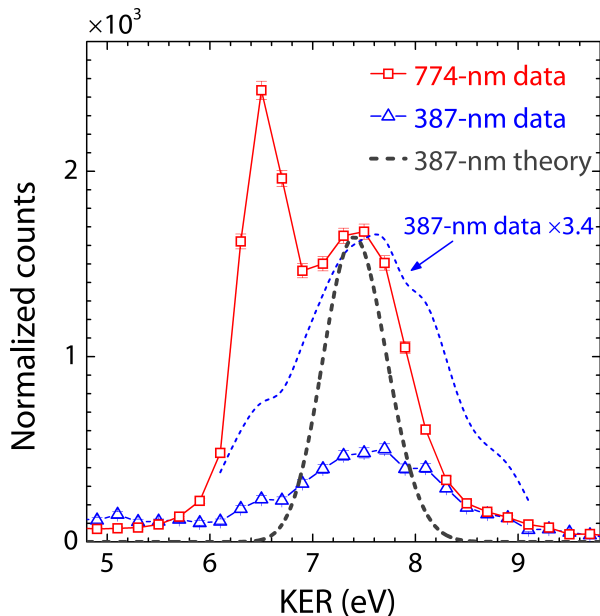
FIG. 5. KER spectra for 774-nm (peak intensity 4×10^{14} W/cm^2) and 387-nm (peak intensity 1×10^{14} W/cm^2) central wavelength pulses, normalized accounting for the total number of target molecules. The dashed blue line corresponds to the 387-nm results scaled to match the amplitude of the higher-KER peak in the 774-nm spectrum. The dashed dark gray line represents the calculated dissociation probability at 387 nm, convoluted with the KER resolution and scaled to the 774-nm data.

two-photon transitions from lower vibrational levels of the $X\,^2\Sigma^+$ state, such as $v' = 0-2$, which have higher initial population, lead to KER matching the higher-energy peak. These transitions are illustrated in Fig. 1(a) by the magenta "2ω" arrow, and their expected KER values are indicated by the magenta comb in Fig. 2(c).

Among the possible two-photon pathways leading to N$^+$ + O$^+$ dissociation are those involving intermediate near-resonant transitions, in addition to direct $X\,^2\Sigma^+ \rightarrow A\,^2\Pi$ transitions. For example, one photon may be absorbed to make a $X\,^2\Sigma^+$ ($v' = 1$) $\rightarrow A\,^2\Pi$ ($v'' = 2$) transition, followed by the absorption of a second photon to drive a $A\,^2\Pi$ ($v'' = 2$) $\rightarrow X\,^2\Sigma^+$ ($v' = 16$) transition. The $v' = 16$ vibrational resonance of the $X\,^2\Sigma^+$ state dissociates fast enough via spin-orbit coupling with a lifetime of 2.9 ns [42].

The angular distribution for the second KER peak, shown in Fig. 3(b), matches well with a $\sin^4\theta$ distribution, i.e., the expected distribution for two-photon perpendicular transitions (either direct or involving near-resonant transitions), further supporting the dominant role of two-photon transitions here.

To further confirm the role of two-photon transitions at 774 nm, we performed an additional measurement employing second-harmonic pulses at about 387-nm central wavelength. It is expected that the one-photon peak for the 387-nm pulses would appear at the same KER as

the two-photon peak for the 774-nm pulses. The 387-nm KER spectrum, shown overlaid with that of the 774-nm measurement in Fig. 5, does indeed match up reasonably well with the higher-KER peak measured with 774-nm pulses. The peak at 6.5 eV has also disappeared in the 387-nm KER spectrum, lending further credence to the idea that this peak in the 774-nm measurement is due to one-photon absorption. Furthermore, the angular distribution for the peak in the 387-nm data in Fig. 3(c) agrees well with a $\sin^2\theta$ distribution, confirming that it is due to the expected $X\,^2\Sigma^+ \rightarrow A\,^2\Pi$ one-photon perpendicular transitions.

Finally, the calculated $X\,^2\Sigma^+ \rightarrow A\,^2\Pi$ transition probability for one 387-nm photon, shown in Fig. 5, agrees reasonably well with the 387-nm data. These calculations are also convoluted with the estimated instrumental resolution as before.

As one may note from Fig. 5, first-order perturbation theory results in a peak that is noticeably narrower than that in the 387-nm measurement. The broadening of the measured spectrum relative to the theory is likely due to some leakage of the 774-nm fundamental beam through the dichroic filter used in our second harmonic generation setup [52]. While the angular distributions could in theory provide an indication of this leakage, the limited statistics of our 387-nm data prevent this. As the calculations reproduce the main feature in the data, further exploration is beyond the scope of this discussion. We thus conclude that our observations suggest that the higher-KER peak in the 774-nm data is indeed due to two-photon $X\,^2\Sigma^+ \rightarrow A\,^2\Pi$ transitions.

V. SUMMARY AND CONCLUSIONS

In strong-field studies of NO^{2+} fragmentation starting from neutral NO targets [53–56], the absorption of more than twenty 800-nm photons is required for double ionization. Hence, the NO^{2+} molecules probed in these experiments are most likely born near the laser beam focus and near the peak of the temporal profile. In contrast, in our study of an NO^{2+} ion beam, since ionization is not needed, one can expect low-order processes occurring in lower-intensity regions of the laser focal volume to play a more significant role. To emphasize this point, at the peak laser intensity of about 10^{14} W/cm^2, highlighted in this manuscript, ionization of NO^{2+} constitutes less than 1% of dissociation.

Indeed, as we have shown, the dominant dissociation pathways at these intensities are one- and two-photon transitions involving the lowest two electronic states, $X\,^2\Sigma^+$ and $A\,^2\Pi$. Through the examination of the KER and angular distributions at 774-nm and 387-nm central wavelength along with first-order perturbation theory calculations, we have uncovered the most likely pathways leading to the observed dissociation.

VI. ACKNOWLEDGMENT

[1] A. H. Zewail, Angew. Chem., Int. Ed. **39**, 2586 (2000).

[2] M. A. Yandell, S. B. King, and D. M. Neumark, Journal of the American Chemical Society **135**, 2128 (2013).

[3] R. D. Levine, Proc. Natl. Acad. Sci. **114**, 13594 (2017).

[4] M. S. Schuurman and A. Stolow, Annu. Rev. Phys. Chem. **69**, 427 (2018).

[5] J. Yang, X. Zhu, T. J. A. Wolf, Z. Li, J. P. F. Nunes, R. Coffee, J. P. Cryan, M. Gühr, K. Hegazy, T. F. Heinz, K. Jobe, R. Li, X. Shen, T. Veccione, S. Weathersby, K. J. Wilkin, C. Yoneda, Q. Zheng, T. J. Martinez, M. Centurion, and X. Wang, Science **361**, 64 (2018).

[6] Y. Albeck, K. Lunny, Y. Benitez, A. Shin, D. Strasser, and R. Continetti, Angew. Chem. **0** (2019), 10.1002/ange.201900386.

[7] P. Brumer and M. Shapiro, Annu. Rev. Phys. Chem. **43**, 257 (1992).

[8] A. Zewail, Pure Appl. Chem. **72**, 2219 (2000).

[9] M. Shapiro and P. Brumer, Rep. Prog. Phys. **66**, 859 (2003).

[10] M. Dantus and V. V. Lozovoy, Chem. Rev. **104**, 1813 (2004).

[11] P. Nuernberger, G. Vogt, T. Brixner, and G. Gerber, Phys. Chem. Chem. Phys. **9**, 2470 (2007).

[12] D. Keefer and R. de Vivie-Riedle, Acc. Chem. Res. **51**, 2279 (2018).

[13] J. L. White, B. J. Pearson, and P. H. Bucksbaum, J. Phys. B **37**, L399 (2004).

[14] E. Wells, K. J. Betsch, C. W. S. Conover, M. J. DeWitt, D. Pinkham, and R. R. Jones, Phys. Rev. A **72**, 063406 (2005).

[15] A. T. J. B. Eppink and D. H. Parker, Rev. Sci. Instrum. **68**, 3477 (1997).

[16] R. Dörner, V. Mergel, O. Jagutzki, L. Spielberger, J. Ullrich, R. Moshammer, and H. Schmidt-Böcking, Phys. Rep. **330**, 95 (2000).

[17] J. Ullrich, R. Moshammer, A. Dorn, R. Dörner, L. P. H. Schmidt, and H. Schmidt-Böcking, Rep. Prog. Phys. **66**, 1463 (2003).

[18] A. S. Alnaser, T. Osipov, E. P. Benis, A. Wech, B. Shan, C. L. Cocke, X. M. Tong, and C. D. Lin, Phys. Rev. Lett. **91**, 163002 (2003).

[19] B. J. Whitaker, *Imaging in molecular dynamics: technology and applications* (Cambridge University Press, 2003).

[20] A. S. Alnaser, X. M. Tong, T. Osipov, S. Voss, C. M. Maharjan, P. Ranitovic, B. Ulrich, B. Shan, Z. Chang, C. D. Lin, and C. L. Cocke, Phys. Rev. Lett. **93**, 183202 (2004).

[21] A. S. Alnaser, S. Voss, X. M. Tong, C. M. Maharjan, P. Ranitovic, B. Ulrich, T. Osipov, B. Shan, Z. Chang, and C. L. Cocke, Phys. Rev. Lett. **93**, 113003 (2004).

[22] A. G. Suits, Rev. Sci. Instrum. **89**, 111101 (2018).

[23] X. Gong, P. He, Q. Song, Q. Ji, K. Lin, W. Zhang, P. Lu, H. Pan, J. Ding, H. Zeng, F. He, and J. Wu, Optica **3**, 643 (2016).

[24] M. Kunitski, N. Eicke, P. Huber, J. Köhler, S. Zeller, J. Voigtsberger, N. Schlott, K. Henrichs, H. Sann, F. Trinter, L. P. H. Schmidt, A. Kalinin, M. S. Schöffler, T. Jahnke, M. Lein, and R. Dörner, Nat. Commun. **10**, 1 (2019).

[25] K. Sändig, H. Figger, and T. W. Hänsch, Phys. Rev. Lett. **85**, 4876 (2000).

[26] D. Pavičić, A. Kiess, T. W. Hänsch, and H. Figger, Phys. Rev. Lett. **94**, 163002 (2005).

[27] I. Ben-Itzhak, P. Q. Wang, J. F. Xia, A. M. Sayler, M. A. Smith, K. D. Carnes, and B. D. Esry, Phys. Rev. Lett. **95**, 073002 (2005).

[28] P. A. Orr, I. D. Williams, J. B. Greenwood, I. C. E. Turcu, W. A. Bryan, J. Pedregosa-Gutierrez, and C. W. Walter, Phys. Rev. Lett. **98**, 163001 (2007).

[29] H. Hultgren and I. Y. Kiyan, Phys. Rev. A **84**, 015401 (2011).

[30] U. Lev, L. Graham, C. B. Madsen, I. Ben-Itzhak, B. D. Bruner, B. D. Esry, H. Frostig, O. Heber, A. Natan, V. S. Prabhudesai, D. Schwalm, Y. Silberberg, D. Strasser, I. D. Williams, and D. Zajfman, J. Phys. B **48**, 201001 (2015).

[31] D. M. Kandhasamy, Y. Albeck, K. Jagtap, and D. Strasser, J. Phys. Chem. A **119**, 8076 (2015).

[32] A. Shahi, Y. Albeck, and D. Strasser, J. Phys. Chem. A **121**, 3037 (2017).

[33] P. Wustelt, F. Oppermann, L. Yue, M. Möller, T. Stöhlker, M. Lein, S. Gräfe, G. G. Paulus, and A. M. Sayler, Phys. Rev. Lett. **121**, 073203 (2018).

[34] J. McKenna, A. M. Sayler, F. Anis, N. G. Johnson, B. Gaire, U. Lev, M. A. Zohrabi, K. D. Carnes, B. D. Esry, and I. Ben-Itzhak, Phys. Rev. A **81**, 061401 (2010).

[35] P. Q. Wang, A. M. Sayler, K. D. Carnes, J. F. Xia, M. A. Smith, B. D. Esry, and I. Ben-Itzhak, Phys. Rev. A **74**, 043411 (2006).

[36] A. M. Sayler, *Measurements of Ultrashort Intense Laser-Induced Fragmentation of Simple Molecular Ions*, Ph.D. thesis, Kansas State University (2008).

[37] R. Trebino, K. W. DeLong, D. N. Fittinghoff, J. N. Sweetser, M. A. Krumbügel, B. A. Richman, and D. J. Kane, Rev. Sci. Instrum. **68**, 3277 (1997).

[38] The peak intensity of the pulse is evaluated by picking off a portion of the beam after the parabolic focusing mirror and imaging the laser beam profile with a CCD camera, as described in Ref. [39].

[39] A. M. Sayler, P. Q. Wang, K. D. Carnes, and I. Ben-Itzhak, J. Phys. B **40**, 4367 (2007).

[40] R. W. Boyd, *Nonlinear Optics, Third Edition*, 3rd ed. (Academic Press, Inc., Orlando, FL, USA, 2008).

[41] D. Edvardsson, M. Lundqvist, P. Baltzer, B. Wannberg, and S. Lunell, Chem. Phys. Lett. **256**, 341 (1996).

[42] R. Baková, J. Fišer, T. Šedivcová Uhlíková, and V. Špirko, J. Chem. Phys. **128**, 144301 (2008).

[43] F. von Busch and G. H. Dunn, Phys. Rev. A **5**, 1726 (1972).

[44] H. Helm and P. C. Cosby, J. Chem. Phys. **86**, 6813 (1987).

[45] Z. Amitay, A. Baer, M. Dahan, J. Levin, Z. Vager, D. Zajfman, L. Knoll, M. Lange, D. Schwalm, R. Wester, A. Wolf, I. F. Schneider, and A. Suzor-Weiner, Phys. Rev. A **60**, 3769 (1999).

[46] E. Y. Sidky and I. Ben-Itzhak, Phys. Rev. A **60**, 3586 (1999).

[47] A. M. Sayler, P. Q. Wang, K. D. Carnes, B. D. Esry, and I. Ben-Itzhak, Phys. Rev. A **75**, 063420 (2007).

[48] A. Hishikawa, S. Liu, A. Iwasaki, and K. Yamanouchi, J. Chem. Phys. **114**, 9856 (2001).

[49] J. McKenna, F. Anis, B. Gaire, N. G. Johnson, M. Zohrabi, K. D. Carnes, B. D. Esry, and I. Ben-Itzhak, Phys. Rev. Lett. **103**, 103006 (2009).

[50] B. Jochim, R. Erdwien, Y. Malakar, T. Severt, B. Berry, P. Feizollah, J. Rajput, B. Kaderiya, W. L. Pearson, K. D. Carnes, A. Rudenko, and I. Ben-Itzhak, New J. Phys. **19**, 103006 (2017).

[51] The KER resolution in our experimental setup scales with $\sqrt{KER}$ [35]. We estimate the KER resolution in the present measurement by scaling from a previous measurement of dissociation of vibrationally-cold CO^{2+} [34], wherein the instrumental broadening dominated the width of the KER peak.

[52] We estimate the fundamental beam leakage to be on the order of 1%. Under these circumstances, the low-energy edge of the KER spectrum could be due to the one-photon 774-nm transitions previously discussed. The high-energy portion of the KER spectrum, on the other hand, could be due to two-photon transitions involving absorption of one photon of the fundamental beam followed by absorption of one photon of the second-harmonic beam.

[53] A. Talebpour, S. Larochelle, and S. L. Chin, J. Phys. B **30**, 1927 (1997).

[54] C. Guo and K. Wright, Phys. Rev. A **71**, 021404 (2005).

[55] C. Guo, J. Phys. B **38**, L323 (2005).

[56] J. Wu, H. Zeng, and C. Guo, J. Phys. B **39**, 3849 (2006).

Chapter 5

Adaptive femtosecond control

5.1 Scope

This chapter focuses on studies using shaped femtosecond laser pulses to control molecular dynamics through the use of a closed-loop feedback scheme that involves an evolutionary algorithm. The work highlighted in this chapter was a collaborative effort with Eric Wells from Augustana University, who is the driving force for this research direction.

5.2 Introduction

As highlighted in Chapter 1, ultrashort, intense laser pulses are compelling tools for probing molecular processes. The use of optimally-tailored laser pulses to control molecular dynamics, a method first proposed by Richard S. Judson and Herschel Rabitz [115], has been an active field of research over the past few decades [9]. In this approach, a genetic algorithm (GA) [116] guides the search for an optimal laser pulse to perform a given control objective, for instance, the cleavage of a certain molecular bond. This approach can be taken without prior knowledge of the underlying dynamics and has hence been described as "solving Schrödinger's equation exactly in real time" [115].
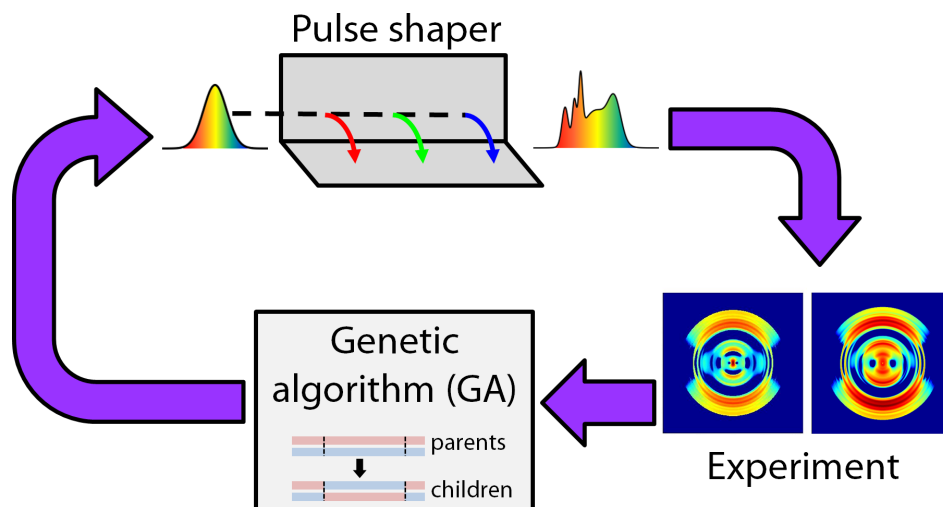
Figure 5.2.1: Schematic of the adaptive closed-loop control method. The experimental images correspond to two different fragment species whose relative ratio may be controlled using this method.

The idea of a closed-loop control scheme, inspired by evolutionary principles [9, 115, 117], is illustrated in Fig. 5.2.1. Generally speaking, the experiment begins with a seed "generation," consisting of randomly-shaped laser pulses with random "genomes." The shaped laser pulses interact with the target molecules in an experimental apparatus and are scored with a "fitness" value based on their performance of the control objective. The fitness values are relayed to the GA, and the pulses with the highest fitness values in every generation survive to "mate" and produce the next generation of pulses. The process repeats itself for subsequent generations until the GA converges and "learns" the optimal solution.

This type of feedback scheme has been employed for controlling the dynamics of a variety of systems, including diatomics, simple polyatomics, relatively large organic molecules, biomolecules, and clusters [9]. These efforts have involved different pulse shaping methods, including phase and/or amplitude shaping and polarization shaping [118, 119]. The robustness of this adaptive feedback approach has been demonstrated by the markedly better fitness values of optimally-shaped pulses compared to that of FTL pulses [9].

5.3 Our closed-loop control experiments

In our specific case, an acousto-optic pulse dispersive filter (AOPDF) pulse shaper (Fastlite Dazzler) [120, 121] is used to perform phase-only shaping of the pulses. The bandwidth of the laser is divided into sixteen sections, and the phases or "genes" are applied to these sections. The pulses are transported to either a time-of-flight or VMI spectrometer, which provide measured feedback for the GA. Typically, the control objective to be enhanced (or suppressed) is a ratio of fragment or fragment-pair yields. The latter allows for more specificity in optimizing a fragmentation channel. We have utilized this type of approach in several previous studies, e.g., Refs. [96, 122]. Fig. 5.3.1 illustrates the convergence of the genomes for a typical run.
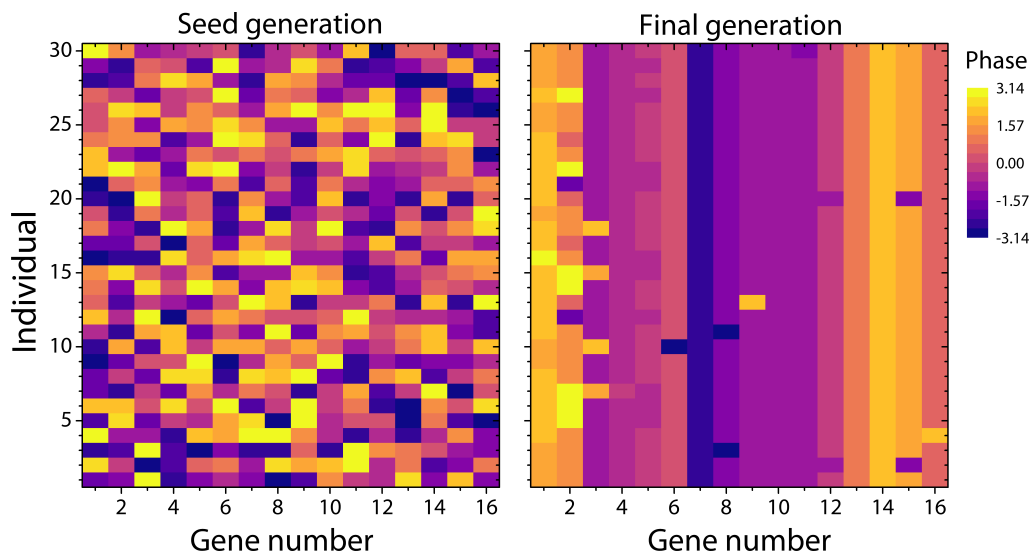
Figure 5.3.1: Genomes at the beginning and end of a GA run. The genomes of the laser pulses in the seed generation are random, while those of generation 40, the final generation, have converged.

5.4 Connection to ion beam studies

As the resulting pulses from closed-loop pulse shaping experiments can be quite complex, interpretation is often difficult [117]. Therefore, a strong synergy connects these adaptive

control experiments to basic experiments probing specific questions, such as those we perform on ion beam targets. While closed-loop control experiments pinpoint where understanding of the underlying dynamics is needed, basic experiments carry equal importance, as they provide insight into the dynamics that might underlie control.

5.5 Adaptive strong-field control of vibrational population in NO^{2+}

This section contains a paper published in *The Journal of Chemical Physics* [123] demonstrating the use of a closed-loop scheme to control the ratio of non-dissociative to dissociative double ionization of NO molecules, i.e., the $NO^{2+}/(N^+ + O^+)$ ratio. Significant enhancement and suppression of this ratio are achieved relative to the results of an FTL pulse. The mechanism underlying this control is thought to be selective population of the vibrational states of NO^{2+}. More specifically, pulses that maximize the $NO^{2+}/(N^+ + O^+)$ ratio predominantly populate the lower vibrational levels of NO^{2+}, whereas pulses that minimize the ratio tend to populate the higher-lying vibrational levels that more readily dissociate.

The following paper is reproduced from O. Voznyuk, B. Jochim *et al.* J. Chem. Phys. **151**, 124310 (2019), with the permission of AIP publishing.

Adaptive strong-field control of vibrational population in NO²⁺

View Online   Export Citation   CrossMark

O. Voznyuk,[1,a)] Bethany Jochim,[1,2,a)] (ID) M. Zohrabi,[2] (ID) Adam Broin,[1] R. Averin,[1] K. D. Carnes,[2] (ID)
I. Ben-Itzhak,[2] (ID) and E. Wells[1,b)] (ID)

AFFILIATIONS

[1] Department of Physics, Augustana University, Sioux Falls, South Dakota 57197, USA
[2] J.R. Macdonald Laboratory, Department of Physics, Kansas State University, Manhattan, Kansas 66506, USA

[a)] Contributions: O. Voznyuk and B. Jochim contributed equally to this work.
[b)] Electronic mail: eric.wells@augie.edu

ABSTRACT

An adaptive closed-loop system employing coincidence time-of-flight feedback is used to determine the optimal pulse shapes for manipulating the branching ratio of NO dications following double ionization by an intense laser pulse. Selection between the long-lived NO^{2+} and the dissociative $N^+ + O^+$ final states requires control of the vibrational population distribution in the transient NO^{2+}. The ability to both suppress and enhance NO^{2+} relative to $N^+ + O^+$ is observed, with the effectiveness of shaped pulses surpassing near Fourier transform-limited pulses by about an order of magnitude in each direction, depending on the pulse energy. The control is subsequently investigated using velocity map imaging, identifying plausible dissociation pathways leading to $N^+ + O^+$. Combining the information about the $N^+ + O^+$ dissociation with a well-defined control objective supports the conclusion that the primary control mechanism involves selectively populating long-lived NO^{2+} vibrational states.

https://doi.org/10.1063/1.5115504

I. INTRODUCTION

In adaptive femtosecond control experiments,[1–3] measurement-based feedback is used in conjunction with a learning algorithm to tailor an ultrafast laser pulse to optimize a particular process. While adaptive femtosecond control has been widely applied,[4–19] controlling the photofragmentation and rearrangement of molecules in the gas phase has been an area that has received particular attention.[3,20–33] Nearly all of these experiments describe an ability to influence the fragmentation patterns of the target molecules, but only a smaller subset report progress toward understanding the mechanisms underlying the control.[34–47] Given the complexity of the intense laser-molecule interaction and the nearly infinite variety of laser pulses that can be produced by modern pulse shaping devices,[48–50] it is not surprising that unraveling the physical process behind the control is often difficult.

In many of these molecular fragmentation experiments, the feedback signal is derived from fragment ion yields acquired via time-of-flight (TOF) mass spectrometry. The advantages of this method are clear; the data acquisition is relatively straightforward, and when a current mode is employed (as opposed to counting individual ions), the yields may be obtained quickly, which is generally a requirement for effective feedback in adaptive control experiments. These single fragment yields, however, are uncorrelated, and so it becomes difficult to separate various final products. A somewhat simplistic example of this problem is illustrated by a hypothetical molecule AB, for which the $A^+ + B^+$ channel cannot generally be separated from the $A^+ + B$ channel since both contribute to the A^+ yield.

In addition, a large intensity range is present in the focal volume. The range of contributing intensities can be reduced by operating near the appearance intensity of a process, but this is often incompatible with the experimental desire for timely feedback in closed-loop control. Subsequent interpretation of the results can then become convoluted due to the ambiguities in the intensity and photofragment channel. More specific control objectives can focus
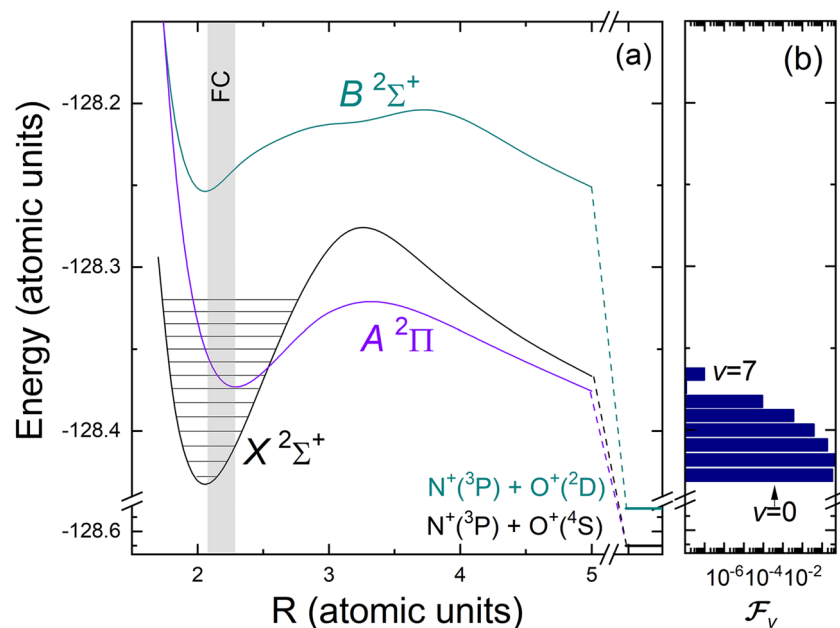
FIG. 1. (a) The lowest lying doublet potential energy curves for NO^{2+}, adapted from Ref. 53. The energies at the separate atom limit are -128.65 a.u. for the X $^2\Sigma^+$ and A $^2\Pi$ states and -128.52 a.u. for the B $^2\Sigma^+$ state. The shaded box marks the region of vertical Franck-Condon (FC) transitions from neutral NO. (b) Franck-Condon populations for the X $^2\Sigma^+$ state of NO^{2+} assuming field-free NO $\rightarrow$ NO^{2+} vertical ionization.

the search process on a more limited set of pathways and intensity range and therefore inform efforts to understand the resulting solution produced by the learning algorithm.

We have developed a coincidence time-of-flight feedback (CTOF) technique[51] to provide more specific feedback for closed loop control. In our initial experiment with this CTOF feedback, we enhanced or suppressed the ratio of CO^{2+} to $C^+ + O^+$ following strong-field double ionization of CO molecules. This was particularly interesting in CO^{2+}, since only the $v = 0$ and $v = 1$ states of the $^3\Pi$ ground state and the $v = 0$ state of the lowest $^1\Sigma^+$ state live long enough to be detected as CO^{2+} in our experimental setup, while all the higher vibrational states rapidly decay to $C^+ + O^+$. Thus, the ability to unambiguously select between CO^{2+} and $C^+ + O^+$ represented control of vibrational population.

As shown in Fig. 1, NO^{2+} is somewhat similar to CO^{2+} in that higher vibrational levels ($v > 12$) of the X $^2\Sigma^+$ ground electronic state dissociate within 18 ns due to spin-orbit coupling with the A $^2\Pi$ state. The $v \geq 8$ vibrational states of the A $^2\Pi$ excited electronic state decay by tunneling with a lifetime less than or equal to ~45 ns.[52] In addition, these two states are easily coupled by one-photon transitions, leading to dissociation, while the B $^2\Sigma^+$ state is well separated from the X $^2\Sigma^+$ and A $^2\Pi$ states. Experimentally, the $N^+ + O^+$ and NO^{2+} channels offer similar feedback as the initial CO experiment,[51] but the increased complexity of the relevant potential energy curves provides an additional interpretation challenge.

With this increased complexity in mind, we have employed velocity map imaging[54–58] (VMI) to examine the differences in the three-dimensional momentum images produced by unshaped and optimized laser pulses. In diatomic molecules, the angle-resolved kinetic energy release (E_k) data can be used in conjunction with a Floquet approach[59–61] to understand which dissociation pathways are enhanced by the optimized pulses. Our first efforts using this combination of VMI measurements and Floquet analysis resulted

in an improved understanding of control experiments with CO molecules.[62]

In this article, we discuss the results from adaptive femtosecond control experiments using CTOF feedback to control the vibrational population of the transient NO^{2+} molecular ion. We are able to either increase or decrease the $NO^{2+}/(N^+ + O^+)$ ratio by approximately an order of magnitude, primarily through suppression or enhancement of the NO^{2+} yield. The results are then analyzed with the aid of VMI measurements of the dissociating N^+ and O^+ photofragments, as well as kinetic energy release distributions evaluated from coincidence time-of-flight measurements.

II. EXPERIMENTAL METHOD

Our experimental setup consists of an ultrafast laser system equipped with an acousto-optic programmable dispersive filter (AOPDF)[49] pulse shaping device and a high resolution time-of-flight mass spectrometer, linked by a control computer running the genetic algorithm (GA) that uses the feedback signals to determine the optimal pulse shapes. This is illustrated in Fig. 2(a). The laser pulses are provided by a Ti:sapphire laser system with a center wavelength of 788 nm, a pulse energy of approximately 1 mJ, and a repetition rate of 2.0 kHz. The near-Fourier transform-limited (FTL) pulse duration is approximately 40 fs (FWHM in intensity) following passage through the AOPDF, multipass amplifier, and transport optics to the vacuum chamber. In these measurements, the AOPDF was only used to control the spectral phase, and therefore, the pulse energy remains constant as the pulse characteristics are changed (note that the pulse intensity changes as pulse duration is modified). Laser pulse characteristics were measured using second harmonic generation frequency-resolved optical gating (SHG FROG).[50,63]
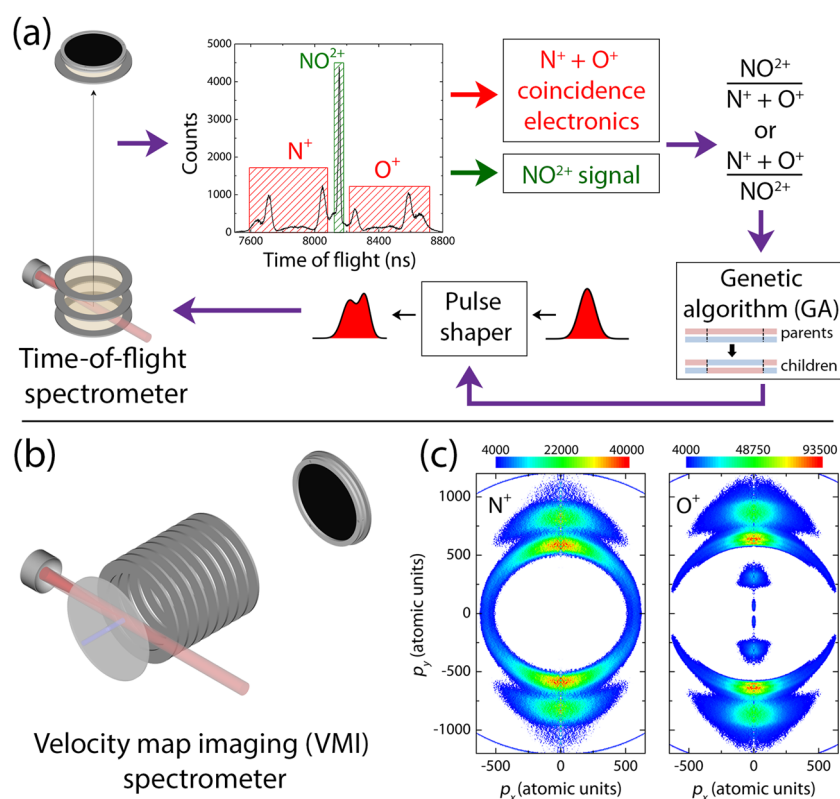
FIG. 2. (a) A schematic of the CTOF closed-loop control scheme. The NO^{2+} ions were measured along with coincident $N^+ + O^+$ events using a high-resolution TOF spectrometer.[51] The boxes on the TOF spectra conceptually represent the gates on the ions of interest. (b) Once the optimal pulses were identified, the interaction between the pulses and NO was probed with velocity map imaging in a different spectrometer.[58,62,64] The laser pulses were focused into the CTOF and VMI spectrometers by identical $f = 75$ mm spherical mirrors. By matching the incoming laser beam diameters, the focal conditions were similar in both measurements. (c) Momentum distributions of N^+ (left) and O^+ (right) photofragments obtained via velocity map imaging. The laser polarization direction is in the y-direction in both panels. The data presented are for measurements using FTL laser pulses at 0.04 mJ/pulse or approximately 5×10^{14} W/cm^2. While VMI provides angular information, it lacks the coincidence condition that identifies the $N^+ + O^+$ channel.

The laser beam was focused by an $f = 75$ mm spherical mirror to a point in the extraction region of a two-stage Wiley-McLaren[65] time-of-flight (TOF) spectrometer. In most of these experiments, the pulse energy was attenuated to between 0.02 and 0.06 mJ, although some data were recorded at higher pulse energy. This translates to a peak intensity of about $3-8 \times 10^{14}$ W/cm^2 for a FTL pulse and a beam waist of ~10 μm. The TOF spectrometer is located in an ultrahigh vacuum chamber that had a base pressure of about 5×10^{-10} Torr. Typical target pressures for the experiment were in the low 10^{-8} Torr range and were adjusted using a precision leak valve to control the counting rate. The laser beam was linearly polarized with the polarization parallel to the TOF spectrometer axis. Ions were detected by a microchannel plate (MCP) detector.[66] Importantly, the spectrometer did not use a small aperture along the polarization (TOF) axis as is often the case in laser-initiated TOF measurements (for example, in one of our previous experiments[67]), therefore avoiding discrimination in the angular distribution of the resulting ions.

As described more fully in a previous publication,[51] the signals from the MCP are processed on-the-fly to determine the NO^{2+} and coincident $N^+ + O^+$ rates that are used to determine the fitness value for the control objective. A photodiode monitors the laser pulses and that timing signal is converted to a NIM-standard pulse via a constant fraction discriminator and delayed until shortly before the N^+ arrival time on the MCP. This delayed photodiode signal starts three time-to-amplitude converters (TAC). The MCP signals are amplified, processed by a constant fraction discriminator, and used as the

stop signals on each of the TACs. Each TAC is used in single-channel analyzer mode, producing an output only in cases in which the ion signal falls within a specified time window appropriate for N^+, NO^{2+} and O^+ events. The O^+ TAC is gated by the condition that the N^+ TAC has produced an output signal, thus producing a signal for $N^+ + O^+$ coincidence events. The rates from the NO^{2+} and the gated O^+ TAC outputs are converted to an analog signal, averaged over some time constant (typically about 5–10 s), and sent to the control computer. These rates are used to evaluate the "fitness" of the GA control objective: $NO^{2+}/(N^+ + O^+)$ or $(N^+ + O^+)/NO^{2+}$.

Our GA implements tournament selection, two-point crossover, elitism, and a moderate 1% mutation rate per gene.[43,51,58] Typically, 40–50 individuals populate each generation, and the algorithm ran for 20–40 generations, depending on the convergence rate and the laser stability. A constant, approximately equal to 10% of the denominator channel of the control objective obtained with a FTL pulse, is used to prevent high fitness values when no denominator signal is present.

Once the closed-loop adaptive control measurement has optimized the pulse shape corresponding to a particular control objective, the result is examined using two other techniques. First, the TOF spectrum is recorded using a time-to-digital converter in full multihit mode, thus correlating all the "stop" signals associated with a single "start" signal from the photodiode that monitors the laser pulse. This allows more precise measurements of the true coincidence rate since random coincidences (N^+ and O^+ pairs that do not arise from the same molecule) and lost fragments (ion-pairs in which
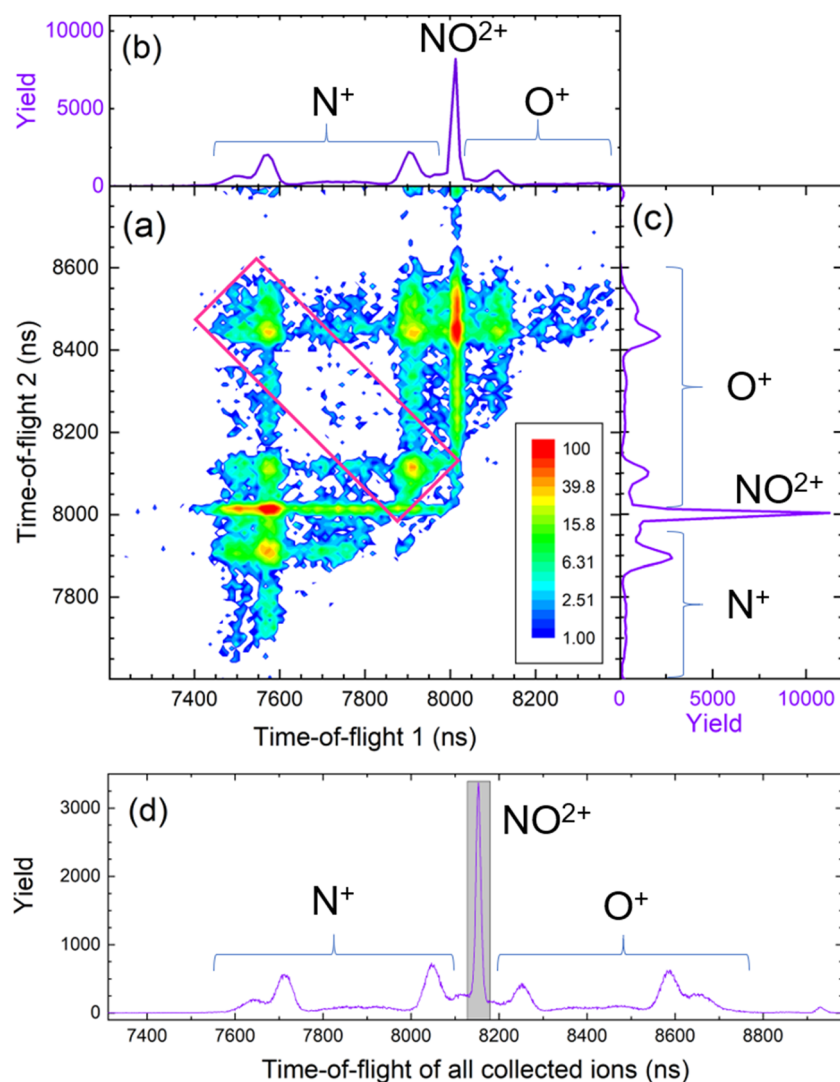
FIG. 3. One- and two-dimensional representations of coincidence-time-of-flight data of NO^{2+} dissociation. Panel (a) shows the coincidence yield (log scale) as a function of the TOF of the first and second fragments. The magenta box identifies $N^+ + O^+$ coincidences. Panels (b) and (c) show the yield vs TOF of the first and second fragments, respectively, integrated over the yield of the other fragment. Panel (d) shows the yield vs time-of-flight for all fragments. The shaded area in (d) indicates the region from which the NO^{2+} yield is determined. Panels (a)–(c) have their time resolution compressed by a factor of ten to control the size of the two-dimensional spectrum, while panel (d) shows higher 1 ns/channel time resolution. The data presented were obtained with FTL laser pulses at 0.04 mJ/pulse or approximately 5×10^{14} W/cm^2. The lack of events in the center of the coincidence stripe indicates a strong preference for the ions to be ejected along the polarization (TOF) direction. By rotating and projecting the events within the diagonal box shown in panel (a), the $P(E_k)$ distribution for the coincidence events may be evaluated from the time-difference between the ion-pairs.[68,69]

one ion is lost due to detection efficiencies less than one) can be subtracted.[68] A typical coincidence time-of-flight (CTOF) plot is shown in Fig. 3. The corrected $N^+ + O^+$ yield and the NO^{2+} yield from the same measurement, shown in Fig. 3, were used to derive the value of the control objective reported in Sec. III. As described later, the CTOF data can also be used to deduce the fragment dissociation energy.

Figure 3 shows a moderate number of purely random coincidences, such as $N^+ + NO^{2+}$. Experimentally, controlling these random coincidence rates is the most difficult part of the measurement, since the adaptive control loop requires a relatively high rate for feedback. Too high of a target gas pressure, however, can increase the random coincidence rate to a level that will produce spurious feedback. Balancing the overall ion production rate is important and in some cases can limit the effective dynamic range of the experiment. This can be partially avoided by starting the experiment at a higher

gas pressure until the fitness values begin to "take off" and then stopping the experiment and reducing the gas pressure. The GA is then restarted from the preceding generation.

The second part of the postoptimization analysis is to obtain the momentum distribution, and therefore the E_k and angular distribution, of the dissociating fragments using VMI. Specifically, the N^+ and O^+ fragments produced by the optimally shaped and FTL laser pulses were measured using a VMI spectrometer.[58,62,64] While the VMI spectrometer is different from the Wiley-McLaren TOF spectrometer, the laser focusing optic is identical ($f = 75$ mm), and care is taken to reproduce the laser beam profile as closely as possible to the conditions of the CTOF measurement. To verify that this was achieved, we checked that the details of the TOF spectrum obtained using the VMI spectrometer, such as the ratio of the various ions, were the same as expected from earlier measurements with the TOF spectrometer. The TOF spectra could not be exactly matched,

however, due to the differences in the TOF resolution between the two spectrometers and the different laser polarization direction relative to the TOF axis used in the two setups.

The raw two-dimensional VMI data are inverted to recover a slice through the center of the three-dimensional momentum distribution using a modified "onion-peeling" or "back-projection" algorithm as described by Rallis *et al.*[58] Several other methods[70–72] of performing the inverse-Abel transformation were also tested to ensure that any relevant features were not due to numerical artifacts associated with the inversion process.

The probability of dissociation as a function of kinetic energy release, $P(E_k)$, can also be evaluated from CTOF data[68,69] by using the difference in arrival times of the coincident N^+ and O^+ fragments, although the angular distribution cannot be measured as directly as with VMI. The two methods are complimentary, since the CTOF-generated $P(E_k)$ distribution can be correlated with $N^+ + O^+$ coincidences, while the VMI-derived $P(E_k)$ distribution measures all N^+ or, separately, all O^+ ions, including those from different charge states of the intermediate NO^{q+} ions.

For our two-stage Wiley-McLaren[65] time-of-flight (TOF) spectrometer, the kinetic energy release from dissociative ionization is

$$E_k = \frac{(V_2 - V_1)^2}{8md^2} q^2 \Delta t^2, \qquad (1)$$

where V_2 and V_1 are the voltages on the extraction and acceleration meshes, respectively, d is the distance between the meshes, m and q are the mass and charge of the ion, and Δt is the time between the forward and backward traveling ions.[68] The associated probability of dissociation as a function of E_k is

$$P(E_k) = \left[t_{21}(E_k, 0^\circ) - t_{21}(E_k, 180^\circ)\right] \frac{dt_{21}}{dE_k} \frac{dY}{dt_{21}}, \qquad (2)$$

where $t_{21}(E_k, 0^\circ)$ and $t_{21}(E_k, 180^\circ)$ (i.e., $\theta = 0^\circ$ and 180°) associated with the short-TOF fragment having initial velocity toward and away-from the recoil detector, respectively, are the maximum and minimum time differences, respectively. dY/dt_{21} is the numerical time derivative of the large time-difference side of the spectrum. The $P(E_k)$ distributions obtained with both VMI and CTOF methods are shown in Fig. 4, which reveals that the KER of the $N^+ + O^+$ channel falls within the 5–9 eV range.

In summary, the experimental procedure consists of two steps: (1) The optimization step in which the learning algorithm searches for a pulse shape guided by CTOF feedback and (2) the subsequent analysis step, in which multihit TOF spectra, VMI data, and SHG-FROG pulse measurements are recorded using the optimized laser pulses that are obtained in the first step.

III. RESULTS AND DISCUSSION

The $NO^{2+}/(N^+ + O^+)$ ratio changes with the pulse intensity, as shown in Fig. 5, for FTL pulses of about 40 fs FWHM in duration. As the intensity increases, the ratio of nondissociative to dissociative double ionization decreases, dropping from 4.0 at 2×10^{14} W/cm^2 to 0.23 at 7×10^{15} W/cm^2. The fact that the $NO^{2+}/(N^+ + O^+)$ ratio decreases as the intensity increases can be attributed to the fact that highly excited vibrational states of NO^{2+} ($v \geq 12$ for the electronic ground state) rapidly dissociate, and these states, including excited electronic states, are more readily populated at higher intensities. For this reason, the main control experiments were conducted at intensities between 5 and 8×10^{14} W/cm^2 for which the $NO^{2+}/(N^+ + O^+)$ ratio was near unity and simple intensity changes (i.e., "trivial control"[3]) might not have a dramatic impact on this ratio.

We did, however, examine the effectiveness of the control at higher pulse energies, in light of several suggestions in the literature that the behavior of NO might evolve as the intensity increases.[53,73] In these higher energy experiments, the $NO^{2+}/(N^+ + O^+)$ ratio could be enhanced by a factor of 3.9 over the result with a FTL pulse. Attempts to minimize the same ratio were quantitatively
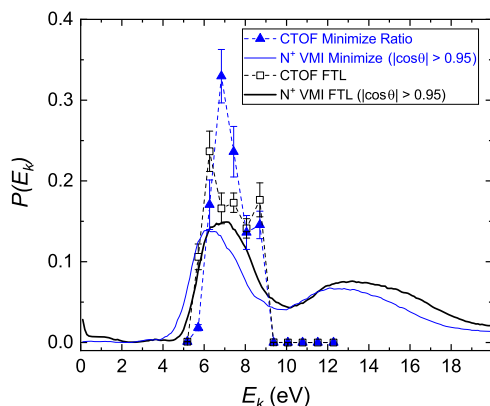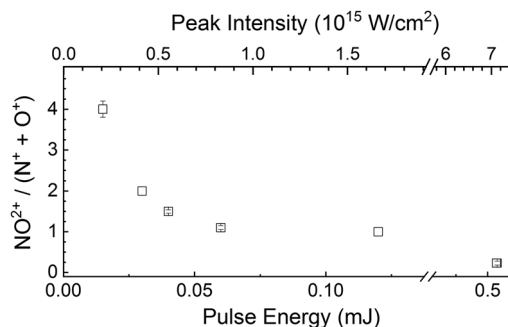

FIG. 4. The probability of dissociation, $P(E_k)$, as a function of E_k for FTL pulses (black) and pulses that minimize the $NO^{2+}/(N^+ + O^+)$ ratio (blue) at 0.04 mJ/pulse. The probabilities are obtained using two different methods. The symbols are a result of analysis of the CTOF data shown in Fig. 3 (as described in the text), while the solid lines represent the VMI data. Specifically, the solid lines are projections of the density plots shown in Figs. 7(a) and 7(b). The CTOF-derived probability unambiguously identifies the $N^+ + O^+$ coincidence channel, while the VMI-derived data have higher KER resolution but are recorded for all N^+ ions, i.e., including channels such as $N^+ + O$. Since the CTOF-data in Fig. 3 fall almost exclusively along the polarization direction, the VMI-derived data are restricted to $|\cos \theta| > 0.95$ for comparison.

FIG. 5. The $NO^{2+}/(N^+ + O^+)$ ratio for 40 fs FWHM near-Fourier transform limited (FTL) pulses as a function of pulse energy. The corresponding intensity is shown on the upper axis. The error bars represent the statistical uncertainty including "lost fragment" and random coincidence corrections.

TABLE I. The measured $NO^{2+}/(N^+ + O^+)$ ratio acquired with different pulse energies. The different columns represent the values obtained with FTL pulses as well as pulses optimized to maximize or minimize this ratio.

Pulse energy (mJ)	FTL ratio	Maximize ratio	Minimize ratio
0.015	4.0 ± 0.2		
0.03	2.0 ± 0.1		
0.04	1.50 ± 0.04	2.8 ± 0.9	0.80 ± 0.05
0.06	1.10 ± 0.05	13.8 ± 2.1	0.90 ± 0.03
0.06		6.0 ± 0.9	0.77 ± 0.04
0.12	1.0 ± 0.1		
0.52	0.23 ± 0.05	0.9 ± 0.2	0.0001 ± 0.0002
0.51	0.23 ± 0.10	0.7 ± 0.2	0.0005 ± 0.0004

more successful, with essentially all the NO^{2+} yield eliminated. The control results for all measured pulse energies are summarized in Table I.

The ability to decrease the $NO^{2+}/(N^+ + O^+)$ ratio with higher energy pulses is unsurprising, since all that is required is that the NO^{2+} yield be reduced. As the pulse energy increases, the laser-molecule interaction becomes more nonperturbative in character. As a result, there are many ways[21,74,75] the lower-lying NO^{2+} X $^2\Sigma^+$ vibrational population can be excited to dissociative levels, including nonresonant dynamic Stark shifts.[76,77] A signature that strong-field dynamics, such as the nonresonant dynamic Stark shifts, are dominant is the depletion of the ground state,[78] which we observe as a NO^{2+} yield that is consistent with zero.

On the surface, it would seem more surprising that the $NO^{2+}/(N^+ + O^+)$ ratio could be enhanced at these higher intensities. Some of this enhancement, however, can be explained by the range of intensities in the focal volume. While the $N^+ + O^+$ coincidence condition selects a certain intensity range from within the focal volume, the NO^{2+} yield need not arise from the same focal volume as the $N^+ + O^+$ ion-pairs. Thus, at peak intensities where the dissociative double ionization dominates, the NO^{2+} can still be produced by slightly lower intensity portions of the focal volume.

Another feature of the higher pulse energy experiments is the significant complexity of the optimized pulses, for both maximizing and minimizing $NO^{2+}/(N^+ + O^+)$. While it may be possible to unravel the mechanisms that occur in these complex pulse shapes at higher intensities,[26,27,37,44,79,80] attempting to understand the control mechanisms at lower pulse energies seems a more promising starting point. At pulse energies around 0.04–0.06 mJ, the $NO^{2+}/(N^+ + O^+)$ value is around one for the FTL pulses and neither the NO^{2+} nor $N^+ + O^+$ channels are near an appearance intensity threshold. This minimizes the possibility of control due to simple intensity changes. As shown in Table I, using pulse energies of 0.04 and 0.06 mJ to maximize the $NO^{2+}/(N^+ + O^+)$ ratio results in an increase by as much as 12.5 times the values obtained with a FTL pulse. Minimizing the same ratio results in a decrease of approximately 1.9 times the FTL value.

Figures 6(a) and 6(b) show the time-of-flight spectra for two specific trials we examine in detail. Optimizing the pulse shape to minimize the $NO^{2+}/(N^+ + O^+)$ ratio, as shown in Fig. 6(b), results in a TOF spectrum that appears very similar to the TOF spectrum
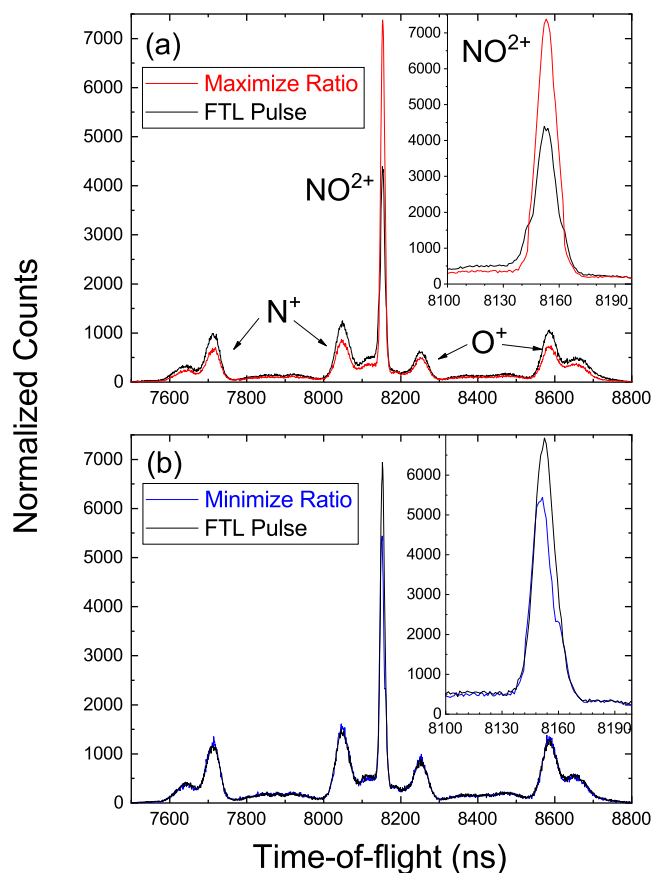
FIG. 6. Time-of-flight spectra of all ions in the relevant time window measured in association with (a) 0.06 mJ/pulse and (b) 0.04 mJ/pulse laser pulses. The narrow peak around 8150 ns is associated with NO^{2+} and is highlighted in each inset. The N^+ and O^+ fragments appear as "forward" (short TOF) and "backward" (long TOF) peaks. The highest energy N^+ (backward) and O^+ (forward) fragments overlap the NO^{2+} peak but should have little effect on our conclusions. In panel (a), the yield from pulses optimized to maximize the $NO^{2+}/(N^+ + O^+)$ ratio (red line) are compared to those measured with FTL pulses of the same energy (black line). Panel (b) is similar, but for the pulses optimized to minimize the same ratio (blue line). The number of counts are normalized to the number of laser shots in both panels.

obtained with an FTL pulse at the same energy, save for a reduction in the NO^{2+} yield shown in the inset. Closed-loop optimization with the aim of maximizing the $NO^{2+}/(N^+ + O^+)$ ratio, on the other hand, seems to enhance the amount of NO^{2+} and also slightly decrease the amount of dissociative double ionization, i.e., $N^+ + O^+$. We note that the data shown in Fig. 6 include all ions, similar to the time-of-flight data shown in Fig. 3(d), and thus, the value of the $NO^{2+}/(N^+ + O^+)$ ratio cannot be directly evaluated from this plot.

Before examining the changes that occur when the optimized pulses are used, it is worthwhile to examine the results acquired with the FTL pulses. Figure 7 shows the N^+ and O^+ VMI data, corresponding to the FTL-TOF spectra shown in Fig. 6(b), as a function of E_k and the cosine of the angle between the N^+ fragment
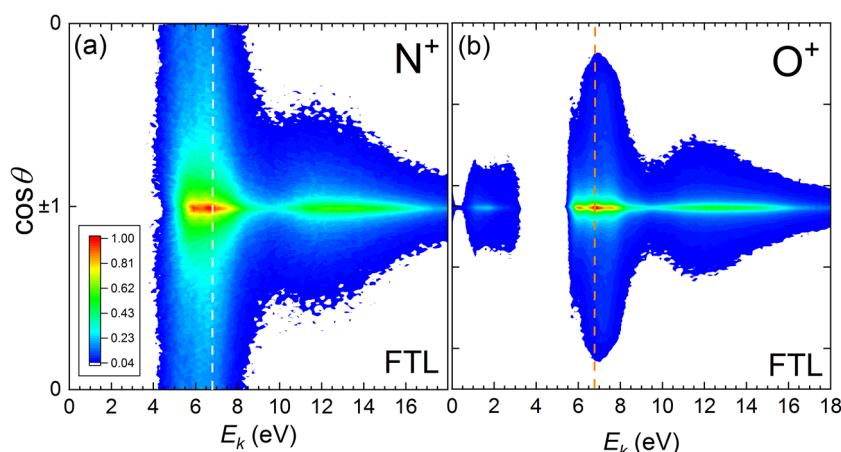
FIG. 7. The yield of N^+ (a) and O^+ (b) photofragments as a function of E_k and $\cos\theta$, where θ is the angle between the N^+ fragment velocity and the laser polarization direction. These plots are obtained by transforming the VMI data shown in Fig. 2(c). Panel (a) shows N^+ fragments produced using FTL pulses at 0.04 mJ/pulse or approximately 5×10^{14} W/cm^2, while panel (b) shows O^+ fragments at the same pulse conditions. The dotted lines at 6.8 eV in each panel represent the peak E_k value, and the angular distributions along those lines are shown in Fig. 9.

velocity and the laser polarization axis, $\cos\theta$. The same data are presented in Fig. 2(c) as a momentum plot, but the representation in Fig. 7 is often more useful for interpretation. Figure 4 shows $P(E_k)$ of the $N^+ + O^+$ ion-pair events unambiguously identified by the CTOF method. This $P(E_k)$ spectrum has two maxima, at 6.3 eV and at 8.7 eV. The VMI data (Fig. 7) have higher E_k resolution, but are not restricted to $N^+ + O^+$ ion-pair events. Since the CTOF data shown in Fig. 3(a) indicate that the $N^+ + O^+$ ion-pairs are strongly aligned with the laser polarization direction, we can select the aligned portion of the $E_k - \cos\theta$ plots (Fig. 7) in order to compare the CTOF- and VMI-based measurements of $P(E_k)$. Slices from Figs. 7(a) and 7(b) with $|\cos\theta| > 0.98$ show the yield in a 5–9 eV region, as illustrated in Fig. 8, which is similar to the region of large $P(E_k)$ in Fig. 4. The most likely E_k value from these VMI-derived measurements is at about 6.8 eV. The $P(E_k)$ distributions derived from the aligned
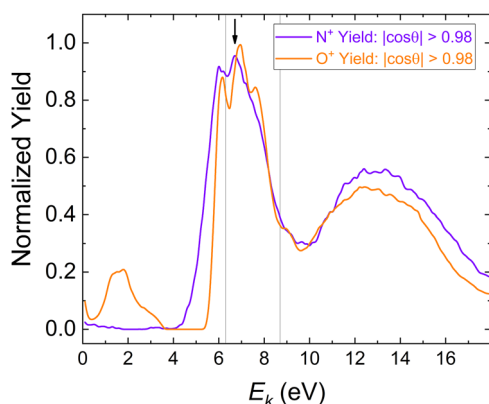
N^+ and O^+ fragments (shown in Fig. 8) have different features. Furthermore, these details also differ from the $P(E_k)$ distribution determined from the $N^+ + O^+$ ion-pair distribution shown in Fig. 4. The different $P(E_k)$ distributions indicate that the VMI measurement is probably dominated by dissociative single ionization leading to $N^+ + O$ or $N + O^+$, since $N^+ + O^+$ ion-pairs produced from the dissociation of NO^{2+} would have the same momentum for the N^+ and O^+ fragments.

The angular distribution of the features in the $P(E_k)$ distributions, illustrated in Fig. 9, confirms that the $N^+ + O^+$ ion-pairs are not the dominant contributor to the VMI $E_k - \cos\theta$ data shown in Fig. 7. When excited with a linearly polarized laser pulse, electric dipole transitions between the initial and final states with the same angular momentum, $\Delta\Lambda = 0$, are expected to have a $\cos^{2n}\theta$ angular distribution (where n is the number of photons), while for a $\Delta\Lambda = 1$ transition, the angular distribution should follow a $\sin^{2n}\theta$ distribution.[60,61,81] A transition accessing an intermediate state so as to make a parallel transition ($\Delta\Lambda = 0$) followed by a perpendicular transition ($\Delta\Lambda = 1$) or vice versa should be fit by a function of the form $\cos^{2n}\theta \sin^{2m}\theta$. The angular distributions for both the N^+ and O^+ fragments with E_k between 6.75 and 6.85 eV, shown in Figs. 9(c) and 9(d), seem to contain multiple components. Examining the angular distributions for E_k between 6.25 and 6.35 eV and between 8.65 and 8.75 eV, corresponding to the peaks in the CTOF-E_k data obtained with the FTL pulse (see Fig. 4) and shown in Figs. 9(a) and 9(b) and Figs. 9(e) and 9(f), yields the same conclusion. For all three E_k regions, the main parallel component of the angular distribution is much broader in the N^+ case, fitting to $\cos^6\theta$, while the narrower O^+ distribution is best fit with $\cos^{16}\theta$ at E_k between 6.75 and 6.85 eV and $\cos^{18}\theta$ in the other two cases. Thus, even for fragments ejected nearly along the laser polarization, the angular distributions associated with the N^+, O^+, and $N^+ + O^+$ ion-pairs (see Fig. 3) are quite different.

Since the VMI-derived data contain a significant amount of $N^+ + O$ and $N + O^+$ fragments in addition to the $N^+ + O^+$ channel of interest, can we use the CTOF-derived data to better understand the multiple ionization process that leads to NO^{2+}? Multiple ionization of diatomic molecules has been studied in many experiments, and there are several possible routes for the transition
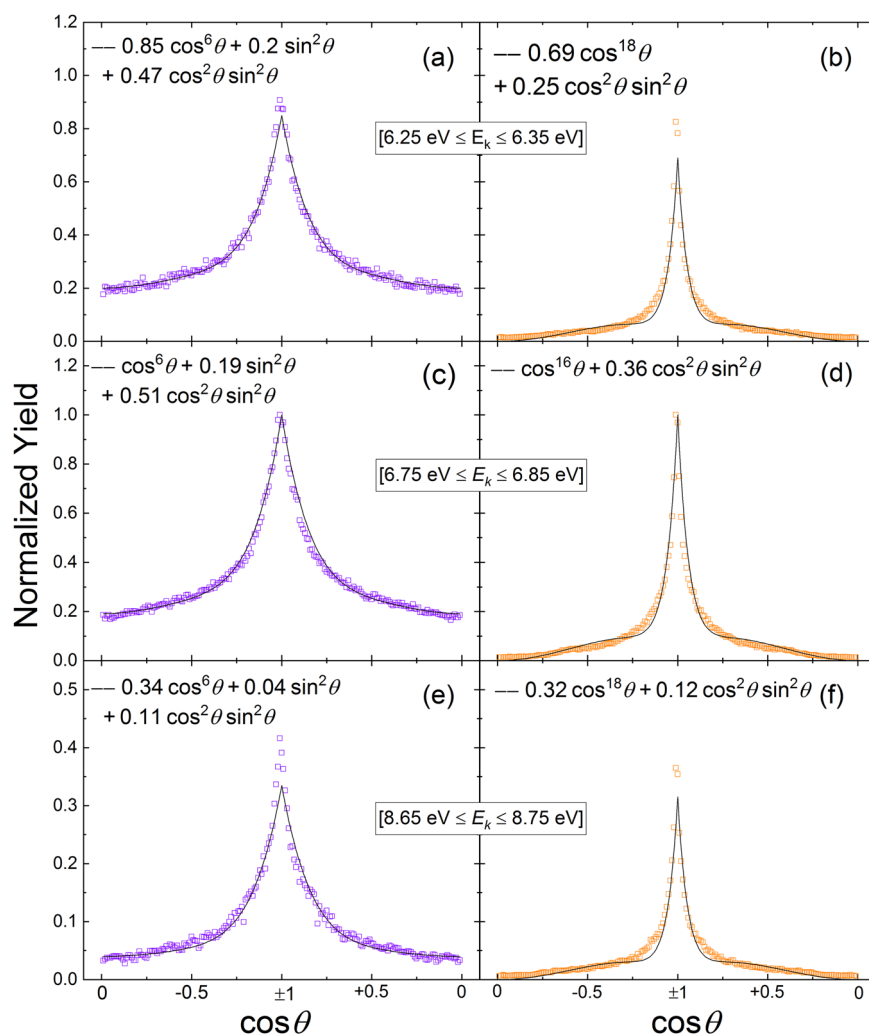

FIG. 8. The yield of N^+ (violet) and O^+ (orange) as a function of E_k for $|\cos\theta| \geq 0.98$. The peaks around 13 eV are due to NO^{3+} (or higher charge state) dissociation. CTOF measurements identify the 5–9 eV region as the location of the $N^+ + O^+$ ion-pairs. The approximate peak of the VMI data at 6.8 eV is indicated by an arrow, while the vertical lines label the locations of the 6.3 eV and 8.7 eV peaks in the $P(E_k)$ distribution shown in Fig. 4.

FIG. 9. The normalized yield of N^+ (left column) and O^+ (right column) as a function of $\cos\theta$. The slices through the data shown in Fig. 7 are made at three locations: $(6.25 \leq E_k \leq 6.35)$, the first peak in the $P(E_k)$ distribution from Fig. 4 [panels (a) and (b)], $(6.75 \leq E_k \leq 6.85)$, the peak of the VMI yield as indicated by the line in Fig. 7 [panels (c) and (d)], and $(8.65 \leq E_k \leq 8.75)$, the second peak in the $P(E_k)$ distribution from Fig. 4 [panels (e) and (f)]. The fits shown are of the form $A\cos^{2n}\theta + B\sin^{2m}\theta + C\cos^{2k}\theta\sin^{2l}\theta$ for the N^+ fragments and $A\cos^{2n}\theta + C\cos^{2k}\theta\sin^{2l}\theta$ for the O^+ fragments.

from neutral NO to NO^+ and ultimately NO^{2+}: Both direct ionization[82,83] and electron rescattering[83–87] (also called nonsequential or recollision ionization) occur near the equilibrium internuclear distance, R_e, since the nuclei do not have much time to respond to the laser field in either case. The recolliding electron can carry considerable energy, up to $3.17U_p$, where U_p is the pondermotive energy,[84] potentially leading to electronic excitation of the parent ion as well as multiple ionization.[88] Various Coulomb explosion[89–96] and enhanced ionization mechanisms[96–109] provide a link between E_k and the internuclear distance at which ionization occurs (often called the critical internuclear distance, R_c). These models, however, work best for molecules that have dissociative states with purely repulsive potential energy curves and are not easily applied to the metastable potential energy curves of NO^{2+}, which are illustrated in Fig. 1.

A simple application of the Coulomb explosion model, $E_k = 1/R_e$, gives an E_k value that is larger than the measured, while applications of the enhanced ionization models[109] lead to lower than

the observed E_k values at very large R_c. While it is not surprising that these models do not work well for NO, the upper and lower limits they supply for E_k suggest some sort of intermediate behavior with the ionization occurring between R_e and R_c. One such possibility would be a stairstep ionization process[110] in which the molecule stretches before each sequential ionization step.

Previous experimental studies of laser-induced ionization and dissociation of neutral NO leading to $N^+ + O^+$ fragments[73,111–116] have generally not employed coincidence measurements. Most of these studies suggest that the N^+ and O^+ fragments are produced indirectly, either by first dissociating NO and ionizing one or more fragments[111] or by population of another intermediate state of NO^+ or NO^{2+}. Furthermore, the measured $P(E_k)$ of the $N^+ + O$ and $N + O^+$ dissociation channels of NO^+ (see Fig. 8) is consistent with ionization at $R_e < R < R_c$.
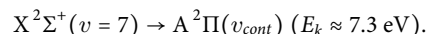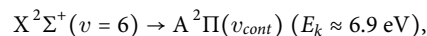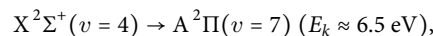
The angular distributions of the ionization process can also help clarify the underlying dynamics. Given the duration of the pulses used in these experiments, both geometrical and

dynamic molecular alignment must be considered.[117–122] Molecular Ammosov-Delone-Krainov (MO-ADK) theory,[123] which employs the principle of geometrical alignment, predicts that the angular distribution should reflect the symmetry of the most loosely bound electron of the molecule. For neutral NO, the HOMO has π_g symmetry, and thus, MO-ADK would suggest that the maximum ionization rate occurs at about 40° away from the polarization axis. As Voss and co-workers have shown, at higher intensities (near 1×10^{15} W/cm^2), this effect becomes smaller due to dynamic alignment,[124] including postpulse alignment.[121] While the intensity here is not as high, the ionization potential of NO is low (9.264 eV), and therefore, the initial ionization leading to NO^{2+} may be more peaked along the polarization direction than the MO-ADK prediction.

Intense laser interactions with beams of NO cations[110] and dications[53] produce angular distributions of fragments that can help clarify the current results from neutral NO targets. In the ion-beam experiments, the distributions of NO$^+$ and NO^{2+} ions in the laser focus are known to be isotropic.[53,110] In the NO^{2+} beam measurement, the subsequent laser-induced dissociation leads to perpendicular transitions at intensities comparable to the current experiment. Thus, we can conclude that the laser-induced NO → NO^{2+} process does not produce an isotropic distribution of NO^{2+} ions, since these perpendicular transitions are not dominant in the current experiment, as shown in Figs. 3(a), 7, and 9. Stated another way, we know that NO^{2+} tends to dissociate more easily when it is perpendicular to the laser pulse,[53] but we do not observe that angular behavior in our data. Instead, we see more ion-pairs emitted along the laser polarization. Thus, we infer that the initial NO → NO^{2+} ionization is not isotropic and is more probable for molecules that have $\cos \theta = \pm 1$.

In general, the angular distribution we observe in Fig. 7 resembles the observations of Gaire et al.[110] for single ionization of a NO$^+$ beam leading to N$^+$ + O$^+$ ion-pairs. In both that work[110] and in the current experiment, the angular distribution is predominantly aligned along the laser polarization but is wider than expected for a purely parallel transition. The presence of both perpendicular and parallel ionization routes suggests at least some contribution from stepwise processes in which the transition from NO → NO$^+$ and the subsequent NO$^+$ → NO^{2+} step can both influence the angular distributions even before the final NO^{2+} → N$^+$ + O$^+$ dissociation.

Since the minimum of the X $^2\Sigma^+$ electronic state of NO^{2+} is 1.6 eV lower in energy than the minimum of the A $^2\Pi$ state, we can assume that the initial ionization preferentially populates the X $^2\Sigma^+$ electronic state, even though the Franck-Condon overlap between the neutral NO ground state and the NO^{2+} X $^2\Sigma^+$ state is similar to the Franck-Condon overlap between the neutral NO and the NO^{2+} A $^2\Pi$ state (see Fig. 1). This assumption does not mean that we can exclude population of other states through more complex mechanisms, for example, stepping through the monocation states and stretching before ionization of the second electron. Under the assumption that the X $^2\Sigma^+$ is preferentially populated, we can exclude a number of possible routes to dissociative double-ionization based on the observed angular distribution of the N$^+$ + O$^+$ ion-pairs shown in Fig. 3. While the observed $P(E_k)$ is consistent with what is expected for several one-photon NO^{2+} X $^2\Sigma^+$ → A $^2\Pi$ transitions, such as

$$X\,^2\Sigma^+(v = 4) \rightarrow A\,^2\Pi(v = 7)\ (E_k \approx 6.5\ \text{eV}),$$

$$X\,^2\Sigma^+(v = 6) \rightarrow A\,^2\Pi(v_{cont})\ (E_k \approx 6.9\ \text{eV}),$$

$$X\,^2\Sigma^+(v = 7) \rightarrow A\,^2\Pi(v_{cont})\ (E_k \approx 7.3\ \text{eV}).$$

X $^2\Sigma^+$ → A $^2\Pi$ transitions have $\Delta\Lambda = 1$, and therefore, the breakup should be perpendicular to the laser polarization,[60,61,81] or at least show a $\cos^{2n}\theta\sin^{2m}\theta$ distribution if the initial NO → NO^{2+} X $^2\Sigma^+$ ionization step is aligned along the laser polarization. The X $^2\Sigma^+$ → B $^2\Sigma^+$ are $\Delta\Lambda = 0$ transitions that can result in similar E_k values, which are consistent with the current measurements, but this requires either two or three more photons than the one-photon X $^2\Sigma^+$ → A $^2\Pi$ transitions and, in some cases, needs to start in a higher vibrational level of the X $^2\Sigma^+$ state.

Energetically, the lower 6.3 or 6.8 eV peak in the measured E_k distribution would be consistent with a near-vertical transition from the neutral ground state to the NO^{2+} ground state followed by three-photon X $^2\Sigma^+$ $(v = v_i)$ → X $^2\Sigma^+$ $(v = v_f)$ vibrational excitation leading to dissociation, where v_i and v_f are the initial and final vibrational states, respectively. In other words, the leading portion of the pulse removes the electrons, without stretching the molecule much, and the role of any additional photons is to shift the vibrational population from a bound state to a dissociative state via a permanent dipole transition. Calculations of the field-free Franck-Condon overlap factors, displayed in Fig. 1(b), show that direct vertical transitions to NO^{2+} X $^2\Sigma^+$ from the neutral NO ground state predominantly populate the $v = 0$ through $v = 5$ levels of NO^{2+} (peaked at $v = 1$), consistent with the observed E_k and X $^2\Sigma^+$ → X $^2\Sigma^+$ transitions. Jochim et al.[53] have shown that X $^2\Sigma^+$ → X $^2\Sigma^+$ permanent dipole transitions leading to vibrational excitation and dissociation into N$^+$ + O$^+$ are more likely than competing channels over the range of E_k values discussed here.

The secondary peak at $E_k = 8.7$ eV in the $P(E_k)$ distribution (shown in Fig. 4) supports the interpretation presented in the previous paragraph, since permanent dipole transitions dominate over X $^2\Sigma^+$ → B $^2\Sigma^+$ transitions leading to N$^+$ + O$^+$ fragments with $E_k > 8$ eV.[53] Besides the calculations[53] showing the dominance of the X $^2\Sigma^+$ → X $^2\Sigma^+$ over the X $^2\Sigma^+$ → B $^2\Sigma^+$ transitions due to the smaller number of required photons and the relative magnitudes of the couplings between these states, resonance-enhanced multiphoton ionization may further bolster this pathway relative to direct nonresonant multiphoton ionization.[103,105]

Thus, given the prevalence of the X $^2\Sigma^+$ → X $^2\Sigma^+$ transitions over the X $^2\Sigma^+$ → B $^2\Sigma^+$ transitions and a photofragment angular distribution that seems to make one-photon NO^{2+} X $^2\Sigma^+$ → A $^2\Pi$ transitions unlikely, we believe that the FTL-driven dissociative double ionization process likely involves ionization to a low-lying vibrational state of NO^{2+} followed by X $^2\Sigma^+$ → X $^2\Sigma^+$ vibrational excitation leading to dissociation aligned with the laser polarization with the observed E_k values.

What role, then, does the optimized pulse shape play in enhancing or suppressing the NO^{2+}/(N$^+$ + O$^+$) ratio? Examining the suppression case first, we note that the optimized TOF spectrum, shown by the blue line of Fig. 6(b), is nearly identical to the TOF spectrum obtained with the FTL pulse (black line), except for the region of the NO^{2+} events. The optimized pulse seems to keep the TOF yield of the photofragment distributions largely unchanged while reducing the yield of the nondissociative NO^{2+} ions. This is supported by the
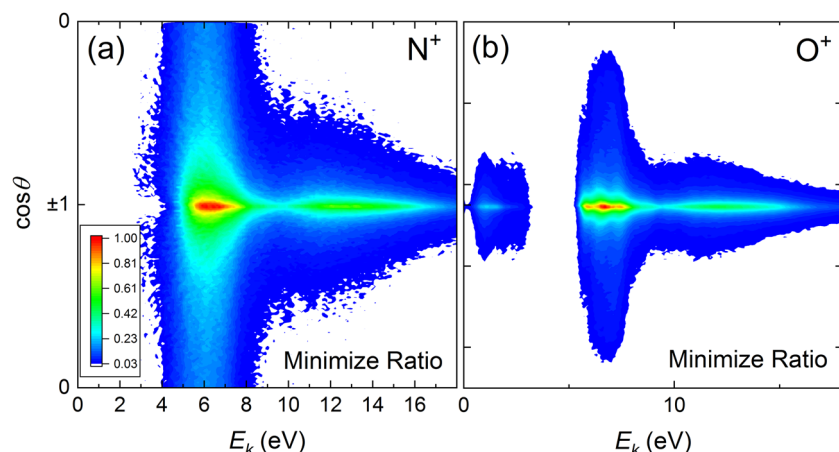
FIG. 10. The yield of N$^+$ (a) and O$^+$ (b) as a function of E_k and cos θ. (a) shows N$^+$ fragments produced using pulses that minimize the NO^{2+}/(N$^+$ + O$^+$) ratio at 0.04 mJ/pulse ($\sim$5 $\times$ 10^{14} W/cm^2). (b) shows O$^+$ fragments produced by the same optimized pulse. Both distributions are nearly identical to those shown in Fig. 7.

E_k − cos θ distributions of the N$^+$ and O$^+$ ions produced with optimized pulses shown in Fig. 10, which also appear nearly identical to the FTL-generated E_k − cos θ distributions shown in Fig. 7.

The measured SHG FROG traces of the optimized pulse that minimized the NO^{2+}/(N$^+$ + O$^+$) ratio are shown in Fig. 11. This pulse has a FWHM of 65 fs, or about 60% wider than the FTL pulse. While the spectral intensity shows some modulation, neither the spectral nor temporal phases show much variation over the main intensity of the pulse. Thus, the optimized pulse seems to be somewhat longer in duration than a FTL pulse but does not appear to have many other significant features.

Since there are no significant changes to the photofragment distributions between the optimized and FTL pulse, the control by the optimized pulse can be interpreted as moving NO^{2+} population to higher vibrational states by allowing the molecule more time to stretch in the field before the last transition occurs. As shown by the Franck-Condon region in Fig. 1, when R increases, the probability of accessing higher vibrational levels of the X $^2\Sigma^+$ state increases. Support for this interpretation is provided in Fig. 4, which shows that the optimized pulses increase the number of N$^+$ + O$^+$ coincidence events at around E_k = 7 eV. If the penultimate step in the process drives the population to a higher X $^2\Sigma^+$ vibrational level than the
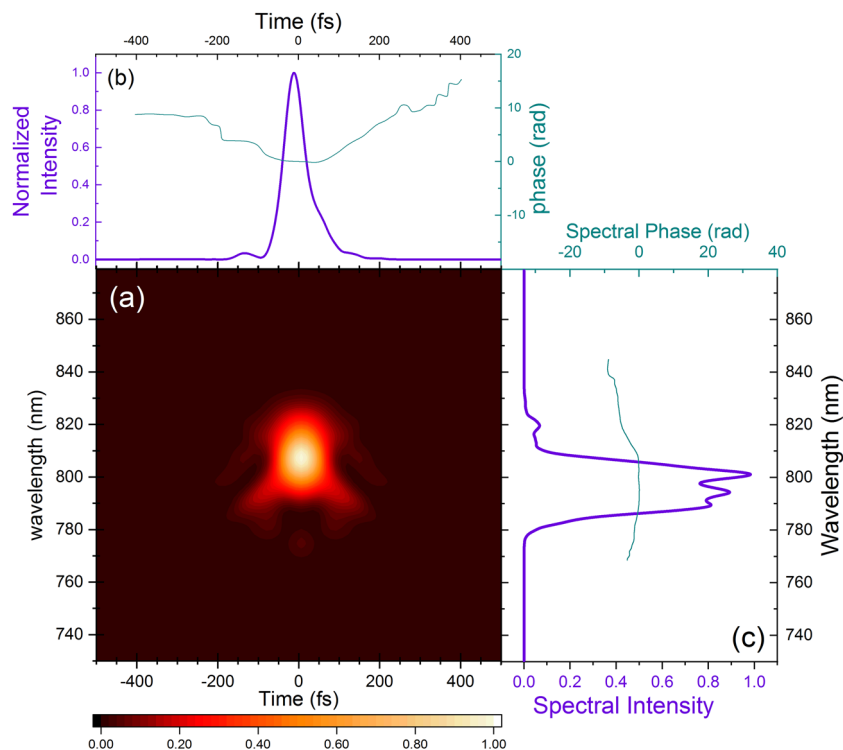

FIG. 11. Measured SHG FROG[63] trace (a) of the laser pulse optimized to minimize the NO^{2+}/(N$^+$ + O$^+$) ratio at 0.04 mJ/pulse. The linear color scale is normalized, so the peak signal is 1.0. (b) The associated temporal intensity (thick purple) and phase (thin cyan) of the laser pulse. The FWHM of the pulse in intensity is 65 fs. (c) The spectral intensity (thick purple) and phase (thin cyan) of the laser pulse. The measured phase values are not meaningful at low intensities.

FTL pulse, then the final step could land the same population in the dissociative region, with E_k consistent with the values that are enhanced in Fig. 4. In this explanation, the dissociation into $N^+ + O^+$ channels moves through the same pathways as when the FTL pulse is present, thereby explaining why the data in Figs. 7 and 10 are nearly identical, but the small shift in vibrational population depletes the bound NO^{2+} population, reducing the overall $NO^{2+}/(N^+ + O^+)$ ratio.

While this explanation seems fairly simple, lengthening the pulse to minimize the $NO^{2+}/(N^+ + O^+)$ ratio is the opposite of the "trivial" control behavior that would be predicted from the results shown in Fig. 5. Roughly extrapolating from Fig. 5, lengthening the pulse by 60% reduces the intensity of the 0.04 mJ/pulse to 3×10^{14} W/cm^2, which approximately doubles the $NO^{2+}/(N^+ + O^+)$ ratio. The longer pulse duration, then, is able to reduce the population of long-lived NO^{2+} even though the lower intensity should increase that same population. This indicates that the pulse duration effect on the vibrational population might be quite significant. On the other hand, the search algorithm had freedom to modulate the phase and extend the pulse duration further but did not choose this path, which may indicate that limiting the intensity eventually starts to increase the $NO^{2+}/(N^+ + O^+)$ ratio again. All three optimization trials in this pulse energy range (0.04 mJ/pulse and 0.06 mJ/pulse, see Table I) resulted in pulse characteristics similar to the pulse shown in Fig. 11.

As Table I details, the $NO^{2+}/(N^+ + O^+)$ ratio has also been increased by as much as a factor of 12.5 times over the value acquired with the FTL pulse using CTOF-based feedback. The comparison of the TOF spectra obtained with the 0.06 mJ/pulse FTL ($\sim 8 \times 10^{14}$ W/cm^2) and optimized laser pulses is shown in Fig. 6(a). As noted previously, the two distinguishing features of this TOF measurement are the enhancement of the NO^{2+} yield and the smaller, but still notable, suppression of the N^+ and O^+ fragments, especially those with lower E_k.

The FROG trace of the optimized pulse that maximizes the $NO^{2+}/(N^+ + O^+)$ ratio is shown in Fig. 12. Unlike the pulse that minimizes the $NO^{2+}/(N^+ + O^+)$ ratio, the present pulse has an interesting structure in both the temporal and spectral domains. The main feature seems to be the two-pulse structure in the time domain. These two pulses are separated by about 151 fs. The FWHM of the individual peaks (88 and 69 fs) is similar to the width of the pulse that manipulated the vibrational population in the trials that minimized the $NO^{2+}/(N^+ + O^+)$ ratio. Thus, looking for a similar shift in vibrational population here seems reasonable, although we are now seeking to enhance, rather than suppress, the population of long-lived NO^{2+} states.

Some further information may be provided by the $P(E_k)$ distribution evaluated from the CTOF data, shown in Fig. 13 for the pulse that maximizes the $NO^{2+}/(N^+ + O^+)$ ratio and the FTL pulse at the same energy. The $P(E_k)$ values for the optimized pulse are lower than the FTL pulse up until $E_k \approx 6.5$ eV, which is consistent with the differences in the fragment yield observed in Fig. 6(a). This reduction of lower-E_k $N^+ + O^+$ fragments may indicate that the population has shifted to bound NO^{2+} vibrational levels.

The $E_k - \cos\theta$ distributions obtained by VMI measurements of N^+ or O^+ fragments for the laser pulses that maximized the $NO^{2+}/(N^+ + O^+)$ ratio are shown in Fig. 14. These photofragments are strongly peaked along the laser polarization, as shown in Fig. 15. While the bulk of the O^+ photofragment $E_k - \cos\theta$ distributions [Figs. 14(b) and 14(d)] are unchanged by the switch from
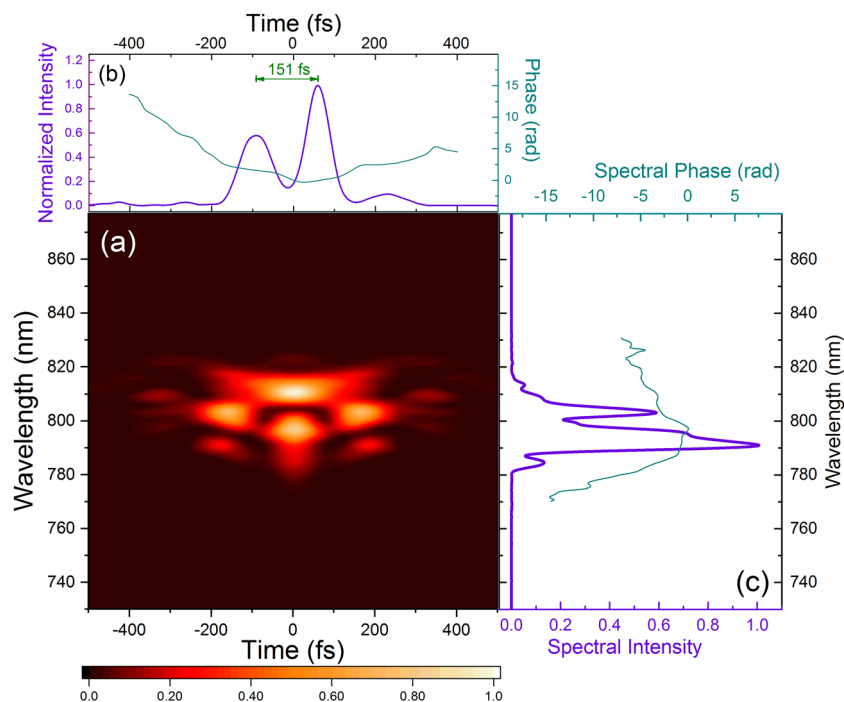

FIG. 12. Measured SHG FROG[63] trace (a) of the laser pulse optimized to maximize the $NO^{2+}/(N^+ + O^+)$ ratio at 0.06 mJ/pulse. The linear color scale is normalized, so the peak signal is 1.0. (b) The associated temporal intensity (thick purple) and phase (thin cyan) of the laser pulse. The centers of the two pulses are separated by 151 fs, with the earlier (left) pulse having 88 fs FWHM and the later (right) pulse having 69 fs FWHM. (c) The spectral intensity (thick purple) and phase (thin cyan) of the laser pulse.
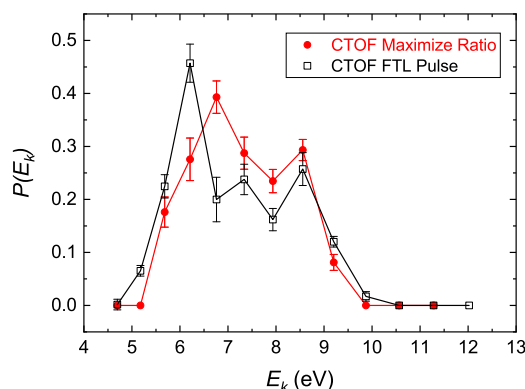
FIG. 13. The probability of dissociation, $P(E_k)$, as a function of E_k for FTL pulses (black) and for pulses that maximize the $NO^{2+}/(N^+ + O^+)$ ratio (red) at 0.06 mJ/pulse. The $P(E_k)$ distribution is derived from the CTOF data similar to that shown in Fig. 3 as described in the text. At lower E_k, the optimized pulse seems less likely to produce $N^+ + O^+$ ion pairs, in agreement with the TOF data shown in Fig. 6(a).

the FTL to the optimized pulses and have almost identical angular distributions in Fig. 15(b), there are some differences between the N^+ photofragment $E_k − \cos\theta$ distributions shown in Figs. 14(a) and 14(c). The optimized pulse tends to produce N^+ fragments

with slightly lower E_k values than the FTL pulse. This is the opposite of the observation made from the CTOF-derived E_k data in Fig. 13, which showed that the FTL pulses were more likely to produce N^+ + O^+ ion pairs for $E_k \leq 6.5$ eV. Thus, the population of aligned N^+ photofragments near $E_k = 6$ eV evaluated from the VMI data must not originate from NO^{2+}, but instead come from a different parent ion, such as NO^+ dissociating into $N^+ + O$. The possibility of NO^{3+} dissociating into $(N^+ + O^{2+})$ with $E_k \sim 6$ eV is less likely since triple ionization requires increased laser intensity, and the resulting dissociation is expected to lead to larger E_k. For $NO^{3+} \rightarrow (N^+ + O^{2+})$, $E_k = 2/R_e \gg 6$ eV within the approximation of the Coulomb explosion model.

For the trials minimizing the $NO^{2+}/(N^+ + O^+)$ ratio, we developed the hypothesis that the increase in pulse duration (shown in Fig. 11) compared to the FTL pulse allowed higher vibrational states of NO^{2+} to be populated. Consistency would mean that the similar-in-duration first pulse in the sequence shown in the FROG trace of Fig. 12 must have much the same effect as the longer duration pulse that minimizes the $NO^{2+}/(N^+ + O^+)$ ratio even though the aim of this trial is to maximize the $NO^{2+}/(N^+ + O^+)$ ratio. One difference between the pulses optimized for minimization and maximization of the ratio, however, is that the maximizing pulse should have lower intensity than the minimization pulse measured in Fig. 11 since the pulse energy in Fig. 12 is split between two subpulses. An explanation for the utility of pulse characteristics of the maximization trial is that the first pulse populates higher vibrational states of NO^+ than a
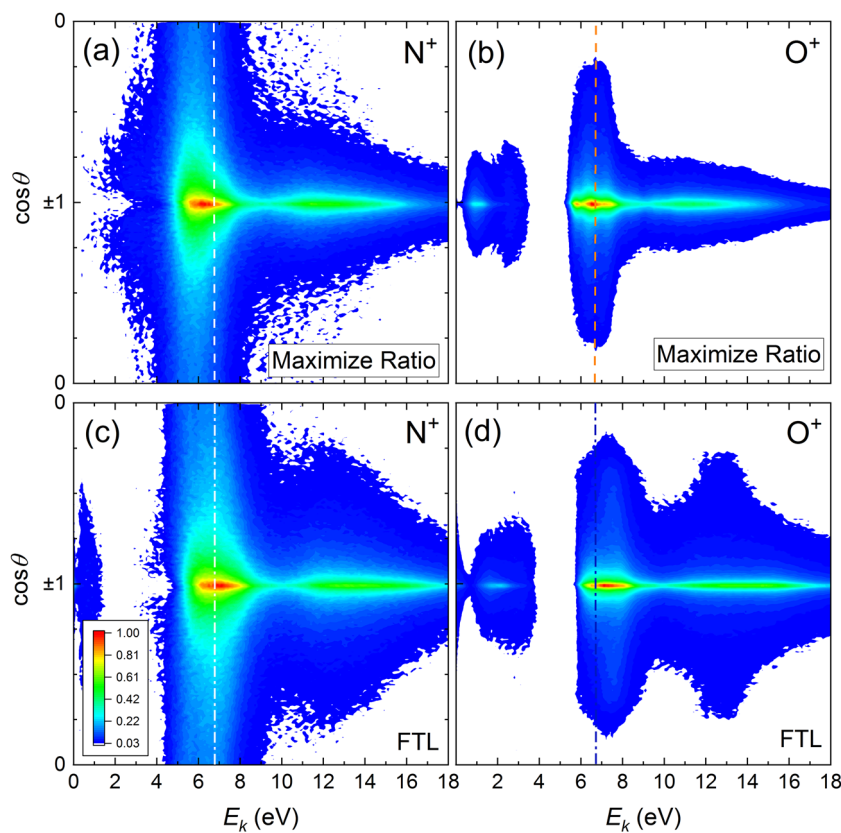

FIG. 14. Yields of N^+ and O^+ fragments as a function of E_k and $\cos\theta$. (a) N^+ fragments produced by the laser pulses optimized to maximize the $NO^{2+}/(N^+ + O^+)$ ratio at 0.06 mJ/pulse shown in Fig. 12. (b) O^+ fragments produced by the same laser pulse. (c) N^+ fragments produced by the FTL laser pulses at 0.06 mJ/pulse, equivalent to $\sim 8 \times 10^{14}$ W/cm². (d) O^+ fragments produced by the same FTL laser pulses. The dotted lines in each panel at $E_k = 6.7$ eV represent cuts used to produce the angular distributions shown in Fig. 15.
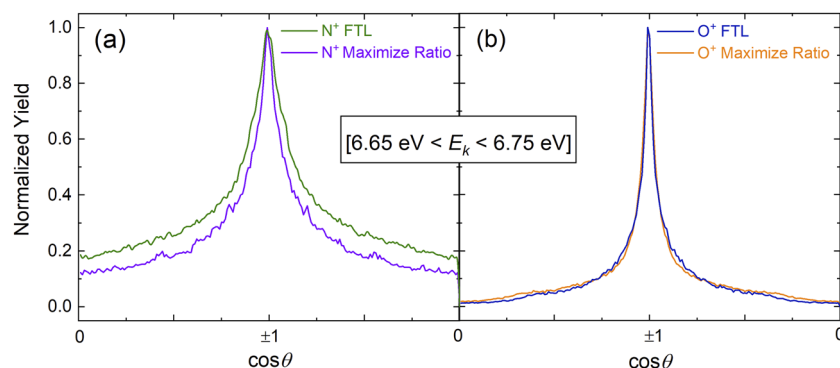
FIG. 15. (a) Angular distributions of N^+ photofragments, integrated over (6.65 eV $\leq E_k \leq$ 6.75 eV), produced by pulses optimized to maximize the $NO^{2+}/(N^+ + O^+)$ ratio at 0.06 mJ/pulse (violet) and by FTL pulses of the same energy (olive), equivalent to ~8 $\times 10^{14}$ W/cm^2. (b) Angular distributions of O^+ photofragments, also integrated over (6.65 eV $\leq E_k \leq$ 6.75 eV), produced by pulses optimized to maximize the $NO^{2+}/(N^+ + O^+)$ ratio at 0.06 mJ/pulse (orange) and by the FTL pulses of the same energy (blue). The slice around E_k = 6.7 eV chosen to examine the angular distributions matches the peak of the measured $P(E_k)$ distribution shown in Fig. 13. As in Fig. 9, the O^+ angular distributions are more strongly peaked than the N^+ fragments.

corresponding FTL pulse, leading to dissociation of the NO^+ cation by the secondary pulse rather than a second sequential ionization step. These dissociation channels, however, would be quite different than the $E_k \sim$ 1–2 eV $NO^+ \rightarrow N^+ + O$ dissociations observed by Gaire *et al.*[110] for shorter pulses. The $E_k - \cos\theta$ distribution in Fig. 14(a) indicates the presence of $N^+ + O$ fragments [absent from the CTOF-derived $P(E_k)$ distribution shown in Fig. 13], which are fairly strongly peaked along the laser polarization direction [see Fig. 15(a)].

To fit this single-ionization followed by dissociation understanding of the double-pulse structure of Fig. 12, we should be able to identify parallel transitions between a bound vibrational state of NO^+ and a dissociative state of NO^+ leading to N^+ fragments with $E_k \sim$ 6 eV. Two potential transitions that match these criteria are displayed in Fig. 16, which shows (at least in the field-free picture) that eight photon, $\Delta\Lambda = 0$ transitions from the $v = 8$ state of the NO^+ X $^1\Sigma^+$ ground electronic state would lead to the B $^1\Sigma^+$ state and dissociate with $E_k \sim$ 6 eV. A similar seven photon transition from $v = 13$ also leads to the B $^1\Sigma^+$ state and has nearly the same E_k.

These transitions leading to dissociation of NO^+ could explain some of the "missing" $N^+ + O^+$ ion pairs in Fig. 13. With a more intense pulse, the pathway leading to bound vibrational states of the NO^{2+} ground electronic state and subsequent dissociation via X $^2\Sigma^+ \rightarrow$ X $^2\Sigma^+$ permanent dipole transitions would be open. In lowering the overall pulse intensity by forming a double-pulse structure, the maximization pulse avoids production of $N^+ + O^+$ ion pairs by enhancing a competing transition to $NO^+ \rightarrow N^+ + O$. Since the adaptive search uses coincidence-based feedback, the $NO^+ \rightarrow N^+ + O$ dissociation does not contribute to the fitness calculation, while the avoided $N^+ + O^+$ coincidence events would otherwise diminish the $NO^{2+}/(N^+ + O^+)$ ratio. This outcome would also explain why the $N^+ E_k - \cos\theta$ distributions are different for the optimized and FTL pulses in Figs. 14(a) and 14(c), while the O^+ fragment distributions shown in Figs. 14(b) and 14(d) are more similar to each other, since the $N + O^+$ states are not involved in this scheme.

An additional attribute of the delayed second pulse shown in Fig. 12 is that the 150 fs delay between the first and second pulses gives the NO^+ vibrational wave packets time to evolve toward their equilibrium distance. Ionization near the NO^+ equilibrium would tend to populate lower vibrational levels of NO^{2+}, accounting for the increase in the nondissociative double ionization observed in the TOF spectra for this trial, shown in the inset of Fig. 6(a). The multiple pulse structure shown in Fig. 12 is one of the common features of the pulses that maximize the $NO^{2+}/(N^+ + O^+)$ ratio. As shown in Fig. 17, the other $NO^{2+}/(N^+ + O^+)$ optimization trials at similar pulse energies had multiple pulses and a similar overall trend to the phase, although the details of both differ from each other and from Fig. 12. Still, the explanation developed for the most effective
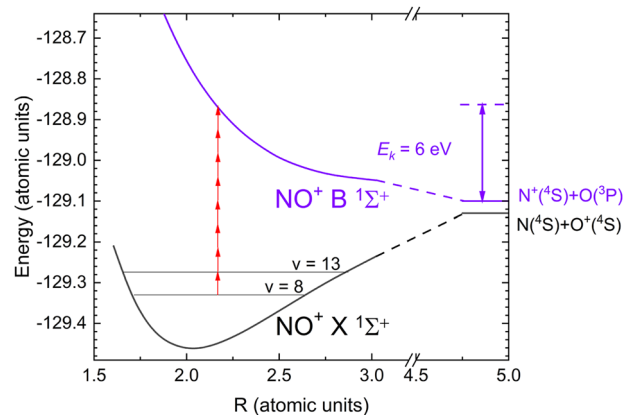

FIG. 16. Potential energy curves[125] for the NO^+ X $^1\Sigma^+$ (black line) and B $^1\Sigma^+$ (purple line) states. The $v = 8$ and $v = 13$ vibrational levels[126] of the X $^1\Sigma^+$ state are shown. The energies at the separate atom limits[126] are −128.79 a.u. for the NO^+ X $^1\Sigma^+$ state and −128.76 a.u. for the B $^1\Sigma^+$ state. The dissociative B $^1\Sigma^+$ state can be reached via eight 790 nm photons from the $v = 8$ state or seven photons from the $v = 13$ state of X $^1\Sigma^+$, both resulting in an E_k of 6 eV.
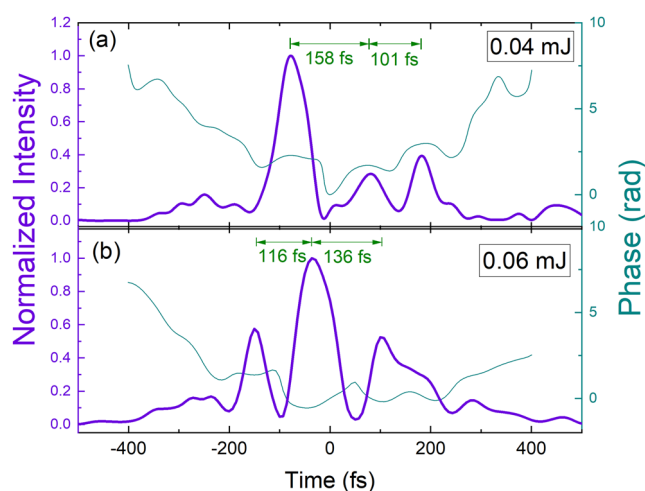
FIG. 17. The temporal intensity (thick purple) and phase (thin cyan) of the additional laser pulses that optimized $NO^{2+}/(N^+ + O^+)$ at pulse energies below 0.5 mJ. The temporal separation between the peaks of the different pulses is indicated in the figure. (a) The pulse that yielded $NO^{2+}/(N^+ + O^+)$ = 2.8 ± 0.9 at 0.04 mJ. (b) The pulse that resulted in $NO^{2+}/(N^+ + O^+)$ = 6.0 ± 0.9 at 0.06 mJ.

0.06 mJ pulse can reasonably be applied to the other optimized 0.06 mJ and 0.04 mJ pulses that are reported in Table I.

The efforts to use closed-loop coincidence feedback to both maximize and minimize the $NO^{2+}/(N^+ + O^+)$ ratio at intensities around 10^{14} W/cm^2 were successful, with all trials resulting in some enhancement or suppression of the ratio with the best exceeding a factor of 10. The VMI-based analysis yields additional information. First, the difference in the uncorrelated VMI measurements of the N^+ and O^+ fragments indicate that simply trying to use one of these fragments as a proxy for the $N^+ + O^+$ coincidence yield in the optimization feedback would not lead to the desired outcome, since there are clearly other channels, such as $N^+ + O$, present in the VMI data. This is true even in the same range of E_k where the $N^+ + O^+$ coincidences appear, so separation based on fragment energy would be difficult. The angular information derived from the VMI data assists in separating the various dissociation channels. Second, most of the control seems to be associated with an increase or decrease in the NO^{2+} yield, rather than significant changes in the number of $N^+ + O^+$ dissociative double-ionization events. From an analysis perspective, this is unfortunate, since VMI measurements on the nondissociative NO^{2+} just reveal a thermal distribution of ions. Still, the fragment VMI information, along with the CTOF-based $P(E_k)$ distributions, provides enough clues about the fragment behavior to allow us to indirectly surmise some plausible routes to the observed control. This analysis is helped by the nature of the pulse shapes, which are not extremely complex.

IV. SUMMARY AND OUTLOOK

Adaptive strong field control that uses coincidence-time-of-flight feedback has been successfully employed to control the ratio of nondissociative to dissociative double ionization $NO^{2+}/(N^+ + O^+)$ of NO molecules. The use of the CTOF feedback allowed the separation of the $N^+ + O^+$ ion pairs from the $N^+ + O$ or $N + O^+$ dissociative single ionization products. The $NO^{2+}/(N^+ + O^+)$ ratio was increased or decreased by about an order of magnitude at pulse energies between 0.04 and 0.06 mJ or around 10^{14} W/cm^2 for FTL pulses at our focusing conditions. Without the use of the CTOF feedback, it is unlikely that the optimization would have been possible due to the large magnitude of the dissociative single ionization channels and the range of intensities present in the laser focal volume.

The work by Rabitz and co-workers demonstrating the robustness of feedback-based optimization,[127–130] even in the face of experimental constraints, coupled with the experimental efforts that demonstrate how laser-induced Stark shifts can activate many unimolecular reaction pathways,[21,74–78] has led to an understanding that strong-field closed-loop control results cannot easily be "reverse-engineered" to gain knowledge of the control mechanism.[27,40] In this article, we show that when the laser intensity is not too high and the feedback is well-defined, CTOF and VMI analysis of the resulting photofragments identifies a plausible control mechanism that links the optimized pulse to the measured ion characteristics. More detailed theoretical efforts are required to confirm the mechanistic analysis presented here.

At higher energy (~0.5 mJ), the pulse complexity increases significantly, and determining the underlying molecular dynamics clearly becomes more difficult, although the control is at least as successful as at lower intensities.

In both intensity regimes, the role of focal volume averaging is limited by the CTOF technique, since the $N^+ + O^+$ coincidences are required to originate from the same charge state as the nondissociative NO^{2+} ions. The focal volume effect is not completely eliminated, however, since the dissociative and nondissociative NO^{2+} states have different energies, resulting in some ambiguities in the interpretation. That said, this work does not employ the sort of highly sophisticated, correlated, multihit electron-ion momentum imaging methods such as COLTRIMS/reaction microscopes[131] or advanced VMI methods.[132–135] Those techniques could potentially provide more differential information that might illuminate important dynamics and further restrict uncertainty due to focal volume averaging. This would be particularity interesting if highly differential experimental signals could be incorporated into the closed-loop control as feedback.

REFERENCES

[1] R. S. Judson and H. Rabitz, Phys. Rev. Lett. **68**, 1500 (1992).

[2] A. Assion, T. Baumert, M. Bergt, T. Brixner, B. Kiefer, V. Seyfried, M. Strehle, and G. Gerber, Science **282**, 919 (1998).

[3] R. J. Levis, G. M. Menkir, and H. Rabitz, Science **292**, 709 (2001).

[4] H. Rabitz, Science **288**, 824 (2000).

[5] S. A. Rice and S. P. Shah, Phys. Chem. Chem. Phys. **4**, 1683 (2002).

[6] M. Shapiro and P. Brumer, Rep. Prog. Phys. **66**, 859 (2003).

[7] C. Brif, R. Chakrabarti, and H. Rabitz, New J. Phys. **12**, 075008 (2010).

[8] B. J. Pearson, J. L. White, T. C. Weinacht, and P. H. Bucksbaum, Phys. Rev. A **63**, 063412 (2001).

[9] J. L. Herek, W. Wohlleben, R. J. Cogdell, D. Zeidler, and M. Motzkus, Nature **417**, 533 (2002).

[10] T. Brixner, G. Krampert, T. Pfeifer, R. Selle, G. Gerber, M. Wollenhaupt, O. Graefe, C. Horn, D. Liese, and T. Baumert, Phys. Rev. Lett. **92**, 208301 (2004).

[11] G.-Y. Chen, Z. W. Wang, and W. T. Hill, Phys. Rev. A **79**, 011401 (2009).

[12] M. Kotur, T. Weinacht, B. J. Pearson, and S. Matsika, J. Chem. Phys. **130**, 134311 (2009).

[13] D. G. Kuroda, C. P. Singh, Z. Peng, and V. D. Kleiman, Science **326**, 263 (2009).

[14] M. Roth, L. Guyon, J. Roslund, V. Boutou, F. Courvoisier, J.-P. Wolf, and H. Rabitz, Phys. Rev. Lett. **102**, 253001 (2009).

[15] J. Plenge, A. Wirsing, I. Wagner-Drebenstedt, I. Halfpap, B. Kieling, B. Wassermann, and E. Ruhl, Phys. Chem. Chem. Phys. **13**, 8705 (2011).

[16] S. Singha, Z. Hu, and R. J. Gordon, J. Phys. Chem. A **115**, 6093 (2011).

[17] P. Nuernberger, D. Wolpert, H. Weiss, and G. Gerber, Phys. Chem. Chem. Phys. **14**, 1185 (2012).

[18] S. Rosi, A. Bernard, N. Fabbri, L. Fallani, C. Fort, M. Inguscio, T. Calarco, and S. Montangero, Phys. Rev. A **88**, 021601 (2013).

[19] I. R. Solá, J. González-Vázquez, R. de Nalda, and L. Bañares, Phys. Chem. Chem. Phys. **17**, 13183 (2015).

[20] M. Bergt, T. Brixner, B. Kiefer, M. Strehle, and G. Gerber, J. Phys. Chem. A **103**, 10381 (1999).

[21] R. J. Levis and H. A. Rabitz, J. Phys. Chem. A **106**, 6427 (2002).

[22] A. Bartelt, S. Minemoto, C. Lupulescu, Š. Vajda, and L. Wöste, Eur. Phys. J. D **16**, 127 (2001).

[23] M. Bergt, T. Brixner, C. Dietl, B. Kiefer, and G. Gerber, J. Organomet. Chem. **661**, 199 (2002).

[24] N. Damrauer, C. Dietl, G. Krampert, S.-H. Lee, K.-H. Jung, and G. Gerber, Eur. Phys. J. D **20**, 71 (2002).

[25] A. Lindinger, C. Lupulescu, M. Plewicki, F. Vetter, A. Merli, S. M. Weber, and L. Wöste, Phys. Rev. Lett. **93**, 033001 (2004).

[26] C. Trallero-Herrero, D. Cardoza, T. C. Weinacht, and J. L. Cohen, Phys. Rev. A **71**, 013423 (2005).

[27] E. Wells, K. J. Betsch, C. W. S. Conover, M. J. DeWitt, D. Pinkham, and R. R. Jones, Phys. Rev. A **72**, 063406 (2005).

[28] T. Laarmann, I. Shchatsinin, A. Stalmashonak, M. Boyle, N. Zhavoronkov, J. Handt, R. Schmidt, C. P. Schulz, and I. V. Hertel, Phys. Rev. Lett. **98**, 058302 (2007).

[29] T. Laarmann, I. Shchatsinin, P. Singh, N. Zhavoronkov, M. Gerhards, C. P. Schulz, and I. V. Hertel, J. Chem. Phys. **127**, 201101 (2007).

[30] B. J. Pearson, S. R. Nichols, and T. Weinacht, J. Chem. Phys. **127**, 131101 (2007).

[31] L. Palliyaguru, J. Sloss, H. Rabitz, and R. J. Levis, J. Mod. Opt. **55**, 177 (2008).

[32] J. González-Vázquez, L. González, S. R. Nichols, T. C. Weinacht, and T. Rozgonyi, Phys. Chem. Chem. Phys. **12**, 14203 (2010).

[33] Z. Hu, S. Singha, Y. Zhao, G. E. Barry, T. Seideman, and R. J. Gordon, J. Phys. Chem. Lett. **3**, 2744 (2012).

[34] T. Baumert, M. Grosser, R. Thalweiser, and G. Gerber, Phys. Rev. Lett. **67**, 3753 (1991).

[35] C. Daniel, J. Full, L. González, C. Lupulescu, J. Manz, A. Merli, S. Vajda, and L. Wöste, Science **299**, 536 (2003).

[36] D. Cardoza, C. Trallero-Herrero, F. Langhojer, H. Rabitz, and T. Weinacht, J. Chem. Phys. **122**, 124306 (2005).

[37] F. Langhojer, D. Cardoza, M. Baertschy, and T. Weinacht, J. Chem. Phys. **122**, 014102 (2005).

[38] D. Cardoza, B. J. Pearson, M. Baertschy, and T. Weinacht, J. Photochem. Photobiol., A **180**, 277 (2006).

[39] G. Vogt, P. Nuernberger, R. Selle, F. Dimler, T. Brixner, and G. Gerber, Phys. Rev. A **74**, 033413 (2006).

[40] J. L. White, E. C. Carroll, K. G. Spears, and R. J. Sension, Isr. J. Chem. **52**, 397 (2012).

[41] D. Geißler, P. Marquetand, J. González-Vázquez, L. González, T. Rozgonyi, and T. Weinacht, J. Phys. Chem. A **116**, 11434 (2012).

[42] R. R. de Castro, R. Cabrera, D. I. Bondar, and H. Rabitz, New J. Phys. **15**, 025032 (2013).

[43] E. Wells, C. Rallis, M. Zohrabi, R. Siemering, B. Jochim, P. Andrews, U. Ablikim, B. Gaire, S. De, K. Carnes, B. Bergues, R. de Vivie-Riedle, M. Kling, and I. Ben-Itzhak, Nat. Commun. **4**, 2895 (2013).

[44] X. Xing, R. R. de Castro, and H. Rabitz, New J. Phys. **16**, 125004 (2014).

[45] D. Geißler and T. Weinacht, Phys. Rev. A **89**, 013408 (2014).

[46] P. Sándor, A. Zhao, T. Rozgonyi, and T. Weinacht, J. Phys. B: At., Mol. Opt. Phys. **47**, 124021 (2014).

[47] X. Xing, R. R. de Castro, and H. Rabitz, J. Phys. Chem. A **121**, 8632 (2017).

[48] A. M. Weiner, Rev. Sci. Instrum. **71**, 1929 (2000).

[49] F. Verluise, V. Laude, Z. Cheng, C. Spielmann, and P. Tournois, Opt. Lett. **25**, 575 (2000).

[50] A. Monmayrant, S. Weber, and B. Chatel, J. Phys. B: At., Mol. Opt. Phys. **43**, 103001 (2010).

[51] E. Wells, J. McKenna, A. M. Sayler, B. Jochim, N. Gregerson, R. Averin, M. Zohrabi, K. D. Carnes, and I. Ben-Itzhak, J. Phys. B: At., Mol. Opt. Phys. **43**, 015101 (2010).

[52] R. Baková, J. Fišer, T. Šedivcová Uhlíková, and V. Špirko, J. Chem. Phys. **128**, 144301 (2008).

[53] B. Jochim, M. Zohrabi, B. Gaire, F. Anis, T. Uhlíková, K. D. Carnes, E. Wells, B. D. Esry, and I. Ben-Itzhak, "Direct evidence of the dominant role of multiphoton permanent-dipole transitions in strong-field dissociation of NO^{2+}," Phys. Rev. Lett. (submitted).

[54] D. W. Chandler and P. L. Houston, J. Chem. Phys. **87**, 1445 (1987).

[55] A. T. J. B. Eppink and D. H. Parker, Rev. Sci. Instrum. **68**, 3477 (1997).

[56] D. H. Parker and A. T. J. B. Eppink, J. Chem. Phys. **107**, 2357 (1997).

[57] *Imaging in Molecular Dynamics: Technology and Applications*, edited by B. J. Whitaker (Cambridge University Press, Cambridge, UK, 2003).

[58] C. E. Rallis, T. G. Burwitz, P. R. Andrews, M. Zohrabi, R. Averin, S. De, B. Bergues, B. Jochim, A. V. Voznyuk, N. Gregerson, B. Gaire, I. Znakovskaya, J. McKenna, K. D. Carnes, M. F. Kling, I. Ben-Itzhak, and E. Wells, Rev. Sci. Instrum. **85**, 113105 (2014).

[59] G. Floquet, Ann. Sci. Ec. Norm. Super. **12**, 47 (1883).

[60] A. Hishikawa, S. Liu, A. Iwasaki, and K. Yamanouchi, Chem. Phys. **114**, 9856 (2001).

[61] A. M. Sayler, P. Q. Wang, K. D. Carnes, B. D. Esry, and I. Ben-Itzhak, Phys. Rev. A **75**, 063420 (2007).

[62] B. Jochim, R. Averin, N. Gregerson, J. McKenna, S. De, D. Ray, M. Zohrabi, B. Bergues, K. D. Carnes, M. F. Kling, I. Ben-Itzhak, and E. Wells, Phys. Rev. A **83**, 043417 (2011).

[63] R. Trebino, *Frequency-Resolved Optical Gating* (Kluwer Academic Publishers, 2000).

[64] N. G. Kling, D. Paul, A. Gura, G. Laurent, S. De, H. Li, Z. Wang, B. Ahn, C. H. Kim, T. K. Kim, I. Litvinyuk, C. L. Cocke, I. Ben-Itzhak, D. Kim, and M. F. Kling, J. Instrum. **9**, P05005 (2014).

[65] W. C. Wiley and I. H. McLaren, Rev. Sci. Instrum. **26**, 1150 (1955).

[66] J. L. Wiza, Nucl. Instrum. Methods **162**, 587 (1979).

[67] E. Wells, M. Todt, B. Jochim, N. Gregerson, R. Averin, N. G. Wells, N. L. Smolnisky, N. Jastram, J. McKenna, A. M. Sayler, N. G. Johnson, M. Zohrabi, B. Gaire, K. D. Carnes, and I. Ben-Itzhak, Phys. Rev. A **80**, 063402 (2009).

[68] I. Ben-Itzhak, S. Ginther, and K. Carnes, Nucl. Instrum. Methods Phys. Res. B **66**, 401 (1992).

[69] I. Ben-Itzhak, S. G. Ginther, V. Krishnamurthi, and K. D. Carnes, Phys. Rev. A **51**, 391 (1995).

[70] M. J. J. Vrakking, Rev. Sci. Instrum. **72**, 4084 (2001).

[71] G. A. Garcia, L. Nahon, and I. Powis, Rev. Sci. Instrum. **75**, 4989 (2004).

[72]G. M. Roberts, J. L. Nixon, J. Lecointre, E. Wrede, and J. R. R. Verlet, Rev. Sci. Instrum. **80**, 053104 (2009).

[73]C. Guo, Phys. Rev. A **71**, 021405 (2005).

[74]T. Bayer, M. Wollenhaupt, and T. Baumert, J. Phys. B: At., Mol. Opt. Phys. **41**, 074007 (2008).

[75]M. Krug, T. Bayer, M. Wollenhaupt, C. Sarpe-Tudoran, T. Baumert, S. S. Ivanov, and N. V. Vitanov, New J. Phys. **11**, 105051 (2009).

[76]J. G. Underwood, M. Spanner, M. Y. Ivanov, J. Mottershead, B. J. Sussman, and A. Stolow, Phys. Rev. Lett. **90**, 223001 (2003).

[77]B. J. Sussman, D. Townsend, M. Y. Ivanov, and A. Stolow, Science **314**, 278 (2006).

[78]C. Trallero-Herrero and T. C. Weinacht, Phys. Rev. A **75**, 063401 (2007).

[79]J. L. White, B. J. Pearson, and P. H. Bucksbaum, J. Phys. B: At., Mol. Opt. Phys. **37**, L399 (2004).

[80]M. A. Montgomery, R. R. Meglen, and N. H. Damrauer, J. Phys. Chem. A **110**, 6391 (2006).

[81]R. N. Zare, Mol. Photochem. **4**, 1 (1972).

[82]F. Légaré, I. V. Litvinyuk, P. W. Dooley, F. Quéré, A. D. Bandrauk, D. M. Villeneuve, and P. B. Corkum, Phys. Rev. Lett. **91**, 093002 (2003).

[83]A. S. Alnaser, X. M. Tong, T. Osipov, S. Voss, C. M. Maharjan, P. Ranitovic, B. Ulrich, B. Shan, Z. Chang, C. D. Lin, and C. L. Cocke, Phys. Rev. Lett. **93**, 183202 (2004).

[84]P. B. Corkum, Phys. Rev. Lett. **71**, 1994 (1993).

[85]M. Lewenstein, P. Balcou, M. Y. Ivanov, A. L'Huillier, and P. B. Corkum, Phys. Rev. A **49**, 2117 (1994).

[86]H. Niikura, F. Légaré, R. Hasbani, A. D. Bandrauk, M. Y. Ivanov, D. M. Villeneuve, and P. B. Corkum, Nature **417**, 917 (2002).

[87]A. S. Alnaser, T. Osipov, E. P. Benis, A. Wech, B. Shan, C. L. Cocke, X. M. Tong, and C. D. Lin, Phys. Rev. Lett. **91**, 163002 (2003).

[88]I. Znakovskaya, P. von den Hoff, S. Zherebtsov, A. Wirth, O. Herrwerth, M. J. J. Vrakking, R. de Vivie-Riedle, and M. F. Kling, Phys. Rev. Lett. **103**, 103002 (2009).

[89]K. Codling, L. J. Frasinski, and P. A. Hatherly, J. Phys. B: At., Mol. Opt. Phys. **21**, L433 (1988).

[90]K. Codling and L. J. Frasinski, Contemp. Phys. **35**, 243 (1994).

[91]S. Chelkowski and A. D. Bandrauk, J. Phys. B: At., Mol. Opt. Phys. **28**, L723 (1995).

[92]H. Stapelfeldt, E. Constant, and P. B. Corkum, Phys. Rev. Lett. **74**, 3780 (1995).

[93]S. Chelkowski, A. Conjusteau, T. Zuo, and A. D. Bandrauk, Phys. Rev. A **54**, 3235 (1996).

[94]A. D. Bandrauk and H. Z. Lu, Phys. Rev. A **62**, 053406 (2000).

[95]H. Ren, R. Ma, J. Chen, X. Li, H. Yang, and Q. Gong, J. Phys. B: At., Mol. Opt. Phys. **36**, 2179 (2003).

[96]Q. Liang, C. Wu, Z. Wu, M. Liu, Y. Deng, and Q. Gong, Phys. Rev. A **79**, 045401 (2009).

[97]K. Codling, L. J. Frasinski, and P. A. Hatherly, J. Phys. B: At., Mol. Opt. Phys. **22**, L321 (1989).

[98]T. Zuo and A. D. Bandrauk, Phys. Rev. A **52**, R2511 (1995).

[99]T. Seideman, M. Y. Ivanov, and P. B. Corkum, Phys. Rev. Lett. **75**, 2819 (1995).

[100]S. Chelkowski, T. Zuo, O. Atabek, and A. D. Bandrauk, Phys. Rev. A **52**, 2977 (1995).

[101]T. Zuo and A. D. Bandrauk, Phys. Rev. A **54**, 3254 (1996).

[102]J. H. Posthumus, A. J. Giles, M. R. Thompson, W. Shaikh, A. J. Langley, L. J. Frasinski, and K. Codling, J. Phys. B: At., Mol. Opt. Phys. **29**, L525 (1996).

[103]C. R. Scheper, W. J. Buma, C. A. de Lange, and W. J. van der Zande, J. Chem. Phys. **109**, 8319 (1998).

[104]A. Saenz, Phys. Rev. A **61**, 051402 (2000).

[105]J. H. Posthumus, B. Fabre, C. Cornaggia, N. de Ruette, and X. Urbain, Phys. Rev. Lett. **101**, 233004 (2008).

[106]J. McKenna, M. Suresh, B. Srigengan, I. D. Williams, W. A. Bryan, E. M. L. English, S. L. Stebbings, W. R. Newell, I. C. E. Turcu, J. M. Smith, E. J. Divall, C. J. Hooker, A. J. Langley, and J. L. Collier, Phys. Rev. A **73**, 043401 (2006).

[107]G. L. Kamta and A. D. Bandrauk, Phys. Rev. Lett. **94**, 203003 (2005).

[108]G. L. Kamta and A. D. Bandrauk, Phys. Rev. A **76**, 053409 (2007).

[109]A. Bandrauk and F. Légaré, in Progress in Ultrafast Intense Laser Science VIII, edited by K. Yamanouchi, M. Nisoli, and W. T. Hill III (Springer-Verlag GmbH, 2012).

[110]B. Gaire, J. McKenna, N. G. Johnson, A. M. Sayler, E. Parke, K. D. Carnes, and I. Ben-Itzhak, Phys. Rev. A **79**, 063414 (2009).

[111]A. Talebpour, S. Larochelle, and S. L. Chin, J. Phys. B: At., Mol. Opt. Phys. **30**, 1927 (1997).

[112]C. Guo and K. Wright, Phys. Rev. A **71**, 021404 (2005).

[113]C. Guo and K. Wright, Phys. Rev. A **74**, 019904 (2006).

[114]C. Guo, J. Phys. B: At., Mol. Opt. Phys. **38**, L323 (2005).

[115]J. Wu, H. Zeng, and C. Guo, Phys. Rev. A **74**, 031404 (2006).

[116]J. Wu, H. Zeng, and C. Guo, J. Phys. B: At., Mol. Opt. Phys. **39**, 3849 (2006).

[117]J. H. Posthumus, J. Plumridge, M. K. Thomas, K. Codling, L. J. Frasinski, A. J. Langley, and P. F. Taday, J. Phys. B: At., Mol. Opt. Phys. **31**, L553 (1998).

[118]F. Rosca-Pruna, E. Springate, H. L. Offerhaus, M. Krishnamurthy, N. Farid, C. Nicole, and M. J. J. Vrakking, J. Phys. B: At., Mol. Opt. Phys. **34**, 4919 (2001).

[119]J. H. Posthumus, Rep. Prog. Phys. **67**, 623 (2004).

[120]K. Miyazaki, T. Shimizu, and D. Normand, J. Phys. B: At., Mol. Opt. Phys. **37**, 753 (2004).

[121]X. M. Tong, Z. X. Zhao, A. S. Alnaser, S. Voss, C. L. Cocke, and C. D. Lin, J. Phys. B: At., Mol. Opt. Phys. **38**, 333 (2005).

[122]F. Anis, T. Cackowski, and B. D. Esry, J. Phys. B: At., Mol. Opt. Phys. **42**, 091001 (2009).

[123]X. M. Tong, Z. X. Zhao, and C. D. Lin, Phys. Rev. A **66**, 033402 (2002).

[124]S. Voss, A. S. Alnaser, X.-M. Tong, C. Maharjan, P. Ranitovic, B. Ulrich, B. Shan, Z. Chang, C. D. Lin, and C. L. Cocke, J. Phys. B: At., Mol. Opt. Phys. **37**, 4239 (2004).

[125]I. Rabadán and J. Tennyson, J. Phys. B: At., Mol. Opt. Phys. **30**, 1975 (1997).

[126]D. L. Albritton, A. L. Schmeltekopf, and R. N. Zare, J. Chem. Phys. **71**, 3271 (1979).

[127]G. J. Tóth, A. Lőrincz, and H. Rabitz, J. Chem. Phys. **101**, 3715 (1994).

[128]H. A. Rabitz, Science **303**, 1998 (2004).

[129]K. W. Moore, A. Pechen, X.-J. Feng, J. Dominy, V. J. Beltrani, and H. Rabitz, Phys. Chem. Chem. Phys. **13**, 10048 (2011).

[130]C.-C. Shu, T.-S. Ho, X. Xing, and H. Rabitz, Phys. Rev. A **93**, 033417 (2016).

[131]J. Ullrich, R. Moshammer, A. Dorn, R. Dörner, L. P. H. Schmidt, and H. Schmidt-Böcking, Rep. Prog. Phys. **66**, 1463 (2003).

[132]A. T. Clark, J. P. Crooks, I. Sedgwick, R. Turchetta, J. W. L. Lee, J. J. John, E. S. Wilman, L. Hill, E. Halford, C. S. Slater, B. Winter, W. H. Yuen, S. H. Gardiner, M. L. Lipciuc, M. Brouard, A. Nomerotski, and C. Vallance, J. Phys. Chem. A **116**, 10897 (2012).

[133]A. Zhao, M. van Beuzekom, B. Bouwens, D. Byelov, I. Chakaberia, C. Cheng, E. Maddox, A. Nomerotski, P. Svihra, J. Visser, V. Vrba, and T. Weinacht, Rev. Sci. Instrum. **88**, 113104 (2017).

[134]A. Zhao, P. Sándor, and T. Weinacht, J. Chem. Phys. **147**, 013922 (2017).

[135]J. Long, F. J. Furch, J. Durá, A. S. Tremsin, J. Vallerga, C. P. Schulz, A. Rouzée, and M. J. J. Vrakking, J. Chem. Phys. **147**, 013919 (2017).

Chapter 6

Summary and outlook

To close, we have investigated laser-induced fragmentation of an assortment of molecular ions, striving to further our knowledge of molecular dynamics in ultrafast, intense laser fields. Each molecule studied advances this goal, serving as a testing ground for probing different dynamics. Here, we briefly summarize the results presented in this dissertation and comment on future directions to be pursued.

The case of NO^{2+} dissociation reminds us of the importance of focal-volume averaging, which can lead to the dominance of processes involving low total photon numbers under certain conditions in strong-field experiments. Studying the dissociation of this molecule has also allowed us to obtain direct experimental evidence of the key role of multiphoton permanent-dipole transitions, which are often ignored in the interpretation of strong-field experiments. These findings, which have been further confirmed by theory, are particularly relevant given the growing importance of permanent-dipole transitions at long wavelengths, currently a burgeoning topic of interest within strong-field physics. Moreover, the careful consideration of permanent-dipole transitions is important in advancing our understanding towards more complex molecules, which will in many cases have permanent dipole moments.

Our foray into polyatomic molecules beyond simple triatomics has also been a valuable effort thus far. The examination of dissociation without ionization through the use of ion beam targets is complementary to studies starting from neutral molecules. As our approach

allows isolation of $C_2H_2^q$ isomerization to a single charge state, it holds promise in circumventing some of the ambiguity of current strong-field C_2H_2 isomerization studies. We have also explored $C_2H_2^q$ in different configurations, observing the acetylene-like and vinylidene-like fragmentation branching ratios to be extremely dependent upon the initial configuration. We hope that this work will stimulate future theoretical endeavors to shed light on these intriguing results. Interesting experiments along these lines also remain. For instance, a pump-probe study of $C_2H_2^-$ with fine delay steps and guidance from theory regarding the laser pulse parameters could allow tracking of the isomerization of neutral C_2H_2 following photodetachment. Such experimental ventures will likely be within reach once we manage to bunch the ion beam and thus increase its target density. Another topic that we hope to delve into is hydrogen elimination from simple hydrocarbon ions, which will be facilitated by a two-detector system for measuring fragment pairs with large mass ratios.

These investigations are made possible by our powerful coincidence 3D momentum imaging technique. The KER and angular distributions it provides offer invaluable insight in disentangling the often complicated dynamics incited by strong laser fields. Furthermore, we are continually extending our imaging methods, increasing the number of systems and types of dynamics that we can study. These developments include the analysis of neutral–neutral channels and a method to image the dissociation of metastable molecules in flight to the detector. Implementation of these methods will likely enable more studies in the future.

Our collaborative work in pulse shaping continues to enrich us with a broader perspective, and the interplay between these efforts and our ion beam work has been profitable. For instance, findings from our NO^+ and NO^{2+} ion beam studies have helped to inform some of the conclusions about plausible pathways in the closed-loop control experiments on NO molecules.

Collectively, this thesis work has explored and made progress towards answering several questions in intense, ultrafast laser-induced molecular dynamics. As in any scientific pursuit, with each gain in insight, new doors for future efforts have opened.

Bibliography

[1] A. Zewail, Pure and Applied Chemistry **72**, 2219 (2000), URL https://doi.org/10.1351/pac200072122219.

[2] A. H. Zewail, Angewandte Chemie International Edition **39**, 2586 (2000), URL https://onlinelibrary.wiley.com/doi/abs/10.1002/1521-3773%2820000804%2939%3A15%3C2586%3A%3AAID-ANIE2586%3E3.0.CO%3B2-O.

[3] A. Einstein, Annalen der Physik **17**, 132 (1905).

[4] P. Agostini, F. Fabre, G. Mainfray, G. Petite, and N. K. Rahman, Physical Review Letters **42**, 1127 (1979), URL https://link.aps.org/doi/10.1103/PhysRevLett.42.1127.

[5] C. D. Lin, A.-T. Le, C. Jin, and H. Wei, *Attosecond and Strong-Field Physics: Principles and Applications* (Cambridge University Press, 2018).

[6] P. B. Corkum, Physical Review Letters **71**, 1994 (1993), URL https://link.aps.org/doi/10.1103/PhysRevLett.71.1994.

[7] P. Agostini and L. F. DiMauro, Reports on Progress in Physics **67**, 813 (2004), URL https://doi.org/10.1088%2F0034-4885%2F67%2F6%2Fr01.

[8] R. J. Gordon, L. Zhu, and T. Seideman, Accounts of Chemical Research **32**, 1007 (1999), https://doi.org/10.1021/ar970119l, URL https://doi.org/10.1021/ar970119l.

[9] C. Brif, R. Chakrabarti, and H. Rabitz, New Journal of Physics **12**, 075008 (2010), URL https://doi.org/10.1088%2F1367-2630%2F12%2F7%2F075008.

[10] M. Shapiro and P. Brumer, *Quantum Control of Molecular Processes* (Wiley-VCH, 2012).

[11] P. H. Bucksbaum and R. Eisenstein, *AMO2010: "Controlling the Quantum World"* (2006).

[12] A. D. Bandrauk, *Molecules in laser fields* (Marcel Dekker, Inc., 1994).

[13] A. Giusti-Suzor, F. H. Mies, L. F. DiMauro, E. Charron, and B. Yang, Journal of Physics B: Atomic, Molecular and Optical Physics **28**, 309 (1995), URL https://doi.org/10.1088%2F0953-4075%2F28%2F3%2F006.

[14] K. Sändig, H. Figger, and T. W. Hänsch, Physical Review Letters **85**, 4876 (2000), URL https://link.aps.org/doi/10.1103/PhysRevLett.85.4876.

[15] J. H. Posthumus, Reports on Progress in Physics **67**, 623 (2004), URL https://doi.org/10.1088%2F0034-4885%2F67%2F5%2Fr01.

[16] D. Pavičić, A. Kiess, T. W. Hänsch, and H. Figger, Physical Review Letters **94**, 163002 (2005), URL https://link.aps.org/doi/10.1103/PhysRevLett.94.163002.

[17] I. Ben-Itzhak, P. Q. Wang, J. F. Xia, A. M. Sayler, M. A. Smith, K. D. Carnes, and B. D. Esry, Physical Review Letters **95**, 073002 (2005), URL https://doi.org/10.1103/PhysRevLett.95.073002.

[18] B. D. Esry, A. M. Sayler, P. Q. Wang, K. D. Carnes, and I. Ben-Itzhak, Physical Review Letters **97**, 013003 (2006), URL https://link.aps.org/doi/10.1103/PhysRevLett.97.013003.

[19] P. A. Orr, I. D. Williams, J. B. Greenwood, I. C. E. Turcu, W. A. Bryan, J. Pedregosa-Gutierrez, and C. W. Walter, Physical Review Letters **98**, 163001 (2007), URL https://link.aps.org/doi/10.1103/PhysRevLett.98.163001.

[20] J. McKenna, A. M. Sayler, F. Anis, B. Gaire, N. G. Johnson, E. Parke, J. J. Hua, H. Mashiko, C. M. Nakamura, E. Moon, et al., Physical Review Letters **100**, 133001 (2008), URL https://link.aps.org/doi/10.1103/PhysRevLett.100.133001.

[21] J. McKenna, F. Anis, B. Gaire, N. G. Johnson, M. Zohrabi, K. D. Carnes, B. D. Esry, and I. Ben-Itzhak, Physical Review Letters **103**, 103006 (2009), URL https://link.aps.org/doi/10.1103/PhysRevLett.103.103006.

[22] M. Odenweller, N. Takemoto, A. Vredenborg, K. Cole, K. Pahl, J. Titze, L. P. H. Schmidt, T. Jahnke, R. Dörner, and A. Becker, Physical Review Letters **107**, 143004 (2011), URL https://link.aps.org/doi/10.1103/PhysRevLett.107.143004.

[23] T. Rathje, A. M. Sayler, S. Zeng, P. Wustelt, H. Figger, B. D. Esry, and G. G. Paulus, Physical Review Letters **111**, 093002 (2013), URL https://link.aps.org/doi/10.1103/PhysRevLett.111.093002.

[24] N. G. Kling, K. J. Betsch, M. Zohrabi, S. Zeng, F. Anis, U. Ablikim, B. Jochim, Z. Wang, M. Kübel, M. F. Kling, et al., Physical Review Letters **111**, 163004 (2013), URL https://link.aps.org/doi/10.1103/PhysRevLett.111.163004.

[25] U. Lev, L. Graham, C. B. Madsen, I. Ben-Itzhak, B. D. Bruner, B. D. Esry, H. Frostig, O. Heber, A. Natan, V. S. Prabhudesai, et al., Journal of Physics B: Atomic, Molecular and Optical Physics **48**, 201001 (2015), URL http://stacks.iop.org/0953-4075/48/i=20/a=201001.

[26] A. Natan, M. R. Ware, V. S. Prabhudesai, U. Lev, B. D. Bruner, O. Heber, and P. H. Bucksbaum, Physical Review Letters **116**, 143004 (2016), URL https://link.aps.org/doi/10.1103/PhysRevLett.116.143004.

[27] H. Ibrahim, C. Lefebvre, A. D. Bandrauk, A. Staudte, and F. Légaré, Journal of Physics B: Atomic, Molecular and Optical Physics **51**, 042002 (2018), URL https://doi.org/10.1088%2F1361-6455%2Faaa192.

[28] Z. Chang, *Attosecond transient absorption spectroscopy* (CRC Press, 2018).

[29] R. Geneaux, H. J. B. Marroux, A. Guggenmos, D. M. Neumark, and S. R. Leone, Philosophical Transactions of the Royal Society A: Mathematical, Physical and Engineering Sciences **377**, 20170463 (2019), URL https://royalsocietypublishing.org/doi/abs/10.1098/rsta.2017.0463.

[30] D. M. Neumark, Annual Review of Physical Chemistry **52**, 255 (2001), pMID: 11326066, URL https://doi.org/10.1146/annurev.physchem.52.1.255.

[31] A. Stolow, A. E. Bragg, and D. M. Neumark, Chemical Reviews **104**, 1719 (2004), pMID: 15080710, URL https://doi.org/10.1021/cr020683w.

[32] A. H. Zewail, The Journal of Physical Chemistry **100**, 12701 (1996), URL https://doi.org/10.1021/jp960658s.

[33] D. M. Neumark, Science **272**, 1446 (1996), ISSN 0036-8075, URL https://science.sciencemag.org/content/272/5267/1446.

[34] T. Zuo, A. Bandrauk, and P. Corkum, Chemical Physics Letters **259**, 313 (1996), ISSN 0009-2614, URL http://www.sciencedirect.com/science/article/pii/0009261496007865.

[35] C. D. Lin, A.-T. Le, Z. Chen, T. Morishita, and R. Lucchese, Journal of Physics B: Atomic, Molecular and Optical Physics **43**, 122001 (2010), URL https://doi.org/10.1088%2F0953-4075%2F43%2F12%2F122001.

[36] B. J. Whitaker, *Imaging in molecular dynamics: technology and applications* (Cambridge University Press, 2003).

[37] R. Dörner, V. Mergel, O. Jagutzki, L. Spielberger, J. Ullrich, R. Moshammer, and H. Schmidt-Böcking, Physics Reports **330**, 95 (2000), ISSN 0370-1573, URL https://doi.org/10.1016/S0370-1573(99)00109-X.

[38] J. Ullrich, R. Moshammer, A. Dorn, R. Dörner, L. P. H. Schmidt, and H. Schmidt-Böcking, Reports on Progress in Physics **66**, 1463 (2003), URL https://doi.org/10.1088/0034-4885/66/9/203.

[39] A. M. Sayler, Ph.D. thesis, Kansas State University (2008), URL https://krex.k-state.edu/dspace/handle/2097/2611.

[40] B. Gaire, Ph.D. thesis, Kansas State University (2011), URL https://krex.k-state.edu/dspace/handle/2097/8852.

[41] B. Gaire, J. McKenna, A. M. Sayler, N. G. Johnson, E. Parke, K. D. Carnes, B. D. Esry, and I. Ben-Itzhak, Physical Review A **78**, 033430 (2008), URL https://link.aps.org/doi/10.1103/PhysRevA.78.033430.

[42] M. Zohrabi, J. McKenna, B. Gaire, N. G. Johnson, K. D. Carnes, S. De, I. A. Bocharova, M. Magrakvelidze, D. Ray, I. V. Litvinyuk, et al., Physical Review A **83**, 053405 (2011), URL https://link.aps.org/doi/10.1103/PhysRevA.83.053405.

[43] L. Graham, M. Zohrabi, B. Gaire, U. Ablikim, B. Jochim, B. Berry, T. Severt, K. J. Betsch, A. M. Summers, U. Lev, et al., Physical Review A **91**, 023414 (2015), URL https://link.aps.org/doi/10.1103/PhysRevA.91.023414.

[44] J. McKenna, A. M. Sayler, B. Gaire, N. G. Johnson, K. D. Carnes, B. D. Esry, and I. Ben-Itzhak, Physical Review Letters **103**, 103004 (2009), URL https://link.aps.org/doi/10.1103/PhysRevLett.103.103004.

[45] B. Gaire, J. McKenna, M. Zohrabi, K. D. Carnes, B. D. Esry, and I. Ben-Itzhak, Physical Review A **85**, 023419 (2012), URL https://link.aps.org/doi/10.1103/PhysRevA.85.023419.

[46] A. M. Sayler, J. McKenna, B. Gaire, N. G. Kling, K. D. Carnes, and I. Ben-Itzhak, Physical Review A **86**, 033425 (2012), URL https://link.aps.org/doi/10.1103/PhysRevA.86.033425.

[47] A. M. Sayler, J. McKenna, B. Gaire, N. G. Kling, K. D. Carnes, B. D. Esry, and I. Ben-Itzhak, Journal of Physics B: Atomic, Molecular and Optical Physics **47**, 031001 (2014), URL https://doi.org/10.1088%2F0953-4075%2F47%2F3%2F031001.

[48] P. Q. Wang, A. M. Sayler, K. D. Carnes, J. F. Xia, M. A. Smith, B. D. Esry, and I. Ben-Itzhak, Physical Review A **74**, 043411 (2006), URL http://link.aps.org/doi/10.1103/PhysRevA.74.043411.

[49] U. Boesl, Mass Spectrometry Reviews **36**, 86 (2017), URL https://onlinelibrary.wiley.com/doi/abs/10.1002/mas.21520.

[50] A. T. J. B. Eppink and D. H. Parker, Review of Scientific Instruments **68**, 3477 (1997), URL https://doi.org/10.1063/1.1148310.

[51] B. Shan, C. Wang, and Z. Chang, *U. S. Patent No. 7050474* (23 May 2006).

[52] X. Ren, A. M. Summers, Kanaka Raju P., A. Vajdi, V. Makhija, C. W. Fehrenbach, N. G. Kling, K. J. Betsch, Z. Wang, M. F. Kling, et al., Journal of Optics **19**, 124017 (2017), URL http://stacks.iop.org/2040-8986/19/i=12/a=124017.

[53] B. Gaire, J. McKenna, M. Zohrabi, K. D. Carnes, B. D. Esry, and I. Ben-Itzhak, Physical Review A **85**, 023419 (2012), URL https://link.aps.org/doi/10.1103/PhysRevA.85.023419.

[54] B. Berry, Ph.D. thesis, Kansas State University (2018), URL https://krex.k-state.edu/dspace/handle/2097/39160.

[55] C. M. Maharjan, Ph.D. thesis, Kansas State University (2007), URL https://krex.k-state.edu/dspace/handle/2097/378.

[56] B. Jochim, R. Erdwien, Y. Malakar, T. Severt, B. Berry, P. Feizollah, J. Rajput, B. Kaderiya, W. L. Pearson, K. D. Carnes, et al., New Journal of Physics **19**, 103006 (2017), URL https://doi.org/10.1088%2F1367-2630%2Faa81ab.

[57] G. A. Garcia, L. Nahon, and I. Powis, Review of Scientific Instruments **75**, 4989 (2004), URL https://doi.org/10.1063/1.1807578.

[58] M. J. J. Vrakking, Review of Scientific Instruments **72**, 4084 (2001), URL https://doi.org/10.1063/1.1406923.

[59] C. Bordas, F. Paulig, H. Helm, and D. L. Huestis, Review of Scientific Instruments **67**, 2257 (1996), URL https://doi.org/10.1063/1.1147044.

[60] D. Ray, Ph.D. thesis, Kansas State University (2010), URL https://krex.k-state.edu/dspace/handle/2097/3901.

[61] N. G. Kling, Ph.D. thesis, Kansas State University (2013), URL https://krex.k-state.edu/dspace/handle/2097/16821.

[62] S. S. Zumdahl and S. A. Zumdahl, *Chemistry* (Brooks Cole, 2008), 8th ed.

[63] G. Wald, Science **162**, 230 (1968), ISSN 0036-8075, URL http://science.sciencemag.org/content/162/3850/230.

[64] F. Gai, K. C. Hasson, J. C. McDonald, and P. A. Anfinrud, Science **279**, 1886 (1998), ISSN 0036-8075, URL http://science.sciencemag.org/content/279/5358/1886.

[65] S. Allmann and I. T. Baldwin, Science **329**, 1075 (2010), ISSN 0036-8075, URL http://science.sciencemag.org/content/329/5995/1075.

[66] S. F. Perry, Industrial & Engineering Chemistry **44**, 2037 (1952), URL https://doi.org/10.1021/ie50513a027.

[67] R. P. Durán, V. T. Amorebieta, and A. J. Colussi, Journal of the American Chemical Society **109**, 3154 (1987), URL https://doi.org/10.1021/ja00244a053.

[68] G. Valavarasu and B. Sairam, Petroleum Science and Technology **31**, 580 (2013), URL https://doi.org/10.1080/10916466.2010.504931.

[69] B. L. Feringa and W. R. Browne, *Molecular switches* (Wiley-VCH, 2011), 2nd ed.

[70] H. F. Schaefer, Accounts of Chemical Research **12**, 288 (1979), URL https://doi.org/10.1021/ar50140a004.

[71] K. M. Ervin, J. Ho, and W. C. Lineberger, The Journal of Chemical Physics **91**, 5974 (1989), URL https://doi.org/10.1063/1.457415.

[72] S. M. Burnett, A. E. Stevens, C. S. Feigerle, and W. C. Lineberger, Chemical Physics Letters **100**, 124 (1983), ISSN 0009-2614, URL http://www.sciencedirect.com/science/article/pii/0009261483806988.

[73] E. Abramson, R. W. Field, D. Imre, K. K. Innes, and J. L. Kinsey, The Journal of Chemical Physics **83**, 453 (1985), URL https://doi.org/10.1063/1.449560.

[74] Y. Chen, D. M. Jonas, J. L. Kinsey, and R. W. Field, The Journal of Chemical Physics **91**, 3976 (1989), URL https://doi.org/10.1063/1.456828.

[75] K. Yamanouchi, N. Ikeda, S. Tsuchiya, D. M. Jonas, J. K. Lundberg, G. W. Adamson, and R. W. Field, The Journal of Chemical Physics **95**, 6330 (1991), URL https://doi.org/10.1063/1.461554.

[76] M. P. Jacobson, R. J. Silbey, and R. W. Field, The Journal of Chemical Physics **110**, 845 (1999), URL https://doi.org/10.1063/1.478052.

[77] M. P. Jacobson and R. W. Field, The Journal of Physical Chemistry A **104**, 3073 (2000), URL https://doi.org/10.1021/jp992428u.

[78] H. K. Gerardi, K. J. Breen, T. L. Guasco, G. H. Weddle, G. H. Gardenier, J. E. Laaser, and M. A. Johnson, Journal of Physical Chemistry A **114**, 1592 (2010), URL https://doi.org/10.1021/jp9095419.

[79] J. A. DeVine, M. L. Weichman, B. Laws, J. Chang, M. C. Babin, G. Balerdi, C. Xie, C. L. Malbon, W. C. Lineberger, D. R. Yarkony, et al., Science **358**, 336 (2017), ISSN 0036-8075, URL http://science.sciencemag.org/content/358/6361/336.

[80] J. H. D. Eland, F. S. Wort, P. Lablanquie, and I. Nenner, Zeitschrift für Physik D Atoms, Molecules and Clusters **4**, 31 (1986), ISSN 1431-5866, URL https://doi.org/10.1007/BF01432496.

[81] J. H. D. Eland, S. D. Price, J. C. Cheney, P. Lablanquie, I. Nenner, and P. G. Fournier, Philosophical Transactions of the Royal Society of London A: Mathematical, Physical and Engineering Sciences **324**, 247 (1988), ISSN 0080-4614, URL http://rsta.royalsocietypublishing.org/content/324/1578/247.

[82] G. Cooper, T. Ibuki, Y. Iida, and C. Brion, Chemical Physics **125**, 307 (1988), ISSN 0301-0104, URL http://www.sciencedirect.com/science/article/pii/030101048887085X.

[83] R. Thissen, J. Delwiche, J. M. Robbe, D. Duflot, J. P. Flament, and J. H. D. Eland, The Journal of Chemical Physics **99**, 6590 (1993), URL https://doi.org/10.1063/1.465851.

[84] T. Osipov, C. L. Cocke, M. H. Prior, A. Landers, T. Weber, O. Jagutzki, L. Schmidt, H. Schmidt-Böcking, and R. Dörner, Physical Review Letters **90**, 233002 (2003), URL https://link.aps.org/doi/10.1103/PhysRevLett.90.233002.

[85] R. Flammini, E. Fainelli, F. Maracci, and L. Avaldi, Physical Review A **77**, 044701 (2008), URL https://link.aps.org/doi/10.1103/PhysRevA.77.044701.

[86] T. Osipov, T. N. Rescigno, T. Weber, S. Miyabe, T. Jahnke, A. S. Alnaser, M. P. Hertlein, O. Jagutzki, L. P. H. Schmidt, M. Schöffler, et al., Journal of Physics B: Atomic, Molecular, and Optical Physics **41**, 091001 (2008), URL http://stacks.iop.org/0953-4075/41/i=9/a=091001.

[87] Y. H. Jiang, A. Rudenko, O. Herrwerth, L. Foucar, M. Kurka, K. U. Kühnel, M. Lezius, M. F. Kling, J. van Tilborg, A. Belkacem, et al., Physical Review Letters **105**, 263002 (2010), URL https://link.aps.org/doi/10.1103/PhysRevLett.105.263002.

[88] B. Gaire, S. Y. Lee, D. J. Haxton, P. M. Pelz, I. Bocharova, F. P. Sturm, N. Gehrken, M. Honig, M. Pitzer, D. Metz, et al., Physical Review A **89**, 013403 (2014), URL https://link.aps.org/doi/10.1103/PhysRevA.89.013403.

[89] C. E. Liekhus-Schmaltz, I. Tenney, T. Osipov, A. Sanchez-Gonzalez, N. Berrah, R. Boll, C. Bomme, C. Bostedt, J. D. Bozek, S. Carron, et al., Nature Communications **6**, 8199 (2015), URL http://dx.doi.org/10.1038/ncomms9199.

[90] Z. Li, L. Inhester, C. Liekhus-Schmaltz, B. F. E. Curchod, J. W. Snyder, N. Medvedev, J. Cryan, T. Osipov, S. Pabst, O. Vendrell, et al., Nature Communications **8**, 453 (2017), ISSN 2041-1723, URL https://doi.org/10.1038/s41467-017-00426-6.

[91] A. S. Alnaser, I. Litvinyuk, T. Osipov, B. Ulrich, A. Landers, E. Wells, C. M. Maharjan, P. Ranitovic, I. Bochareva, D. Ray, et al., Journal of Physics B: Atomic, Molecular, and Optical Physics **39**, S485 (2006), URL http://stacks.iop.org/0953-4075/39/i=13/a=S21.

[92] A. Hishikawa, A. Matsuda, M. Fushitani, and E. J. Takahashi, Physical Review Letters **99**, 258302 (2007), URL https://link.aps.org/doi/10.1103/PhysRevLett.99.258302.

[93] A. Hishikawa, A. Matsuda, E. J. Takahashi, and M. Fushitani, The Journal of Chemical Physics **128**, 084302 (2008), URL https://doi.org/10.1063/1.2828557.

[94] A. Matsuda, M. Fushitani, E. J. Takahashi, and A. Hishikawa, Physical Chemistry Chemical Physics **13**, 8697 (2011), ISSN 1463-9076, URL http://dx.doi.org/10.1039/C0CP02333G.

[95] X. Xie, K. Doblhoff-Dier, S. Roither, M. S. Schöffler, D. Kartashov, H. Xu, T. Rathje, G. G. Paulus, A. Baltuška, S. Gräfe, et al., Physical Review Letters **109**, 243001 (2012), URL https://link.aps.org/doi/10.1103/PhysRevLett.109.243001.

[96] E. Wells, C. E. Rallis, M. Zohrabi, R. Siemering, B. Jochim, P. R. Andrews, U. Ablikim,

B. Gaire, S. De, K. D. Carnes, et al., Nature Communications **4**, 2895 (2013), URL http://dx.doi.org/10.1038/ncomms3895.

[97] H. Ibrahim, B. Wales, S. Beaulieu, B. E. Schmidt, N. Thiré, E. P. Fowe, E. Bisson, C. T. Hebeisen, V. Wanie, M. Giguére, et al., Nature Communications **5**, 4422 (2014), URL http://dx.doi.org/10.1038/ncomms5422.

[98] X. Xie, K. Doblhoff-Dier, H. Xu, S. Roither, M. S. Schöffler, D. Kartashov, S. Erattupuzha, T. Rathje, G. G. Paulus, K. Yamanouchi, et al., Physical Review Letters **112**, 163003 (2014), URL https://link.aps.org/doi/10.1103/PhysRevLett.112.163003.

[99] X. Gong, Q. Song, Q. Ji, K. Lin, H. Pan, J. Ding, H. Zeng, and J. Wu, Physical Review Letters **114**, 163001 (2015), URL https://link.aps.org/doi/10.1103/PhysRevLett.114.163001.

[100] C. Burger, N. G. Kling, R. Siemering, A. S. Alnaser, B. Bergues, A. M. Azzeer, R. Moshammer, R. de Vivie-Riedle, M. Kübel, and M. F. Kling, Faraday Discussions **194**, 495 (2016), ISSN 1359-6640, URL http://dx.doi.org/10.1039/C6FD00082G.

[101] M. Kübel, R. Siemering, C. Burger, N. G. Kling, H. Li, A. S. Alnaser, B. Bergues, S. Zherebtsov, A. M. Azzeer, I. Ben-Itzhak, et al., Physical Review Letters **116**, 193001 (2016), URL https://link.aps.org/doi/10.1103/PhysRevLett.116.193001.

[102] C. Burger, A. Atia-Tul-Noor, T. Schnappinger, H. Xu, P. Rosenberger, N. Haram, S. Beaulieu, F. Légaré, A. S. Alnaser, R. Moshammer, et al., Structural Dynamics **5**, 044302 (2018), URL https://doi.org/10.1063/1.5037686.

[103] B. Jochim, B. Berry, T. Severt, P. Feizollah, M. Zohrabi, Kanaka Raju P., E. Wells, K. D. Carnes, and I. Ben-Itzhak, The Journal of Physical Chemistry Letters **10**, 2320 (2019), URL https://doi.org/10.1021/acs.jpclett.9b00520.

[104] J. J. Thomson, *Rays of positive electricity, and their application to chemical analyses* (Longmans, Green and Co., 1921).

[105] L. Pauling, The Journal of Chemical Physics **1**, 56 (1933), URL https://doi.org/10.1063/1.1749219.

[106] D. Mathur, Physics Reports **225**, 193 (1993), ISSN 0370-1573, URL https://doi.org/10.1016/0370-1573(93)90006-Y.

[107] D. Schröder and H. Schwarz, The Journal of Physical Chemistry A **103**, 7385 (1999), URL https://doi.org/10.1021/jp991332x.

[108] D. Mathur, Physics Reports **391**, 1 (2004), ISSN 0370-1573, URL https://doi.org/10.1016/j.physrep.2003.10.016.

[109] S. D. Price, International Journal of Mass Spectrometry **260**, 1 (2007), ISSN 1387-3806, URL http://www.sciencedirect.com/science/article/pii/S1387380606003150.

[110] J. I. Steinfeld, *Molecules and Radiation: an Introduction to Modern Molecular Spectroscopy* (Dover Publications, 2005), 2nd ed.

[111] B. H. Bransden and C. J. Joachain, *Physics of atoms and molecules* (Prentice Hall, 2003), 2nd ed.

[112] P. Wustelt, F. Oppermann, L. Yue, M. Möller, T. Stöhlker, M. Lein, S. Gräfe, G. G. Paulus, and A. M. Sayler, Physical Review Letters **121**, 073203 (2018), URL https://link.aps.org/doi/10.1103/PhysRevLett.121.073203.

[113] A. Kiess, D. Pavičić, T. W. Hänsch, and H. Figger, Physical Review A **77**, 053401 (2008), URL http://link.aps.org/doi/10.1103/PhysRevA.77.053401.

[114] J. McKenna, A. M. Sayler, B. Gaire, N. G. Johnson, M. Zohrabi, K. D. Carnes, B. D. Esry, and I. Ben-Itzhak, Journal of Physics B: Atomic, Molecular and Optical Physics **42**, 121003 (2009), URL http://stacks.iop.org/0953-4075/42/i=12/a=121003.

[115] R. S. Judson and H. Rabitz, Physical Review Letters **68**, 1500 (1992), URL https://link.aps.org/doi/10.1103/PhysRevLett.68.1500.

[116] D. E. Goldberg, *Genetic algorithms in search, optimization, and machine learning* (Addison-Wesley, 1989), 1st ed.

[117] R. J. Levis, G. M. Menkir, and H. Rabitz, Science **292**, 709 (2001), ISSN 0036-8075, URL https://science.sciencemag.org/content/292/5517/709.

[118] A. M. Weiner, Review of Scientific Instruments **71**, 1929 (2000), URL https://doi.org/10.1063/1.1150614.

[119] A. Monmayrant, S. Weber, and B. Chatel, Journal of Physics B: Atomic, Molecular and Optical Physics **43**, 103001 (2010), URL https://doi.org/10.1088%2F0953-4075%2F43%2F10%2F103001.

[120] P. Tournois, Optics Communications **140**, 245 (1997), ISSN 0030-4018, URL http://www.sciencedirect.com/science/article/pii/S0030401897001533.

[121] F. Verluise, V. Laude, Z. Cheng, C. Spielmann, and P. Tournois, Optics Letters **25**, 575 (2000), URL http://ol.osa.org/abstract.cfm?URI=ol-25-8-575.

[122] C. E. Rallis, T. G. Burwitz, P. R. Andrews, M. Zohrabi, R. Averin, S. De, B. Bergues, B. Jochim, A. V. Voznyuk, N. Gregerson, et al., Review of Scientific Instruments **85**, 113105 (2014), URL https://doi.org/10.1063/1.4899267.

[123] O. Voznyuk, B. Jochim, M. Zohrabi, A. Broin, R. Averin, K. D. Carnes, I. Ben-Itzhak, and E. Wells, The Journal of Chemical Physics **151**, 124310 (2019), URL https://doi.org/10.1063/1.5115504.

Appendix A

Procedure for selection of a specific fragmentation channel

This appendix details the analysis procedure for coincidence three-dimensional (3-D) momentum imaging briefly outlined in Section 2.4. We utilize an example dissociation channel, $C_2H_2^+ \rightarrow CH^+ + CH$, to illustrate each of the key steps.

A.1 Pre-selection of the data

To start the analysis, we select the measured x, y, and t values in the region of the channel of interest. This "pre-selection" is most easily done using the coincidence time-of-flight (CTOF) map, which is a density plot of the yield as a function of the true time-of-flight of the second hit, t_2, and the true time-of-flight of the first hit, t_1. Due to momentum conservation, each two-body fragmentation channel appears as a diagonal line on this map, as shown in Fig. A.1.1(a). Demonstrated in Fig. A.1.1(b), we rotate the CTOF spectrum so that the channel of interest is horizontal. This way, pre-selection is easier, as it is more straightforward to define a rectangular gate along the axes. It is important to use a generously-wide gate for pre-selection, as illustrated by the black box in Fig. A.1.1(b), as one does not want to bias the data or exclude counts belonging to the channel of interest. It is acceptable for parts of

other channels to lie in this pre-selection gate because those contributions will be eliminated later in the analysis by imposing momentum conservation.
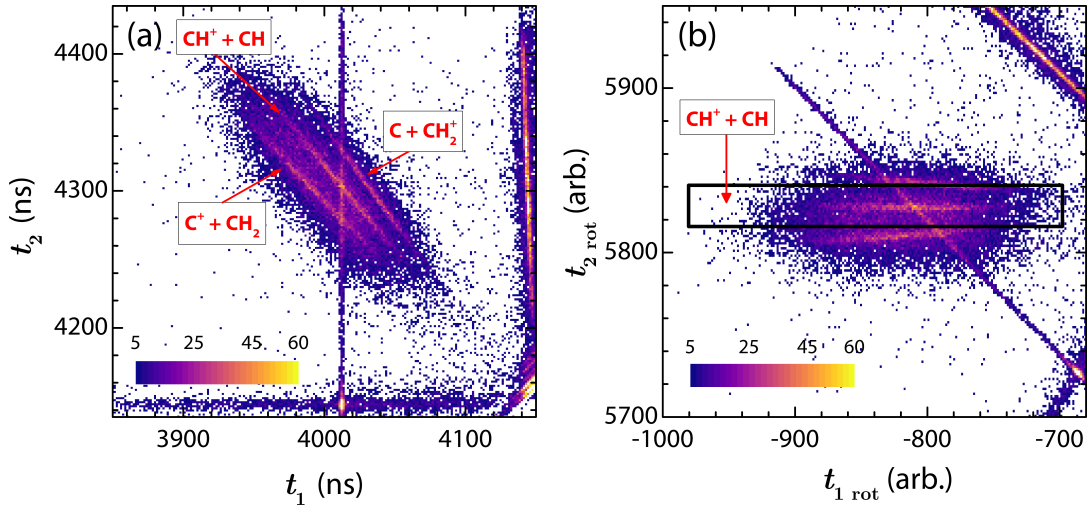

Figure A.1.1: (a) Sample coincidence time-of-flight (CTOF) spectrum of dissociation channels of $C_2H_2^+$ and (b) a pre-selection gate (in black) for the CH^++CH channel on the rotated CTOF spectrum. Note that this gate is generously sized, even including portions of the other channels.

A.2 Setting analysis parameters using symmetry

Having pre-selected the data, one can move on to the next stage of the analysis, setting the parameters for imaging. Sample parameters include the laser polarization direction, the imaging field strengths E_s and E_d (refer back to Fig. 2.3.1), and x_0, y_0, and z_0 (i.e., the interaction point). The values of E_s and E_d are well known, whereas the polarization direction is known approximately. In contrast, the average values $\bar{x}_0$, $\bar{y}_0$, and $\bar{z}_0$ (see Section 2.4) must be obtained in analysis, as we do not know them *a priori*. To determine $\bar{x}_0$, $\bar{y}_0$, and $\bar{z}_0$, we exploit known symmetries of the fragmentation process in a strong laser field. For measurements conducted using long, linearly-polarized laser pulses, one expects the center-of-mass (CM) frame fragment momentum distributions to have cylindrical symmetry about the laser polarization. For long enough pulses, we also expect a forward-backward symmetry along the laser field. For these momenta, we therefore also expect reflection symmetry about zero in the x, y, and z directions. These symmetries are used as a guide for obtaining $\bar{x}_0$,

$\overline{y}_0$, and $\overline{z}_0$. Figure A.2.1 illustrates this procedure for the x direction. The red trace is the distribution of p_{1x}, the x-direction momentum of the first fragment. The blue trace is the reflection of this distribution about zero. Because we expect the p_{1x} distribution to be symmetric about zero, the two traces should lie on top of each other. The parameter $\overline{x}_0$ is adjusted until this condition is satisfied, a process we call "symmetrization" of the data. For the sample data in Fig. A.2.1, the optimal $\overline{x}_0$ value is 0 mm. One should note, however, that the optimal $\overline{x}_0$, $\overline{y}_0$, and $\overline{z}_0$ values can vary somewhat from measurement to measurement, depending on the tuning of the laser-ion beam crossing. This same procedure is performed for the y and z momenta.
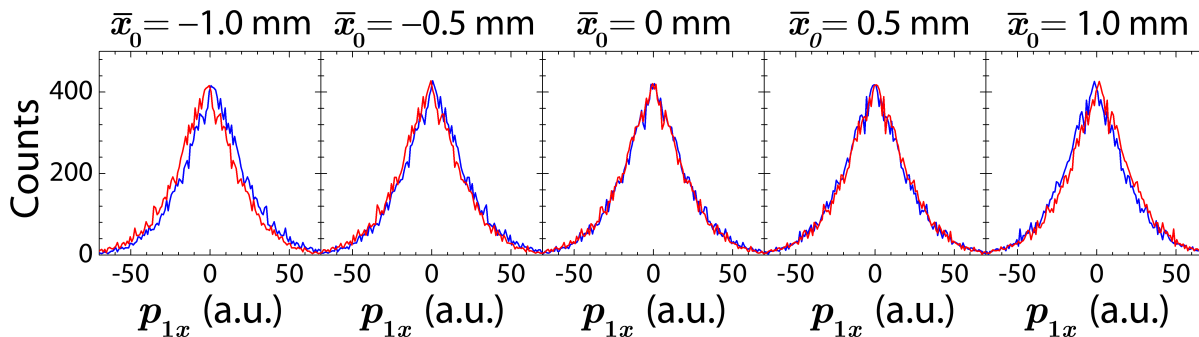
Figure A.2.1: Momentum symmetrization in the x direction for the CH^+ + CH channel. Each panel shows the p_{1x} distribution (red) and its reflection about zero (blue) for a different $\overline{x}_0$ choice. As one can see, $\overline{x}_0 = 0$ mm is the optimal choice.

A.3 Selecting true events of interest based on the center-of-mass momenta

Once the momentum distributions have been symmetrized, we turn our attention to the momenta of the CM, p_{CMx}, p_{CMy}, and p_{CMz}. Momentum-conserving events will lead to CM momentum distributions that are narrow spikes, like the p_{CMx} distribution shown in Fig. A.3.1(b). The data is selected based on conditions placed on the p_{CMx}, p_{CMy}, and p_{CMz} distributions. Explicitly, of the pre-selected data, only those within some range of p_{CM} are selected, while data not meeting these criteria are rejected. The orange curve in

Fig. A.3.1(b) shows the p_{CMx} distribution after implementing p_{CM} conditions in all three dimensions. This procedure imposes momentum conservation.
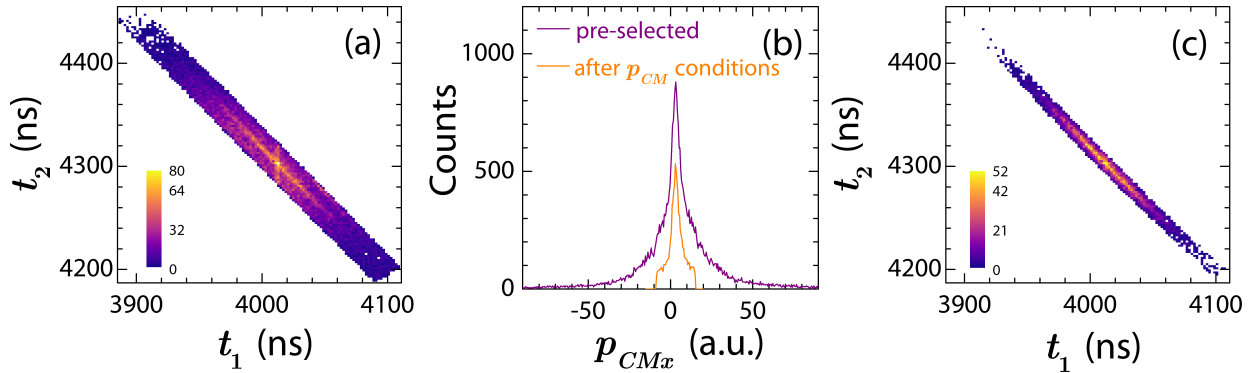

Figure A.3.1: Selecting data using the momentum of the center of mass (CM). (a) The CTOF map after pre-selection. (b) The p_{CMx} distribution for the $CH^+ + CH$ channel before (purple) and after (orange) the p_{CMx}, p_{CMy}, and p_{CMz} momentum conservation conditions are applied. (c) The CTOF map after symmetrization and application of the p_{CM} conditions.

As demonstrated by comparison of Figs. A.3.1(a) and (c), application of the p_{CM} conditions significantly reduces the background and contributions of other channels that pre-selection included. Therefore, a "clean" CTOF stripe for $CH^+ + CH$ emerges, as shown in Fig. A.3.1(c).

After selecting data based on the CM momenta, one should revisit the fragment momentum distributions discussed in the previous section to verify that they still have reflection symmetry about zero. If not, the $\overline{x}_0$, $\overline{y}_0$, and $\overline{z}_0$ values may need to be slightly adjusted (and the p_{CM} conditions revisited after that). Note that as the described p_{CM} data selection procedure is subject to the judgment of the person performing the analysis, it is typically one of the dominant sources of error. To estimate this source of error, several p_{CM} tolerances are tested.

Instead of placing conditions on each of the CM momentum components, one could compute the magnitude $p_{CMr} = \sqrt{p_{CMx}^2 + p_{CMy}^2 + p_{CMz}^2}$ and use its distribution for selecting data. As the spread in each of the p_{CM} components may be different, however, in many cases, this approach is not as effective at suppressing background as using all three components. After performing the procedures described above, information like the kinetic energy release (KER) and angular distributions may be readily retrieved from the fragment momenta.

Appendix B

Neutral–neutral channel identification simulations

In this appendix, we detail simulations to examine the efficiency of neutral–neutral channel identification using the center of mass (CM) momenta.

Simulated datasets are generated for both the CH + CH and C +CH$_2$ channels. Both have an isotropic angular distribution, similar to the experiment, and a gaussian kinetic energy release (KER) distribution. The centroid of the KER is varied (discussed below), while its full width at half maximum (FWHM) is fixed at 2.36 eV. A sample input distribution of yield as a function of KER and $\cos\theta$ for the CH + CH channel is shown in Fig. B.0.1(a).
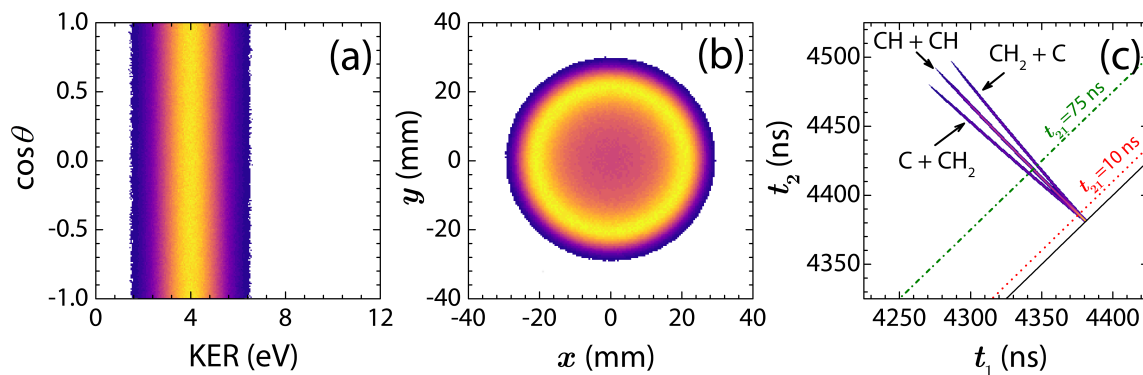
Figure B.0.1: (a) Input distribution of CH + CH yield as a function of KER and $\cos\theta$. (b) Position information computed from the input in (a). (c) Computed CTOF spectrum of the simulated data for CH + CH and C + CH$_2$.

From the input KER and angular distributions, we compute the momenta of both fragments. We also simulate input distributions for the CM motion, v_{0x}, v_{0y}, and v_{0z}, which determine the widths and centroids of the p_{CMx}, p_{CMy}, and p_{CMz} distributions. The x, y and t values may then be back-calculated from the momenta. This simulated x, y, and t data is used to test our identification algorithm, which is outlined in Sec. 2.5. As mentioned in that section, it is difficult to identify events with small t_{21} ($t_{21} \equiv t_2 - t_1$), as in this region, the coincidence time-of-flight (CTOF) stripes overlap, as shown in Fig. B.0.1(c). We test simulated events with $t_{21} < 10$ ns, marked on this CTOF map. As demonstrated by the green line marking $t_{21}=75$ ns in Fig. B.0.1(c), for larger t_{21}, identification of the different channels is straightforward based on the CTOF slopes (detailed in Sec. 2.5).

Our identification algorithm is based upon use of $p_{CMr} \equiv \sqrt{p_{CMx}^2 + p_{CMy}^2}$ to identify the events. There are three possible channel assignments: (1) CH + CH, (2) C + CH$_2$ (i.e., the C fragment arrives to the detector first), and (3) CH$_2$ + C (i.e., the CH$_2$ fragment arrives to the detector first). Thus, for each simulated event, p_{CMr} is calculated three times, once for each channel assignment. The assignment that leads to a value of p_{CMr} closest to the centroid of the true p_{CMr} distribution is taken to be the channel assignment. Then, as we know the true "identity" of each simulated event, that channel identity is checked against the assignment, and the fraction of correct identifications is computed.

Two factors that affect the performance of the identification algorithm are the spread in the CM velocity, specifically v_{0x} and v_{0y}, and the KER. These factors influence the degree to which the p_{CMr} distributions overlap, as well as the image size on the detector. The range of KER used in the simulations roughly matches that measured in the experiment. We tested three different widths for v_{0x} and v_{0y}. We also varied the KER centroid for each width. Note that v_{0x} and v_{0y} were assumed to have the same width, which is typically true in our experiments.

The results of the simulations are shown in Fig. B.0.2. As can be seen, the higher the KER, the better the channel assignment performs. This makes sense, as our algorithm relies on the position separation of the fragments, which increases with KER. Also, narrower spreads in v_{0x} and v_{0y} lead to more accurate channel assignment. Therefore, especially in
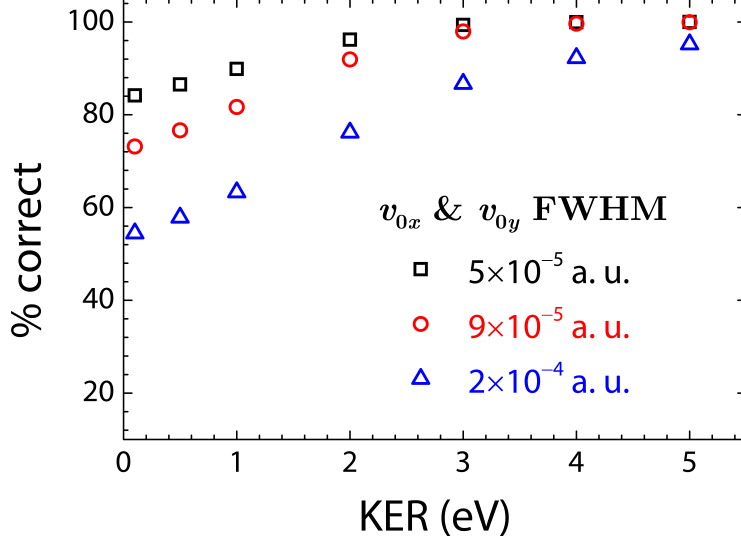
111

Figure B.0.2: Percentage of correct neutral–neutral channel identifications for the CH + CH and C + CH$_2$ channels as a function of KER. These efficiency estimates were performed for different v_{0x} and v_{0y} spreads, shown by the different symbols. The FWHM values of the v_{0x} and v_{0y} distributions are indicated.

cases with very close fragment mass ratios, such as the present case of the CH + CH and C + CH$_2$ channels (i.e., 13:13 versus 14:12), it is critical to have a well-collimated ion beam to be able to identify the events correctly.

The v_{0x} and v_{0y} widths in our experiment were about 2×10^{-4} a.u. (blue symbols in Fig. B.0.2). Given that the measured KER for the C + CH$_2$ and CH + CH channels spans from about 1–4 eV, even for small t_{21}, where separation is difficult, our algorithm still allows correct identification better than about 70% of the time on average.

An alternative approach is to avoid the uncertainty in identification caused by small t_{21} altogether. This is the method we use to evaluate the C + CH$_2$ and CH + CH yields, considering events with $t_{21} >75$ ns, as marked on the CTOF map in Fig. B.0.1(c). One must note, however, that limiting t_{21} is equivalent to a cut in the angular distribution. As the KER and fragment masses are similar in our case, selection based on t_{21} corresponds to approximately the same range of $\cos\theta$ for both channels ($|\cos\theta| \gtrsim 0.48$). In cases where a more detailed comparison is of interest, however, one should select events directly using the $\cos\theta$ distributions.

On a final note, this algorithm clearly works well in certain cases and not in others, but

prudent choice of experimental conditions can help. As already mentioned, collimation of the ion beam is crucial. The beam energy is another key consideration, as it influences the image size on the detector. Additionally, piecewise approaches [43, 56] may be appropriate. For example, if the angular distribution of a particular channel peaks at $\cos\theta = 0$, it may be advantageous to perform measurements both with the laser polarization parallel to and perpendicular to the plane of the detector.

Appendix C

Simulations for imaging dissociation in flight

In Section 2.7, we presented a technique for imaging the dissociation in flight to the detector of metastable molecules and measuring their lifetimes. In this appendix, we discuss the use of simulations to identify important sources of error in this approach. Specifically, we investigate the impact of uncertainty in the time-of-flight on our lifetime retrieval. In Appendix D of the paper in Section 2.7, one source of time-of-flight uncertainty, namely the number truncation by the time-to-digital converter (TDC), is explored. Here we discuss two additional sources of error, specifically uncertainty in the zero point of the true time of flight (see the next section) and finite experimental resolution.

The input data for the simulations discussed in this appendix, shown in Fig. C.0.1, are for $C_2D_4^{2+} \rightarrow C_2D_3^+ + D^+$ dissociation. The KER distribution is a gaussian centered at 4 eV with a full width at half maximum (FWHM) of 1 eV, similar to the KER distribution in the experiment. Also, to match the measurement, the angular distribution is assumed to be isotropic, i.e., uniform in $\cos\theta$, where θ is the angle between the velocity of the light fragment and the laser polarization. Furthermore, the distribution of survival times $N(t_d)$ is a single exponential decay, i.e., $N(t_d) = N_0 e^{-t_d/\tau}$, where the lifetime τ is 1100 ns.
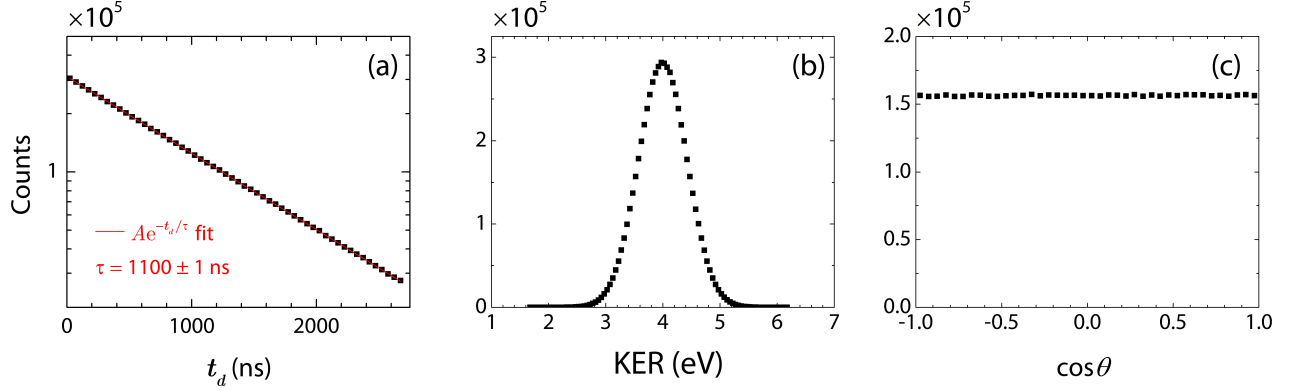
Figure C.0.1: Input data for simulations related to imaging dissociation in flight. (a) $N(t_d)$ distribution (b) KER distribution (c) Isotropic angular distribution.

C.1 Uncertainty in true time of flight

As detailed in Ref. [39], a time-of-flight value recorded by our TDC has a delay due to the electronics used and therefore must be corrected to its true value, i.e., the time between the laser-molecule interaction and the fragment's arrival at the detector. We designate the recorded time of flight as TOF and the true time of flight as t. The correction term linking these two is t_0, where $t = \text{TOF} - t_0$. Here, t_0 is chosen such that $t = 0$ is the time the laser pulse interacts with the target molecule. Furthermore, the difference between the obtained t_0 and its actual value is denoted as δt_0. We perform simulations to determine how δt_0 impacts the recovered lifetimes. To do so, the simulated input data mentioned above are inserted into the dissociation-in-flight equations of motion for two-body fragmentation, Eqs. (4) in the paper in Section 2.7, repeated here for convenience:

$$1 - t_{dm}^2 = 2\left(t_{dm} + \frac{v'_{jz}}{v_m}\right)(t_{jm} - t_{dm}) + \eta_j(t_{jm} - t_{dm})^2 \qquad [j = 1, 2] \qquad \text{(C.1.1)}$$

$$\sum_{j=1}^{2} m_j v'_{jz} = 0. \qquad \text{(C.1.2)}$$

In the above equations, as defined in the aforementioned manuscript, $t_{dm} \equiv t_d/t_m$, i.e., the ratio of the survival time of the metastable dication, t_d, to the time of flight of intact dications, t_m. Similarly, t_{jm} is the true time of flight of the jth fragment divided by t_m. The z-component (longitudinal) dissociation velocity of the jth fragment is v'_{jz}, and the fragment's

115

mass is m_j. The final velocity of an intact metastable dication is $v_m = a_m t_m$, where a_m is its acceleration. The ratio of the acceleration of the jth fragment to that of the metastable dication, a_j/a_m, is represented by η_j. Eqs. C.1.1 and C.1.2 are combined and rearranged into quadratic equations that can be solved for t_1 and t_2:

$$0 = \eta_1 t_1^2 + 2\left((1 - \eta_1)t_d + \frac{v'_{1z}t_m}{v_m}\right)t_1 + (\eta_1 - 1)t_d^2 - \frac{2v'_{1z}t_d t_m}{v_m} - t_m^2 \qquad \text{(C.1.3)}$$

$$0 = \eta_2 t_2^2 + 2\left((1 - \eta_2)t_d - \frac{\beta v'_{1z}t_m}{v_m}\right)t_2 + (\eta_2 - 1)t_d^2 + \frac{2\beta v'_{1z}t_d t_m}{v_m} - t_m^2. \qquad \text{(C.1.4)}$$

Note that β is the mass ratio of the light fragment to the heavy fragment, m_1/m_2. In solving the quadratic formula, we choose the positive root because it is the root that makes physical sense.
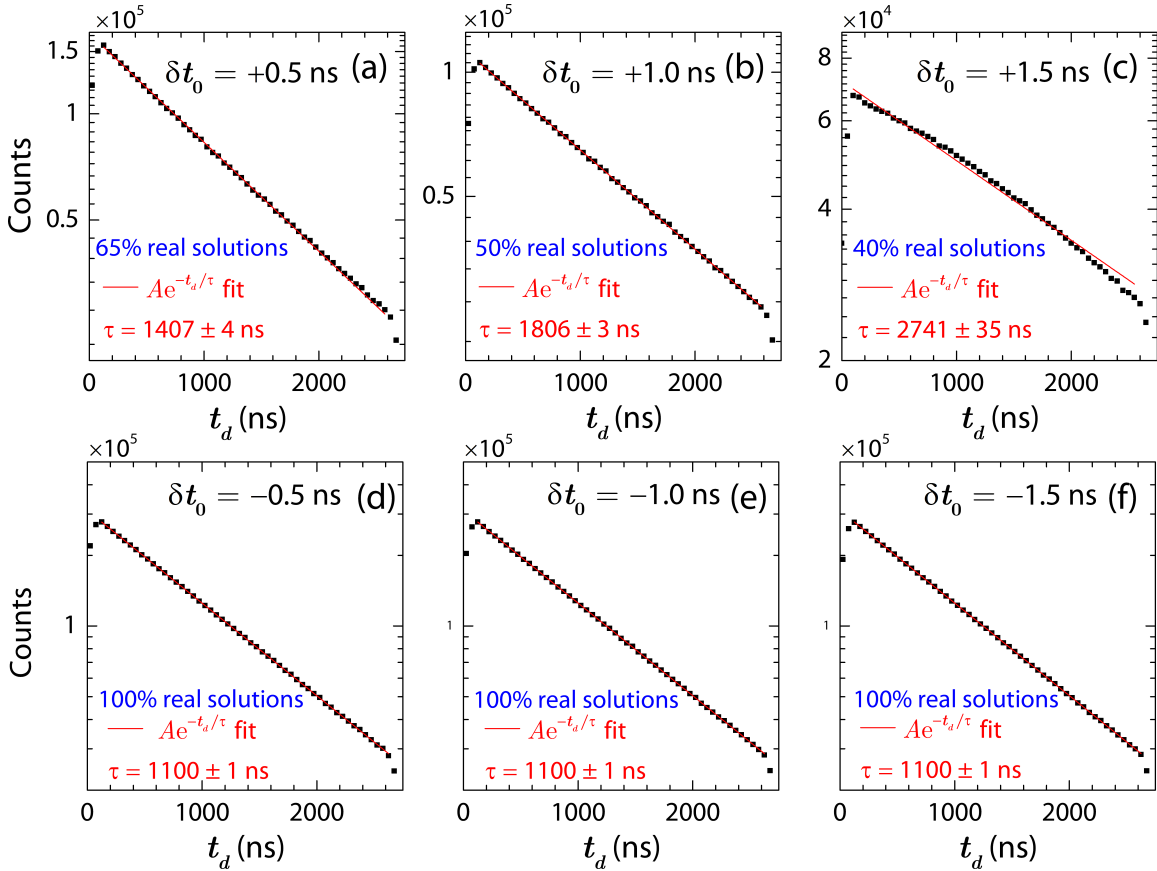
Figure C.1.1: Effect of inaccuracy in t_0 determination on the retrieved lifetime for dissociation in flight. Each panel indicates the degree of this inaccuracy, the fraction of real t_d solutions, and the retrieved lifetime τ. Recall that the input lifetime is 1100 ns.

Next, t_1 and t_2 are shifted from the true values by some amount δt_0. The new time-of-flight values of the fragments and the metastable dication, $t'_1 = t_1 - \delta t_0$, $t'_2 = t_2 - \delta t_0$, and $t'_m = t_m - \delta t_0$, are then used to compute a new t_d distribution, which is compared to the input distribution.

The results of these simulations are shown in Fig. C.1.1. When the t values are too low (positive δt_0), some of the t_d solutions become complex, with the fraction of complex solutions increasing as δt_0 grows. Thus, a large number of complex solutions can be indicative that the obtained t_0 is too high. Moreover, the retrieved lifetime deteriorates rapidly, and as one can clearly see in Fig. C.1.1(c), the range of the $N(t_d)$ distribution suitable for fitting narrows. When δt_0 is negative, on the other hand, all the t_d solutions are real. Moreover, the effect that $\delta t_0 < 0$ has on the retrieved lifetime is far less dramatic compared to the $\delta t_0 > 0$ case, as one can see in Fig. C.1.1(d)-(f). Therefore, if there are doubts about the accuracy of t_0, it is best to err on the side of lower t_0.

C.2   Uncertainty due to finite experimental resolution

Another source of error is finite experimental resolution. To examine this effect, we use the same simulated data ($\tau = 1100$ ns) as the previous section, again solving Eqs. C.1.3 and C.1.4 for t_1 and t_2. We then add a gaussian distribution to these t values to simulate the experimental time resolution (i.e., jitter). One such sample experimental resolution distribution with a width of 0.5 ns (σ) is shown in Fig. C.2.1.
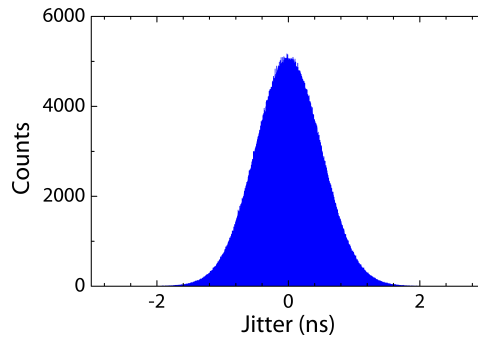

Figure C.2.1: Sample distribution of a gaussian with $\sigma = 0.5$ ns added to t values to test the influence of finite experimental resolution.

The results of these simulations for a few representative experimental resolutions are shown in Fig. C.2.2. As can be seen, with poorer resolution (larger σ), the retrieved lifetime deviates from that of the input $N(t_d)$ distribution and has a larger uncertainty. More significantly, the range of the $N(t_d)$ distribution that can be fitted to for lifetime retrieval shrinks, and the fraction of complex t_d solutions becomes significant.

Finally, the number truncation simulations highlighted in the paper in Section 2.7 led to results similar to those exploring the effect of finite experimental resolution. When considering these sources of error and the previously-discussed error linked to δt_0, the fit range and fraction of complex t_d solutions can serve as a guide for the quality of our approach.
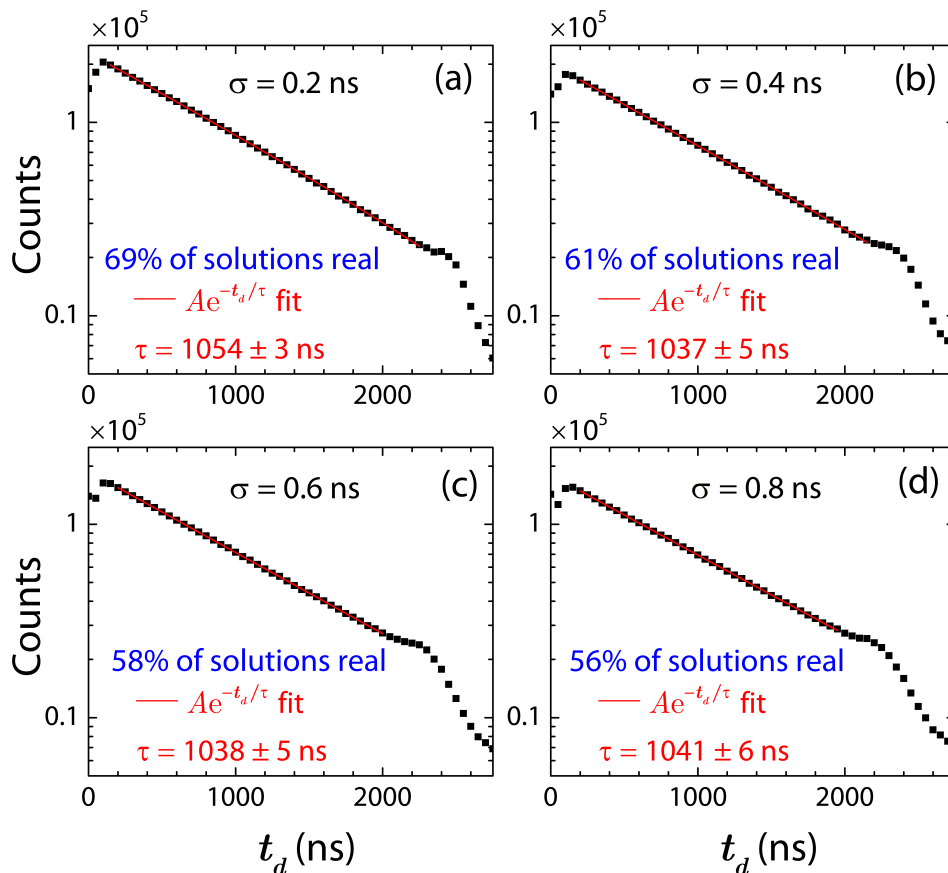

Figure C.2.2: Effect of finite experimental resolution on the retrieved lifetime for dissociation in flight, shown for a few sample values of experimental resolution.

Appendix D

Permission from publishers to include previously-published works

D.1 Permission to reproduce B. Jochim *et al.* New. J. Phys. 19, 103006 (2017)

From:	Permissions <permissions@ioppublishing.org>
Sent:	Tuesday, October 15, 2019 4:07 AM
To:	Jochim, Bethany
Subject:	Re: permission to reproduce my NJP article in my dissertation

Dear Bethany,

Thank you for your email and for taking the time to seek this permission.

When you transferred the copyright in your article to IOP Publishing & Deutsche Physikalische Gesellschaft, you were granted back certain rights, including the right to include the Final Published Version of the article within any thesis or dissertation. Please note you may need to obtain separate permission for any third party content you included within your article.

Please include citation details, "© IOP Publishing & Deutsche Physikalische Gesellschaft. Reproduced with permission. All rights reserved" and for online use, a link to the Version of Record.

The only restriction is that if, at a later date, you wanted your thesis/dissertation to be published commercially, further permission would be required.

I wish you the best of luck with the completion of your thesis/dissertation.

Kind regards,

Harriet

Copyright & Permissions Team
Rebecca Broere - Rights & Permissions Assistant
Harriet Shaw - Legal Adviser
Contact Details
E-mail: permissions@iop.org

For further information about copyright and how to request permission:
https://publishingsupport.iopscience.iop.org/copyright-journals/
See also: https://publishingsupport.iopscience.iop.org/
Please see our Author Rights Policy https://publishingsupport.iopscience.iop.org/author-rights-policies/
Please note: We do not provide signed permission forms as a separate attachment. Please print this email and provide it to your publisher as proof of permission. **Please note**: Any statements made by IOP Publishing to the effect that authors do not need to get permission to use any content where IOP Publishing is not the publisher is not intended to constitute any sort of legal advice. Authors must make their own decisions as to the suitability of the content they are using and whether they require permission for it to be published within their article.

To whom it may concern:

I am a doctoral student at Kansas State University, and I am writing to request permission to include my article "Three-dimensional momentum imaging of dissociation in flight of metastable molecules" published in New Journal of Physics (Bethany Jochim et al. 2017 New J. Phys. 19 103006) in my PhD dissertation.

My dissertation will be made available online through the K-State Research Exchange (http://krex.ksu.edu), a repository of scholarly materials created by Kansas State University faculty, staff, and students. In addition, I am required to submit my dissertation to ProQuest, a firm that will make copies of my dissertation available for purchase.

Could you please email me a signed letter granting me permission to reproduce the aforementioned article in my dissertation? Thank you.

Sincerely,

Bethany Jochim

D.2 Permission to reproduce B. Jochim *et al.* J. Phys. Chem. Lett. 10, 2320 (2019)

ACS Publications
Most Trusted. Most Cited. Most Read.

Title: Dependence on the Initial Configuration of Strong Field-Driven Isomerization of C2H2 Cations and Anions

Author: Bethany Jochim, Ben Berry, T. Severt, et al

Publication: Journal of Physical Chemistry Letters

Publisher: American Chemical Society

Date: May 1, 2019

Copyright © 2019, American Chemical Society

Quick Price Estimate

Permission for this particular request is granted for print and electronic formats, and translations, at no charge. Figures and tables may be modified. Appropriate credit should be given. Please print this page for your records and provide a copy to your publisher. Requests for up to 4 figures require only this record. Five or more figures will generate a printout of additional terms and conditions. Appropriate credit should read: "Reprinted with permission from {COMPLETE REFERENCE CITATION}. Copyright {YEAR} American Chemical Society." Insert appropriate information in place of the capitalized words.

I would like to...	reuse in a Thesis/Dissertation ▼
Requestor Type	Author (original work) ▼
Portion	Full article ▼
Format	Print and Electronic ▼
Will you be translating?	No ▼
Select your currency	USD - $ ▼
Quick Price	Click Quick Price

This service provides permission for reuse only. If you do not have a copy of the article you are using, you may copy and paste the content and reuse according to the terms of your agreement. Please be advised that obtaining the content you license is a separate transaction not involving Rightslink.

QUICK PRICE   **CONTINUE**

To request permission for a type of use not listed, please contact the publisher directly.

D.3 Permission to reproduce O. Voznyuk, B. Jochim *et al.* J. Chem. Phys. 151, 124310 (2019)

From:	AIPRights Permissions <Rights@aip.org>
Sent:	Monday, October 14, 2019 1:28 PM
To:	Jochim, Bethany
Subject:	RE: permission to reproduce my JCP article in my dissertation

Dear Dr. Jochim:

You are permitted to include your published article in your dissertation, provided you also include a credit line referencing the original publication.

Our preferred format is (please fill in the citation information):

"Reproduced from [FULL CITATION], with the permission of AIP Publishing."

Please let us know if you have any questions.

Sincerely,
Susann LoFaso
Manager, Rights & Permissions

AIP Publishing
1305 Walt Whitman Road | Suite 300 | Melville NY 11747-4300 | USA
t +1.516.576.2268
rights@aip.org | publishing.aip.org
Follow us: Facebook | **Twitter** | **LinkedIn**

From: Jochim, Bethany <bjochim@phys.ksu.edu>
Sent: Monday, October 14, 2019 1:35 PM
To: AIPRights Permissions <Rights@aip.org>
Subject: permission to reproduce my JCP article in my dissertation

To whom it may concern:

I am a doctoral student at Kansas State University, and I am writing to request permission to include my article "Adaptive strong-field control of vibrational population in NO^{2+}" recently published in The Journal of Chemical Physics (O. Voznyuk, B. Jochim et al., J. Chem. Phys. **151**, 124310 (2019)).

My dissertation will be made available online through the K-State Research Exchange (http://krex.ksu.edu), a repository of scholarly materials created by Kansas State University faculty, staff, and students. In addition, I am required to submit my dissertation to ProQuest, a firm that will make copies of my dissertation available for purchase.

Could you please email me a signed letter granting me permission to reproduce the aforementioned article in my dissertation? Thank you.

Sincerely,

Bethany Jochim